

HIGH QUANTUM EFFICIENCY MEGAVOLTAGE IMAGING WITH THICK
SCINTILLATOR DETECTORS FOR IMAGE GUIDED RADIATION THERAPY

By

ARUN GOPAL

A DISSERTATION PRESENTED TO THE GRADUATE SCHOOL
OF THE UNIVERSITY OF FLORIDA IN PARTIAL FULFILLMENT
OF THE REQUIREMENTS FOR THE DEGREE OF
DOCTOR OF PHILOSOPHY

UNIVERSITY OF FLORIDA

2009

© 2009 Arun Gopal

To my late father
For teaching me to think well, be simple, and always keep learning

ACKNOWLEDGMENTS

I have been fortunate to have had the support and encouragement of several individuals during my pursuit of a doctoral degree. My graduate advisor, Dr. Sanjiv Samant, has been a strong mentor and motivator throughout my graduate studies. I have also had the privilege of working alongside some of the most talented researchers in medical physics - Junyi Xia, Heeteak Chung, and Bart Lynch.

I would like to thank Drs. Chihray Liu, James Baciak, and Scott Banks for investing their valuable time and effort in serving on my dissertation committee, and for their ideas and suggestions to improve the quality of my research and dissertation. In particular, I am thankful to Dr. Liu for access to clinical equipment at the University of Florida Shands Cancer Center, and also to Jean Peng and Srijit Kamath for their help during imaging measurements. I am especially grateful to David Sobczak (St. Jude Children's Research Hospital, Memphis, TN) for his considerable assistance with system development, installation, and optical measurements.

Finally, I will forever be indebted to my family and friends for their love and encouragement over the last several years. My mother, Rathi Gopalakrishnan, has been vital in instilling the values of education and academic excellence in me. My late father, Dr. V. Gopalakrishnan, taught me the unique virtue of simple living guided by intelligent thought and hard work. He also represented my strongest motivation for research when he went back to school at the age of 60 to complete a doctorate in nuclear physics! And lastly although not in any bit the least, I have had the luxury of being surrounded by wonderful and supportive friends who made my time at the University of Florida extremely rewarding despite the demands and hard work of graduate school. None more so than Joanne D'Silva, who has been with me every step of the way as my best friend and much more!

TABLE OF CONTENTS

	<u>page</u>
ACKNOWLEDGMENTS.....	4
LIST OF FIGURES	8
ABSTRACT	13
CHAPTER	
1 INTRODUCTION.....	15
1.1 Cancer	15
1.2 Radiation Therapy.....	15
1.3 Intensity Modulated Radiation Therapy (IMRT).....	17
1.4 Image Guided Radiation Therapy (IGRT)	18
1.5 Portal Imaging (2-D IGRT).....	19
1.5.1 Challenges in Megavoltage Imaging	20
1.5.2 Clinical Portal Imaging Systems.....	22
1.5.3 Advanced Scintillators for Megavoltage Imaging	29
1.6 CT Based Image Guidance (3-D IGRT).....	32
1.7 Research Goals.....	34
2 METHODS OF CHARACTERIZING RADIOGRAPHIC IMAGING SYSTEMS	39
2.1 Modulation Transfer Function (MTF).....	40
2.1.1 Principles of Measurement.....	40
2.1.2 Sampling and Aliasing.....	44
2.1.3 Slit and Edge Response	45
2.1.4 Line-pair Modulation Response (Bar-pattern Technique)	48
2.2 Noise Power Spectrum (NPS).....	49
2.3 Detective Quantum Efficiency (DQE).....	51
2.4 Theoretical Analysis of Imaging Systems.....	54
2.4.1 Monte Carlo Simulations.....	54
2.4.2 Linear Cascaded Systems Modeling.....	56
3 PROTOTYPE 1 – THICK SCINTILLATION CRYSTAL (TSC).....	63
3.1 CsI(Tl) as a Scintillator.....	63
3.2 Monte Carlo Simulations.....	64
3.3 Prototype TSC Video EPID System	68
3.3.1 Design Considerations.....	69
3.3.4 Imaging Measurements	76
3.4 Optimization of the TSC EPID System.....	91
3.4.1 Imaging Geometry	91
3.4.2 Optical Geometry.....	93

3.4.3	Extra-focal blurring	94
3.4.4	Choice of Parameters	95
4	PROTOTYPE 2 – FIBER-OPTIC SCINTILLATION GLASS ARRAY (FOSGA).....	118
4.1	Background	118
4.2	Detector Concept.....	119
4.3	Manufacturing and Assembly	120
4.3.1	Scintillation Glass Fibers.....	120
4.3.2	Grid Housing	121
4.3.3	Photodiode Panel	122
4.3.4	Pixel Loading	122
4.4	Radiation Transport Calculations.....	123
4.4.1	MCNPX Simulation Model.....	124
4.4.2	Intrinsic QE and DQE(0).....	125
4.4.3	Intrinsic MTF	126
4.4.4	Intrinsic DQE(f)	130
4.5	Optical Transport Calculations	130
4.5.1	Emission of Light Quanta.....	132
4.5.2	Free Flight	134
4.5.3	Optical Interactions.....	135
4.5.4	Output Tallies.....	138
4.5.5	Simulations.....	138
4.6	Linear Cascaded Systems Analysis	142
5	BAR-PATTERN METHODOLOGY FOR EPID QUALITY ASSURANCE	163
5.1	Background	163
5.2	Practical Aspects of MTF Measurements.....	165
5.3	Development of Bar-pattern Methodology	167
5.3.1	Zero Frequency Normalization	167
5.3.2	Bar-pattern Design	170
5.3.3	Effect of Scatter	171
5.3.4	Beam Divergence.....	172
5.4	MTF Measurements for Clinical Portal Imagers	172
5.4.1	Description of Portal Imagers	172
5.4.2	Slit and Edge Measurements.....	173
5.4.3	Bar-pattern Measurements	174
5.4.4	Comparison of Slit, Edge, and Bar-pattern Techniques	176
5.5	Implementation for EPID QA	177
5.6	Sensitivity Analysis	178
6	BAR-PATTERN METHODOLOGY FOR 3-D IGRT QUALITY ASSURANCE	193
6.1	Imaging Performance QA for CBCT.....	193
6.2	Description of CBCT Systems	194
6.3	Imaging Measurements.....	196

6.4 Fluence Normalization of DQE	197
6.5 Qualitative Evaluation of Image Quality	198
6.6 Quantitative Characterization of Imaging Performance	199
7 SUMMARY AND CONCLUSIONS	210
LIST OF REFERENCES	215
BIOGRAPHICAL SKETCH	229

LIST OF FIGURES

<u>Figure</u>	<u>page</u>
1-1 Relative contributions of photoelectric absorption and Compton scattering to the total x-ray interaction cross-section in water.....	37
1-2 Effect of x-ray beam energies on image quality.	37
1-3 Schematic representation of a first generation video EPID system.	38
1-4 Schematic representation of an indirect detection a-Si flat-panel EPID system.	38
2-1 MTF measurement using slit and edge response techniques.....	60
2-2 Modulation response technique – measurement of modulations from a sine pattern.	60
2-3 Modulation response technique – calculations of MTF from modulation profiles.....	61
2-4 Angulated slit and edge methods – incremental sub-pixel shifting of pixel centers.....	61
2-5 Angulated slit and edge methods – reconstruction of oversampled LSF and ESF	62
3-1 Monte Carlo simulation set-up to characterize the CsI(Tl) scintillator for the TSC.....	100
3-2 Simulation tallies indicating AED pulseheight spectra for CsI(Tl).	101
3-3 Simulation tallies indicating LSF profiles for CsI(Tl).	101
3-4 Influence of scintillator thickness on intrinsic QE and DQE(0) for CsI(Tl).	102
3-5 Influence of scintillator thickness on intrinsic MTF for CsI(Tl).	102
3-6 Influence of scintillator thickness on intrinsic DQE(f) for CsI(Tl).	103
3-7 Refractive and geometric optical blurring in thick and clear scintillators.	103
3-8 Reverse coupling geometry for the TSC video EPID system.	104
3-9 The 12 mm thick CsI(Tl) scintillating screen used for the TSC test prototype system. ...	104
3-10 Removal of artifacts due to crystal imperfections in the image of a pediatric chest phantom by simple flat-field correction.....	104
3-11 Images of a pediatric chest phantom.....	105
3-12 Images of a femur and humerus bone phantoms in water	106
3-14 Image of an angulated slit acquired for MTF measurements for the TSC prototype.	107

3-15	Profile of slit response peak intensities over successive rows to determine slit angle. ...	108
3-16	Profile of slit response peak positions over successive rows to determine slit angle.	108
3-17	LSF profile of the TSC prototype measured using the angulated slit technique.....	109
3-18	Overall system and component MTF contributions for the TSC prototype.....	109
3-19	Comparison of MTF spectra for the CsI(Tl) and phosphor screen scintillators.....	110
3-20	Comparison of MTF spectra for the Siemens Beamview and TSC prototype systems...110	
3-21	Comparison of NPS spectra for the Siemens Beamview and TSC prototype systems....	111
3-22	Comparison of DQE spectra for the Siemens Beamview and TSC prototype systems...111	
3-23	Linear cascaded systems model for the TSC system.	112
3-24	Comparison of the theoretical DQE of the TSC prototype from a linear cascaded systems model with its measured DQE.	113
3-25	Quantum accounting diagram for the TSC prototype indicating quantum levels per stage for selected spatial frequencies.	113
3-26	Stage – wise theoretical DQE calculations for the TSC prototype indicating its serial variation over stages.....	114
3-27	Schematic layout of the proposed TSC prototype.....	114
3-28	Effect of EPID clearance on the imaging and optical design parameters for the TSC	115
3-29	The MTF contribution due to extra-focal blurring as a function of blur diameter.	116
3-30	The expected MTF of the proposed TSC prototype.	116
3-31	The expected DQE of the proposed TSC prototype.	117
4-1	The functional and structural layout of the FOSGA detector depicting the constitution of each fiber and its placement in the grid housing.....	146
4-2	Terbium doped scintillation glass fibers used in the FOSGA detector.....	147
4-3	The functional outline of tomolithographic molding (TLM) for the cast production of advanced structured grids	148
4-4	Initial tests for automated fiber insertion based on electrostatic and vacuum gradients.....	148
4-5	Specification of the FOSGA detector array in MCNPX for Monte Carlo simulations. ..	149

4-6	Specification of detector geometry based on thickness and pixel fill factor in a FOSGA detector for Monte Carlo simulations.....	149
4-7	Simulation tallies indicating AED pulseheight spectra for the FOSGA detector.	150
4-8	Influence of detector thickness and pixel fill factor on intrinsic x-ray sensitivity for a FOSGA detector	150
4-9	Effect of septal build-up on the oversampled LSF of a FOSGA detector.	151
4-10	Oversampled LSF profiles for a FOSGA detector of varying thicknesses and 70% fill factor.	151
4-11	Oversampled LSF profiles for a FOSGA detector of varying fill factors and a thickness of 6 cm.....	152
4-12	Influence of detector thickness and pixel fill factor on intrinsic MTF for a FOSGA detector.....	152
4-13	Comparison of the overall intrinsic MTF for the FOSGA detector obtained with shifted source reconstruction of LSF profiles with hypothetical MTF spectra from central source LSF profiles only.	153
4-14	Influence of detector thickness and pixel fill factor on intrinsic DQE(f) for a FOSGA detector.....	153
4-15	A general outline of the process flow for the optical transport algorithm used to model fiber-optic light transmission in the FOSGA detector.....	154
4-16	Distribution of energy deposition along radial distance from the central axis within the luminescent core of the scintillation glass fiber.	155
4-17	Distribution of energy deposition along depth within the luminescent core of the scintillation glass fiber.	155
4-18	Fresnel reflection coefficients for the prototype scintillation glass fibers as a function of the angle of incidence.	156
4-19	Effect of varying scatter conditions on simulated fiber-optic light transmission.	156
4-20	Light transmission efficiency for various fiber geometries obtained from light transport calculations.	157
4-21	Polar angle distribution of light transmission obtained from light transport calculations.	157
4-22	Optical LSF profiles for scintillation glass fibers obtained from light transport calculations.	158

4-23	Optical MTF profiles for scintillation glass fibers obtained from light transport calculations.	158
4-24	Sensitivity of the optical MTF to the fiber – photodiode contact gap.	159
4-25	Linear cascaded systems model for the FOSGA detector.	160
4-26	The overall MTF for a FOSGA detector at selected prototype configurations.	161
4-27	The overall MTF for a FOSGA detector in comparison with its component contributions.	161
4-28	The overall DQE for a FOSGA detector for various prototype configurations.	162
5-1	Effect of beam divergence on line-pair modulations.	184
5-2	Effect of the normalization condition on the accuracy of the zero frequency normalization in bar-pattern MTF measurements.	184
5-3	The custom designed bar-patterns used for MTF measurements of clinical EPIDs.	185
5-4	Kilovoltage radiographs of the bar-patterns used for MTF measurements of clinical EPIDs with constituent spatial frequencies specified.	185
5-5	Comparison of MTF measurements with the slit, edge, and bar-pattern techniques.	186
5-6	Snap shot of a bar-pattern image with relevant ROI selections identified using the computation algorithm developed for clinical EPID QA.	187
5-7	Effects of simulated blurring on bar-pattern MTF measurements.	188
5-8	Effects of simulated additive noise on NPS measurements.	189
5-9	Effects of simulated additive noise on DQE measurements.	190
5-10	Comparison of sensitivities of the bar-pattern MTF and PIPspro F_{50} to simulated blurring.	191
5-11	Comparison of sensitivities of the NPS and PIPspro Σ to simulated additive noise.	191
5-12	Comparison of sensitivities of the DQE and PIPspro CNR to simulated additive noise.	192
5-13	Degradation in the imaging performance of an Elekta iViewGT a-Si EPID over time. .	192
6-1	The schematic layout of line-pairs in a conventional CatPhan phantom.	202
6-2	Extraction of line-pair variance and open field ROIs for MTF and NPS calculations. ...	202

6-3	The functional schematic of the measurement set-up for $CTDI_w$ values for CBCT imaging.	203
6-4	Line-pair slices from a CBCT scan of the CatPhan phantom with the XVI indicating the effect of gantry rotation	203
6-5	Line-pair slices from a CBCT scan of the CatPhan phantom with the XVI indicating the effects of field size and beam filter	204
6-6	Line-pair slices from a CBCT scan of the CatPhan phantom with the OBI.....	205
6-7	Effect of gantry rotation on the MTF for the XVI CBCT system.....	206
6-8	Effect of field size on the MTF for the XVI CBCT system.	206
6-9	Effect of the F1 filter on the MTF for the XVI CBCT system.....	207
6-10	Effect of field size on the DQE for the XVI CBCT system.	207
6-11	Effect of the F1 filter on the DQE for the XVI CBCT system.....	208
6-12	The MTF for the OBI CBCT system at various scan acquisition settings.	208
6-13	The DQE for the OBI CBCT system for various scan acquisitions settings.	209
7-1	Comparison of the projected MTF spectra for the proposed TSC and FOSGA prototypes compared to current conventional EPID systems.....	214
7-2	Comparison of the projected DQE spectra for the proposed TSC and FOSGA prototypes compared to current conventional EPID systems.....	214

Abstract of Dissertation Presented to the Graduate School
of the University of Florida in Partial Fulfillment of the
Requirements for the Degree of Doctor of Philosophy

HIGH QUANTUM EFFICIENCY MEGAVOLTAGE IMAGING WITH THICK
SCINTILLATOR DETECTORS FOR IMAGE GUIDED RADIATION THERAPY

By

Arun Gopal

August 2009

Chair: Sanjiv S. Samant

Major: Nuclear Engineering Sciences

In image guided radiation therapy (IGRT), imaging devices serve as guidance systems to aid patient set-up and tumor volume localization. Traditionally, 2-D megavoltage x-ray imagers, referred to as electronic portal imaging devices (EPIDs), have been used for planar target localization, and have recently been extended to perform 3-D volumetric reconstruction via cone-beam computed tomography (CBCT). However, current EPIDs utilize thin and inefficient phosphor screen detectors and are subsequently limited by poor soft tissue visualization, which limits their use for CBCT. Therefore, the use of thick scintillation media as megavoltage x-ray detectors for greater x-ray sensitivity and enhanced image quality has recently been of significant interest. In this research, two candidates for thick scintillators: CsI(Tl) and terbium doped scintillation glass were investigated in separate imaging configurations. In the first configuration, a thick scintillation crystal (TSC) consisting of a thick, monolithic slab of CsI(Tl) was coupled to a mirror-lens-camera system. The second configuration is based on a fiber-optic scintillation glass array (FOSGA), wherein the scintillation glass is drawn into long fiber-optic conduits, inserted into a grid-type housing constructed out of polymer-tungsten alloy, and coupled to an array of photodiodes for digital read-out. The imaging prototypes were characterized using theoretical studies and imaging measurements to obtain fundamental metrics of imaging

performance. Spatial resolution was measured based on a modulation transfer function (MTF), noise was evaluated in terms of a noise power spectrum (NPS), and overall contrast was characterized in the form of detective quantum efficiency (DQE). The imaging studies were used to optimize the TSC and FOSGA imagers and propose prototype configurations for order-of-magnitude improvements in overall image quality. In addition, a fast and simple technique was developed to measure the MTF, NPS, and DQE metrics for clinical EPID and CBCT systems based on a novel adaptation of a traditional line-pair resolution bar-pattern. This research provides two significant benefits to radiotherapy: the characterization of a new generation of thick scintillator based megavoltage x-ray imagers for CBCT based IGRT, and the novel adaptation of fundamental imaging metrics from imaging research to routine clinical performance monitoring.

CHAPTER 1 INTRODUCTION

1.1 Cancer

Cancer is a form of a tumor or abnormality in cells due to which the normally ordered process of cell division is disrupted and the cells divide at an excessively high rate. This uncontrolled division can result in more abnormal cells, which compounds the growth of the cancer. In other words, cancerous cells can multiply without limits, grow quickly, and invade surrounding normal tissues. Although cancer only refers to the malignant subset of all tumors exhibiting such uncontrolled growth, the term “cancer” and “tumor” will both be used interchangeably in this dissertation to refer to the diseased group of cells or organs. Cancer is the second leading cause of death after heart disease. According to statistical estimates by the American Cancer Society (<http://www.cancer.org>), over 1.5 million people will be diagnosed with cancer in the United States this year, resulting in more than 500,000 deaths with 1380 of these being children. There are several methods of treatment for cancer that include surgery, chemotherapy, biotherapy and radiation therapy and are usually selected based on the type and stage of the cancer, age, personal health and preference, and depending on whether the general goal of the treatment is palliative or curative. In this dissertation, only the last therapy technique is addressed – radiation therapy.

1.2 Radiation Therapy

The fundamental aim in treating cancer is to stop the ability of the cells to divide by damaging their genetic contents. To accomplish this, high energy ionizing radiation (x-rays, γ -rays, or charged particles) is directed at the cancer cells, and this technique is termed as radiation therapy or radiotherapy. While tumor irradiation may be carried out via an implanted radionuclide within the diseased organ (referred to as brachytherapy)¹, the radiation source is

typically an external device and the therapy itself is referred to as external beam radiation therapy. The external source may be a γ -ray emitter like ${}_{60}\text{Co}$ but more commonly, x-rays of the desired energy characteristics are generated with a linear accelerator (or linac), and the delivered radiation beam is often referred to as the treatment or therapy beam. Treatment beam energies are typically in the range of million electron volts (MeV) compared to the kilo electron volt (keV) x-rays from standard x-ray tubes used in clinical diagnostic imaging, and imaging beams of these energy ranges are often referred to as “megavoltage” and “kilovoltage” beams respectively. Commercially available linacs can also be used to deliver electron beams² for therapy while dedicated delivery units called cyclotrons are required to administer proton therapy³. This dissertation will only focus on linac based external beam radiotherapy with megavoltage x-rays.

The essential goal of radiation therapy is to provide maximal dose and damage to the tumor while healthy organs surrounding the cancer receives minimal dose. In this case, the term dose refers to the x-ray energy absorbed by unit mass and is usually expressed in units of grays or Gy's ($1 \text{ Gy} = 10^{-3} \text{ J/gm}$). Upon diagnosis of the disease, radiological or diagnostic imaging techniques like computed tomography (CT) and magnetic resonance imaging (MRI) are used to determine the exact location, size and shape of the cancer. Based on various clinical and physical aspects of the cancer, the 3-D treatment region is typically identified as the tumor or target volume, which includes the diseased volume as well as appropriately devised treatment margins to spare surrounding healthy organs from excessive radiation exposure. Based on these precise 3-D imaging scans, detailed treatment planning systems are used to derive a series of fractionated sessions, in which the patient is irradiated with the prescribed therapy beams. The treatment plans include specific beam orientations and the patient dose for each orientation specified in

terms of the linac output in monitor units (MUs) based on a reference calibration condition between the linac output in MU and patient dose in cGy. In this case, the radiation beams are shaped into multi-directional treatment windows called radiation ports or portals that are commonly realized with the help of the extendable and retractable leaves of a multileaf collimator (MLC)⁴. Radiation is typically delivered in discrete sessions, referred to as treatment fractions, a few times per week over several weeks. The fractionated approach is designed to exploit the ability of healthy cells to repair themselves following radiation damage while cancerous cells are less capable of such repair. In conventional radiotherapy, radiation dose is concentrated at the tumor volume by shaping the beam via MLC ports to conform to the shape of the tumor along several beam angles. Dedicated software in treatment planning systems are used to specify the beam energy, radiation dose, number of fractions, and the number of beam angles as well as the size and shapes of the beam ports for each angle based on the 3-D CT or MRI images of the tumor. Such treatment plans are usually administered with some trial and error based adjustment along with the occasional use of beam modification and patient immobilization aids. However, in the last two decades more sophisticated treatment delivery techniques have evolved for better targeting of the tumor and sparing of critical structures.

1.3 Intensity Modulated Radiation Therapy (IMRT)

With the aim of conforming the delivered radiation dose more precisely to the diagnosed target volume, IMRT is an advanced form of treatment delivery that combines computer-controlled modulation of the beam intensity over the radiation field with an optimized combination of beam angles to obtain sophisticated radiation beam sequences that produce precise and complex dose distributions to accurately target the tumor volume⁵⁻⁷. IMRT allows targeted dose escalation to the tumor while still sparing critical structures which in principle allows tighter treatment margins and more effective disease control. There are several strategies

in place to implement IMRT that differ in the equipment and methods used to modulate beam intensities and deliver radiation. At its simplest, IMRT can be implemented with the aid of beam compensators or filters^{8,9} that attenuate the radiation to conform to a specific 2-D spatial distribution. More commonly, the intensity of the radiation beam is controlled by dividing it into segments or “beamlets” and the radiation field for each segment is varied by controlling the positions of MLC leaves. In this way, the total beam intensity seen by each point within the field can be controlled by adjusting the number of segments in which an MLC leaf is used to attenuate the beam in its path¹⁰. In one form of implementation, irradiation is turned off between segments and the MLC leaves are repositioned to prepare for the delivery of the next segment¹¹⁻¹³. This is often referred to as “step and shoot” IMRT or static field IMRT while in dynamic field IMRT¹⁴, radiation is continually delivered even as the MLC leaves are in motion. Other recent variations of IMRT include helical tomotherapy^{15,16}, in which the collimation of the intensity modulated radiation into fan beams to irradiate “slices” as the linac is made to rotate along helical arcs about the patient as the table is scanned longitudinally to mimic a helical CT geometry.

1.4 Image Guided Radiation Therapy (IGRT)

With tremendous improvements in radiotherapy over the last few decades, which includes diagnostic imaging modalities, physics acumen, treatment planning algorithms, and computer capabilities, therapy plans can be devised that target the tumor volume extremely precisely^{17,18}. However, the efficacy of the treatment could still be compromised by errors in the set-up of the patient with respect to the delivered radiation. Before each treatment fraction the patient is set-up under the radiation beam by using skin markings for alignment, and significant variation in the positioning of the tumor volume may be possible from human error, anatomical changes in the shape of the tumor between fractions, and organ motion within a fraction¹⁷. Particularly, with the steep dose gradients associated with IMRT and tight margins around the

tumor volume, there is enhanced risk of dose to surrounding organs due to set-up errors and organ motion¹⁹⁻²⁸. To circumvent this, the advent of image guided radiation therapy (IGRT), wherein imaging devices are used as guidance systems to aid patient set-up and tumor volume localization has been crucial in order to sustain the effectiveness of IMRT¹⁹⁻²⁸. It must be noted that while the interest in IGRT modalities has been enhanced in the wake of IMRT, the concept of image guidance for patient set-up is not a recent philosophy. The practice of imaging treatment fields to visualize and localize the tumor volume has been carried out for several decades, and has been referred to as portal imaging or megavoltage imaging. Traditionally, portal imaging has been performed using 2-D x-ray detectors to verify orthogonal localization fields that are typically acquired along anterior-posterior (AP) and lateral projections of the treatment volume. More recently, CT based imaging systems have been introduced for 3-D volumetric localization and more accurate verification of treatment delivery. Since most of the recent innovations in IGRT have been based on volumetric imaging, the concept of IGRT could be somewhat ambiguously reserved only for recent 3-D imaging modalities. However, in this dissertation, all forms of imaging tools that assist in 2-D or 3-D target localization and treatment verification will be regarded as IGRT systems, and these includes 2-D portal imagers.

1.5 Portal Imaging (2-D IGRT)

Portal or megavoltage imaging is implemented by placing a megavoltage x-ray imaging device directly under the patient as images of the treatment field are acquired using the therapy beam itself either before or during treatment to verify patient position and dose^{17,29,30}. Typically, portal imaging is performed to obtain AP and lateral fields of the patient set-up on a weekly basis for target localization relative to the treatment planning CT data sets, and in some cases, before and during each fraction for verification of IMRT fields. Portal images may also be used for in vivo measurements of the dose delivered to the patient (typically referred to as dosimetry)³⁰. In

this section, the essential challenges of megavoltage imaging have been summarized, and a brief history of the development of currently available clinical imagers has been presented along with some prominent research studies in the field.

1.5.1 Challenges in Megavoltage Imaging

The biggest concern in megavoltage imaging is the poor quality of portal images, which is the result of two fundamental factors – the unfavorable physics of megavoltage x-ray interactions in matter, and the inefficiency of currently used x-ray detection media^{17,29}. The influence of x-ray interaction physics and the subsequent disparity in image quality due to the effects of two prominent types of interactions (photoelectric absorption, and Compton scatter) when using kilovoltage x-rays (typically < 100 keV in diagnostic radiology) and megavoltage x-rays (up to 18 MeV in radiotherapy) is a well known concept^{17,29,30}. In Compton scattering, an x-ray photon can scatter off an atom in the interaction medium in any possible direction and energy while ejecting an electron from its outer shell, and its likelihood is weakly dependent on atomic number (Z) and generally proportional to electron density (number of electrons per gm)³¹. On the other hand, a photoelectric event results in the complete absorption of an x-ray photon³¹, and it is also material specific with a strong dependence on atomic number (\sim proportional to Z^3). As a result, photoelectric absorption is extremely beneficial to image quality while Compton scatter is quite detrimental to both spatial resolution and contrast, especially when delineating soft tissue structures that have similar electron density. While the probability of a third type of interaction (pair production) rises with photon energy (> 1.022 MeV), its relevance at the specific energy range (typically < 6 MeV) of portal imaging is limited due to the predominance of low Z materials in patient anatomy (pair production is proportional to Z).

Therefore, the quality of any x-ray image is generally dependent on the photon energy characteristics of the incident x-ray beam and the relative contributions of photoelectric

absorption and Compton scatter interactions that affect the characteristics of the radiation beam exiting the patient to reach the detector. The cross-sectional probabilities of photoelectric and Compton scatter events in water are shown in Figure 1-1 as a function of the primary x-ray photon energy. Also included here is a plot of the total photon interaction cross-section, which includes contributions from several other forms of interactions besides photoelectric absorption and Compton scatter. However, only the influences of photoelectric and Compton events on radiographic image quality are relevant in this discussion. As seen from these cross-section plots, Compton scatter is significantly more dominant over photoelectric absorption with megavoltage x-rays compared to kilovoltage x-ray energies. Therefore, kilovoltage imaging in diagnostic radiology exhibits significantly superior image quality compared to megavoltage imaging in radiotherapy as demonstrated below in Figure 1-2, which shows images of a tungsten line-pair resolution bar-pattern acquired with kilovoltage and megavoltage x-ray beams. The kilovoltage image (40 kVp tube voltage, 30 mAs tube current) in Figure 1-2 (A) provides significantly better delineation of the line-pairs compared to the megavoltage image in Figure 1-2 (B) that was acquired with a clinical radiotherapy beam (6 MV energy, 10 MU exposure). In this case, beam energies are specified in terms of the peak tube voltage in kilo volts (kVp) for kilovoltage x-rays to indicate the maximum energy of the x-rays in the beam spectrum (40 kVp indicates an x-ray energy range of 0 – 40 keV). Similarly, the megavoltage beam energy is typically specified in terms of the maximum energy in the beam spectrum (6 MV indicates an x-ray energy spectrum in the range of 0 – 6 MeV).

The second fundamental reason for the poor quality of megavoltage images, i.e. inefficient x-ray detection, is the result of a key trade-off between x-ray sensitivity and spatial resolution that affects all x-ray imagers but is particularly severe in megavoltage imaging. Since

x-ray detection is relatively depleted at higher photon energies (see the decrease of the total interaction cross-section with x-ray energy in Figure 1-1), the thickness of an x-ray detector required to detect a given fraction of the incident x-rays is much greater for megavoltage imaging compared to kilovoltage imaging. However, the lateral migration of secondary x-rays and electrons (and all subsequent imaging quanta – light, ions, etc) that increases with detector thickness results in a deterioration of the imaging spatial resolution, as the imaging signal associated with any point in the patient imaging plane is spread over a large area in the final image. Therefore, while an increase in detector thickness leads to greater x-ray detection, it also results in lower spatial resolution. Currently, megavoltage x-ray detectors are designed to be thin in order to preserve spatial resolution and meet clinical requirements (delineation of 0.5 – 1 mm structures)³⁰. As a result, the quality of megavoltage imaging that is already poor due to excessive Compton scatter is degraded even further by the lack of adequate x-ray sensitivity, which manifests as image noise and reduced contrast.

1.5.2 Clinical Portal Imaging Systems

The methods and equipment used in portal imaging have progressed considerably over the last several decades as megavoltage imaging devices have seen radical improvements in their form and realization. Initially, portal imaging was performed using x-ray films ordinarily used for diagnostic radiological imaging. The first references to film exposures of treatment fields in radiotherapy can be traced to 1942 in the treatment of esophageal cancer³². In 1951, Hare *et al* described a detailed imaging set-up for clinical verification of patient set-up in radiotherapy of esophageal cancer³³, which laid the foundation for much scientific interest in the 1950's towards megavoltage imaging in radiation therapy³⁴⁻³⁶. The last two decades have seen the development of digital portal imaging systems referred to as electronic portal imaging devices (EPIDs). Some popularly used commercially available portal imagers have been described below.

1.5.2.1 Portal film

Historically, x-ray film has been a popular medium for clinical portal imaging mainly due to its precedence in diagnostic radiology, compactness and simplicity²⁹. An x-ray film cassette typically consists of a front metal plate and a rear metal/plastic plate that sandwich an emulsion of silver halide crystals^{17,29}. The process of image formation in a film system starts with the detection of an incident x-ray, electron or light photon in the emulsion, which excites the electrons in the halide ions. The electrons are captured by trapping centers called sensitivity specks located at the sites of lattice impurities in the halide grains, and the precipitation of metallic silver at these sites leads to the development of a latent image. The front plate assists in the latent image formation by interacting with the incident radiation to produce high energy electrons (also referred to as build-up) and stops the low energy x-ray scatter from reaching the film. Similarly the rear plate provides back-scatter electrons to the halide grains. The exposed film is then developed by physically processing with reducing agents and other chemicals to form visible patterns along the latent image. While x-ray films provide good quality portal images relative to other megavoltage x-ray imagers, they operate within a limited exposure range and suffer from other limitations including a lack of real-time verification due to processing and handling delays, difficulty of storage and remote access, and deterioration over time¹⁷.

1.5.2.2 Mirror – lens – camera based video EPID systems (first generation EPIDs)

Megavoltage imaging in digital or electronic form using EPID systems was developed in the wake of the aforementioned limitations of portal film cassettes in an effort to render real-time verification with good image quality, broader exposure range for operation, and the convenience of electronic processing, archiving, sharing, and retrieval^{17,29}. The so called first generation commercial EPID prototypes were based on fluoroscopic imaging units (depicted in Figure 1-3), wherein a luminescent detector (also referred to as a luminescent or scintillating screen) was

used to convert the incident x-rays to light, which was coupled to a camera system via a mirror angled at 45° and a focusing lens^{17,29,30}. Over the years, various groups have referred to such fluoroscopic megavoltage imaging systems by different names such as lens-coupled EPIDs, TV or video camera EPIDs, and video EPIDs. Megavoltage imaging has been realized using video cameras since as early as 1958³⁷⁻³⁹. In 1980, Baily *et al* reported the first fluoroscopic imaging system dedicated to radiotherapy imaging, thus providing the precedent for commercial first generation EPIDs⁴⁰. In commercial video EPIDs, the luminescent detector is a Lanex Fast-B screen (Eastman Kodak, Rochester, NY), which includes a 1 mm thick copper build-up plate overlaid on a 0.365 mm thick phosphor screen containing powdered terbium doped gadolinium oxysulfide ($\text{Gd}_2\text{O}_2\text{S:Tb}$) in a paste with a binding mixture (with a bulk density of 3.67 gm/cm^3)⁴¹. Typically, a newvicon tube camera (zinc selenide and zinc cadmium telluride target) that provides high sensitivity in low light fields is used to detect the light produced by phosphor screens⁴².

In general, video EPIDs provide several advantages as a portal imager including the ease of imaging large radiation fields with simultaneous frame acquisitions with camera systems for real-time fluoroscopic verification^{17,29}. However, the optical coupling mechanism renders two significant limitations for video EPIDs. The inclusion of a 45° mirror to reflect the luminescent signal to the camera (necessary to protect the sensitive camera electronics from possible radiation damage due to direct irradiation) makes the imaging system extremely large and bulky^{17,29}. Most importantly, the lens focusing mechanism of light sensing by the camera target is limited by an extremely low light collection efficiency as only a small fraction ($\sim 0.01\%$) of the light produced by the luminescent screen is channeled into the volumetric focusing cone of the lens^{17,29,43}. With such low levels of light collection, the usually high quantum gain from the

conversion of x-rays to light is significantly compromised, which leads to high imaging noise and reduced contrast. In addition, there is significant blurring of light in the lens and the camera target, which severely degrades the system spatial resolution⁴². The large volume of the light coupling enclosure and the highly reflective surfaces of the mirror and the phosphor screen (bottom surface of the Lanex Fast-B screen is white) lead to multiple light scattering due to which, light rays originating from one part of the screen may be detected by the camera following several reflections that distort the spatial orientation of the imaging signal. This phenomenon can result in reduced spatial resolution and potentially severe errors in dosimetry and is referred to as optical glare^{17,44}.

1.5.2.3 Liquid matrix ionization chamber EPID systems

In 1985, Meertens and van Herk *et al* developed a two-dimensional matrix ionization chamber that utilized an iso-octane liquid film (2,2,4-trimethylpentane) as the detection medium⁴⁵⁻⁴⁹. The liquid matrix ion chamber was the first alternative system to video EPIDs to be commercialized and used for clinical portal imaging. The imager was realized as a compact parallel plate system filled with the iso-octane medium, along with a frontal plastoferrite layer for build-up. Upon irradiation and subsequent generation of charge pairs in the detection medium, the ionic current was measured using two orthogonally oriented arrays of 256 parallel electrodes situated in separate planes, thus rendering a 256 x 256 matrix of pixels to be read out sequentially by electrometers. However, the system had limited spatial resolution due to sparse pixel sampling, and since only one electrode matrix was operative at a time, a large fraction of the x-rays was not utilized in imaging thus increasing the dose required per image^{17,29}.

1.5.2.4 Indirect detection flat-panel EPID systems

The current standard for commercially available megavoltage imagers for clinical treatment set-up and dose verification is the so called flat-panel EPID system, which is based on

a conventional Lanex Fast-B phosphor screen whose luminescent response is digitized by an active matrix of thin film transistor (TFT) switches along the same lines as liquid crystal display (LCD) panels⁵⁰⁻⁵⁸. Each TFT element consist of one or more semiconductor diode switches made out of hydrogenated amorphous silicon (a-Si or a-Si:H). Such systems have been referred to as active matrix flat-panel imagers (AMFPIs) or simply as a-Si or flat-panel EPIDs. However, they may be more appropriately addressed as indirect detection flat-panel (or a-Si) EPIDs, which indicates that the AMFPI does not detect the incident x-rays directly but instead provides an indirect read-out of the radiation intensity via the light produced by the luminescent screen following a short but distinct capacitive or storage phase. The schematic arrangement of a conventional a-Si EPID is shown in Figure 1-4. The system consists of a luminescent screen coupled to the flat-panel active matrix that in turn consists of a photosensing layer and a panel of TFT switches. In this dissertation, the combination of the photosensor and the TFT panel will be collectively referred to as the a-Si read-out array or panel.

During irradiation, the TFT elements are disabled while the x-rays detected by the screen generates light photons that interact in the photosensor to liberate electron – hole pairs (a “hole” refers to the vacancy left behind by a migrating electron in a semiconductor lattice structure that is equivalent to a positive charge). During read-out, the TFT switches are turned on and the ionic current proportional to the density of electron-hole pairs over each pixel is acquired and digitized for image reconstruction and processing. The significant advantage of indirect detection flat-panel EPIDs over first generation video EPIDs is in the light collection efficiency of the a-Si read-out panel (~ 50% for conventional screens and flat-panels)¹⁷, which results in significantly greater image quality with a-Si EPIDs^{57,58}. The read-out electronics adds minimal dark noise and negligible electronic cross talk to provide excellent noise and spatial resolution characteristics⁵⁸.

Several studies have suggested that a-Si arrays are remarkably resistant to prolonged exposure to radiation with little degradation in performance due to radiation damage⁵⁹. However, the read-out circuitry located at the periphery of the detector panel is susceptible to radiation damage and requires shielding from primary radiation¹⁷. Moreover, since a flat-panel imager does not require a lens, camera or mirror, there is significantly lesser optical blurring, minimal glare, and subsequently improved spatial resolution compared to video EPIDs^{17,58}. As a result, megavoltage imaging with a-Si EPIDs offers high image quality that is greater or comparable to film systems at lesser dose⁵⁶.

1.5.2.5 Other notable research prototypes

Following the transition from the use of portal film to first generation video EPIDs, several alternative research prototype systems have been studied with the objective of improving the quality of the portal images. These prototype systems are based on entirely new and innovative imaging principles and represent notable ongoing research in megavoltage imaging although they have not been commercialized to date. In one of the earlier efforts to improve the light output in video EPIDs, Wong *et al* used a modified EPID configuration that consisted of a fiber-optic bundle to channel the light produced by a conventional phosphor screen towards a camera system⁶⁰. However, despite the advantage of eliminating the lens from the system design, the improvement in light coupling was not significant on account of the light losses incurred along the large length of the fiber-optic bundle²⁹. Moreover, spatial resolution was quite limited,²⁹ and the portal images were affected by significant spatial distortion due to fiber misalignments^{17,29}. Another popular strategy to counter the poor optical coupling of the mirror – lens assembly was based on using more sophisticated camera systems for image noise reduction. Munro *et al* utilized extended charge integration on the camera target instead of frame averaging⁶¹. For more effective noise reduction, Drake *et al* used an externally cooled charge

coupled device (CCD) camera system⁶² to exploit the characteristically low dark noise of cooled CCD targets while Pang *et al* incorporated avalanche based multiplication of charges in the camera target for high signal gain⁶³. However, despite the improvements with sophisticated camera systems, video EPIDs were still limited by the inefficiency of phosphor screen detectors. Moreover, the large size associated with a mirror – lens coupled camera unit remained an inevitable mechanical constraint. The subsequent need for compact and less bulky systems fueled extensive research on EPID prototypes based on solid state detectors²⁹.

The initial interest in semiconductor diodes for megavoltage imaging began with the use of scanning 1-D imagers featuring silicon and cadmium telluride (CdTe) based diode arrays⁶⁴⁻⁶⁶. While these systems provided limited spatial resolution and required high exposures for good quality images, they also led to further developments and improvements in solid state arrays that ultimately led to the commercialization of modern indirect detection a-Si flat-panel EPIDs¹⁷. Flat-panel arrays were also studied in an alternative imaging configuration utilizing a photoconductor like amorphous selenium (a-Se) that detects x-rays to directly produce electron – hole pairs for TFT read-out, and such a system is referred to as a direct detection flat-panel EPID⁶⁷⁻⁷⁰. However, just as in the case of indirect detection a-Si EPIDs that use phosphor screen detectors, the imaging performance of a-Se based direct detection EPIDs were limited by inefficient x-ray detection. The major distinction of direct detection flat-panel EPIDs relative to its indirect detection counterpart is the elimination of light photons as intermediate signal carriers. Thus, direct detection flat-panels essentially operate as ionization type detectors as an applied electric field is used to guide the read-out of electron – hole pairs, and in principle, the inherent electrostatic focusing of charges provides high spatial resolution⁶⁷⁻⁷⁰. Other notable efforts in developing ionization type detectors for megavoltage imaging include a gas electron

multiplication (GEM) based imaging system⁷¹, in which the ionization produced in response to incident x-rays is focused through a suitably selected electric field that promotes avalanche multiplication of the charges⁷². More recently, the use of heterogeneous ionization media consisting of metallic activation elements to promote x-ray interactions has been suggested as a replacement for the homogenous a-Se layer in direct detection flat-panel EPIDs⁷³⁻⁷⁶.

Samant *et al* recently developed an innovative portal imager based on a scanning 1-D ionization chamber containing high density (100 atm) xenon gas in tandem with a collimated fan beam, referred to as a kinestatic charge detector (KCD)⁷⁷. Unlike conventional ion chambers, the electric field that guides the ionization charges in the KCD chamber is oriented along one dimension of the image instead of in line with the radiation beam while a 1-D array of collecting electrodes (or collectors) is oriented in the other imaging axis. The KCD featured a unique charge integrating principle, in which the chamber and the fan beam are scanned in tandem across the imaging field such that the chamber scan speed is exactly equal but opposite to the speed of the ions drifting under the electric field⁷⁸. The use of a fan beam improves image quality by reducing scatter while the charge integration mechanism significantly enhances contrast visualization. Theoretical and experimental studies of imaging performance, recombination, and mechanical stability were recently carried out for a prototype KCD system. The results indicated more than an order of magnitude improvement (~ 20X) in x-ray sensitivity and overall imaging performance compared to conventional EPIDs^{77,79}.

1.5.3 Advanced Scintillators for Megavoltage Imaging

The majority of portal imagers in clinical use today are based on the conversion of incident x-ray photons to light by a phosphor screen in video or flat-panel based EPID configurations. As described previously, the major limitation of such systems is the poor x-ray detection efficiency of the phosphor screen, which also decreases its scintillation response

resulting in insufficient imaging quanta and poor image quality. Therefore, a significant amount of research has been devoted over the last two decades to obtaining more efficient scintillation media that provide greater x-ray sensitivity and subsequently more light output. Attempts at utilizing thicker phosphor screens were reported initially by Bissonnette *et al* in combination with mirror – lens – camera – units⁴¹. The exact thicknesses of the tested screens in these studies are not clear since their size was characterized in terms of mass thickness (product of thickness and density or mass per unit area). Assuming comparable bulk densities for the binding mixture of the phosphor, the mass thickness values reported in the above studies represent an increase in phosphor thickness in the range of 2 – 10 times that of conventional Lanex Fast-B screens that are used in clinical EPIDs. The major limitation with such an approach is that the opacity of the Gd₂O₂S:Tb paste denies a clear path to the light produced in response to x-ray interactions. Instead the light photons interact extensively within the screen to be either scattered in an arbitrary direction or absorbed by the phosphor itself, and this results in a reduction in spatial resolution as well as depleted light output^{41,80}. Therefore, despite greater x-ray sensitivity, no significant improvement in the performance of the screen could be observed beyond a certain thickness (approximately three times that of a standard screen)⁴¹. Considering that standard screens are approximately 0.365 mm thick (or 134 mg/cm² mass thickness) and they detect < 2% of incident x-rays in a typical 6 MV radiotherapy beam^{41,42}, an increase in phosphor thickness by a factor of three (~ 400 mg/cm²) provided only modest improvements in x-ray detection and light output (< factor of two)⁴¹, which is unfortunately not adequate based on the current standards and expectations of portal image quality.

The above studies clearly established the limitations of opaque scintillators and corroborated earlier findings of practical limits to phosphor thickness based on light output^{81,82}.

As a result, much of the subsequent interest in advanced luminescent screens was diverted to the use of optically clear or transparent scintillation media¹⁷. A popular choice for clear scintillators that has been widely studied in a variety of imaging configurations in the recent past has been crystalline cesium iodide doped with thallium [CsI(Tl)]. In a pioneering effort, Mosleh-Shirazi *et al* developed a video EPID system consisting of a 2-D array of 1 cm thick CsI(Tl) crystals coupled via a standard mirror and lens to a CCD camera system⁸³⁻⁸⁶. Individual CsI(Tl) elements were optically separated by coating an epoxy resin along their septa to limit the migration of light between CsI(Tl) elements. With its large thickness (~ 27 times the thickness of standard phosphor screens), the 1 cm thick CsI(Tl) array provided significantly greater x-ray sensitivity (~ 18% for 6 MV beams)^{83,86}. However, its spatial resolution was extremely limited to resolving 2 mm wide structures due to a rather coarse pixel sampling grid (pixel width ~ 3 mm) compared to conventional EPIDs (typical pixel width ~ 0.5 mm)⁸³. Moreover, the explicit pixelization of the light produced in the scintillator with the choice of a structured CsI(Tl) array may also have been detrimental to the overall imaging spatial resolution as the focusing mechanism of the lens and the pixelization of the CCD camera would have been sufficient to render effective spatial resolution.

As an alternative configuration to a structured CsI(Tl) array, Zeman and Sawant *et al* incorporated an unsegmented clear slab of crystalline CsI(Tl) coupled to a nitrogen cooled CCD camera^{87,88}. With a comparable scintillator thickness (~ 1.3 cm), this system also featured good x-ray sensitivity (~ 25% for a 6 MV beam)⁸⁷ and illustrated the potential benefit of clear scintillators in megavoltage imaging. More recently, clear crystalline scintillators have been studied in segmented configurations in conjunction with a-Si flat-panel arrays. Rathee and Monajemi *et al* recently developed a prototype EPID using structured arrays of 1 cm thick

cadmium tungstate (CdWO_4) crystals coupled to photodiodes to render high quality megavoltage imaging⁸⁹⁻⁹². Sawant *et al* reported detailed theoretical studies and preliminary measurements with the use of bismuth germinate ($\text{Bi}_4\text{Ge}_3\text{O}_{12}$ or BGO) and CsI(Tl) based structured scintillator arrays with thicknesses up to 4 cm in conjunction with a standard a-Si read-out panel^{93,94}. These recent studies have demonstrated the feasibility of using thick, clear scintillation media for significant improvement in x-ray detection (up to a factor of $\sim 25 - 30$) and subsequently in the luminescent response and overall image quality.

1.6 CT Based Image Guidance (3-D IGRT)

As a result of inherent limitations of megavoltage imaging, the usefulness of IGRT using portal imaging has generally been greatly reduced as bony anatomy has to be used as surrogate landmarks for target localization on account of poor soft tissue visualization¹⁹⁻²⁸. A logical alternative to overcome these limitations was to introduce additional kilovoltage x-ray imaging units as attachments to the linac for diagnostic quality 2-D target localization, and such strategies have been studied even before the inception of commercial EPIDs^{95,96}. But recently, IGRT has been based on 3-D volumetric imaging systems to keep up with the demands of IMRT treatment margins. Although several commercial 3-D IGRT solutions are currently available that may be classified based on functionality, equipment, and clinical application, only a few selected CT based IGRT systems will be briefly described in this section as they represent the most widely used subset of 3-D IGRT solutions based on clinical prevalence and literature reports.

With the aim of achieving target localization with high soft tissue visualization comparable to treatment planning CT images, the so called “in room CT” or “CT-on-rails” system incorporates a conventional CT into the treatment room with the use of rails to relocate the CT bore and the patient table relative to each other⁹⁷⁻¹⁰¹. Another form of CT based IGRT that has recently grown in popularity is based on obtaining a 3-D CT reconstruction of the

treatment field using planar projection images acquired with a x-ray beam that is collimated to a 2-D radiation field (also called a “cone beam”) along with a matched x-ray detector, and this form of IGRT is referred to as cone beam CT (CBCT)^{102,103}. In one form of implementation, a kilovoltage x-ray source and a phosphor screen based a-Si flat-panel imager are integrated into the linac orthogonally relative to the treatment beam, and this is referred to as kilovoltage-CBCT (KV-CBCT)¹⁰⁴⁻¹⁰⁷. Alternatively, the megavoltage treatment beam itself may be used in conjunction with a conventional EPID to render a CBCT reconstruction of the treatment volume, and this is referred to as megavoltage-CBCT (MV-CBCT)¹⁰⁸⁻¹¹⁴. It may be noted that volumetric CT reconstruction based on megavoltage imaging is also performed in a helical tomotherapy system (described in section 1.3), which is a specific implementation of single slice IMRT that utilizes a megavoltage fan beam, and this form of IGRT is distinguished as megavoltage CT (MVCT)¹¹⁵⁻¹¹⁸.

While in-room CT systems provide high quality target localization, the obvious complexity and space constraints associated with such systems have limited their potential benefit. Similarly, KV-CBCT also required additional equipment to be installed on treatment units although the added cost and complexity is relatively less compared to in-room CT. Another major disadvantage associated with these systems is that their spatial accuracy is sensitive to the degree of coincidence between the centers of rotation (commonly referred to as the “isocenter” for conventional linacs) between IGRT imaging and the actual treatment. Therefore, in-room CT and KV-CBCT provide an indirect or surrogate verification of the treatment volume. On the other hand, MV-CBCT imaging provides a direct 3-D visualization of the tumor volume and it can be implemented with most clinical treatment units without the attachment of any additional system components. Unlike conventional CT that utilizes thin fan beams, both KV and MV

based CBCT systems are affected by x-ray scatter on account of the large field size associated with the cone beam, which generally compounds the severity of CT reconstruction artifacts and degrades the overall image quality. The additional dose to the patient on account of frequent CBCT scans is also of concern although MV-CBCT is somewhat less affected by scatter and excess patient dose, and is less prone to artifacts from high Z elements compared to KV-CBCT due to the decreased x-ray interaction cross-sections of megavoltage x-rays¹⁰⁸.

1.7 Research Goals

Despite the mechanical and physical constraints of KV-CBCT and the reduced severity of scatter based artifacts and patient dose in MV-CBCT, the former is currently more widely used mainly due to the significantly better delineation of soft tissue structures, which provides more effective target localization. However, with the use of improved EPID systems that utilize more efficient x-ray detectors, a significant enhancement of soft tissue contrast and overall image quality is expected to improve the quality of MV-CBCT to the point where it can be comparable to or more effective than KV-CBCT for target localization, set-up verification, organ motion tracking, and dosimetric applications¹⁷. Therefore, the research presented in this dissertation is focused on identifying megavoltage x-ray detectors that provide greater x-ray sensitivity, enhanced contrast, low noise, and good spatial resolution. Based on recent trends in megavoltage imaging research, the use of thick scintillators has emerged an attractive choice for such high performance megavoltage x-ray detectors as they offer key radiographic advantages (described in section 1.5.3) and can be readily implemented with existing EPID configurations⁸³⁻⁹⁴.

The greatest advantage with the use of clear scintillators is that it permits greater freedom in the selection of large thicknesses since the light photons produced in response to x-rays can travel over large path lengths without interacting with the scintillation medium depending on its degree of transparency. Therefore, in principle, the trade-off between scintillator thickness and

overall performance is significantly alleviated and is only affected by radiation interaction characteristics (i.e. x-rays and secondary electrons) as light scattering and absorption losses are greatly minimized. While the peripheral image blur due to the divergence of the x-ray beam is accentuated with thicker detectors, this can be rectified by using focused detector elements that angulated towards the radiation source⁹³. In general, the choice of an efficient scintillator candidate depends on several vital factors like x-ray sensitivity and bulk density, scintillation characteristics, optical properties, and practical aspects like cost and ease of fabrication, assembly and handling. Based on the limited number of studies comparing multiple scintillators for megavoltage imaging^{86,92,93}, no singular choice for an ideal or appropriate scintillator is clear so far. Several studies have been recently conducted to investigate the use of thick scintillators in video and flat-panel EPID configurations⁸⁹⁻⁹⁴. However, significant research and development of these systems is still ongoing as they need to be optimized with respect to various aspects associated with their overall imaging performance including the choice of an appropriate scintillator, detector design, and fabrication issues. Moreover, the advent of such advanced thick scintillator arrays may require sophisticated mechanical design and material sciences expertise, which also drives up the cost associated with production and potential commercialization. Therefore, the design of the next generation of high performance, thick scintillator based EPID systems depends not only on radiographic and optical optimization but also on the practical feasibility of constructing and assembling such sophisticated imaging units in a manner that is cost effective, consistent, accurate, and somewhat automated.

In this research, two candidates for thick scintillators were considered for study: CsI(Tl), and terbium doped scintillation glass. The two scintillation media were investigated in separate imaging configurations to test and validate their radiographic imaging characteristics. The first

prototype is based on a thick scintillation crystal (TSC) consisting of a monolithic slab of CsI(Tl) coupled to a mirror – lens – camera system. The second configuration is based on a fiber-optic scintillation glass array (FOSGA), in which scintillation glass is drawn into fiber-optic conduits, inserted into a grid of polymer-tungsten alloy, and coupled to photodiode read-out with an a-Si flat-panel array. The imaging prototypes were characterized using theoretical studies and imaging measurements to obtain fundamental metrics of imaging performance including spatial resolution, noise and contrast. The imaging studies were used to optimize the TSC and FOSGA imagers and propose prototype configurations for order-of-magnitude improvements in overall image quality. As part of this research, detailed studies on the imaging measurements and specific techniques used to determine fundamental imaging metrics were conducted. A fast and simple technique was developed to obtain these metrics for clinical EPID and CBCT systems, in a novel adaptation of these fundamental metrics from imaging research to clinical performance monitoring. The specific aims of this dissertation are detailed below.

- Aim 1 – Optimization of a conceptual prototype TSC EPID system based on simulation studies, imaging measurements, and theoretical modeling of overall imaging performance.
- Aim 2 – Theoretical characterization of the imaging performance of a conceptual FOSGA based EPID system to optimize detector geometry.
- Aim 3 – Development of a simple and fast technique to measure fundamental imaging metrics for clinical EPID and CBCT systems for routine performance monitoring.

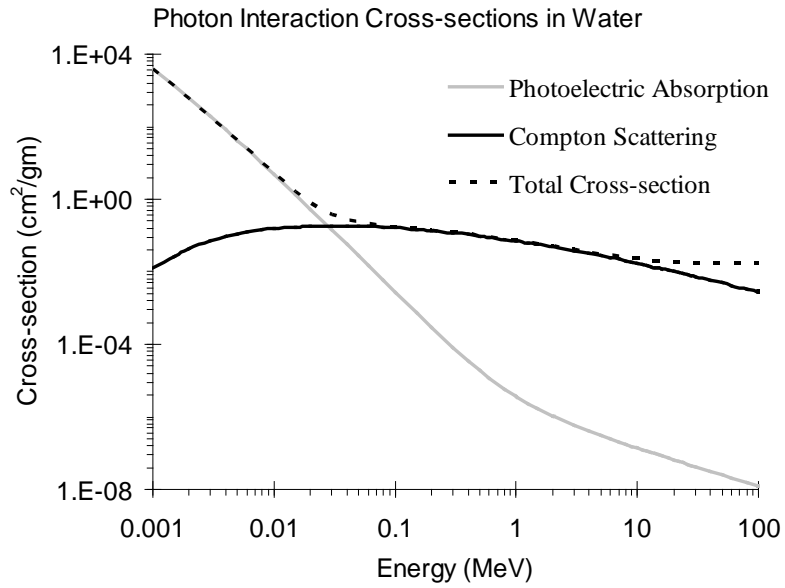


Figure 1-1. Relative contributions of photoelectric absorption and Compton scattering to the total x-ray interaction cross-section in water.

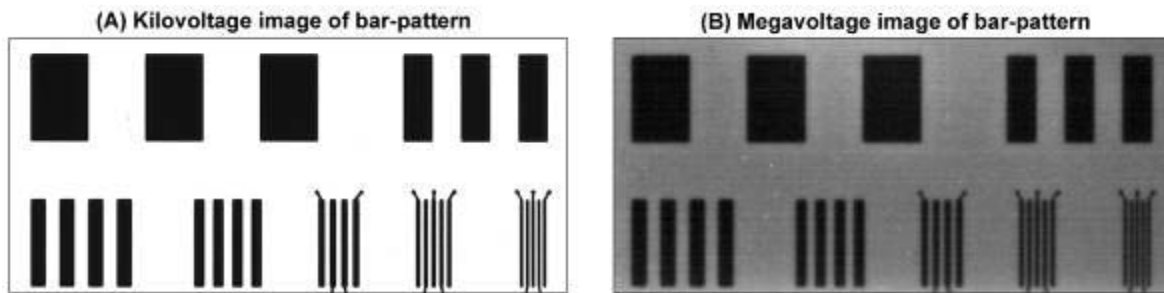


Figure 1-2. Effect of x-ray beam energies on image quality. (A) Kilovoltage image at 40 kVp and 30 mAs (< 0.05 R), and (B) Megavoltage image at 6 MV and 10 MU (> 10 R).

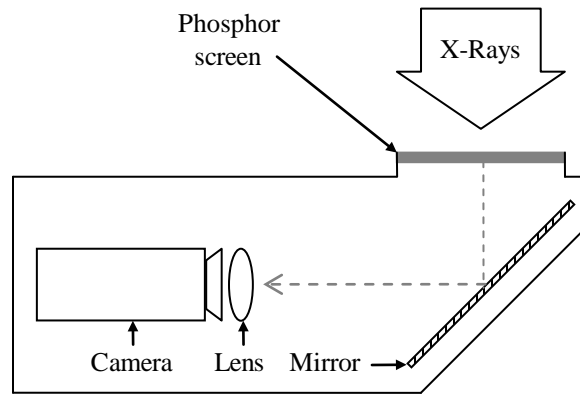


Figure 1-3. Schematic representation of a first generation video EPID system.

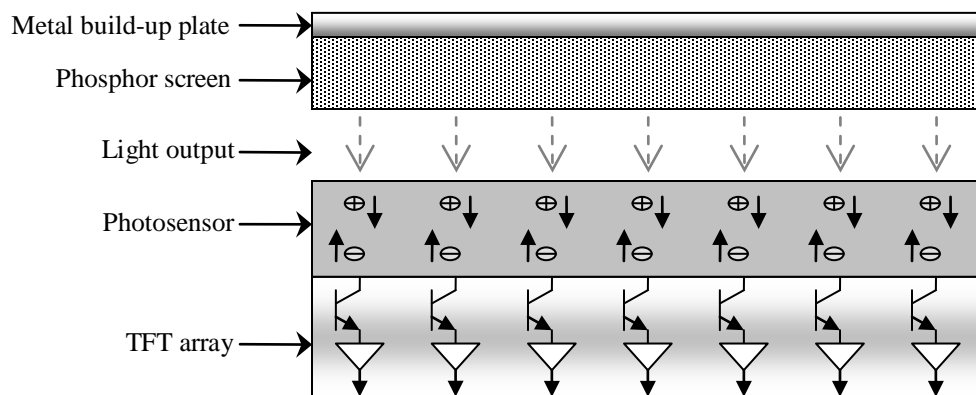


Figure 1-4. Schematic representation of an indirect detection a-Si flat-panel EPID system.

CHAPTER 2

METHODS OF CHARACTERIZING RADIOGRAPHIC IMAGING SYSTEMS

The goal of every radiographic imaging system is to deliver images of high quality. In general, a high quality radiographic image is expected to have good contrast and spatial resolution, and low noise. Contrast refers to the perceivable difference in the image intensities corresponding to two structural regions of varying material or density or both. It depends on the energy and quality of the x-ray beam, the object that is being imaged, and finally the x-ray imaging device. Noise refers to the uncertainty associated with the intensity of an image at any or all given points. For stochastic processes like x-ray incidence and detection, much of the noise in radiography is a result of the Poisson uncertainty associated with x-ray quanta. Spatial resolution (or image sharpness) indicates the accuracy or integrity with which an object or structure of any given size can be visualized (not considering the effects of contrast and noise). While it generally reflects the ability of an imaging system to delineate small structures, spatial resolution is often used to describe the smallest possible structure than can be visualized. In reality, from a “human eye” or observer perspective, the overall contrast in any image includes the combined influence of both noise and spatial resolution.

The majority of methods used to analyze the performance of an imaging device are based on linear systems theory and theoretical concepts developed when imaging was dominated by radiographic and photographic film¹¹⁹. An important assumption in this case is that the imaging detector is a linear and shift invariant system. Although all practical x-ray detectors depart slightly but surely from this assumption, they are treated as black box modules that for all practical purposes, behave like linear and shift invariant control systems¹²⁰. Such a linear systems approach has enabled the characterization of imaging devices using transfer functions in the Fourier or frequency domain. Since 2-D images represent a spatial domain, its Fourier

components represent the so called “spatial frequency” domain. In this case, spatial frequency is an inverse or reciprocal index of space or distance and is commonly expressed in units of mm^{-1} , or cycles per mm (cy/mm). For example, a 1 mm wide object along with 1 mm of air or free space may be combined to represent a spatial frequency of $(1 \text{ mm} + 1 \text{ mm})^{-1} = 0.5 \text{ mm}^{-1}$ or cy/mm. The transfer function parameters that are used to describe the linear systems equivalent of spatial resolution, noise and contrast are described below. These parameters are considered to be fundamental imaging metrics that are widely acclaimed as the best indicators of radiographic imaging performance, and their characterization is currently considered mandatory in imaging research and in the development of new imaging devices.

2.1 Modulation Transfer Function (MTF)

The MTF of a radiographic imaging device describes the resolving power of the system and its dependence on structure size expressed in terms of spatial frequency¹²⁰. An MTF curve is usually a monotonically decreasing function of spatial frequency. The curve is normalized such that the MTF is unity at a spatial frequency of 0 cy/mm, which assumes perfect resolution of infinitely large objects. The MTF gradually declines with spatial frequency until it falls to zero, and the spatial frequency at that point is considered the limiting spatial frequency of the imaging device (in practice, resolution limits may be set more conservatively to when the MTF falls to 10%). Typically, this limiting frequency depends on the intrinsic spatial resolution characteristics and the sampling properties of the imaging system (typically 0.75 – 1 cy/mm for clinical EPIDs).

2.1.1 Principles of Measurement

The resolving capability of an imaging device can typically be well represented by the extent to which the signal at a given point is smeared or blurred across the imaging space. Consider a given x-ray intensity distribution denoted by $\Phi(x,y)$ that is incident on an imaging detector, and let $r(x,y)$ be the resulting detector response or imaging signal distribution. The

distribution in $r(x,y)$ can be expressed as shown in Equation 2-1¹²⁰ as a convolution integral of $\Phi(x,y)$ with a point response distribution given by $p(x,y)$.

$$r(x, y) = k \int_{-\infty}^{\infty} \int_{-\infty}^{\infty} \Phi(x - x', y - y') p(x', y') dx' dy' \quad (2-1)$$

In this case, k is a stochastic scalar indicating the gain or conversion factor between the incident x-ray photons and the intensity values in $r(x,y)$. The convoluting kernel $p(x,y)$ is referred to as the point spread function (PSF) of the detector, which represents the imaging response to x-rays incident at a reference point on the detector. In other words, $p(x,y)$ indicates the extent to which the imaging signal from an x-ray photon interacting in the detector is spread or smeared across the image as a result of the lateral migration of scattered photons, secondary electrons, and any subsequently generated imaging quanta. The PSF is considered a spatial domain representation of the resolving power of an imaging detector, and as Equation 2-1 indicates, it manifests itself as a convolution kernel on the spatial distribution of the incident x-ray beam resulting in some blurring of the final image. The Fourier transform of the PSF provides a frequency domain representation of the image blur as indicated by Equation 2-2. In this case, $m(u,v)$ is a spectral decomposition of $p(x,y)$ that provides a 2-D rendering of the MTF as a function of the spatial frequency indices (u,v) corresponding to the Cartesian co-ordinates (x,y) .

$$m(u, v) = \left| \int_{-\infty}^{\infty} \int_{-\infty}^{\infty} p(x, y) e^{-i2\pi(ux+vy)} dx dy \right| \quad (2-2)$$

In practice, the MTF is typically formulated as a function of a singular index of spatial frequency (commonly referred to by f in units of cy/mm) in 1-D form, i.e. $MTF(f)$. In this 1-D realization, one first obtains the detector response to a line source of radiation, which is referred to as a line spread function (LSF). As seen in Equation 2-3¹²⁰, the LSF is effectively a 1-D representation of the PSF and can be derived as the line integral of $p(x,y)$. The MTF is obtained

from the Fourier transform of the LSF using Equation 2-4¹²⁰. It must be noted that the Fourier integrals in Equations 2-1 and 2-2 usually include an implicit normalization by the area and line integrals of the PSF and LSF respectively to force unit normalization of the transforms at zero spatial frequency, i.e. $m(0,0) = MTF(0) = 1$, in accordance with conventional definitions.

$$LSF(x) = \int_{-\infty}^{\infty} P(x, y) dy \quad (2-3)$$

$$MTF(f) = \int_{-\infty}^{\infty} LSF(x) e^{-i2\pi fx} dx \quad (2-4)$$

Equation 2-4 essentially describes the most common realization of MTF spectra for radiographic imagers. Different techniques can be used to obtain the LSF of an imaging detector that are based on the use of specifically engineered attenuating objects or phantoms to produce the desired incident x-ray intensity distribution as an input to the detector. The two most popular techniques involve the use of thick attenuating metallic blocks to collimate the beam to present either a “slit” or an “edge” profile. In the slit response method, two thick attenuating blocks (typically made of lead, tungsten or steel) are held close together to present an extremely narrow gap¹²¹⁻¹³⁰. As shown in Figure 2-1, when an x-ray beam is passed through the slit the attenuated beam profile that is incident on the detector resembles a line source of radiation, and the resulting imaging response is collected to generate the LSF. On the other hand, the edge response technique is an indirect form of obtaining the LSF as it only uses one such metal attenuator in the path of the beam so that the beam profile incident on the detector resembles a gradient or edge profile¹³¹⁻¹³⁶. The resulting imaging response is referred to as an edge spread function (ESF) whose first derivative is obtained to generate the LSF as shown in Figure 2-1.

An alternative conceptual definition of the MTF is based on the treatment of the detector response to sinusoidal modulations in the intensity of the incident x-rays^{137,138}. Such an incident

radiation profile may be generated by imaging an attenuating object whose thickness varies as a sine wave of a particular discrete frequency denoted by f . The imaging response of the detector to the sinusoidal beam profile is also expected to be approximately sinusoidal in shape with maximum (or “peak”) and minimum (or “valley”) intensities indicated by r_{peak} and r_{valley} respectively, as shown in Figure 2-2. In this case, $M(f)$ is the amplitude of the modulation response (also referred to as the modulation value), and is given by Equation 2-5¹³⁷.

$$M(f) = \frac{R_{peak} - R_{valley}}{R_{peak} + R_{valley}} \quad (2-5)$$

The presence of the argument f in Equation 2-5 denotes that it pertains to the specific discrete spatial frequency associated with the sine wave pattern of the incident modulation. As indicated in Figure 2-2, the frequency of the sinusoidal modulation profile is related to the width of the sine wave profile (indicated by w). According to Equation 2-1, the detected intensity modulation profile is essentially a convolution of the incident modulation profile with $P(x,y)$, and the subsequent blurring results in an attenuation of $M(f)$. Based on the premise that the severity of this attenuation increases with broader PSF distributions (indicating lower MTF and reduced spatial resolution), the MTF can be determined (as illustrated in Figure 2-3) from a series of $M(f)$ values obtained in a similar fashion for several spatial frequencies over a desired range, as shown in Equation 2-6¹³⁷.

$$MTF(f) = \frac{M(f)}{M(0)} \approx \lim_{\delta \rightarrow 0} \frac{M(f)}{M(\delta)} \quad (2-6)$$

In this case, the modulation values in $M(f)$ must ideally be normalized by the true zero frequency modulation or $M(0)$. However, since this essentially requires a sine wave emulating attenuator of infinite width, $M(0)$ may be typically approximated by sufficiently wide sine wave attenuators that present an extremely small limiting frequency indicated by δ . It can be seen that since the

slit and edge response techniques involve Fourier analyses of spread functions, they may be considered frequency domain based methodologies, while the modulation response technique represents a spatial domain approach to determine the MTF. The practical implementations of these techniques to obtain MTF measurements are also affected by several external and sometimes unavoidable factors (noise, scatter, sampling effects, etc) that contaminate the measurement and decrease its accuracy. While the effects of noise and scatter can be somewhat controlled by optimizing the imaging conditions like exposure and radiation field size, the effect of sampling or pixelization is more difficult to predict or control.

2.1.2 Sampling and Aliasing

In general, sampling may be understood as a process of capturing discrete values of an analog signal at regular time or space intervals. With appropriately selected sampling rates or frequencies, these discrete values or samples can represent the original signal sufficiently accurately both in magnitude as well as shape or form. Specifically, the Nyquist – Shannon sampling theorem^{139,140} states that for an analog signal that is discretized by a sampling frequency of f_s , the highest frequency that can theoretically be faithfully rendered is given by $f_N = (1/2) f_s$, where f_N is referred to as the Nyquist frequency limit of the sampled signal. For example, for images sampled using a pixel width of 0.5 mm (typical for most EPIDs), $f_s = (0.5 \text{ mm})^{-1} = 2 \text{ cy/mm}$, and $f_N = 1 \text{ cy/mm}$. This indicates that EPID images obtained using 0.5 mm wide pixels may only be considered an accurate sampling of the actual imaging signal if the highest spatial frequency component contained in the signal is within the Nyquist limit (i.e. $f_N = 1 \text{ cy/mm}$). However, the analog spatial distribution of imaging intensities produced in the x-ray detector often includes high frequency components (eg. sharp edges) that exceed the Nyquist limit since conventional imagers are typically undersampled to mediate the trade-off between image sharpness with finer sampling and excess digitization noise. Due to undersampling, all

analog imaging signal components that exceed the Nyquist frequency limit are included in the sampled or digitized imaging signal in the form of a lower frequency component, and this effect is referred to as aliasing¹⁴¹. Specifically, if f_A represents an analog frequency component such that $f_A > f_N$, it is replicated in the digitized signal as a lower frequency component given by $f_D = 2f_N - f_A$. Aliasing has the potential to cause significant errors in transfer function analysis and particularly in the case of MTF measurements, especially at spatial frequencies in the vicinity of the Nyquist limit. Therefore, the methodologies used to obtain slit, edge, and modulation response profiles require major modifications in order to obtain MTF spectra that are relatively unaffected by any potential contamination due to aliasing. Since such “unaliaised” MTF spectra represent the spatial resolution of imagers prior to sampling effects, they are also referred to as a “presampled” MTF. The practical methods used to obtain presampled MTF measurements for digital imaging systems are described below.

2.1.3 Slit and Edge Response

Despite some fundamental differences in signal characteristics and accuracy, the slit and edge response techniques have several similarities in terms of the principles of measurement, experimental set-up, and image analysis. The slit response technique is based on the use of a pair of closely clamped metallic attenuating blocks to provide an extremely narrow slit gap so that the attenuated x-ray beam closely emulates a line source for the measurement of an LSF profile. Typically, lead, tungsten and steel blocks are used, and the thickness of these blocks depends on the energy of the x-ray beam (in the mm range for kilovoltage beams and several cm thick for megavoltage imaging)¹⁴². The securely clamped pair of metal blocks with a uniform slit gap maintained over its length and thickness is referred to as the slit phantom or target. It is generally positioned as close to the imaging plane of the detector as practically possible, and oriented symmetrically about the center of the radiation field. The slit target is made large enough to

obtain an LSF profile that is at least 5 – 10 cm long in the direction perpendicular to the length of the slit, and with sufficient rows (or columns) of LSF profiles to facilitate the averaging of a large number of LSF samples to minimize measurement error. The overall design of the slit geometry (attenuating thickness and slit gap) is generally optimized based on the imaging field geometry (x-ray source size and source – slit distance), to provide high x-ray attenuation through the blocks and maximal x-ray transmission through the slit gap, which ensures that the uncertainty associated with the tail regions of the LSF profiles is minimized relative to the peak intensity to provide accurate MTF measurements¹³⁰. In order to minimize the effect of scatter, the radiation field is defined to be well within the area of the slit target, and noise is generally minimized by using significantly high imaging exposures for better Poisson statistics. In addition, a separate imaging measurement with the slit gap completely closed (i.e. zero slit width) is also obtained as a surrogate representation of the LSF baseline that may include scatter contribution and residual transmission through the slit target^{42,77,122,142}. In addition to the subtraction of this baseline, the tail regions of the LSF may also be smoothed or fit with appropriately selected functions to minimize the effect of noise¹²². It must be noted that instead of a true line source, the x-rays passing through a slit actually render a rectangular step function with an aperture size equal to the width of the slit gap (g). As a result, the slit response is not a true LSF but rather its convolution with the slit aperture, which requires the correction shown in Equation 2-7¹²².

$$MTF_{true}(f) = MTF_{slit}(f) \left[\frac{(\pi fg)}{\text{Sin}(\pi fg)} \right] \quad (2-7)$$

For an edge response measurement, only one attenuating metal block is required to produce a radiation gradient profile of x-rays incident on the detector. The block is placed close to the imaging plane of the detector with its edge at the center of the radiation field. Relevant

experimental details like attenuating thickness, imaging set-up, exposure, and field size are similar to those for the slit. While no baseline corrections are required, the ESF profiles generated are often subjected to some smoothing or fitting, especially on the attenuated half of the profile that renders a noisy LSF component due to the reduced number of x-rays contributing to the signal^{131,135}.

Before the advent of digital imaging, LSF or ESF measurements for film systems were obtained by scanning the film perpendicular to the direction of the slit or edge^{122,123}. Aliasing effects were effectively avoided by selecting small optical scanning apertures for high Nyquist limits and minimal aliasing at spatial frequencies of interest^{122,123}. However, the explicit pixelization of digital imagers and the previously described issues related to sampling and aliasing artifacts have led to significant modifications to the imaging set-up used in slit or edge response techniques. In order to avoid aliasing effects from regular pixel sampling, the slit and edge response profiles are commonly oversampled by extracting the LSF and ESF profiles at sub-pixel intervals using a special reconstruction technique^{125,143}. In this method, the slit or edge target is slightly angulated at a small angle (θ) with respect to the imaging co-ordinate axes. As shown in Figure 2-4, the angle of the median axis of the slit or edge effectively displaces successive rows of pixels by a very small sub-pixel distance given by $\Delta x = p \tan(\theta)$, where p represents the pixel size of the detector¹²⁵. By superposing slit or edge profile components that are successively shifted by sub-pixel increments on a single composite reconstructed LSF or ESF respectively, the effective sampling size of the slit and edge response is significantly lower compared to the actual pixel size as illustrated in Figure 2-5. For example, for $\theta \approx 2^\circ$, the oversampling factor ($p/\Delta x$) is approximately 30. The oversampling results in a significantly greater Nyquist limit and nearly no aliasing artifacts in the finally calculated MTF at relevant

spatial frequencies. In practice, the oversampled profiles are commonly binned into slightly larger sampling grids to minimize noise¹⁴³ so that the final oversampling factor is in the range of 5 – 10, which is considered sufficient for an aliasing free presampled MTF using Equation 2-4.

2.1.4 Line-pair Modulation Response (Bar-pattern Technique)

The original conception of the method of using modulation response profiles was based on applying sinusoid attenuators to shape the incident x-ray beam¹³⁷. In practice, a pattern of square wave bars is used instead of a sinusoidal pattern since these are easier to fabricate^{42,77,87}. The square wave pattern of attenuating bars is generally referred to as “line-pairs”, which indicates that each functional unit of the resolution pattern consists of a bar and an adjacent gap of the same size. Typically, several sets of such square wave line-pairs are fabricated on a single attenuating metal bar to produce a generic line-pair resolution phantom referred to as a bar-pattern, and the spatial frequencies emulated in the bar-pattern are expressed in units of line-pairs per mm (lp/mm). Since a square wave function has a different Fourier composition compared to a sine wave (a square wave is actually a series of sinusoids), the direct application of Equation 2-6 on a square wave line-pair modulation response results in an overestimation of the MTF since it includes contributions from odd-numbered harmonics of the fundamental frequency (i.e. $3f$, $5f$, $7f$, ... etc)¹³⁷. Therefore, a modified form of Equation 2-6 that includes a correction for the presence of harmonic contributions in the modulation values is generally used and is given in Equation 2-8^{137,142}.

$$MTF(f) = \lim_{\delta \rightarrow 0} \left(\frac{\pi}{4} \right) \left[\frac{M(f) + C_n \frac{M(nf)}{n}}{M(\delta)} \right] \quad (2-8)$$

In this case, $M(nf)$ denote the modulation components from odd harmonics ($n = 3, 5, 7, \dots$) and all modulations are normalized at the near-zero spatial frequency δ . Specifically, $M(\delta)$ is

obtained as the modulation in imaging intensities associated with a large uniform area of the bar and background air. For example, if 50 mm wide regions of the bar and background air are used for normalization, $\delta = (50 \text{ mm} + 50 \text{ mm})^{-1} = 0.01 \text{ cy/mm}$ or lp/mm. The values of the coefficients in C_n are used in the correction for the harmonics, and they depend on the total number of primes P and the number of different primes P' that can be factored into n . Specifically, $C_n = (-1)^{P+(n-1)/2}$ if $P = P'$, and $C_n = 0$ if $P > P'$.

To avoid undersampling effects, a specially adapted aliasing free realization^{144,145} of the bar-pattern technique is used in which the statistical variance $V(f)$ in pixel intensities associated with a given line-pair frequency is used instead of the modulation value $M(f)$. The basic premise of this technique is that while $V(f)$ is proportional to the square of the modulation $M(f)$, it is remarkably unaffected by aliasing. Typically, $V(f)$ is obtained for each spatial frequency by identifying a region of interest (ROI) the line-pairs of that frequency, and computing the variance over all pixel intensities within the ROI. In this implementation, Equation 2-8 takes the form of Equation 2-9^{142,144,145} below with a similar correction for harmonic contributions for which the coefficients in C_n are either 0 (if $P > P'$), 1 (if $P' > 1$) or -1 (if $P' = 1$). The normalization factor M_0 in Equation 2-9 is simply the difference in imaging intensities between large bar and background air regions, i.e. only the numerator in Equation 2-5 with $f = \delta$, which is a subtle variation from the use of $M(\delta)$ in Equation 2-8.

$$MTF(f) = \left(\frac{\pi}{\sqrt{2}} \right) \left[\frac{\sqrt{V(f) - C_n \frac{V(nf)}{n^2}}}{M_0} \right] \quad (2-9)$$

2.2 Noise Power Spectrum (NPS)

The fundamental source of noise or uncertainty in a radiographic image can be generally understood from Equation 2-1, which provides a broad relationship between the imaging

response and the incident x-ray beam. The scalar term (k) that indicates the transduction of x-ray photons to the final form of imaging intensities manifests as a stochastic identity whose value may undergo fluctuations that stem from the physics of x-ray interactions and the nature of production, detection and acquisition of subsequent imaging quanta (light, ions, electrons, etc)¹²⁰. These fluctuations result in the overall uncertainty of the recorded pixel intensities in an image that is broadly classified as noise. It is commonly characterized for imaging devices in the form of the NPS, which is the power spectrum of the variance associated with pixel intensities in the imaging response to an unattenuated or “open” field as indicated by Equation 2-10^{143,146-150}.

$$NPS(u, v) = \left(\frac{p_x p_y}{A} \right) \left| \int_A [I(x, y) - \bar{I}] e^{-i2\pi(ux+vy)} dx dy \right|^2 \quad (2-10)$$

In this case, $I(x, y)$ represents an open field or air image of area A and mean imaging intensity \bar{I} that is acquired using an open field exposure that deposits a uniform radiation field upon the x-ray detector whose co-ordinate pixel dimensions are given by p_x and p_y . Typically, open fields are acquired with field sizes greater than $10 \times 10 \text{ cm}^2$ at exposures that are relevant for the specific imaging application, and often for a series of different exposures to verify the conformation of the detector to expectations of exposure dependent linearity.

The major limitation with the direct implementation of Equation 2-10 is the inevitable presence of structured and systemic artifacts (due to scatter, beam divergence, etc) that hinder the delivery of a truly uniform radiation field^{42,68,77,146,150}. This results in a significant overestimation of the noise at low spatial frequencies and necessitates corrective measures to minimize the inclusion of low frequency artifacts in the computed NPS. To this end, the difference field $\Delta I(x, y)$ between a pair of identically exposed open field images is used to compute the NPS as shown in Equation 2-11^{42,68,143,150}. The additional scaling of the NPS by a factor of two is included in Equation 2-11 to account for the fact that the subtraction of open field images results

in the addition of their respective variance levels (that may be considered equal for identical exposures)^{42,68}. The NPS is also normalized by the mean image intensity \bar{I} to isolate the NPS from system gain settings.

$$NPS(u, v) = \left(\frac{1}{2} \right) \left(\frac{P_x P_y}{A} \right) \left| \frac{1}{\bar{I}} \int_A \Delta I(x, y) e^{-j2\pi(ux+vy)} dx dy \right|^2 \quad (2-11)$$

The NPS obtained in this fashion is a 2-D spectrum of the imaging system variance, and it is often desirable to extract 1-D NPS components along individual axes. Moreover, the acquisition of 1-D NPS spectra is also necessary to conform to MTF measurements that are obtained along individual co-ordinate axes for further characterization of imaging performance. The extreme susceptibility of the NPS to low frequency baseline artifacts make it impractical to extract 1-D NPS components from the axial vectors of $NPS(u, v)$, i.e. $NPS(u, 0)$ and $NPS(0, v)$. Therefore, more sophisticated techniques have been devised that sample the $NPS(u, v)$ field along the elements immediately adjacent to the axes^{42,68,150}. Typically, this is performed by acquiring “slices” of $NPS(u, v)$ parallel to the u and v axes that are commonly 3 or 4 elements thick. The axial frequency indices (u, v) are used to populate the NPS values into suitably selected 1-D frequency bins where $f = (u^2 + v^2)^{-2}$.

2.3 Detective Quantum Efficiency (DQE)

The overall performance of an imaging device and its general ability to provide images of good quality is best represented by the DQE of the imaging system. While overall image quality can be affected by x-ray beam characteristics, the imaged object, and the imaging detector itself, the DQE only reflects the performance of the detector and its ability to preserve the signal to noise ratio (SNR) characteristics of the incident x-ray beam. The DQE can be generally defined according to Equation 2-12¹¹⁹, where SNR_{in} and SNR_{out} reflect the SNR values of the incident x-ray beam and the output image respectively. Based on the Poisson noise distribution of x-ray

quanta, SNR_{in}^2 is effectively reduced to the total number of x-ray photons in the incident beam. The maximum DQE for clinically used EPIDs lie in the range between 0.1% (video EPIDs) to 1% (flat-panel EPIDs).

$$DQE = \frac{SNR_{out}^2}{SNR_{in}^2} \quad (2-12)$$

The interactions of the incident x-rays as well as secondary photons and electrons within the detector results in the absorption of energy by the detection medium, which leads to subsequent generation of imaging quanta. For example, the absorbed energy is converted to light in a scintillator, and ions in an ionization medium. Depending on the quantity of energy that was absorbed in a given interaction, any number of subsequent signal quanta (light photons or ion pairs) may be liberated in the detector, and for a large energy range of interactions, this represents a significant addition to the uncertainty of the image detection. Therefore, the absorbed energy distribution (AED) associated with the detection of an x-ray beam, which indicates the energy distribution of the interaction events within the detection medium, is a fundamental limiting factor that affects imaging performance. Subsequently, a more descriptive form of Equation 2-12 is often used to express the DQE in terms of the characteristics of the AED spectrum associated with an imaging detector for a given x-ray beam^{42,77,87}.

$$DQE = \frac{\left[\int_E E AED(E) dE \right]^2}{N \int_E E^2 AED(E) dE} = \left(\frac{1}{N} \right) \frac{M_1^2}{M_2} \quad (2-13)$$

In Equation 2-13, E indicates a generic index of energy, N is the total number of incident x-ray photons, and M_1 and M_2 represent the first and second moment of the AED. Equation 2-13 can be further adjusted by including the zeroth moment (M_0) of the AED as shown in Equation 2-14. In this case, the ratio of M_0 over the total number of incident photons (N) represents the overall x-

ray sensitivity of the imaging detector that is commonly referred to as the quantum efficiency (QE) of the detector. Further, the moment terms can be rearranged to express the DQE in terms of a scaling term that is referred to as a “Swank factor” (A_S), which reflects the fractional magnitude of the DQE relative to QE¹⁵¹.

$$DQE = \frac{M_0}{N} \frac{M_1^2}{M_0 M_2} = QE \frac{M_1^2}{M_0 M_2} = \frac{QE}{A_S} \quad (2-14)$$

The above realizations of DQE are extremely useful in theoretical evaluations of an imaging detector especially in megavoltage imaging, wherein the effect of x-ray detection efficiency is a major focus of research. It must be noted that Equations 2-12 – 2-14 generally represent qualified forms of DQE that can depart from the true DQE of a practical imaging device due to two factors. First, these expressions only indicate broad imaging signal characteristics reflecting large uniform imaging fields and therefore, the evaluated DQE strictly pertain to zero spatial frequency only, i.e. $DQE(0)$. Second, subsequent stages of image detection commonly introduce more uncertainty into the imaging signal that often requires detailed characterization using more sophisticated theoretical models. Therefore, practical measurements of DQE to determine overall system performance are based on Equation 2-15^{42,58,68,69,77,143,152} below.

$$DQE(f) = \frac{MTF^2(f)}{\Phi NPS(f)} \quad (2-15)$$

In this case, the DQE is obtained as a function of spatial frequency to indicate the combined influence of spatial resolution in the form of MTF and imaging noise in the form of NPS . The normalizing term (Φ) refers to the quantum fluence (in photons/mm²) associated with the open fields used to obtain the NPS measurements. In a general classification, the fluence Φ and the ratio of MTF^2 and NPS can be taken to represent SNR_{in}^2 and SNR_{out}^2 respectively. It must be

noted that Equation 2-11 expresses NPS spectra in units of mm^2 (with explicit scaling with pixel area using p_X and p_Y) to facilitate the use of the fluence Φ in Equation 2-15 so that the overall is obtained as normalized unitless metric.

2.4 Theoretical Analysis of Imaging Systems

The imaging parameters introduced in sections 2.1 – 2.3 can be powerful tools in describing varied imaging properties of any x-ray detector. While they can be directly measured using Equation 2-15 for practical and existing imaging systems, theoretical techniques may be required to obtain these metrics for conceptual or hypothetical prototypes of such systems for research and development. Such theoretical tools may be based on modeling the physics associated with the imaging device as a surrogate for actual measurement, or they may incorporate computational systems based on individually characterized components. These methods have been briefly described in this section.

2.4.1 Monte Carlo Simulations

Any stochastic process that is based on a known probability density function (PDF) can be modeled by the random sampling of such a PDF to simulate or “mimic” its natural occurrence, and this form of non-deterministic modeling is generally referred to as a Monte Carlo simulation^{153,154}. In general, a Monte Carlo simulation models a stochastic process by generating a series of events based on repeated random sampling of its PDF. The effective mean outcome of the simulated events is considered an accurate representation of the true expected outcome if a sufficiently large number of events are sampled, and if the sampling process is truly random^{153,154}. With the recent onset of exceptionally high computational power that includes computing speed, parallel processing, memory, algorithm development, and high quality random number generators, Monte Carlo simulations provide an extremely powerful and popular tool in a variety of applications¹⁵³⁻¹⁵⁵. Since the physics of x-ray interactions in a given medium are

generally well understood, Monte Carlo simulations have been extensively used for radiation transport in various fields including industry and medical physics (radiology and radiotherapy)¹⁵⁶, and several commercial software packages containing stand-alone code systems for photon and electron transport are currently available. Monte Carlo simulations are particularly useful in radiographic imaging research and studying x-ray detectors since they can be used to isolate the intrinsic x-ray detection characteristics of various imaging media that cannot be easily measured experimentally. They are an invaluable tool when evaluating multiple combinations of detector material and geometries, as simulation results can be used to identify optimal detector geometries that provide good x-ray sensitivity as well as spatial resolution. In this research two standard code systems were used to perform radiation transport calculations to characterize the radiographic merits of prototype imaging detectors.

- 1) Integrated Tiger Series, version 3.0 (ITS 3.0), developed by Sandia National Laboratory (Albuquerque, NM), and distributed by Oak Ridge National Laboratory (Oak Ridge, TN)¹⁵⁷
- 2) Monte Carlo N-Particle, “eXtended” version 2.5 (MCNPX 2.5), developed and distributed by Los Alamos National Laboratory (Los Alamos, NM)¹⁵⁸

In ITS 3.0, the 3-D transport code (referred to as “ACCEPTP”) was used with a separate cross section generation code (“XGENP”) to perform simulations. Both the ITS (ACCEPTP) and MCNPX code systems facilitate a 3-D combinatorial geometry to define the simulation field and material regions, and both feature comparable cross section databases and transport physics that were appropriately benchmarked prior to distribution. The codes facilitate the user to specify a variety of simulation parameters including the nature and strength of the source, material and structural geometry, several tracking and scoring options, and termination parameters, and several significant imaging characteristics like dose or energy deposition, spatial intensity distributions, and energy distributions can be tallied for the desired radiation beam and detector. Specific details and user operation of the numerous features involved in selecting simulation

parameters may be easily found in the literature dispersed with the simulation codes and will not be separately described here. In general, the MCNPX codes allow greater freedom to the user in designing and running simulations through the use of more user controlled variables for defining more complex structures, designating particle importance, etc. No code modifications were made prior to running MCNPX simulations. The ITS codes were modified slightly to increase memory parameters allocated to selected variables to facilitate larger geometries with more structures and more energy bins. In this research, the ITS codes were used to model radiation transport calculations for the CsI(Tl) scintillator for the TSC video EPID prototype system (MCNPX was yet to be installed at the time). MCNPX was used to perform simulations for the FOSGA system.

2.4.2 Linear Cascaded Systems Modeling

The linear systems analysis of radiographic imaging devices is generally based on characterizing system performance in terms of the integrity with which the SNR of the imaging signal is preserved as indicated in Equation 2-12. A linear cascaded systems analysis is a compartmentalized extension of Equation 2-12, wherein the overall SNR characteristics of an imaging device are evaluated based on component contributions of individual compartments or “stages” of imaging^{159,160}. In this case, the imaging system is typically compartmentalized into stages based on the relevant processes involved in the conversion of incident x-rays to the final image. Based on the specific nature of the imaging device, the stages may be classified as “gain”, “spreading”, or “additive noise” stages as described below.

2.4.2.1 Gain stages (“ g_i ”)

If a hypothetical “ i^{th} ” stage of the cascaded systems model of an imaging device involves the detection or transduction of quanta (eg. detection of x-rays, conversion of energy from radiation interactions to light or ions, camera light sensitivity, etc), such a stage is characterized by the value of the associated gain factor (g_i), which is typically the efficiency or quantum

conversion factor of that process. The effect of the stochastic nature of the gain on the overall uncertainty in the number of quanta constituting the imaging signal at any point is incorporated in the form of a so called “Poisson excess” term (C_{gi}) as shown in Equation 2-16¹⁶⁰. In this case, N_i and N_{i-1} represent the number of quanta constituting the imaging signal in the $i-1^{th}$ and i^{th} stages respectively, and σ_{gi}^2 indicates the variance associated with the stochastic gain g_i .

$$N_i = g_i N_{i-1} \quad \text{and} \quad \epsilon_{gi} = \frac{\sigma_{gi}^2}{g_i} - 1 \quad (2-16)$$

The Poisson excess C_{gi} essentially quantifies the potential departure of the quantum population from a Poisson distribution ($\sigma_{gi}^2 = g_i$ and $C_{gi} = 0$ for a true Poisson distribution)¹⁶⁰. Therefore, if an i^{th} stage adds to the overall uncertainty of quanta, this is reflected in the value of C_{gi} (since $\sigma_{gi}^2 > g_i$ and $C_{gi} > 0$). It must be noted that since most imaging or detection processes conform to a binomial selection (eg. an x-ray photon is either detected or not), Equation 2-17 holds true in most stages^{159,160}.

$$\sigma_{gi}^2 = g_i(1 - g_i) \quad \text{and} \quad \epsilon_{gi} = -g_i \quad (2-17)$$

2.4.2.2 Spreading stages (“ T_i ”)

Any part of the imaging process that may affect the spatial resolution of the imaging device by contributing to the spread or blurring of quanta in space is considered a spreading stage (eg. spread of secondary photons and electrons, blurring of light within a lens, ion diffusion, etc). As described with Equation 2-1, the spreading of quanta in space can be characterized by an appropriate spread function (PSF or LSF), and similarly component contributions of such a spread function can be determined for a given stage of the cascaded systems model. However, since linear systems analysis is based on DQE characterization in the spatial frequency domain, the spreading associated with a hypothetical i^{th} stage of a system is characterized by an appropriately devised transfer function $T_i(f)$, which is effectively the MTF

contribution of that stage. As shown in Equation 2-18, the overall MTF of an imaging system can be obtained as the product of the individual stage contributions of a cascaded systems model^{159,160}.

$$MTF(f) = T_1(f) \times T_2(f) \times T_3(f) \dots = \prod_i T_i(f) \quad (2-18)$$

A spreading stage does not have a specific gain value associated with it as the gain and spreading processes are typically separated into individual stages. Therefore, a spreading stage is allocated a deterministic gain of unity ($g_i = 1$, $\sigma_{g_i}^2 = 0$, and $C_{g_i} = -1$)¹⁶⁰.

2.4.2.3 Additive noise stages (“ S_i ”)

If a hypothetical i^{th} stage of the cascaded systems model adds to the overall uncertainty in the signal quanta by virtue of additive noise (eg. dark current in electronic circuitry), the contribution of this stage is indicated by the a relative variance component $S_i(f)$. In practice, this additive noise term is obtained as the NPS spectrum associated with the additive noise as a ratio with the number of signal quanta exiting the given stage^{159,160}. Thus, $S_i(f)$ indicates the fractional increase in the variance of the imaging signal in the i^{th} stage as a result of additive noise.

2.4.2.4 System analysis

The cascaded systems model is implemented by identifying and characterizing the component stages of the imaging device as described in sections 2.4.2.1 – 2.4.2.3. The stages are appropriately ordered sequentially, as the output of every stage forms the input to the next stage starting with the incidence of x-rays to final image formation. During the analysis, the signal and noise characteristics of imaging quanta are accounted for and tabulated as they are propagated serially through various stages of detection and transduction. The quantum accounting model can also be used for graphic representation that is commonly referred to as a quantum accounting diagram (QAD), which depicts the number of quanta associated with each stage in the model and

its relative progression through various stages of detection. Such QAD plots can be useful in identifying potential weaknesses in system design on account of significant “quantum sinks”. In this case, a quantum sink represents the stage associated with the fewest number of signal quanta, which essentially sets the fundamental limit for the maximum attainable SNR in the overall imaging signal (eg. the coupling efficiency of the lens in video EPIDs represents a significant quantum sink). For a more detailed representation of imaging performance, the overall DQE of the imaging system can be determined using Equation 2-19^{159,160}.

$$DQE(f) = \frac{1}{1 + \sum_i \frac{1 + \epsilon_{gi} |T_i(f)|^2 + S_i(f)}{\prod_{j=1}^i g_j |T_j(f)|^2}} \quad (2-19)$$

The linear cascaded systems model allows each stage to be evaluated separately as well as in terms of their influence on the performance of the imaging device. It enables a platform that can be used to optimize imaging systems through the use of various combinations of specific system components while eliminating the significant cost and effort involved in actual experiments and imaging measurements. In this research, the linear systems analysis was used to characterize and optimize prototype configurations for the TSC and FOSGA systems. These studies are described in complete detail in the following chapters.

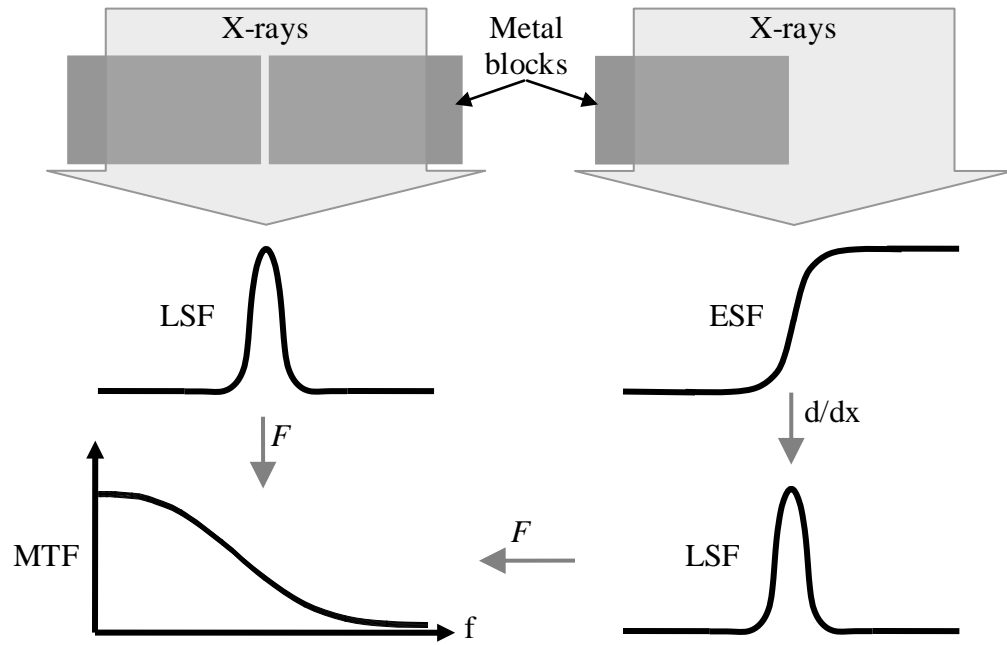


Figure 2-1. MTF measurement using slit and edge response techniques.

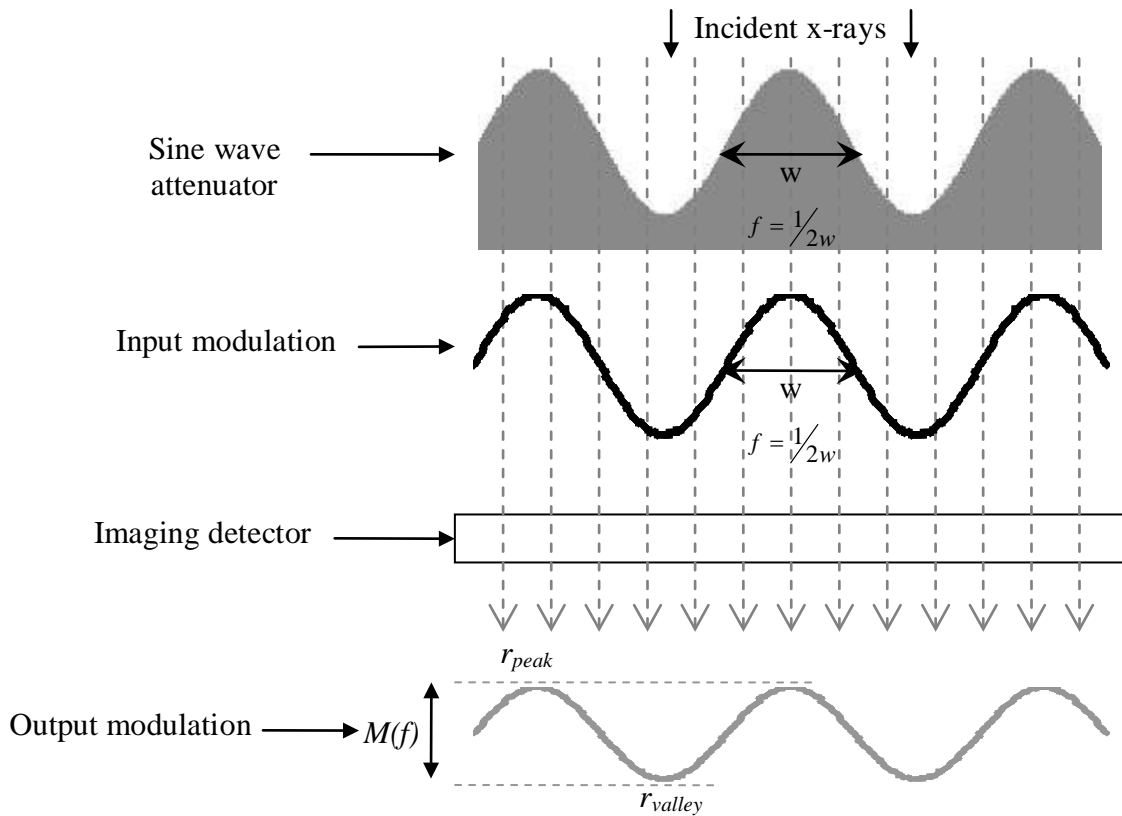


Figure 2-2. Modulation response technique – measurement of modulations from a sine pattern.

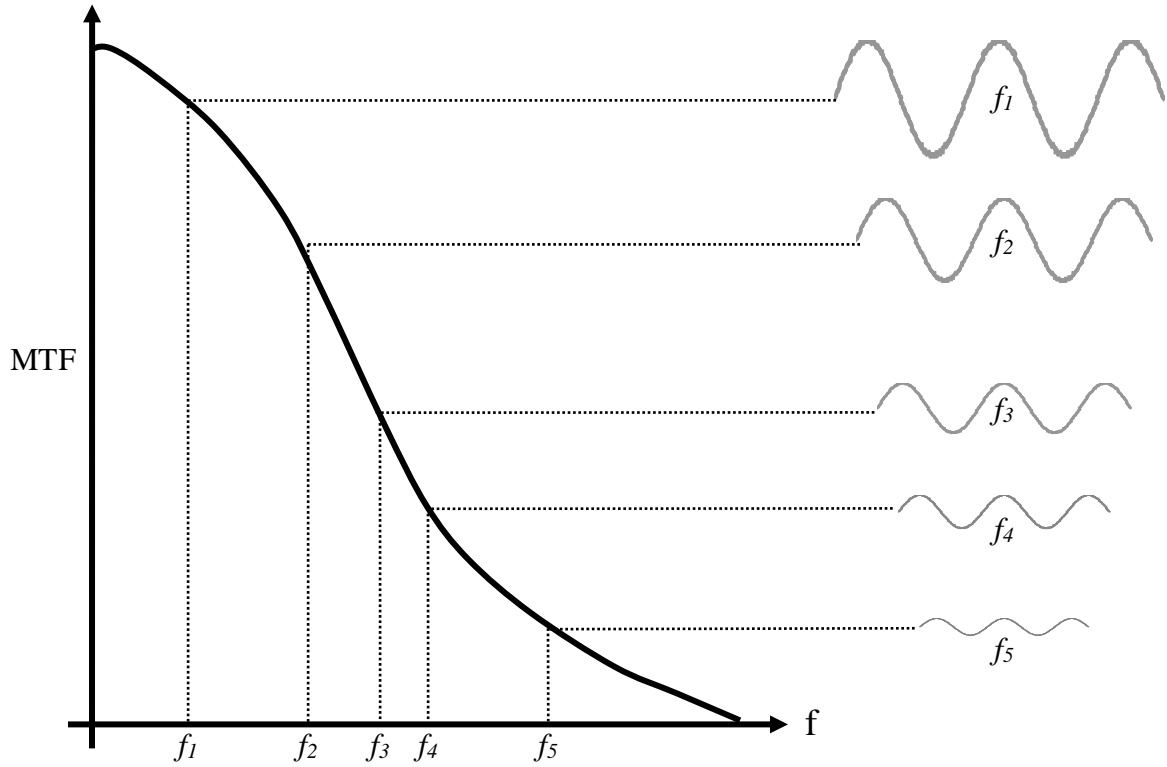


Figure 2-3. Modulation response technique – calculations of MTF from modulation profiles.

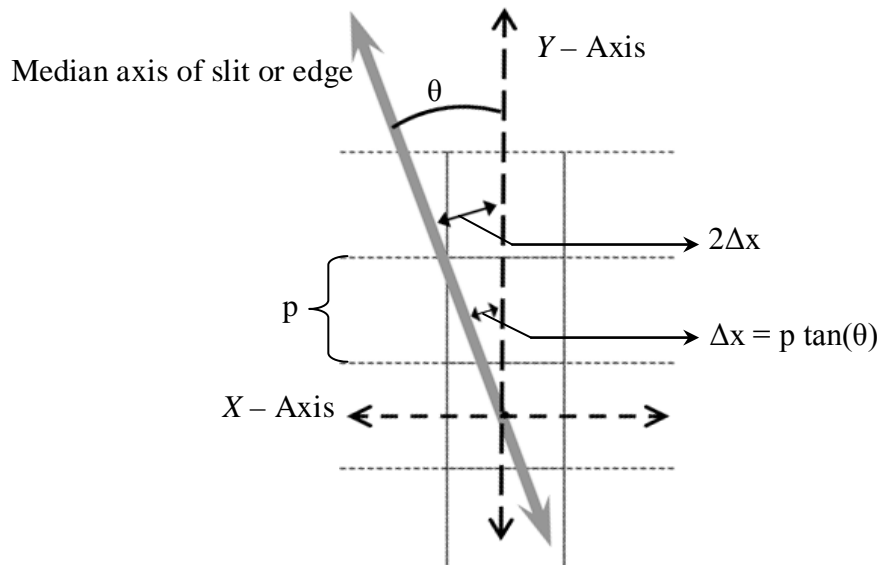


Figure 2-4. Angulated slit and edge methods – incremental sub-pixel shifting of pixel centers.

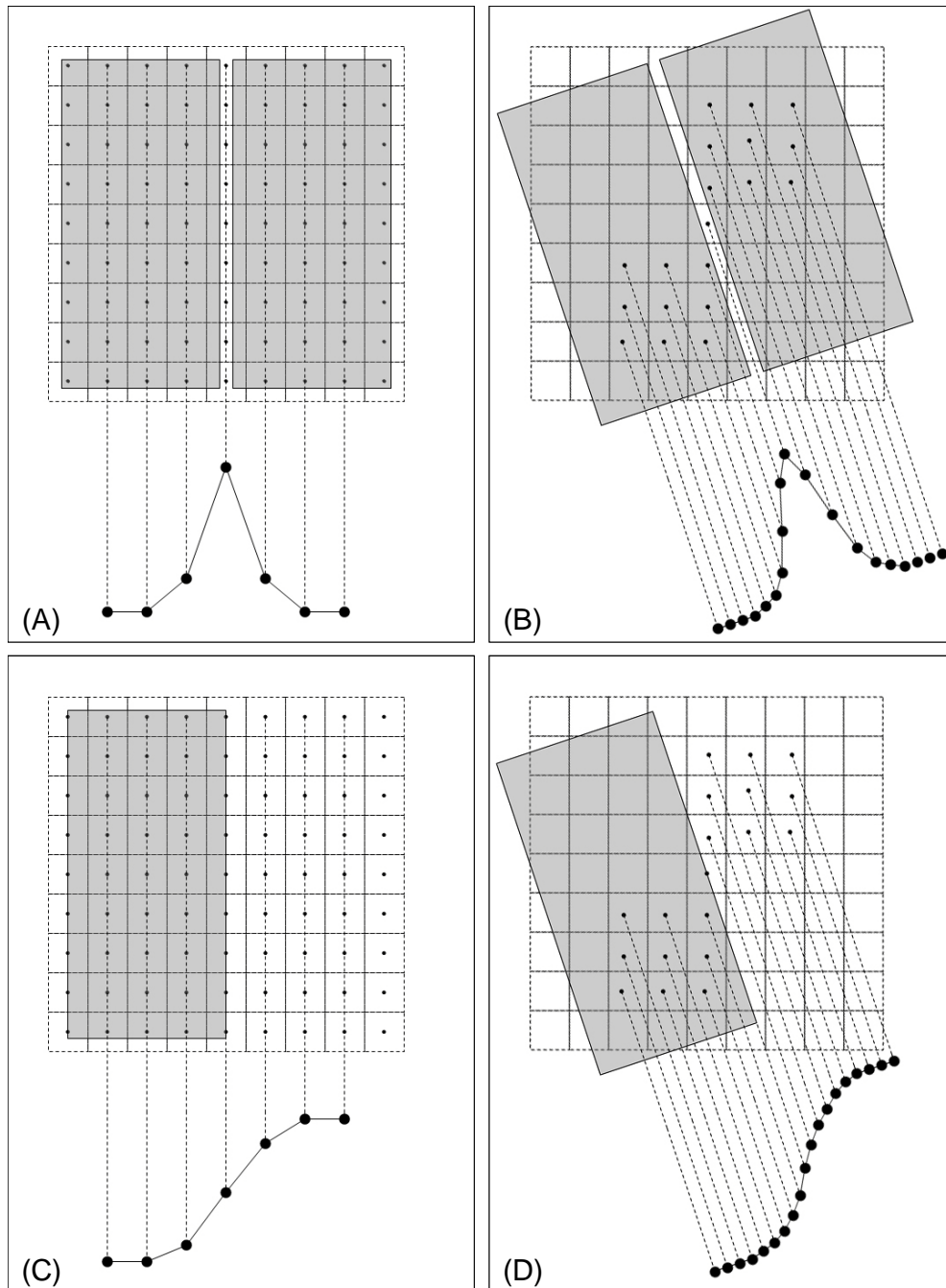


Figure 2-5. Angulated slit and edge methods – reconstruction of oversampled LSF and ESF. (A) Regularly sampled LSF (straight slit), (B) Oversampled LSF (angulated slit), (C) Regularly sampled ESF (straight edge), (D) Oversampled ESF (angulated edge).

CHAPTER 3 PROTOTYPE 1 – THICK SCINTILLATION CRYSTAL (TSC)

The first prototype EPID system investigated in this research was based on a conventional mirror and lens coupled camera system featuring a thick scintillator crystal (TSC) as a high QE luminescent detector. Hereafter, the term “TSC” may be used to describe both a generic scintillation medium for use in the above prototype, and the system itself as a whole. In this chapter, a detailed analysis of a prototype TSC system is presented including intrinsic scintillator characteristics, clinical and imaging measurements to describe imaging performance, and a theoretical modeling of imaging characteristics to optimize the system. In this case, Monte Carlo simulations were used to study the intrinsic x-ray detection characteristics of the TSC and its dependence on scintillator thickness. Based on methods described in sections 2.1 – 2.3, measurements of imaging performance were conducted through MTF, NPS, and DQE calculations for a proof-of-principle TSC system that was installed on a clinical linac gantry for low dose verification imaging. Extensive measurements were carried out to build and validate a linear systems model for the TSC, and an optimized system configuration for a future imaging prototype was developed.

3.1 CsI(Tl) as a Scintillator

In this study, CsI(Tl) was selected as the TSC luminescent screen due to its inherent advantages as an x-ray detector, and partly as a continuation of existing collaborative work⁸⁷. CsI(Tl) has been widely used as a scintillator in radiation detection applications as a result of several attractive and beneficial physical characteristics. It provides high x-ray sensitivity due to its relatively high density (4.51g/cm^3) and high effective Z (~ 54). It lends admirably to mechanical fabrication as it is softer and more malleable than comparable inorganic scintillators, and it can be cut and shaped easily without damage. While it is reactive to water, it is far less

hygroscopic than other alkyl halide scintillators, particularly sodium iodide (NaI). While several scintillators that provide high light output have emerged recently¹⁶¹⁻¹⁶³, CsI(Tl) provides an optimal combination of scintillation properties specific to x-ray imaging (including density, effective Z, light output, emission wavelength, mechanical handling, and cost). Its luminescence spectrum is peaked at 550 nm, which suitably matches the peak sensitivity of conventionally used light sensing systems in x-ray imaging (including camera targets and a-Si arrays). CsI(Tl) has a relatively high decay time ($\sim 1 \mu\text{s}$) associated with its luminescent response, which is characteristic of the use of thallium activation in inorganic alkyl halide type scintillators¹⁶⁴. However, this is not a significant issue in x-ray imaging compared to spectroscopic applications. Studies have also suggested that CsI(Tl) is reasonably resistant to radiation damage ($\sim 14\%$ reduction in light output for radiation doses up to $2 \times 10^6 \text{ rad}$)¹⁶³. One of the most attractive features of CsI(Tl) is its optical clarity compared to standard $\text{Gd}_2\text{O}_2\text{S:Tb}$ based phosphor screens. Light produced in response to radiation interactions can exit the detector more efficiently and with minimal blurring since the clear crystal provides excellent optical coupling to the subsequent light sensor, which is a camera system in the case of the TSC. Although, CsI(Tl) can be used in both segmented and unsegmented configurations, a single monolithic slab of CsI(Tl) was selected as the TSC scintillator based on observed limitations of its use in structured arrays⁸³ and promising results when realized in unsegmented form⁸⁷.

3.2 Monte Carlo Simulations

As a necessary precedent to developing a complete TSC system, Monte Carlo simulations were used to establish the intrinsic x-ray detection characteristics of CsI(Tl) as a scintillator, which refer to its radiographic imaging properties based solely on the specific nature of radiation interactions in response to incident x-rays. The 3-D transport code (ACCEPTP) of the ITS 3.0 Monte Carlo simulation package was used to model the x-ray absorption characteristics of

CsI(Tl) and quantify the influence of scintillator thickness on imaging performance. In this case, the transport problem was set up as shown in Figure 3-1. The standard key word command structure that is built in to the ITS codes were used to specify material and source specifications, the problem geometry, and relevant simulation parameters. The detector was specified to be a block of pure CsI with an area of $20 \times 20 \text{ cm}^2$ and variable thickness. Thallium doping was not explicitly specified since it only affects light activation, and exact concentrations and spatial distributions of activation centers were not easily available. This approximation is common for radiation transport problems in CsI(Tl) scintillators^{85,87,94}, and it is not expected to affect the accuracy of the results. The radiation source was modeled as a point, monodirectional emitter of megavoltage x-rays whose energy spectrum was specified based on reported values for a clinical 6 MV radiotherapy linac¹⁶⁵. Although this misrepresents practical linac sources that deliver divergent beams off a finite source size ($\sim 1 - 3 \text{ mm}$ focal spot size)¹⁶⁶, it is applicable to linear systems based characterization of imaging detectors assuming shift invariance. Since the focal spot size was not modeled, this analysis did not include the loss of spatial resolution due to source size (dependent on magnification), and subsequent calculations represented the MTF associated with the detector only. Also, possible variations in the results due to differences in reported beam spectra are not expected to be significant based on prior tests⁷⁷. The source position was specified to be at the center of the top surface of the scintillator.

Two output tallies were scored to describe the distribution of all radiation interaction events in energy and space. The energy distribution of the recorded events (referred to as a “pulseheights” tally) was scored over 600 linear energy bins (0.01 MeV wide) to reflect the spectral variations in the energy absorption characteristics of the scintillator, which was previously defined as the AED term in Equation 2-13. Similarly, the spatial distribution of the

energy deposition events indicated the 2-D spread function or PSF of the scintillator. In this case, the detector was sectioned into virtual voxels by zoning them into 20 μm wide longitudinal slabs as illustrated in Figure 3-1. By obtaining separate tallies of the energy deposition events recorded in each virtual voxel, the spatial distribution of events was conveniently obtained in the form of the intrinsic LSF of the detector. By sampling the interaction events in 20 μm spatial bins, the LSF could be discretized to near analog perfection as the effective Nyquist frequency limit (25 cy/mm) for this sampling was significantly higher than the spatial frequency range of interest in megavoltage imaging ($\sim 0 - 1 \text{ cy/mm}$). The photon and electron energy cut-offs for the simulations were set at 10 and 521 keV respectively in accordance with recommended norms^{41,42,58,77,87,94,142,159} for transport problems in radiation detection based on benchmarking standards of output accuracy relative to simulation time. All simulations were carried out by running 10 million photon histories (in 10 batches), which resulted in good overall accuracy in the AED and LSF tallies, especially in the energy and spatial bins contributing the dominant portion ($\sim 95\%$) of the AED and LSF tallies respectively.

Simulations were run for a series of scintillator thicknesses ranging from 5 – 100 mm, and selected results of the AED and LSF tallies are shown in Figures 3-2 and 3-3 respectively. The AED plots (expressed in interaction events per incident x-ray photon) indicated that most energy deposition events occurred in the broad energy range of 0.1 – 1 MeV and were peaked in the vicinity of 0.5 MeV, which is consistent with previously reported simulations results⁸⁷. The benefit of utilizing thicker detectors is highlighted by the increasing AED pulseheights for greater scintillator thicknesses. Error bars (typically expressed in terms of standard error) have been excluded from most of the AED plots since they were frequently too small to visualize clearly, and they also decreased the overall clarity and ability to distinguish plot legends. They

have been included for one of the AED tallies (scintillator thickness of 100 mm) to reflect the general magnitude of these standard errors that were generally consistent over all thicknesses. The relative error (fraction of one standard error over the mean) in the AED tallies ranged from a minimum of $< 1\%$ for the bins receiving the highest event counts to a maximum of 100% (some energy bins did not register any events). However, the simulated AED tallies were considered sufficiently accurate with over 95% of the cumulative AED (area under the curve) being from energy bins with $< 5\%$ relative error. The LSF plots in Figure 3-3 have been normalized to unit peak intensities to visualize their relative widths for different scintillator thicknesses. The plots indicated that increasing the thickness of the scintillator resulted in a broadening of the LSF profiles, which can be attributed to the greater pathlengths and lateral spreading of secondary photons and electrons in thicker detectors. Error bars were excluded from the LSF plots since they were too small to visualize (nearly 0% relative error) for the plotted range in Figure 3-3. Specifically, over 95% of the cumulative LSF had a relative error of $< 1\%$, and all LSF values that were $> 0.5\%$ of the peak intensity had $< 1\%$ relative error (maximum relative error was at the tail ends and was $\sim 12\%$).

The AED and LSF tallies were used in the calculation of intrinsic QE, DQE(0), and MTF as a function of scintillator thickness based on Equations 2-14, 2-13, and 2-4 respectively. As shown in Figure 3-4, both QE and DQE(0) increased with scintillator thickness. Compared to standard phosphor screens (QE $< 2\%$ at 6 MV), significant improvements in QE (up to 10 – 100 times greater) can be achieved with CsI(Tl) scintillators for a thickness range in the order of a few cm. Similar improvements can also be observed in the calculated DQE(0), although they only represent intrinsic detector characteristics that reflect upper estimates of imaging performance. The calculated QE values had negligible uncertainty (relative error $< 0.1\%$) as they

were accumulated over the entire AED pulseheight spectrum. The $DQE(0)$ values also had very low relative errors (0.1 – 2%) that were generally reduced with higher scintillator thicknesses. Figure 3-5 illustrates the effect of scintillator thickness on intrinsic MTF. As expected with the observed trends in LSF profiles, the MTF steadily declined with increasing detector thickness, and this effect was more pronounced at lower thicknesses. All the calculated MTF values had negligible relative errors (< 0.1%), and may be considered equivalent to presampled MTF spectra since the LSF profiles were sampled with near analog precision in extremely small voxels (20 μm wide).

Figures 3-4 and 3-5 demonstrate the effective trade-off between x-ray sensitivity (QE) and spatial resolution (MTF), which improve and decline with scintillator thickness respectively. To resolve this trade-off, an approximation for the effective intrinsic $DQE(f)$ spectrum (spatial frequency dependent DQE) of the scintillator was formulated using Equation 3-1.

$$DQE(f) \approx DQE(0) MTF^2(f) \quad (3-1)$$

This estimate of $DQE(f)$ was based on an extension of Equation 2-15 with the assumption that the intrinsic NPS spectrum for the detector was constant over all spatial frequencies (i.e. white noise). The intrinsic $DQE(f)$ spectra obtained in this fashion for the CsI(Tl) scintillator are shown in Figure 3-6. The $DQE(f)$ increased consistently with scintillator thickness at all spatial frequencies, which indicated a more dominant influence on QE and $DQE(0)$ compared to its effect on the MTF.

3.3 Prototype TSC Video EPID System

Following the characterization of the intrinsic radiographic merits of CsI(Tl) in relation to detector thickness, a proof-of-principle prototype of the TSC system was assembled using a test CsI(Tl) scintillating screen and a custom installed camera system. The principal aims of

developing the test prototype system were to extend the intrinsic imaging performance characterization carried out with Monte Carlo simulations to a practical measurement of imaging performance to further classify the system and study the effects of various system components. Imaging protocols including exposure or dose settings, camera operating parameters, and image processing were established following a custom installation of the camera system. Quantitative measurements of MTF, NPS, and DQE were acquired along with images of anthropomorphic phantoms for qualitative visualization of image quality. Detailed measurements to characterize various system components of the prototype were also obtained towards implementing theoretical models of imaging performance.

3.3.1 Design Considerations

The essential design considerations for a practical lens coupled scintillator – camera system include an appropriate choice of scintillator thickness, and the optical parameters of the lens and camera system, all of which depend on specifications and tolerance criteria associated with the imaging field. As indicated by Figures 3-4 – 3-6, the selection of thickness for a CsI(Tl) scintillator was not explicitly limited by spatial resolution since the overall intrinsic DQE steadily increased with thickness at all spatial frequencies. However, it is limited by the finite “depth of focus” of the lens. For a given optical geometry, the lens is configured to focus on a specific surface or plane in the scintillator (typically located near the center). The focus is diminished as one goes away from this median plane towards the top and bottom surfaces of the scintillator, and this effectively restricts its practical thickness. Precise focal depth calculations can be used to identify the maximum scintillator thickness that is feasible within focal tolerances based on the optical geometry and pixel size.

For a given scintillator – camera system, the lens is ordinarily positioned so that the optical path between the lens and the scintillator (sum of scintillator – mirror and mirror – lens

distances) matches the distance between the x-ray source and the scintillator. The choice of the camera system including the camera tube or target type and pixel dimensions is commonly dictated by the imaging application, and the selection of the lens is based on the focusing requirements for a given imaging geometry (field sizes and distances). The optical properties of a lens are commonly described in terms of its focal length (which determines its magnification) and an f-number (also referred to as f-stop or f-ratio), which is the ratio of the focal length to the diameter of the iris aperture. Lens specifications depend on the imaging field size, camera target, source and detector positions, and focal depth tolerances^{42,87}. In practice, there is significant interplay between the above parameters and an optimal combination of these parameters has to be obtained iteratively for the best possible light collection and spatial resolution⁴².

For the most part, these generic optical design techniques can be implemented with thick and clear scintillators like CsI(Tl) in much the same way as with phosphor screens. However, the physical properties of the scintillator need to be considered for certain aspects of optical coupling geometry. When using thick and optically clear scintillators instead of thin diffuse phosphor screens, the increased thickness and transparency of the luminescent detector results in two separate sources of optical blurring in the acquired images. One form of optical blurring that occurs uniformly across the entire image is caused by the refraction of light exiting the scintillation medium⁸⁷. The refractive bending of light rays results in a shift in the plane of focus of the lens that uniformly blurs the final image. This problem can be easily corrected by adjusting the position of the lens to compensate for light refraction. In this case, the ratio of the source – scintillator distance to the scintillator – lens optical path is made equal to the refractive index of the scintillator⁸⁷. Another source of optical blurring with a thick and clear scintillator is a specific spatially variant form of geometric blurring that is illustrated in Figure 3-7. When x-

ray photons originating from arbitrary points in the object plane interact within the scintillator, they generate a succession of light emission events along its path to form a scintillation track for each detected point in the object plane. With a divergent x-ray beam and a conventional light coupling geometry (the mirror and lens are situated below the luminescent screen), the scintillation tracks for all interactions are effectively resolved in the form of their linear projections at the lens' focus plane. This results in a given point in the object plane to be blurred into a line, and the extent of the blurring increases with scintillator thickness and also with the distance of the point from the center of the image (there is no blurring at the center)^{42,87}. Such geometric losses of spatial resolution are particularly undesirable since different parts of an image can suffer from varying degrees of blurring leading to visually distracting image artifacts. Sawant *et al* introduced a novel solution to prevent this form of blurring by incorporating a “back reflecting” or “reverse” optical coupling geometry in which the mirror, lens, and camera assembly are situated on the superior side of the scintillator (i.e. on the same side as the x-ray source)⁸⁷. As indicated in Figure 3-7, the reverse coupling allows scintillation tracks to be focused along optical paths that are parallel to the divergence of the x-rays so that all points in the object plane are faithfully resolved as corresponding points in the image plane. The reverse optical coupling geometry is illustrated in Figure 3-8.

3.3.2 Prototype Description

A complete prototype design requires an elaborate modeling of the effects of several physical and optical components as described in section 3.3.1. However, since the test prototype for the TSC system was developed using existing components (scintillator, linac, and gantry), a completely optimized prototype configuration was not feasible. The test prototype for the TSC system was developed as a modification to an existing clinical Siemens BEAMVIEW^{PLUS} portal imager (hereinafter referred to as the “Beamview”), which is a commercially available first

generation video EPID that was installed on a Siemens PRIMUS dual energy linac (Siemens Oncology Care Systems, Concord, CA). The Beamview is a conventional gantry mounted EPID that utilizes a standard Lanex Fast-B phosphor screen (Eastman Kodak, Rochester, NY). In its original configuration, the phosphor screen was coupled to a Newvicon-tube camera (512 x 480 pixel², ~ 30 μm pixel width, 8-bit ADC) via a conventional mirror – lens optical chain. For the TSC prototype, the phosphor screen was replaced with a clear monolithic CsI(Tl) crystal scintillator (Saint-Gobain Crystals, Paris, France) with a surface area of 25 x 25 cm² and a thickness of 12 mm. The CsI(Tl) scintillator was held by a black support plate mounted to its upper surface as shown in Figure 3-9. The bottom face of this black plate was made rough to minimize the reflection of scattered light in order to prevent the contamination of the imaging signal due to glare. The Beamview camera system was replaced by a Video-Optics V1519 Plumbicon-tube camera (Video-Optics, Los Gatos, CA) for improved spatial and contrast resolution (1240 x 1024 pixel², ~ 30 μm pixel width, 12-bit ADC). A 58 mm, f/1.0 lens (Noct-Nikkor, Nikon,) was used for focusing (i.e. focal length = 58 mm, f-number = 1.0) that rendered a demagnification factor of 22.6. The detector mount provided a source – detector distance (SDD) of 132 cm with an equivalent detector – lens distance, which rendered a pixel width of 0.37 mm at the imaging or detector plane and ~ 0.3 mm at the nominal object plane at the linac isocenter (100 cm from source). The maximum field-of-view that could be rendered by the camera optics was 34 x 28 cm² at isocenter, although the size of the CsI(Tl) scintillator limited imaging fields to 19 x 19 cm².

As shown in Figures 3-4, a 12 mm thick scintillator provides high intrinsic QE and DQE(0) values (24% and 13% respectively), which is a significant improvement over phosphor screens for which QE ~ 2% and DQE(0) ~ 1% (all listed values pertain to a 6 MV beam). The

choice of thickness was motivated by the prior successful use of this scintillator for megavoltage imaging⁸⁷ including good image quality and ample focal depth for conventional camera systems⁴², which provided a good experimental prototype for imaging measurements and future design and optimization of the TSC system. The camera system featured a Plumbicon tube (Phillips Components XQ5002, Narragansett Imaging, North Smithfield, RI) with negligible pixel gain variations and reduced dark noise compared to conventional tubes. The lead oxide based target of the Plumbicon was well suited to low light fields and ideal for high frame-rate megavoltage fluoroscopy with user controlled target integration¹⁵⁹. The camera target integration was user controlled with the help of a programmable camera software interface. A prominent limitation of the prototype was that the reverse optical coupling shown in Figure 3-8 could not be utilized due to the conventional gantry mounting of the original Beamview housing.

3.3.3 Imaging with the TSC prototype

During imaging, the linac was operated at 6 MV with an exposure rate of 300 MU/min. The frame acquisition settings of the camera system were controlled using a dedicated software interface. The exposure and dose settings could be adjusted for each acquisition by controlling the integration time of the camera target. The duty cycle of the camera interface consisted of the camera integration period, which was followed by a blanking signal to clear residual charge (lasting ~ 40 ms), followed by a period of 200 – 300 ms to write the accumulated 12-bit frames to the hard disk (the processor configuration available at the time did not allow a “write” instruction simultaneously with the integration and blanking phases). As a result, fluoroscopic capability was limited (2 – 3 frames/sec) for imaging with low sub-MU exposures (i.e. < 1 MU) even though 10 – 15 frames/sec would have been possible with more efficient processor control depending on processing speed and memory. The images were acquired on the camera control processor in raw format. Initial images revealed that due to non-ideal crystal growth, the CsI(Tl)

screen contained a few manufacturing imperfections (~ 0.1 – 4 mm diameter) that were distributed across the surface of the crystal. These imperfections were varied in shape and size and were specified to be caused by stress fractures during the growth process. Such imperfections act as small pockets that scatter the light produced, resulting in visible specks in the final image. These artifacts could be removed to some extent by a simple flat-field correction, wherein a flat or open field image was divided out from the original image to reduce the intensity variations caused by the imperfections. Figure 3-10 illustrates the effect of flat-field corrections for an image of a pediatric chest phantom acquired with the TSC. It must be noted that the flat-fielding only corrected for the general intensity variations caused by the crystal imperfections as more deep rooted effects like scatter and blurring cannot not be removed with this technique.

For a visual or qualitative inspection of overall image quality with the TSC prototype, anthropomorphic phantoms (pediatric chest, adult head, and femur and humerus bones in water) were imaged at various exposure settings. All phantoms were positioned at the isocenter to reflect clinical patient scatter conditions even though the field of view ($19 \times 19 \text{ cm}^2$) was not sufficient for some phantoms. The camera integration time was adjusted via software control to provide images in the range of 0.2 – 5 MU, where 1 MU = 1 cGy at the isocenter (i.e. 100 cm from the x-ray source). For a comparison with other systems, the chest and bone phantoms were imaged using several clinical portal imagers that included the original Beamview video EPID, an Elekta iView video EPID (Elekta Inc., Crawley, West Sussex, UK), an Elekta iViewGT flat-panel system, conventional Agfa Cronex 10T therapy film (Agfa-Gavaert N.V., Mortsel, Belgium), and Kodak EC-L film (Eastman Kodak, Rochester, NY). As in the case of the TSC, all phantoms were positioned at the isocenter, although this rendered varied image magnification

settings due to differences in the detector position or SDD. The SDD setting was 132 cm for the Beamview and both films, and the Elekta iView and iViewGT systems had their SDDs set to nearly 160 cm. The images were acquired at 5 MU for all clinical systems except for conventional film that required 10 MU, all of which represent typical clinical exposures for these systems. The film images were digitized using a Microtek ScanMaker 9600XL film scanner (Microtek, Los Angeles, CA) at 120 dots per inch (dpi) resolution and with 12-bit grayscale levels (120 dpi indicates ~ 0.2 mm pixel width). The phantom images are shown in Figures 3-11 and 3-12 for visual comparisons. These include TSC images taken with exposures of 0.2, 1, and 5 MU [parts (F), (G), and (H) respectively] to visualize the improvement in image quality with exposure.

The two clinical video EPIDs (Beamview and iView) provided relatively poor image quality especially over smaller anatomical features even as their contrast levels over larger structures were somewhat comparable to the conventional and EC-L film images. This can be attributed to poor spatial resolution that is characteristic of first generation video EPID systems. The TSC images at 1 and 5 MU exposures provided good contrast over larger anatomical structures that was generally comparable to that obtained with the iViewGT flat-panel EPID (imaged at 5 MU), and slightly superior to both films (5 and 10 MU). However, the flat-panel and film images featured superior visualization of finer structures indicating greater spatial resolution relative to the TSC prototype. The sub-MU (0.2 MU) TSC image provided reasonably good image quality despite the order of magnitude reduction of exposure. Greater contrast and finer structure detail could be clearly observed for the TSC image at 0.2 MU compared to those acquired at 5 MU with the Beamview and iView systems. Both conventional and ECL films were generally comparable in image quality, although conventional film required a much larger

exposure (10 MU) than EC-L film (5 MU). To investigate the potential of the TSC for megavoltage fluoroscopy with lower camera integration times, the adult head phantom was imaged with a lower linac exposure rate of 50 MU/min and target integration set to 36 ms, which provided a nominal exposure of 0.03 MU to observe the extent of reduction in image quality. It must be noted that the calculation of the exposure value (product of linac exposure rate and integration time) may be inaccurate due to uncertainties in the camera and processor clock cycles, and the lack of synchronization with the linac beam pulses. Figure 3-13 shows images of the head phantom acquired with the TSC (0.03 and 0.2 MU) and the Beamview (5 MU). In this case, the TSC image at 0.03 MU offered comparable or better image quality than the Beamview at 5 MU, while the TSC image at 0.2 MU provided clearly superior image quality.

3.3.4 Imaging Measurements

Quantitative measurements of MTF, NPS, and DQE were carried out with the TSC prototype to characterize its overall imaging performance based on methods described in Chapter 2 (sections 2.1 – 2.3) and using the imaging set-up and protocol indicated in section 3.3.3.

3.3.4.1 MTF of the TSC prototype

In order to measure the MTF for the prototype TSC, a standard angulated slit response technique was used to determine the LSF. A slit phantom was constructed using two precision machined 10 x 10 x 16 cm³ blocks of steel that were clamped together with a slit gap of 100 μm. In this case, the thickest dimension (16 cm) was oriented along the x-ray beam for maximal attenuation in the LSF tail. Shims (uniform brass foil of 100 μm thickness) were used to maintain the slit gap uniformly between the two blocks. The slit phantom was secured with heavy duty clamps and mounted on the arms of a programmable micro-positioning translation table. The slit was positioned in the imaging field with a small angulation (~ 2°) with respect to the image coordinate axis and held as close to the top surface of the scintillator as possible. Following an

initial approximate alignment with respect to the central-axis of the radiation beam using the linac light field and laser guides, the position of the slit was carefully adjusted in the image plane using shifts of 100 μm to maximize the x-ray transmission through the slit through trial and error. Typically, slit measurements are conducted at high exposures (> 10 MU) to minimize uncertainty. However, the high light output of CsI(Tl) resulted in signal saturation in the camera system, which limited the use of high exposures. Therefore, the slit response was obtained by averaging 25 sub-MU frames. One of the collected frames for the slit response image is shown in Figure 3-14. In order to determine the LSF baseline, the steel blocks were imaged at the same position after being clamped together with no separation between them. The baseline was subtracted from the LSF for accurate determination of the low frequency MTF response.

The method reported by Dobbins *et al* was followed to determine the exact slit angulation, wherein the variations in the intensity and position (or column index) of the transmitted slit response peaks over successive rows (assuming the LSF is measured along the rows) was used to calculate the slit angle¹⁴³. Figure 3-15 illustrates the cyclic variation of the peak intensities over successive rows that were carefully selected from specific regions of the slit response that were relatively unaffected by structural image artifacts due to crystal imperfections (no flat-field correction was used to preserve the integrity of the slit response). In this case, the local maxima of the profile indicated pixels of successive columns whose centers were exactly aligned with the median axis of the slit gap, while the profile minima resulted from the slit axis overlaid on the boundary between the pixels. Along the same lines, Figure 3-16 shows the variation in the relative positions corresponding to the peaks in Figure 3-15, reflecting a step-wise linear shift of column indices due to the slit angle. The exact value of the slit angle was calculated using the distance (in pixel rows) between successive peak maxima in Figure 3-15 and

aided by Figure 3-16. For the measured slit response for the TSC prototype, this distance was found to be approximately 24 pixels, which indicated a slit angle of $\theta \approx \tan^{-1}(1/24) = 2.4^\circ$. The y-axis co-ordinates in Figures 3-15 and 3-16 were not shown since their exact values were not significant. At the calculated slit angle, the effectively rendered sampling increment in the LSF was ~ 0.04 mm. However, to minimize the uncertainty of the oversampled LSF, it was reconstructed into 0.1 mm wide sampling bins and averaged over all the collected frames to obtain a smooth LSF with an oversampling factor of nearly 4. The oversampled LSF was reconstructed as described in section 2.1.3, and is shown in Figure 3-17. For comparison, a regularly sampled LSF obtained by averaging separate row profiles of the slit response is also shown.

The presampled MTF for the TSC prototype was calculated using the oversampled LSF and in Equations 2-4 and 2-7. This measurement represented the overall MTF of the prototype, which includes the effects of intrinsic radiation interaction characteristics (i.e. spreading of secondary photons and electrons) in the CsI(Tl) scintillator, spreading of light due to optical scattering within the scintillator, and the blurring of light by the lens and camera target. The intrinsic MTF of the scintillator due to radiation interactions alone was previously obtained using Monte Carlo simulations as described in section 3.2 and Figure 3-5. Due to the high degree of transparency of CsI(Tl)¹⁶³, the MTF contribution of light interactions in the scintillator is not expected to be significant. Therefore, much of the optical blurring in the TSC prototype can be attributed to the lens and camera system. Separate optical measurements were conducted to determine the joint contribution of the lens and camera target to the overall MTF. Herein, the CsI(Tl) screen was replaced with an optical slit target that consisted of two 5 cm thick plastic blocks separated by a slot gap of 50 μm . The ambient light in the linac room was adjusted to

provide sufficient light quanta to be transmitted through the slit in order to obtain an accurate estimation of the optical slit response for the lens and camera system. The optical slit response was analyzed along the same lines as the previously described treatment of the overall slit response, and the joint MTF contribution of the lens and camera system was determined. Since the overall MTF can be expressed as a product of its constituent component contributions as described by Equation 2-18, the MTF due to the spread of light within the CsI(Tl) scintillator could be isolated from the overall MTF of the TSC prototype using Equation 3-2.

$$MTF_{CsI(Tl) opt} = \frac{MTF_{system}}{MTF_{CsI(Tl) rad} MTF_{lens + camera}} \quad \text{and} \quad MTF_{lens} = \frac{MTF_{lens + camera}}{MTF_{camera}} \quad (3-2)$$

In this case, MTF_{system} indicates the overall system MTF, and its constituent components due to radiation interactions in the scintillator, optical spreading in the scintillator, and the blurring due to the lens and camera system are referred to as $MTF_{CsI(Tl) rad}$, $MTF_{CsI(Tl) opt}$, and $MTF_{lens + camera}$ respectively. Similarly, since the MTF contribution of the camera target alone (MTF_{camera}) was provided separately by the vendor (Video-Optics, Los Gatos, CA), the MTF due to the lens itself (MTF_{lens}) could also be calculated along these lines. It must be noted that Equation 3-2 disregards the locally variant geometric blurring described in Figure 3-7 that resulted from the use of conventional optical coupling for the TSC prototype instead of the recommended reverse coupling geometry. However, this effect is not expected to be significant since much of the spatial frequency range for the MTF measurement was covered in the peak-to-tail transition of the slit response, which was at or very close to the center of the field where the blurring was minimal.

The overall and component MTF spectra determined for the TSC prototype are shown in Figure 3-18. The plots indicated that the overall MTF of the prototype was significantly reduced compared to the intrinsic MTF due to radiation interactions alone. This was mainly due to the

poor MTF associated with the optical coupling through the lens that is characteristic of video EPID systems. Figure 3-19 shows the intrinsic MTF spectra due to radiation interactions alone and when coupled with optical spreading within the screen for the 12 mm thick CsI(Tl) scintillator and a standard Lanex Fast-B phosphor screen (1 mm Cu + 0.365 mm Gd₂O₂S:Tb). As expected, the MTF due to radiation interactions alone was significantly greater for the phosphor screen compared to the CsI(Tl) scintillator due to the large difference in their thicknesses. However, when the effects of light spreading within the screen were included, the subsequent reduction in MTF was significantly more severe for the phosphor screen compared to CsI(Tl), which clearly reflected the inherent advantage of an optically clear scintillator. In other words, the MTF of a 12 mm thick CsI(Tl) scintillator is only slightly lower than that for a thin phosphor screen despite its order-of-magnitude greater thickness due to the optical clarity of CsI(Tl). In this case, the MTF values for the Lanex Fast-B phosphor screen were obtained from reported results⁵⁸.

Finally, MTF measurements were also conducted using the angulated slit response method for the original Siemens Beamview video EPID system (i.e. standard phosphor screen + original Newvicon camera) as well as for the “modified Beamview” with only the camera system replaced by the prototype Plumbicon camera (i.e. phosphor screen + prototype camera). These MTF measurements are shown with those for the TSC prototype in Figure 3-20 to indicate the improved spatial resolution with the prototype camera system alone. Along the same lines as Figure 3-19, the MTF of the modified Beamview was only slightly greater than that for the TSC prototype. This validated the premise of utilizing a thick CsI(Tl) scintillator for greater x-ray detection and light output, as even with the accompanying loss in spatial resolution the MTF due

to a 12 mm thick CsI(Tl) scintillator was still comparable to that for a much thinner phosphor screen.

3.3.4.2 NPS of the TSC prototype

The methods described in section 2.2 were used to determine NPS spectra for the TSC prototype. A series of open fields (i.e. air images) were acquired with a field size of 20 x 20 cm² specified at the isocenter, which rendered an exposed area of ~ 26 x 26 cm² at the scintillator that just exceeded the imaging surface area (25 x 25 cm²). The images were not flat-field corrected to the artifacts from crystal imperfections to preserve the integrity of the statistical distribution of the pixel intensities. Pairs of open field images were randomly selected and subtracted from each other to remove systematic artifacts. Consecutively acquired frames were avoided during the selection of the open field pairs to prevent temporal correlation effects in the calculated NPS spectra. Nearly 50 open field pairs were used to generate difference images to facilitate averaging of the final NPS spectra. A central 512 x 512 array of pixels was selected from the open-field difference images (1240 x 1024 pixel² overall area) to perform NPS calculations, which covered a large portion of the scintillator imaging area (~ 19 x 19 cm²). Equation 2-11 was used to obtain 2-D NPS spectra [i.e. $NPS(u,v)$] for each open field difference image, from which 3-element thick row and column slices adjacent and parallel to the frequency co-ordinate axes (u and v respectively) were extracted to generate 1-D NPS profiles [i.e. $NPS(u)$ and $NPS(v)$ or $\sim NPS(f)$] in 0.1 cy/mm wide spatial frequency bins as described in section 2.2.

As in the case of the MTF measurements, NPS spectra were separately measured for the original Siemens Beamview, modified Beamview with the prototype camera, and the TSC prototype, and are shown in Figure 3-21. The NPS for the TSC has been presented separately along both co-ordinate axes to illustrate directional differences in the spectra due to the orientation of the read-out scan lines for the camera target. In this case, the read-out scan lines

were parallel to the horizontal image axis and perpendicular to the vertical image axis. Although, the NPS spectra along both directions were generally comparable at lower spatial frequencies, the NPS along the horizontal axis (i.e. parallel to scan lines) clearly decreased at spatial frequencies > 0.6 cy/mm. The reduced NPS along the direction of the camera scan lines was consistent with previously reported studies on a similar Plumbicon tube based camera system¹⁶⁷. The exact reasons underlying such axial differences were not specified and are not clear. They may be related to correlation effects due to the lag response of the target. Similar trends have also been reported for MTF measurements¹⁶⁷, although no significant differences were observed with the TSC prototype, which may be due to the relatively low values of the MTF beyond 0.6 cy/mm.

The NPS for the original Beamview system was determined using open fields acquired at a higher exposure (5.25 MU) compared to the sub-MU exposures (0.2 MU) used with the modified Beamview and TSC prototype systems. To account for this, the NPS for the original Beamview shown in Figure 3-21 has been appropriately scaled up to reflect the expected linear reduction in NPS with exposure and provide a more accurate comparison of the NPS spectra. From the NPS plots, the separate improvements in the noise characteristics of the TSC prototype due to the performance of the CsI(Tl) screen and the prototype camera system can be clearly observed. The use of the improved camera system in the modified Beamview results in significantly reduced noise relative to the original Beamview that utilized a conventional Newvicon tube camera. For the TSC prototype, the use of the CsI(Tl) scintillator led to a further reduction of the overall noise that can be attributed to its greater x-ray sensitivity and light output compared to the phosphor screen. Overall, the TSC prototype featured an order-of-magnitude

reduction in the NPS compared to the Beamview and other commercial first generation video EPIDs in general.

3.3.4.3 DQE of the TSC prototype

The MTF and NPS measurements for the TSC and Beamview systems were used for DQE calculations using Equation 2-15. The NPS spectra measured perpendicular to the camera scan direction was used in this case since it was higher than that parallel to the scan lines, and represented a more conservative estimate of the imaging uncertainty. The normalization factor (Φ) that represents the quantum fluence (photons/mm²) associated with the NPS open fields in these calculations was determined for each system from the specific exposure (MU) used to acquire open field images, and a series of fluence – dose conversion factors for water or tissue equivalent media that were generated by Rogers *et al* using Monte Carlo simulations¹⁶⁸. In this case, the imaging exposure for each open field was converted to a reference dose value in cGy through the linac output calibration condition, wherein 1 MU = 1 cGy at the isocenter (at a depth of 1.5 cm in water with a 6 MV beam), and scaled down from the isocenter to an equivalent dose value at the surface of the detector. The dose at the detector surface was converted to an equivalent fluence term (photons/mm²) using a mean effective fluence – dose conversion factor that was obtained by weighting the energy dependent fluence – dose factors¹⁶⁸ calculated by Rogers *et al* by the reported spectrum¹⁶⁵ for a 6 MV beam.

The calculated mean fluence – dose conversion factor for 6 MV beams at the detector plane for the TSC and Beamview systems was found to be 7.7×10^{-8} cGy.mm²/photon. Comparable values of fluence – dose factors for 6 MV beams have been reported by Bissonnette *et al* (7.4×10^{-8} cGy.mm²/photon)^{159,167}, Munro *et al* (8.4×10^{-8} cGy.mm²/photon)⁵⁷, and Lachaine *et al* (7.5×10^{-8} cGy.mm²/photon)⁶⁸. The general variability of these values can be attributed to the use of different beam spectra⁶⁸. The relative uncertainty of the calculation was ~

15%, which was consistent with the general variation in the reported results. The DQE spectra for the TSC and Beamview systems are shown in Figure 3-22. The DQE for the modified Beamview was clearly improved relative to the original Beamview, which reflected the superior spatial resolution and noise characteristics of the prototype Plumbicon tube camera system. The $DQE(0)$ was $\sim 0.1\%$ for the original Beamview, which was consistent with the expected value for conventional first generation video EPIDs. The prototype camera system led to some improvement in the modified Beamview that provided $DQE(0) \sim 0.3\%$, although much of the improvement in imaging performance was in overall spatial resolution. On the other hand, the TSC prototype provided an order-of-magnitude improvement in DQE compared to the Beamview systems [$DQE(0) \sim 1.7\%$], which indicated the considerable improvement in imaging performance due to the enhanced x-ray detection and light output characteristics of the CsI(Tl) scintillator. The intrinsic DQE for a 12 mm thick CsI(Tl) scintillator [$DQE(0) \sim 13\%$] that was previously calculated using Monte Carlo simulations and shown in Figure 3-6 has also been shown in comparison with the measured DQE of the TSC prototype in Figure 3-22. The order-of-magnitude reduction in the overall DQE for the TSC prototype compared to the intrinsic DQE of the scintillator itself indicated a severe degradation in imaging performance due to poor optical coupling.

3.3.5 Linear Cascaded Systems Modeling

The linear systems modeling was implemented with the TSC system to provide a theoretical platform to design and optimize a future prototype configuration.

3.3.5.1 Characterization of component stages

Based on the physical processes underlying the progression of imaging quanta in the TSC system, it could be differentiated into 10 serial stages that were separately identified by their respective gain (g), spreading (T) or additive noise (S) components. These include 5 gain stages,

4 spreading stages, and 1 source of additive noise. The 5 stages of quantum gain were characterized in terms of the detection or conversion efficiencies for x-ray or light photons. The quantum spreading stages were represented by their separate MTF contributions, all of which were previously characterized during the measurement of MTF spectra for the TSC prototype in section 3.3.4.1. The MTF components associated with each quantum spreading stage were described in Equation 3-2. Finally, a source of additive noise was quantified in terms of its relative contribution to the overall NPS spectrum of the TSC EPID system. The linear cascaded systems model highlighting the component stages for the TSC is shown in Figure 3-23.

The first stage of the linear systems model for the TSC can be identified as the detection of incident x-ray photons by the CsI(Tl) scintillator. The corresponding gain (g_1) associated with x-ray detection was previously characterized as the QE of the CsI(Tl) scintillator using Monte Carlo simulations (section 3.2) and is shown in Figure 3-4. The simulation results indicated that for a 12 mm thick CsI(Tl) scintillator, $g_1 = 0.24 \pm 0.001$. Since x-ray detection can be considered a process of binomial selection (an x-ray either interacts in the scintillator or passes through), the Poisson excess term $C_{g1} = -g_1$.

The second component stage of the TSC involves the spread of secondary photons and electrons due to radiation interactions in the CsI(Tl) scintillator. Its associated MTF contribution (T_2) and was previously described as the intrinsic MTF of the scintillator in section 3.2 and Figure 3-5, and also as $MTF_{CsI(Tl) rad}$ in section 3.3.4.1 and Equation 3-2. It was specifically shown for a 12 mm thick CsI(Tl) scintillator in Figures 3-18 and 3-19.

In the third stage of the cascaded systems model, the energy absorbed due to radiation interactions in the CsI(Tl) scintillator is converted to visible light. This scintillation or x-ray to

light conversion quantum gain (g_3) as well as its associated variance ($\sigma_{g_3}^2$) and subsequent Poisson excess value (ϵ_{g_3}) were quantified using Equation 3-3 below.

$$g_3 = \eta_{opt} \frac{\bar{E}_{abs}}{\bar{E}_{opt}} \quad \text{and} \quad \epsilon_{g_3} = \frac{\sigma_{g_3}^2}{g_3} - 1 \quad \text{where} \quad \sigma_{g_3}^2 = \eta_{opt}^2 \frac{\sigma_{abs}^2}{\bar{E}_{opt}^2} \quad (3-3)$$

In this case, \bar{E}_{abs} and σ_{abs}^2 indicate the mean energy absorbed by the scintillator from radiation interactions and its associated variance respectively. The value of \bar{E}_{opt} is the mean energy of the visible light photons emitted via scintillation in response to radiation interactions. The fraction η_{opt} represents the intrinsic energy conversion efficiency of the luminescence process in CsI(Tl), which governs the fraction of the total deposited energy due to radiation interactions that is converted to visible light. The values of \bar{E}_{opt} (= 2.28 eV) and η_{opt} (= 0.123) were obtained from the emission spectrum of the CsI(Tl) crystal and an overall light output value (~ 54 light photons per keV of x-ray deposition energy) provided by the vendors (Saint-Gobain Crystals, Paris, France), while \bar{E}_{abs} and σ_{abs}^2 were calculated according to Equation 3-4 from the moments of the AED pulseheight spectrum obtained using Monte Carlo simulations (section 3.2).

$$\bar{E}_{abs} = \frac{\int E AED(E) dE}{\int AED(E) dE} \quad \text{and} \quad \sigma_{abs}^2 = \frac{\int (E - \bar{E}_{abs})^2 AED(E) dE}{\int AED(E) dE} \quad (3-4)$$

Based on Equations 3-3 and 3-4, $\bar{E}_{abs} = 1.019 \pm 0.001$ MeV, $\sigma_{abs}^2 = 0.9 \pm 0.001$ MeV, $g_3 = 5.5 \times 10^4$, $\sigma_{g_3}^2 = 2.6 \times 10^9$, and $\epsilon_{g_3} = 4.8 \times 10^4$.

The fourth stage of the cascaded systems model involves the spreading of light generated via luminescent emission within the scintillator. Its associated MTF contribution (T_4) was previously evaluated using Equation 3-2 and is shown in Figure 3-18.

The fifth stage of the cascaded systems model reflects the fraction (g_5) of the total number of emitted light photons that can exit the scintillator based on its optical transmission.

The optical linear attenuation coefficient for CsI(Tl) was determined to be $\sim 0.09 \text{ cm}^{-1}$ based on reported measurements of optical transmission for an inch thick CsI(Tl) crystal¹⁶³. For the 12 mm thick CsI(Tl), g_5 was calculated to be ~ 0.9 . Some uncertainty is associated with the value of g_5 depending on the specific location of light emission and the distance travelled by the light photon before exiting the scintillator surface. However, this variability was ignored ($C_{g_5} \approx -g_5$) since it is expected to be relatively small compared to the high optical clarity of CsI(Tl).

The sixth stage of the TSC model is represented by the optical coupling efficiency (g_6) of the focusing cone of the lens. The value of g_6 was obtained using Equation 3-5 based on the method prescribed by Swindell⁴³, wherein the fraction of light entering the focusing cone of the lens can be calculated as a function of the optical transmission of the lens (τ), the refractive index of the scintillator (η), the f-number (f) of the lens, and the demagnification factor (m) of the lens.

$$g_6 = \frac{\tau}{[4 n f (1 + m)]^2} \quad (3-5)$$

In this case, the value of the lens optical transparency τ ($= 0.9$) was selected as a median or typical value within a range (0.7 – 1.0) reported in literature^{43,44,83,86,159,169}. The demagnification m ($= 22.6$) was determined from the ratio of the imaging pixel dimensions at the plane of the scintillator and at the plane of the camera target. The refractive index η for CsI(Tl) is 1.79, while an f/1.0 lens (i.e. $f = 1.0$) was used with the prototype camera system. From these values, g_6 was calculated to be 3.15×10^{-5} ($C_{g_6} = -g_6$). The extremely low value of g_6 indicates a significant loss in light quanta that characteristically degrades the imaging performance of lens – coupled scintillator – camera based imaging systems. It must be noted that Equation 3-5 is specifically applicable to a clear scintillator like CsI(Tl) since optical absorption losses within the scintillator are not significant, and the scintillator effectively acts as an aggregation of independent point isotropic light sources^{43,169}. However, this assumption breaks down for a conventional phosphor

screen with significant light absorption, and the screen effectively acts as a Lambertian emitter as the angular emission distribution of the light exiting the screen is generally forward peaked^{43,169}. According to Liu *et al*¹⁶⁹, the light coupling efficiency for Lambertian light distributions is greater than that described by Equation 3-5 for an isotropic emitter by a factor approximately equal to $4\eta^2$.

The seventh stage of image detection consists of the spreading of light within the lens due to optical scatter, whose effect is greatly compounded by the demagnification of the imaging field via its focusing cone. The associated MTF component (T_7) was previously determined using Equation 3-2 and is shown in Figure 3-18.

The eighth stage of image detection involves the optical detection efficiency (g_8) of the camera target. The value of g_8 for the Plumbicon camera target was calculated to be 0.41 (and $C_{g8} = -g_8$) from the vendor specified optical sensitivity spectrum of the camera target (Video-Optics, Los Gatos, CA) and the vendor specified luminescent emission spectrum for the CsI(Tl) scintillator (Saint-Gobain Crystals, Paris, France).

The ninth stage of the cascaded systems model is represented by the spread of light in the camera target. The associated MTF contribution (T_9) was specified by the camera vendors (Video-Optics, Los Gatos, CA), and is shown in Figure 3-18.

Finally, the tenth and last stage of image detection includes the additive noise component (S_{10}) due to the dark noise of the camera system. In this case, the dark noise additive component of the overall system NPS was determined by collecting several dark field frames with no radiation incident on the scintillator (i.e. no light was incident on the camera), and using a target integration time equivalent to realizing 0.2 MU exposures per frame during regular imaging. The dark field NPS was calculated in the manner described in section 3.3.4.2 and Equation 2-11.

However, to satisfy the requirements of the specific form of S_{10} as it pertains to the cascaded systems model (described in section 2.4.2.3), the mean pixel intensity for an open field frame of 0.2 MU exposure was used for normalization of the NPS. In general, the NPS due to dark noise was observed to be ~ 30% of the total NPS over all spatial frequencies. The values of S_{10} were found to be steadily decreasing with spatial frequency and lay within the range of 0.004 – 4.9, which was consistent with values reported by Bissonnette *et al* for a similar Plumbicon tube camera system¹⁵⁹.

3.3.5.2 Theoretical evaluation of DQE

Based on the linear cascaded systems modeling, the theoretical DQE for the TSC prototype can be determined from its component stages as shown in Equation 2-19. In this case, the parameters governing each stage (g , C_g , and T) are cascaded progressively over all stages. The above parameters indicating the 10 stages of the TSC system were applied to Equation 2-19, and the simplified expression shown in Equation 3-6 was realized.

$$DQE(f) = \frac{g_1 T_2^2(f)}{1 + \left(\frac{\epsilon_{g3}}{g_3} \right) + \left(\frac{1 + S_{10}(f)}{g_3 g_5 g_6 g_8 T_4^2(f) T_7^2(f) T_9^2(f)} \right)} \quad (3-6)$$

The theoretical DQE was evaluated for the TSC prototype and is shown in Figure 3-24 along with the experimentally measured DQE for the prototype. In general, the theoretical DQE values were in very good agreement with the measured DQE within the limits of uncertainty. The intrinsic DQE spectrum obtained for a 12 mm thick CsI(Tl) scintillator from Monte Carlo simulations (i.e. radiation interactions only) is also shown in Figure 3-24, and represents the theoretical limit or maximal DQE for the given scintillator and x-ray beam. The DQE for the TSC prototype (both theoretical and experimental) was generally an order of magnitude lower than the limiting intrinsic DQE of the scintillator. Specifically, $DQE(0) = 0.022 \pm 0.004$, $0.017 \pm$

0.004, and 0.129 ± 0.008 respectively for the theoretical, experimental, and intrinsic DQE spectra. The reason for the reduction in DQE can be identified based on the quantum gains associated with various stages in the TSC prototype. The specific effects of these gains can be visualized graphically through a serial account of quantum levels over all stages of the system. This graphic tally of quanta is referred to as a “quantum accounting diagram” (QAD)^{159,160}, and is often used to visualize the relative influences of various stages on the overall imaging performance of the system. The expression for the spatial frequency dependent QAD of a system is shown in Equation 3-7, and the QAD is shown for the TSC prototype in Figure 3-25.

$$QAD_i(f) = \prod_{j=1}^i g_j T_j^2(f) \quad (3-6)$$

For the TSC prototype, the QAD plots clearly indicated a major quantum sink due to a sharp decline in the number of imaging quanta in stage 6 (optical coupling by the lens) on account of its extremely poor light collection efficiency ($g_6 \sim 0.003\%$). As a result, the immense quantum gain ($g_3 \sim 5.5 \times 10^4$) associated with scintillation and the emission of light did not lead to a proportional improvement in imaging performance since the effect of the optical quantum sink due to the lens was more significant.

To investigate further, the theoretical DQE was calculated progressively to isolate the effects of individual system components. Figure 3-26 shows separately calculated theoretical DQE spectra for the following progressive groups of stages: scintillator only (stages 1 – 4), scintillator + lens (stages 1 – 7), scintillator + lens + camera (stages 1 – 9), and the entire system or scintillator + lens + camera + dark noise (stages 1 – 10). The stage – wise DQE computation was performed for a given group of stages by simply omitting the parameters for higher order stages in Equation 3-6. The results indicated that the effect of the quantum loss due to the camera system was comparable to that of the lens even though the QAD plots suggested a sharper

decline for the latter. The DQE also suffered significant reduction from the addition of dark noise from the camera acquisition electronics, although this effect was predominant at lower spatial frequencies and almost negligible at high frequencies. The decline in DQE at higher spatial frequencies was mostly from the influence of the lens, which could be attributed to its reduced MTF component (T_7) compared to that of the camera (T_9). Based on the results in Figures 3-24 – 3-26, the reduction in the overall DQE for the TSC prototype was due to the combined influences of the poor light collection of the lens (g_6), low camera sensitivity (g_8), and low frequency dark noise (S_{10}). Therefore, an optimized optical coupling configuration that allows greater light collection, detection, and read-out was necessary for the overall DQE of the TSC to approach the intrinsic limits set by the scintillator.

3.4 Optimization of the TSC EPID System

Based on the measurement and theoretical evaluation of the DQE for the TSC prototype, the limitations of an unoptimized optical coupling geometry and its detrimental effects on overall imaging performance was evident. Therefore, to the end of obtaining an optimized prototype configuration based on the 12 mm thick CsI(Tl), the system was redesigned to obtain imaging and optical geometries that provide the best possible imaging performance within practical and clinical constraints. In this case, “imaging” and “optical” geometries will be used hereafter to describe the overall system geometry pertaining to the physical orientation of system components and the optical parameters of the lens and camera system respectively. However, it must be noted that the significant interplay between various design parameters results in only a loose distinction between the two geometry types.

3.4.1 Imaging Geometry

The essential design considerations for designing the imaging geometry for a video EPID system were previously described in section 3.3.1. Based on the specific optical characteristics

(Figure 3-7) of a thick and clear CsI(Tl), the use of reverse optical coupling Figure 3-8) was mandatory. Therefore, the physical arrangement of the system components presented the first mechanical constraint for designing the imaging geometry since the presence of the mirror above the scintillator requires additional clearance for the EPID relative to the isocenter. The general layout for the proposed TSC prototype is shown in Figure 3-27. In order to determine an appropriate source – detector distance (denoted by SDD as defined previously), two clinical constraints were considered: imaging field size, and the required EPID clearance for clinical workflow. As shown in Figure 3-27, the maximum imaging field size is denoted by s , which is defined at the linac isocenter at a distance I from the source. Let C be the desired clearance between the isocenter and the highest part of the inclined mirror. Therefore, it can be seen that the position of the detector or SDD is given by Equation 3-7.

$$SDD = I + C + S \quad (3-7)$$

In this case, S represents the vertical distance occupied by the inclined mirror, which is also equal to the maximum field size projected on to the detector plane (i.e. the minimum dimension of one side of the detector). Based on field magnification, $S = s (SDD / I)$, which when combined with Equation 3-7, provides the expressions in Equation 3-8 for SDD and S .

$$SDD = I \left(\frac{I + C}{I - s} \right) \quad \text{and} \quad S = s \left(\frac{I + C}{I - s} \right) \quad (3-8)$$

The value of I is rigidly set at 100 cm for conventional linacs in radiation therapy, and $s = 25$ cm may be considered a reasonable approximation of the field size requirements (i.e. $25 \times 25 \text{ cm}^2$) for clinical imaging based on the orientation of current commercial EPIDs. Therefore, the imaging geometry can essentially be obtained with SDD and S as a function of C . The choice of an appropriate value for C depends on the space constraints associated with treating the patient in specific therapy rooms and may vary ($\sim 30 - 60$ cm typically). For example, the Siemens

Beamview has an *SDD* setting of 132 cm, which provides $C = 32$ cm. Similarly, $C = 60$ cm for commercial a-Si flat-panel EPIDs ($SDD = 160$ cm). It must be noted that the effective clearance between the isocenter and the scintillator varies between C (at highest part of the mirror), and $C + S$ for the base of the mirror.

3.4.2 Optical Geometry

The relevant parameters associated with the imaging geometry (*SDD* and *S*) represent inherent constraints to the selection of the optical parameters of the lens. The focal length (F) of the lens determines the demagnification (m) provided by the lens in focusing an object of size o on the plane of the camera target as an image of size i (where $m = o / i$) as shown in Figure 3-27. Let D_{DL} and D_{LC} denote the distances between the effective planes of the detector and lens, and the lens and camera target respectively. It can be seen that $m = D_{DL} / D_{LC} = F / (D_{LC} - F)$, which gives Equation 3-9 for the focal length F needed for a lens to render a demagnification of m .

$$F = \frac{D_{DL}}{m + 1} \quad (3-9)$$

The detector – lens distance (D_{DL}) can be related to *SDD* based on the refractive index (η) of the scintillator ($D_{DL} = SDD / \eta$). In addition, the demagnification can be expressed based on its dependence on the relative sizes of the detector (S) and the camera target (T). Assuming that the entire imaging area is precisely focused on to the entirety of the target, $m = S / T$. Subsequently, the focal length F can be reduced to a function of the original physical constraints (I, f , and C) as shown in Equation 3-10 (all distance units are in cm).

$$F = \frac{\left(\frac{I}{\eta}\right)\left(\frac{I+C}{I-s}\right)}{\left(\frac{s}{T}\right)\left(\frac{I+C}{I-s}\right)+1} = \frac{\left(\frac{4}{3\eta}\right)(100+C)}{\left(\frac{1}{3T}\right)(100+C)+1} \quad \text{where } I = 100 \text{ and } s = 25 \quad (3-10)$$

Typically, since focal lengths are available in a standard progression of sizes (eg. 100, 105, etc), the value of F obtained may need to be rounded up to a standard size. The clearance C has to be readjusted to match the new value of F . Equation 3-10 has also been extended to include standard values for I (100 cm) and s (25 cm).

3.4.3 Extra-focal blurring

Based on Equations 3-8 and 3-10, the essential parameters associated with the imaging and optical geometries for the TSC system were realized in terms of a clinical constraint (C) and the size of the target (T) for a given selection of the camera system. For a given focal length F , the f-number (f) of the lens indicates the diameter (D) of its aperture ($f = F / D$). The choice of f represents an important trade-off between light collection and optical blurring for any optical system. Specifically, while more light can be collected when f is as small as possible (eg. $f \leq 1$ may be considered low), the depth of focus is limited (or extra-focal blurring is more significant) as f is reduced. As described previously (section 3.3.1), depth of focus refers to a limitation in the depth of a scintillator (on either side of the optimal focus plane) that can be appropriately focused by the lens. For thick scintillators, any point situated away from the optimal focus plane is projected as a disc (referred to as a “circle of confusion”) on the camera target as a result of extra-focal blurring. The diameter (B) of the projected blur or circle of confusion increases with the distance of the illuminating point from the optimal focus plane. Sawant *et al* reported a method to determine the projected blur B for a thick scintillator based video EPID system as a function of the scintillator thickness (t), the detector – lens distance (D_{DL}), and the lens parameters (F and f) as shown in Equation 3-11⁸⁷.

$$B = \left(\frac{Fm}{f} \right) \left[1 - \left(\frac{D_{DL}}{D_{DL} - F} \right) \left(\frac{D_{DL} - t/2\eta + \varepsilon - F}{D_{DL} - t/2\eta + \varepsilon} \right) \right] \quad \text{where } \varepsilon = \frac{\sqrt{D_{DL}^2 + \left(\frac{t}{\eta} \right)^2}}{2} - \frac{D_{DL}}{2} \quad (3-11)$$

The inclusion of the demagnification m in Equation 3-11 projects the circle of confusion on the detector plane. A representative spread function in the form of an LSF profile can be developed from a given value of B by obtaining its line integral, which is given in Equation 3-12. In this case, $L(x,B)$ indicates the LSF in 1-D space projected at the detector plane for a uniform circular blur of diameter B .

$$L(x,B) = \left(\frac{2}{B}\right) \sqrt{\left(\frac{B}{2}\right)^2 - x^2} \quad (3-12)$$

3.4.4 Choice of Parameters

The analysis in sections 3.4.1 – 3.4.3 revealed that the relevant parameters associated with the design of the imaging and optical geometry for the TSC system could be reduced to computable functions of a set of practical and clinical constraints. Specifically, the system design depended on a judicious selection of the EPID clearance C , the size of the camera target T , and the f-number f of the lens. The choice of the camera system is particularly important in relation to its potential effect on image quality based on its optical sensitivity and dark noise. As well, a camera system with a large target results in increased light collection efficiency since a smaller demagnification factor m is required to focus the light on to the target. A thermoelectrically cooled 2048 x 2048 pixel² thinned, back-illuminated Peregrine 486 CCD (Fairchild Imaging, Milpitas, CA) was selected as the camera system for the proposed TSC prototype. The camera provided a 60 x 60 mm² target area (i.e. $T = 6$ cm), and a pixel width of 30 μm that can provide excellent spatial resolution in the imaging plane for small demagnification factors.

To obtain an appropriate choice of the clearance parameter C , its effect on the imaging geometry (SDD and S), as well as its subsequent or indirect influence on optical parameters like light collection efficiency and extra focal blurring was studied by applying Equations 3-8, 3-10, and 3-11. Figure 3-28 (A) indicates the variation in detector position (SDD) and scintillator size

(S) for C values in the range of 30 – 90 cm. Both SDD and S increased linearly with C , although the increase in SDD was more pronounced. The SDD ranged from ~ 170 cm (for $C = 30$ cm) to ~ 250 cm (for $C = 90$ cm), while the detector size S varied between 40 and 60 cm for the same range of C . On the other hand, the focal length F calculated using Equation 3-10 increased very little with C ($F = 115 - 125$ mm for $C = 30 - 90$ cm). Subsequently calculated values of the demagnification factor m based on the specifications of the CCD camera ($T = 6$ cm) ranged between 7.2 – 10.5, which was significantly lower than the demagnification in the current prototype ($m = 22.6$ for the Plumbicon camera system). Figure 3-28 (B) indicates the effect of C on the light collection efficiency of the lens based on the calculated values of m and with $f = 1.0$. The light collection efficiency was found to decrease with C and its values ranged between 0.01 – 0.03% (for $C = 30 - 90$ cm), which was an order of magnitude greater than its corresponding value for the current prototype (~ 0.003%).

Equation 3-11 was used to evaluate the projected blur diameter (B) for the given variation in C , and the results are shown in Figure 3-28 (C). The values of B ranged from ~ 0.3 mm for $C = 90$ cm, and increased up to ~ 0.4 mm (comparable to pixel dimensions of current commercial EPIDs) for $C = 30$ cm. To examine the specific effects of these values of B , Equation 3-12 was used to obtain LSF profiles corresponding to selected values of B and $f = 1$, and the subsequently calculated MTF spectra are shown in Figure 3-29. The MTF calculations indicated that for the range of the projected blurring in Figure 3-28 (C), the MTF contribution due to extra-focal blur in the range of 0.3 – 0.4 mm could result in a reduction of the overall MTF by 10 – 20% respectively at 1 cy/mm. Although an increased value of f resulted in lower extra-focal blur, the improvement in spatial resolution was not significant enough to outweigh the loss in light collection efficiency. Due to the contrasting influences of the clearance C on light collection

efficiency in Figure 3-28 (B) and on extra-focal blurring in Figure 3-28 (C), its optimal choice for the best possible imaging system design is not clear. Therefore, the selection of C was determined based on practical and clinical constraints. The use of a high value of C increased the SDD and S as shown in Figure 3-28 (A). While high SDD settings decrease the influence of scatter in the acquired images, it also results in reduced x-ray fluence at the detector and increased loss in spatial resolution due to the large focal spots of conventional linacs. Moreover, the increased imaging surface areas required with large SDD and S values adds significantly to the cost of the system. On the other hand, very low values of C may restrict clinical workflow (particularly in the case of obese patients). Therefore, the value of C was selected to 40 cm, which provided $SDD \sim 187$ cm and $S \sim 46$ cm. With $C = 40$ cm, the effective vertical distance between the isocenter and the scintillator panel ranged from 40 cm at the highest end of the mirror up to 86 cm (i.e. $C + S$) at the base of the mirror, which was comparable to current commercial EPIDs (having $C = 60$ cm). The subsequently calculated optical parameters corresponding to the selected value of C were: $F \sim 120$ mm, $m = 7.8$, light collection efficiency or $g_6 \sim 0.02\%$, and extra-focal blur $B = 0.38$ mm. In summary, the proposed TSC prototype consists of a 12 mm thick CsI(Tl) scintillator coupled to a thermoelectrically cooled high end CCD camera system (2048 x 2048 pixel², 60 x 60 mm² target area) via a 120 mm $f/1.0$ lens with $m = 7.8$ (detector pixel width = 0.23 mm).

To appropriately characterize the proposed system, the linear cascaded systems model was used as described in section 3.3.5 to obtain theoretical DQE calculations using Equation 3-6. For the proposed prototype, the parameters for stages 1 – 5 remained unchanged from those for the current prototype. The optical coupling efficiency of the lens (g_6) was recalculated based on the newly designed lens configuration to be $\sim 0.02\%$. The MTF associated with the lens (T_7) is

expected to improve significantly as a result of the lower demagnification factor compared to the current prototype (by a factor of ~ 3). This essentially results in a linear spatial transformation in the corresponding spread function or LSF profile associated with the light spreading in the lens, wherein the spatial indices of the original LSF are uniformly reduced by a factor of 3. This was accounted for by rescaling the spatial frequency indices for T_7 (frequencies were magnified by a factor of 3), and the expected distribution of T_7 for the proposed prototype was obtained. It was also scaled by the MTF associated with the extra-focal blur ($B = 0.38$ mm) using Equation 3-12 to represent the MTF contribution from the focusing cone of the lens.

For the emission spectrum of CsI(Tl) that is peaked at 550 nm, the optical sensitivity (g_8) for the CCD camera target was found to be 0.83 based on vendor provided sensitivity spectra (Fairchild Imaging, Milpitas, CA). With negligible light spreading in the CCD target, the MTF associated with the camera system (T_9) was only limited by its finite pixel size and was obtained as a sinc function of the frequency scaled pixel size (projected on to the detector plane). Dark noise related NPS (S_{10}) was ignored for the camera system since dark noise was reported to be negligible (~ 0.01 e⁻ per pixel per second) based on vendor specifications, which was consistent with previously reported studies of CCD camera systems^{62,87}. Based on the cascaded systems analysis, the expected MTF and DQE spectra that were calculated for the proposed TSC prototype are shown in Figure 3-30 and 3-31 respectively. The MTF plots include component stage contributions for the lens and camera system for the current and proposed prototypes. As a result of the improved MTF of the lens due to lower magnification in the proposed prototype, and due to the superior MTF of the CCD target, the overall MTF for the proposed prototype was significantly greater than that for the current system. In Figure 3-31, the DQE calculated for the proposed prototype was comparable within its order of magnitude to the intrinsic upper limit of

the scintillator alone. The DQE(0) was 0.129 ± 0.1 for the scintillator alone, which reduced to 0.123 ± 0.1 when including the lens, and 0.115 ± 0.1 for the overall prototype. This indicated that the order of magnitude improvement in light coupling efficiency, as well as the improved camera detection and read-out characteristics of the CCD limited the effect of the quantum sink typically associated with the lens. As a result, the expected DQE for the proposed prototype was significantly superior to that for the current prototype, which was additionally verified by their QAD plots that are shown in Figure 3-32. The QAD plots clearly indicated the alleviated quantum sink for the lens of the proposed prototype as a result of higher light collection. Based on these theoretical calculations, the optimized prototype configuration can be expected to provide high QE, high DQE megavoltage imaging. While phantom imaging with the current TSC prototype indicated its potential for sub-MU imaging even in its unoptimized configuration, the DQE calculations indicate that the proposed prototype can provide significantly greater image quality compared to the current test prototype for high frame-rate fluoroscopic imaging and sub-MU treatment verification.

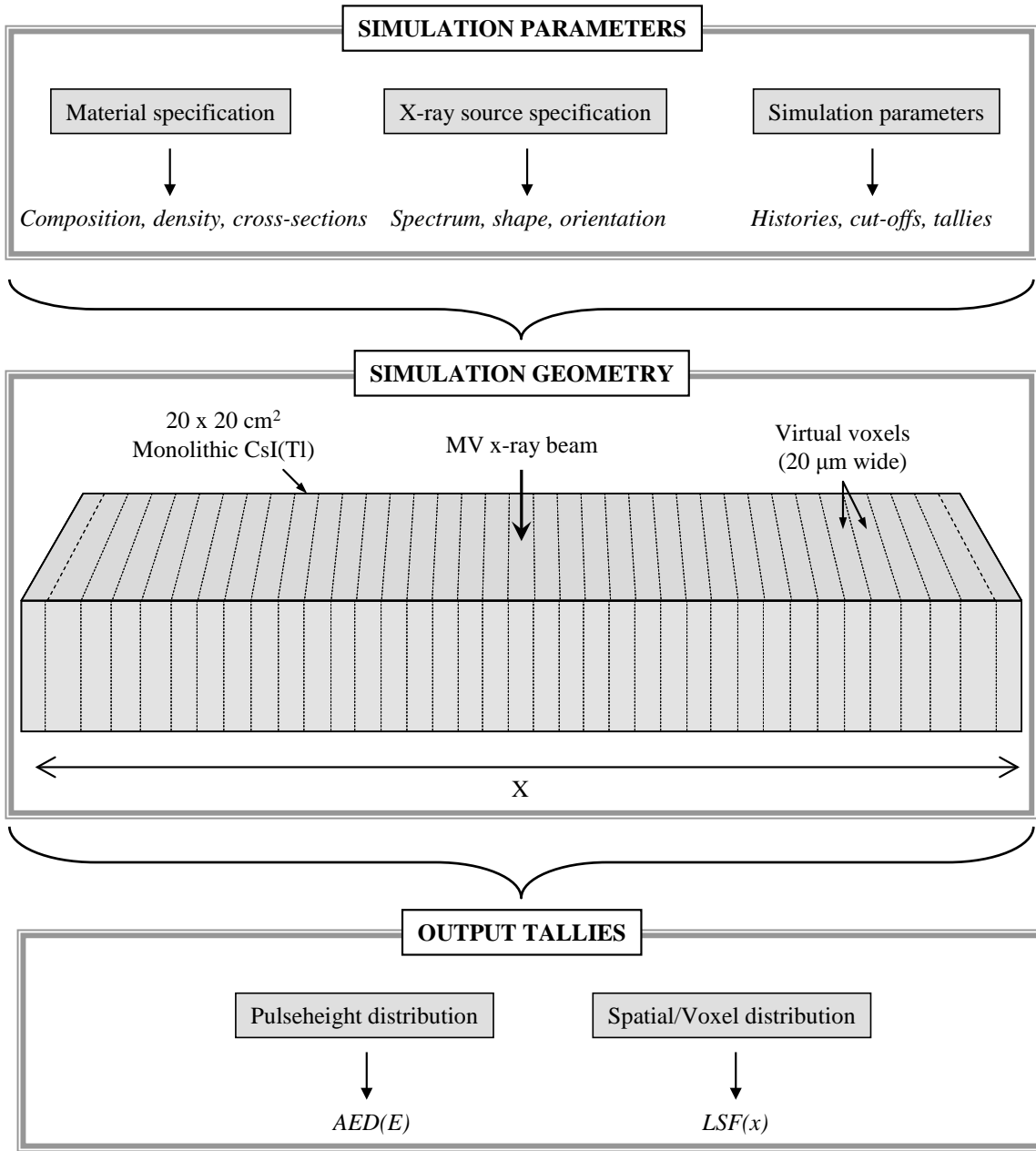


Figure 3-1. Monte Carlo simulation set-up to characterize the CsI(Tl) scintillator for the TSC.

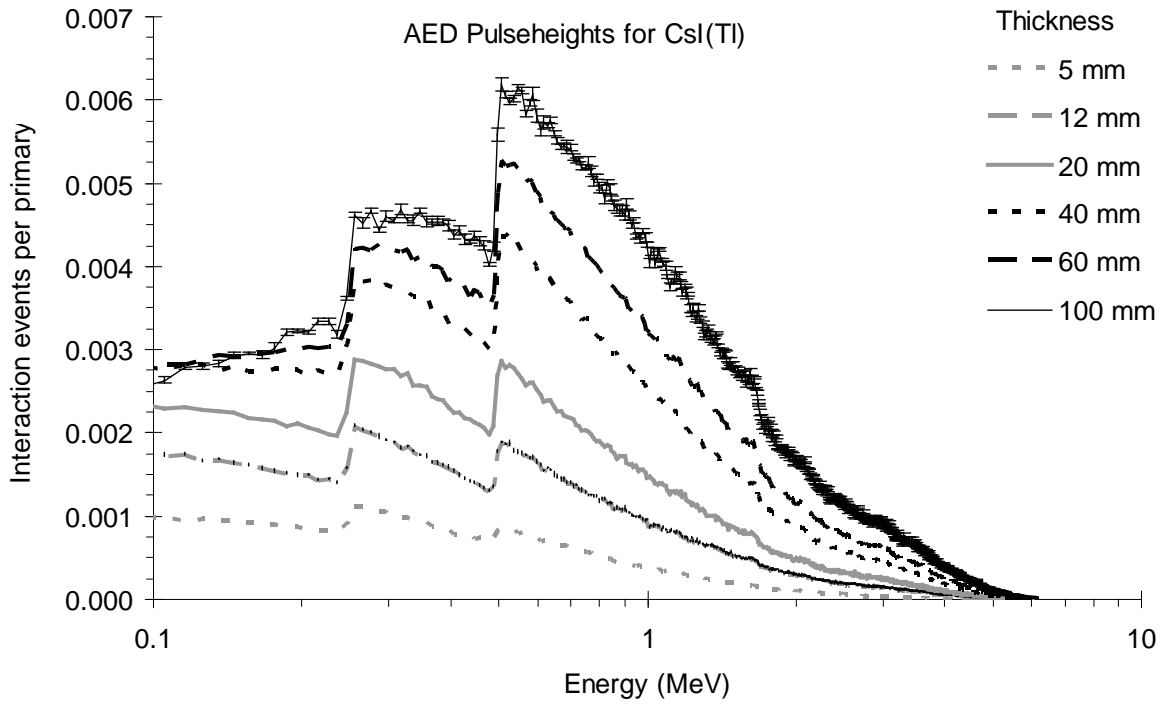


Figure 3-2. Simulation tallies indicating AED pulseheight spectra for CsI(Tl).

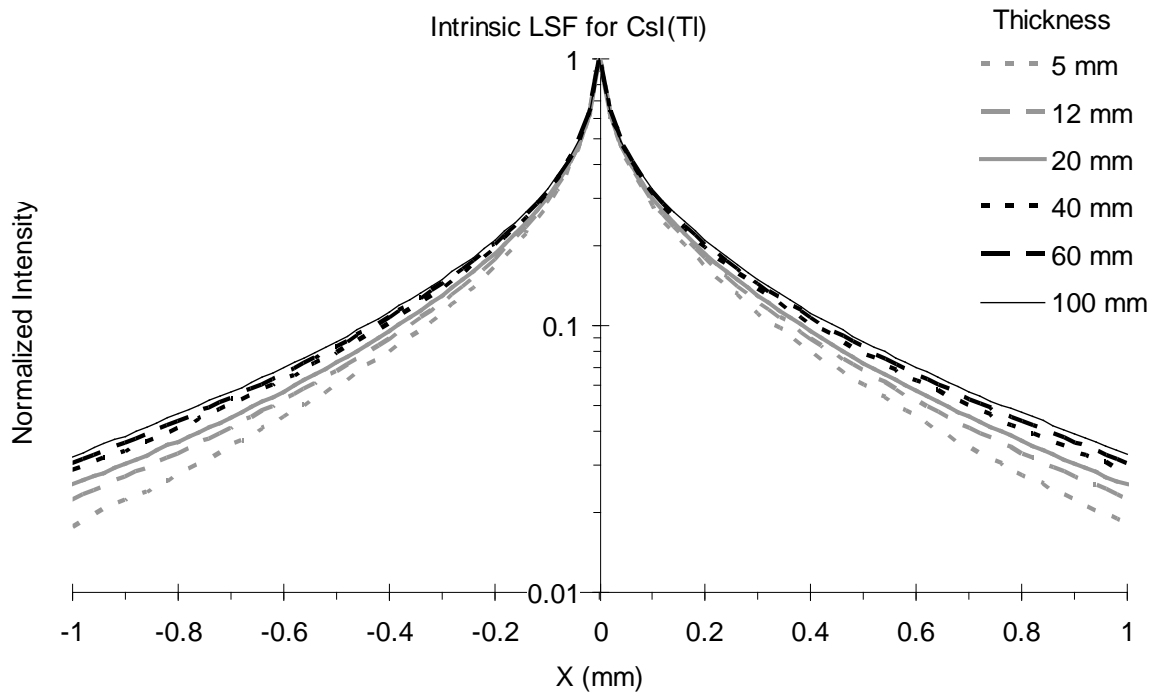


Figure 3-3. Simulation tallies indicating LSF profiles for CsI(Tl).

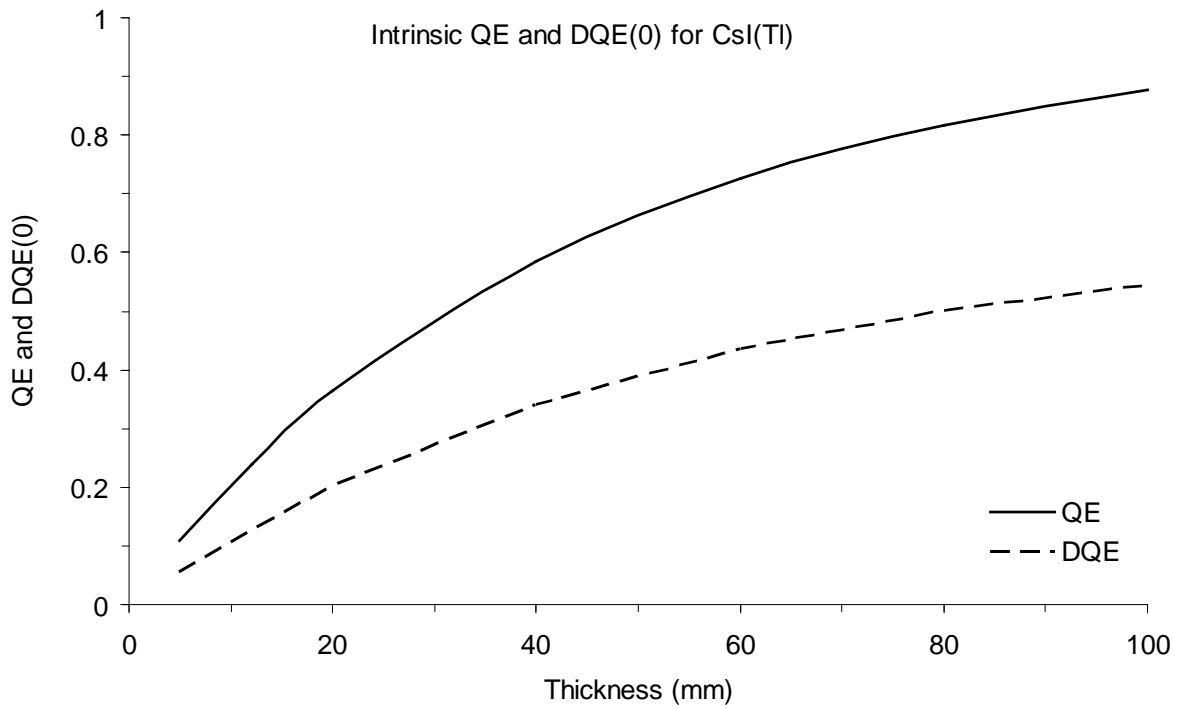


Figure 3-4. Influence of scintillator thickness on intrinsic QE and DQE(0) for CsI(Tl).

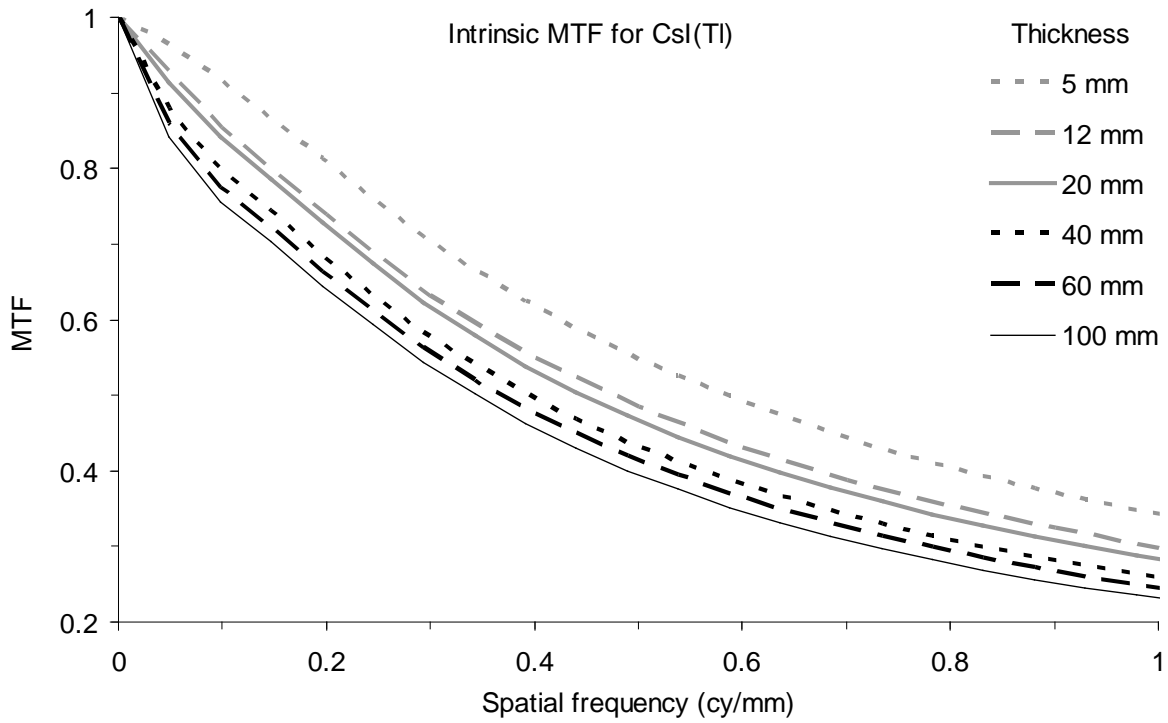


Figure 3-5. Influence of scintillator thickness on intrinsic MTF for CsI(Tl).

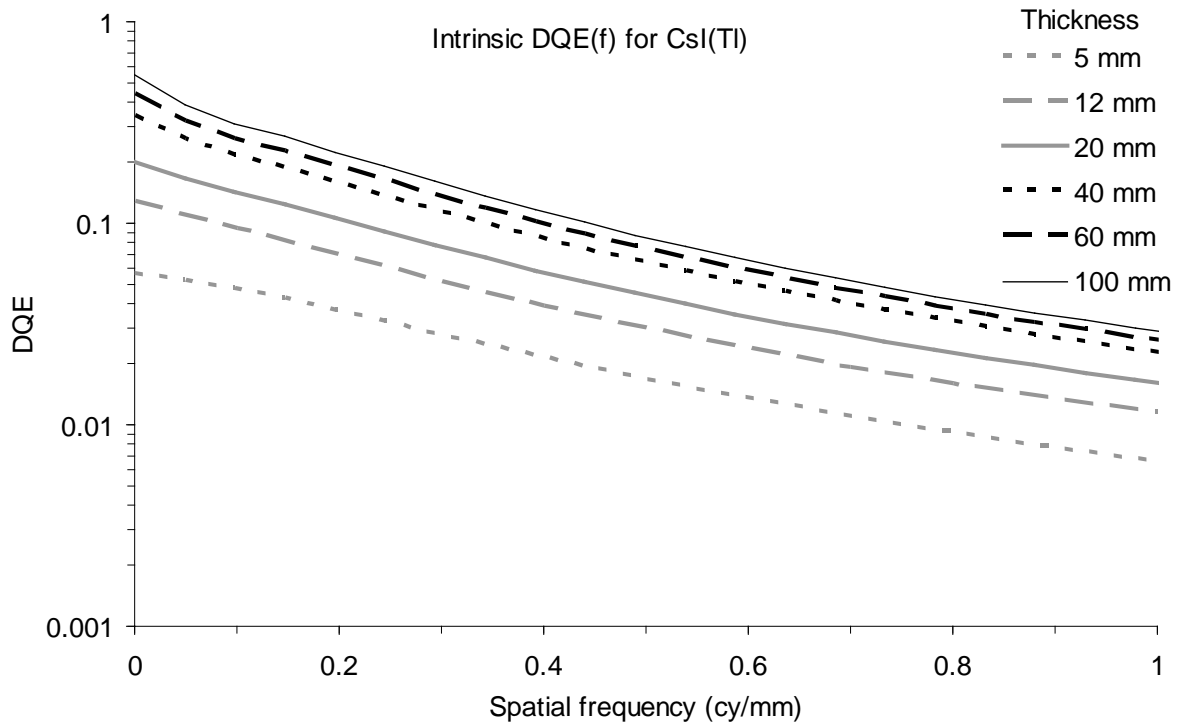


Figure 3-6. Influence of scintillator thickness on intrinsic DQE(f) for CsI(Tl).

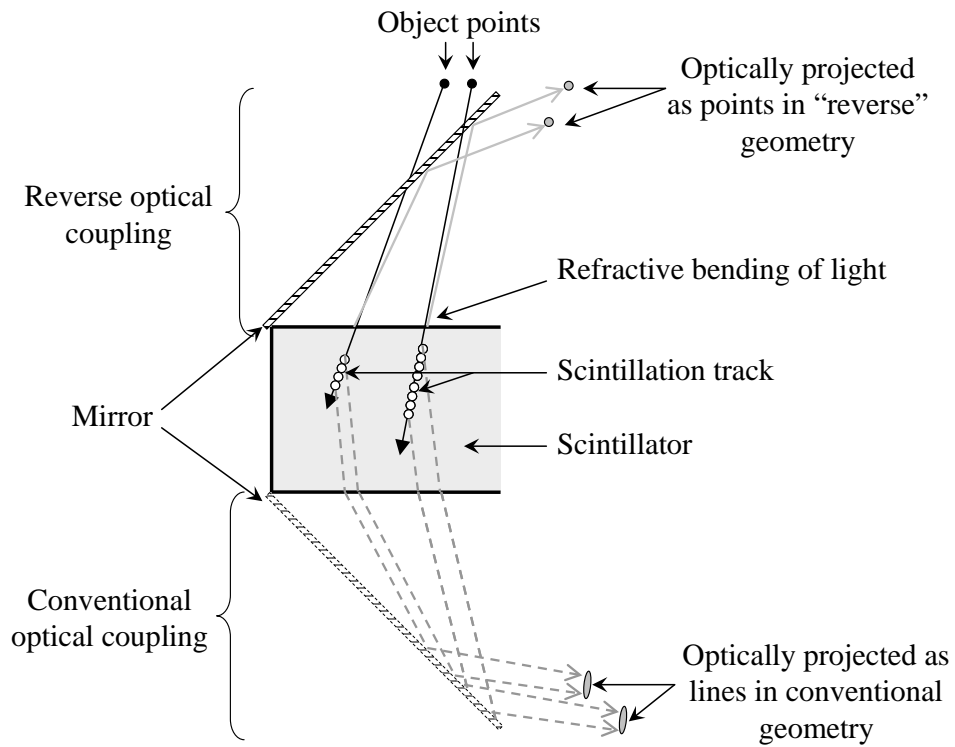


Figure 3-7. Refractive and geometric optical blurring in thick and clear scintillators.

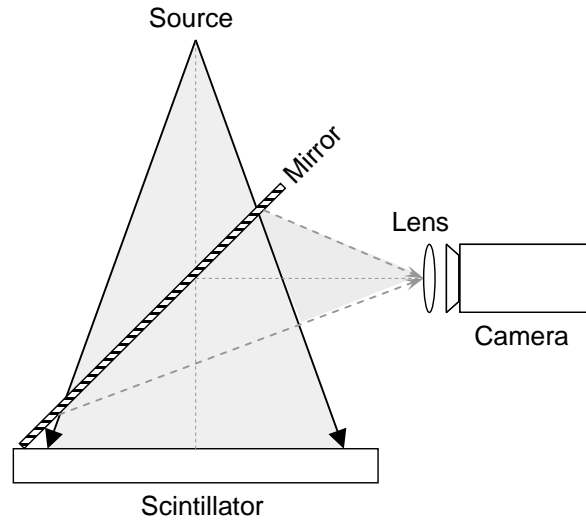


Figure 3-8. Reverse coupling geometry for the TSC video EPID system.

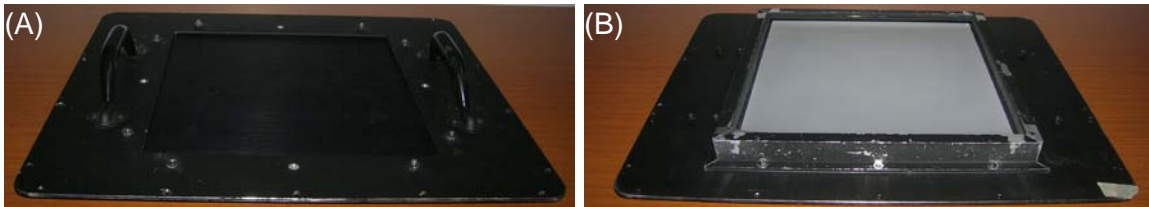


Figure 3-9. The 12 mm thick CsI(Tl) scintillating screen used for the TSC test prototype system. (A) Top surface of scintillator (with mounting plate) that faces the incident x-rays, (B) Bottom surface of the scintillator that faces the mirror.

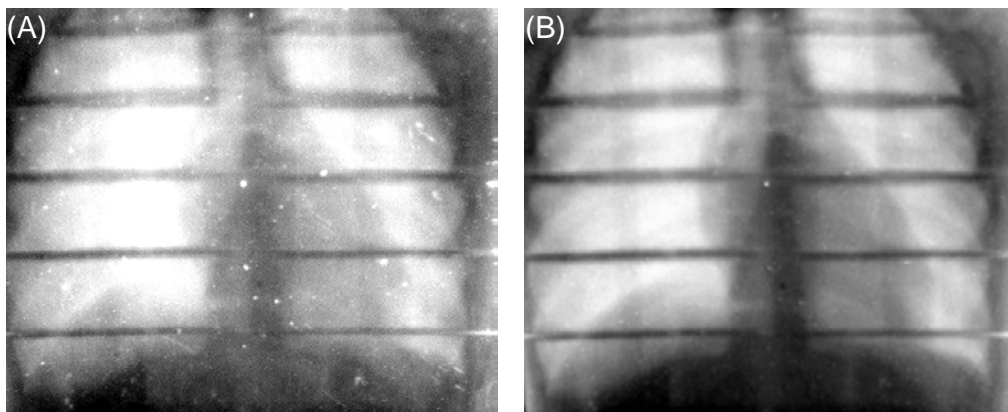


Figure 3-10. Removal of artifacts due to crystal imperfections in the image of a pediatric chest phantom by simple flat-field correction. (A) Raw image with specular artifacts due to imperfections, (B) Flat-fielded image with most artifacts removed.

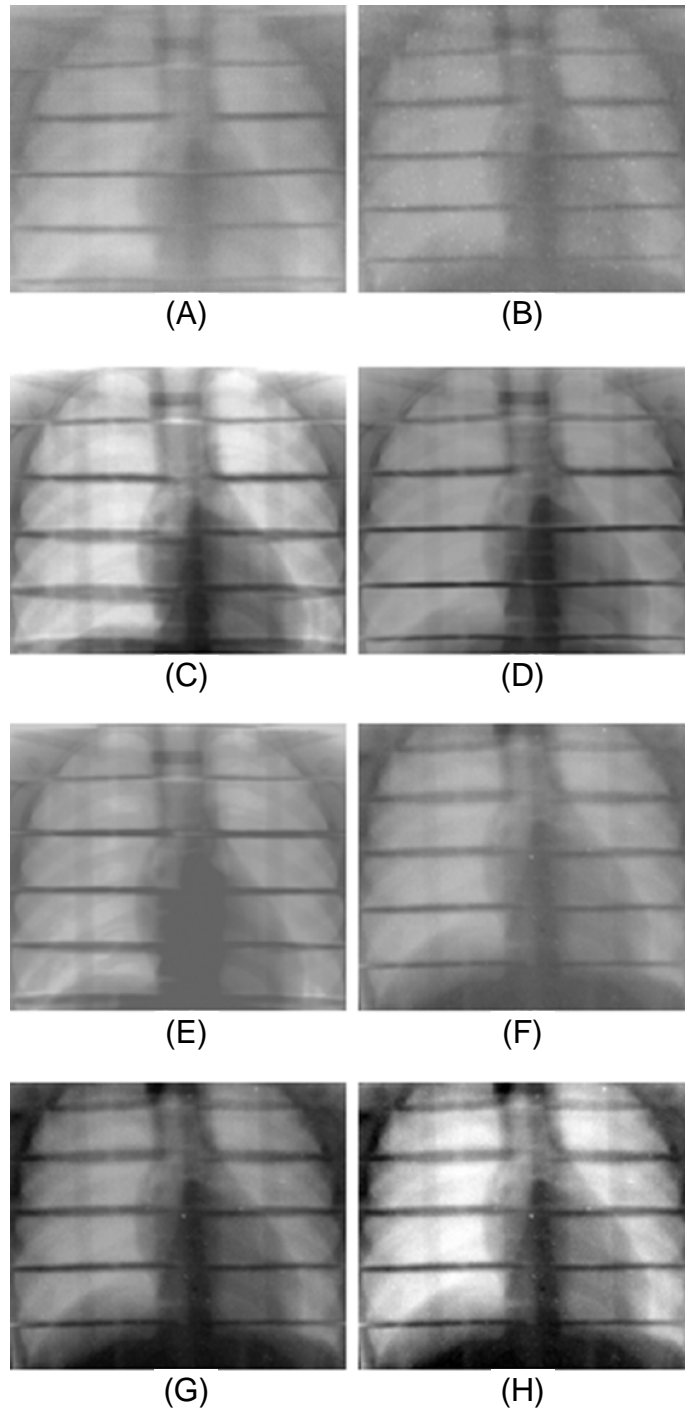


Figure 3-11. Images of a pediatric chest phantom. (A) Siemens BEAMVIEW (5 MU), (B) Elekta iView (5 MU), (C) Elekta iViewGT (5 MU), (D) Agfa Cronex 10T conventional film (10 MU), (E) Kodak EC-L film (5 MU), and TSC at (F) 0.2 MU, (G) 1 MU, and (H) 5 MU.

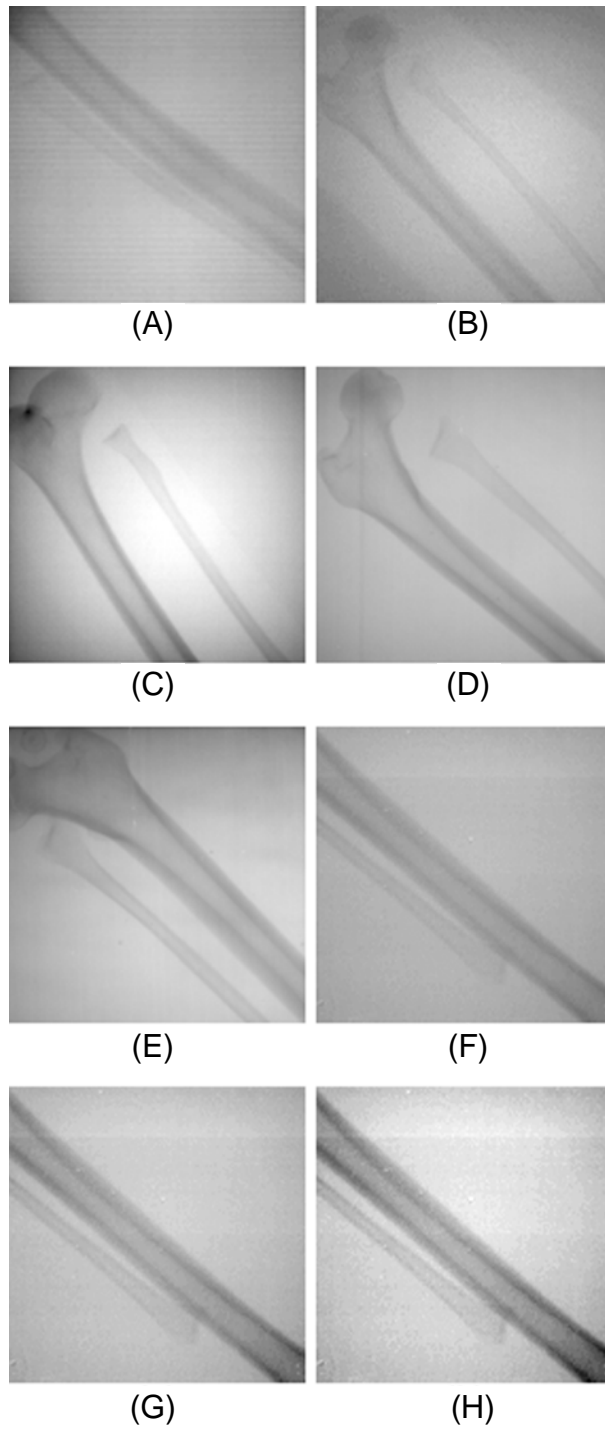


Figure 3-12. Images of a femur and humerus bone phantoms in water. (A) Siemens BEAMVIEW (5 MU), (B) Elekta iView (5 MU), (C) Elekta iViewGT (5 MU), (D) Agfa Cronex 10T conventional film (10 MU), (E) Kodak EC-L film (5 MU), and TSC at (F) 0.2 MU, (G) 1 MU, and (H) 5 MU.

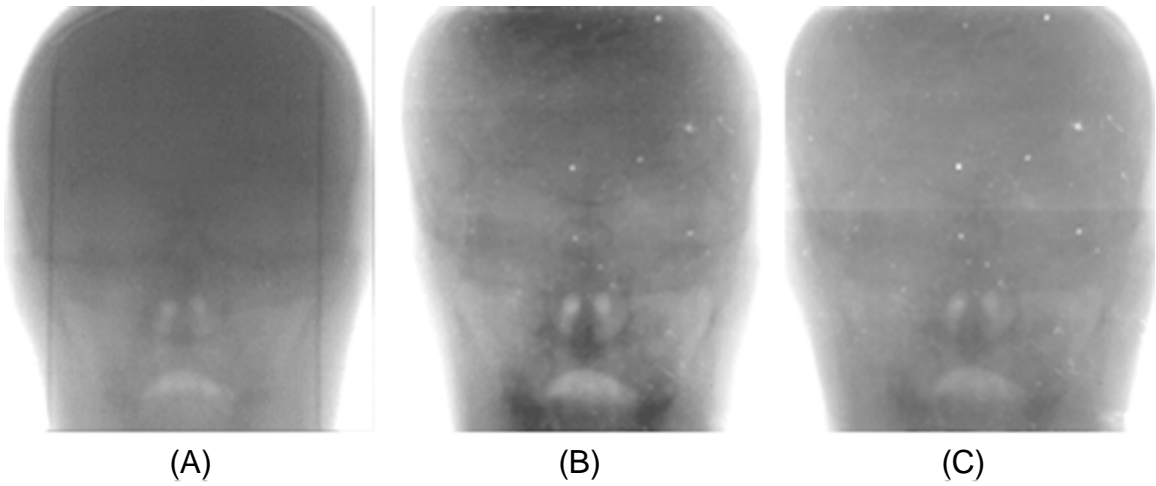


Figure 3-13. Images of an adult head phantom. (A) Siemens Beamview (5 MU), (B) TSC (~ 0.03 MU), and (C) TSC (0.2 MU).



Figure 3-14. Image of an angulated slit acquired for MTF measurements for the TSC prototype.

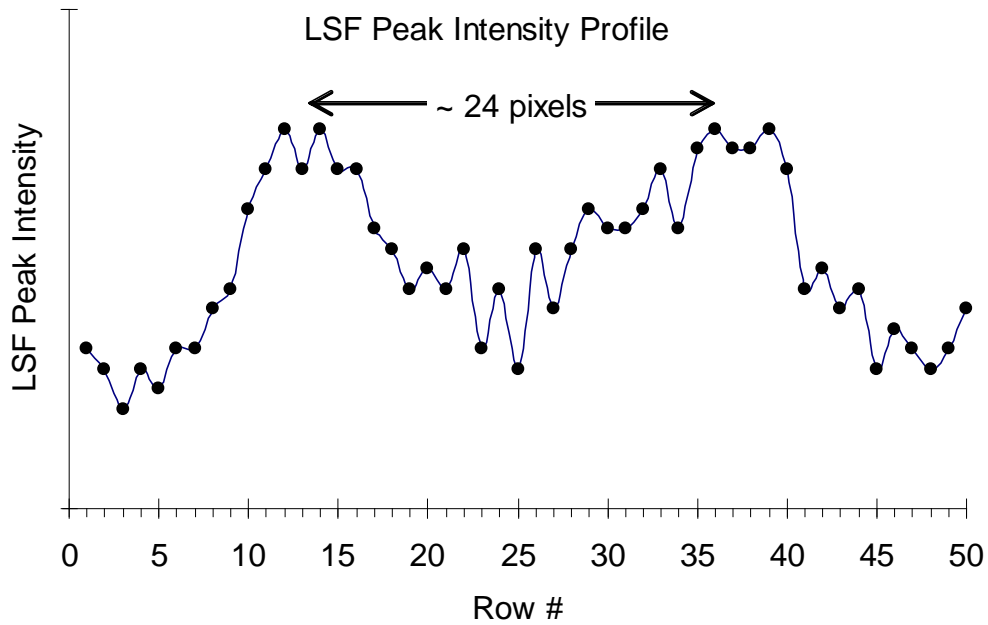


Figure 3-15. Profile of slit response peak intensities over successive rows to determine slit angle.

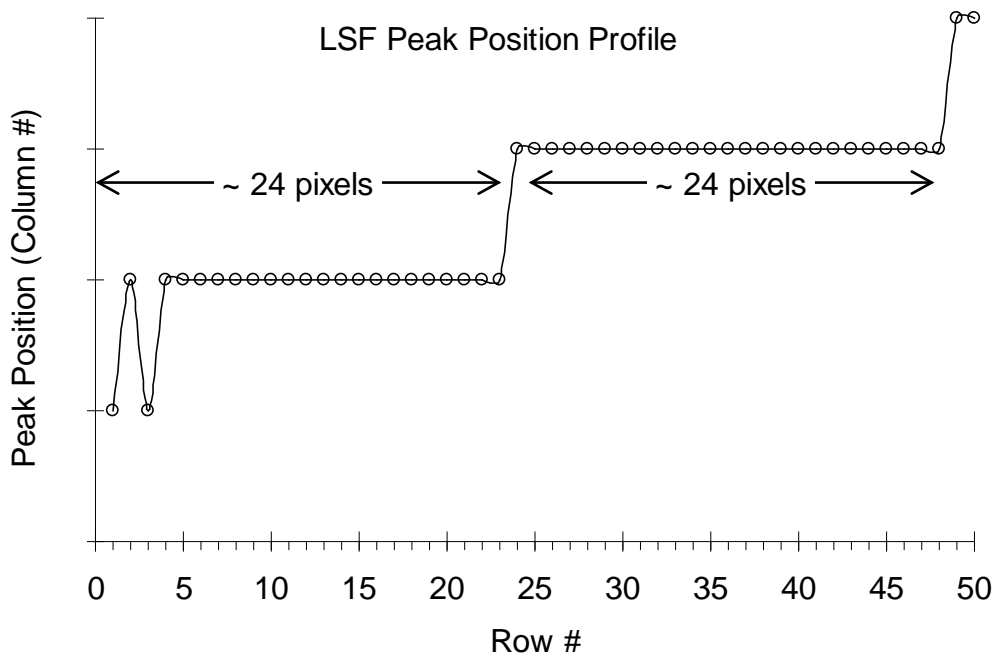


Figure 3-16. Profile of slit response peak positions over successive rows to determine slit angle.

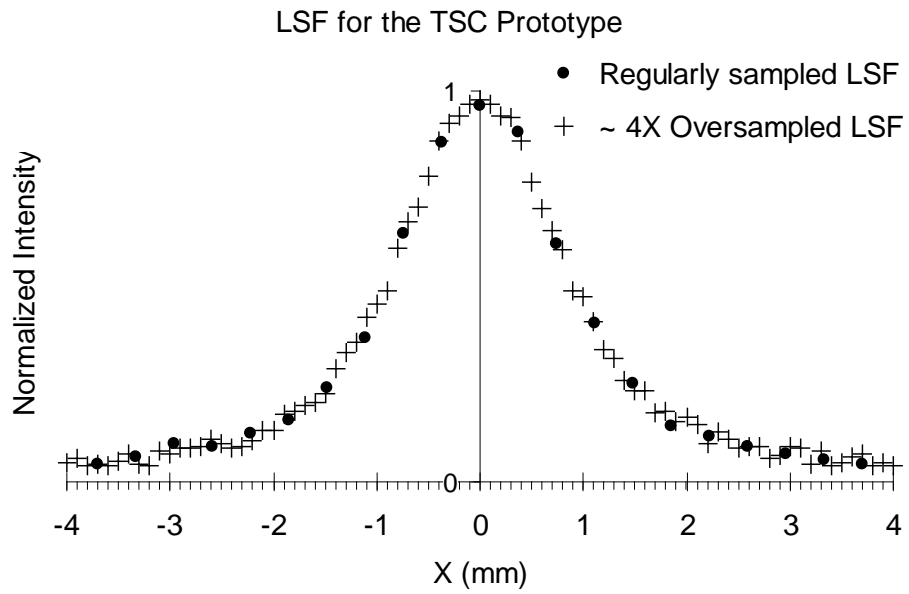


Figure 3-17. LSF profile of the TSC prototype measured using the angulated slit technique.

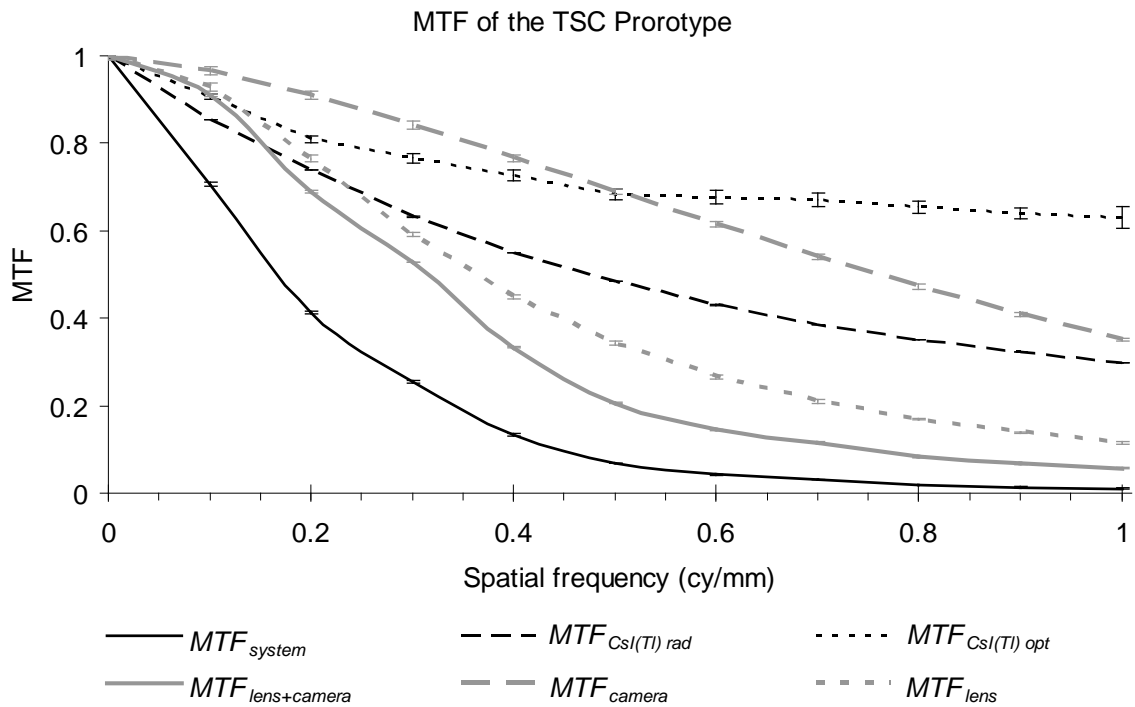


Figure 3-18. Overall system and component MTF contributions for the TSC prototype.

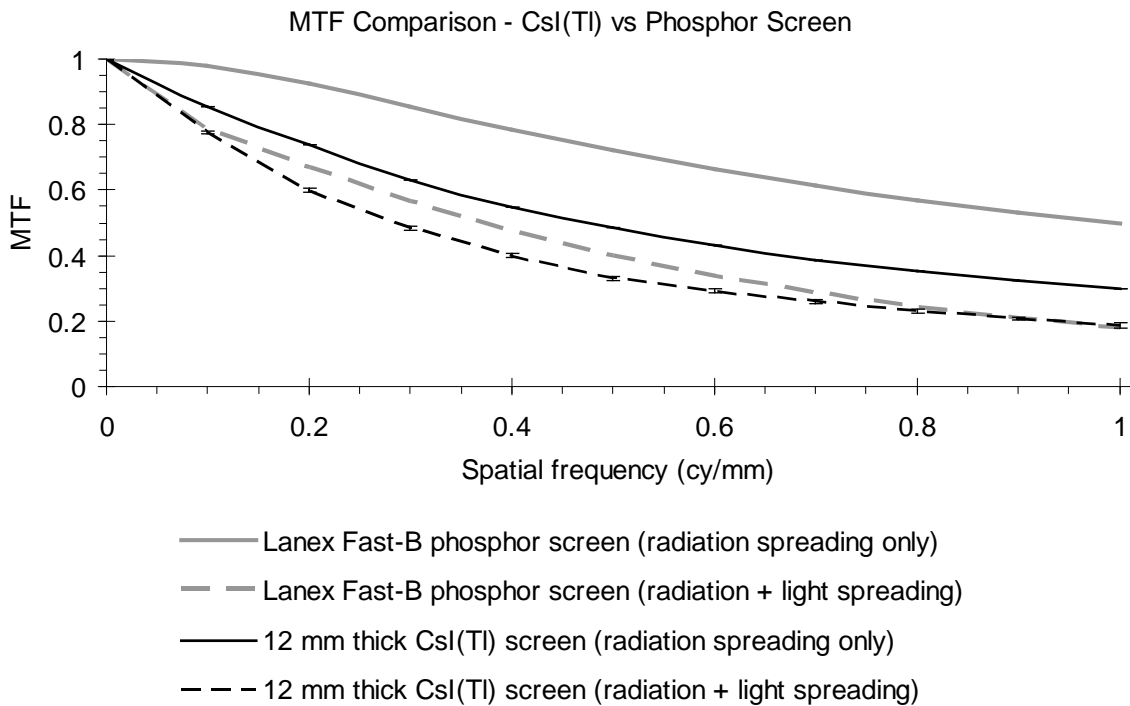


Figure 3-19. Comparison of MTF spectra for the CsI(Tl) and phosphor screen scintillators.

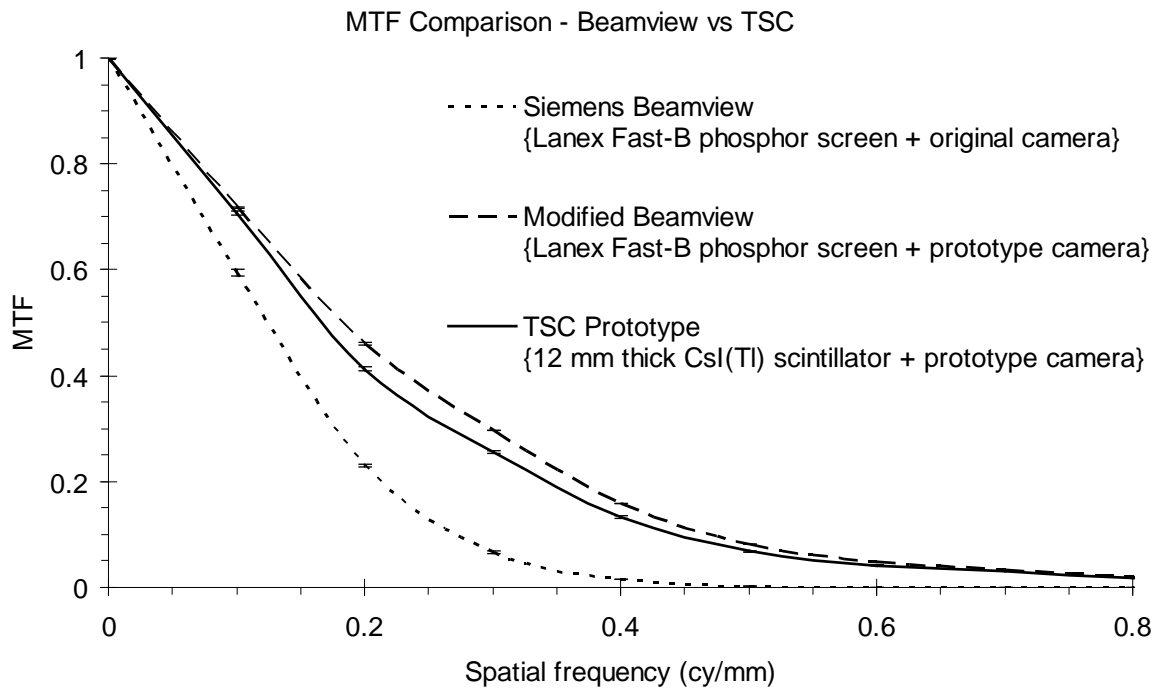


Figure 3-20. Comparison of MTF spectra for the Siemens Beamview and TSC prototype systems.

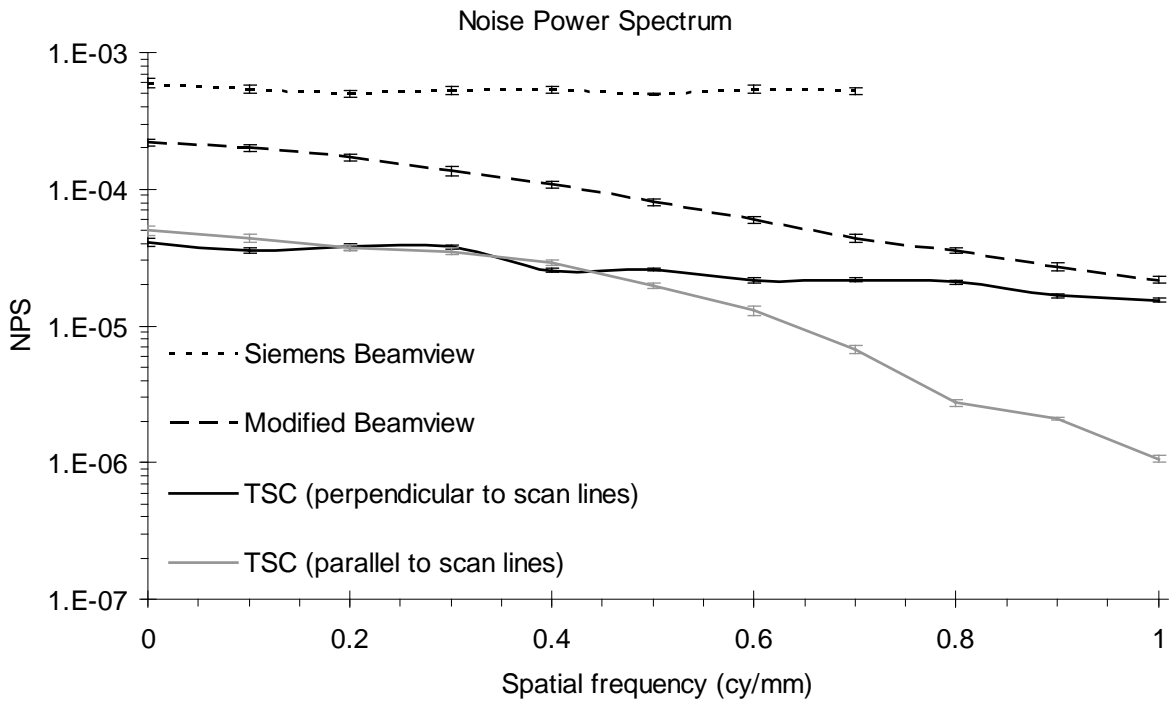


Figure 3-21. Comparison of NPS spectra for the Siemens Beamview and TSC prototype systems.

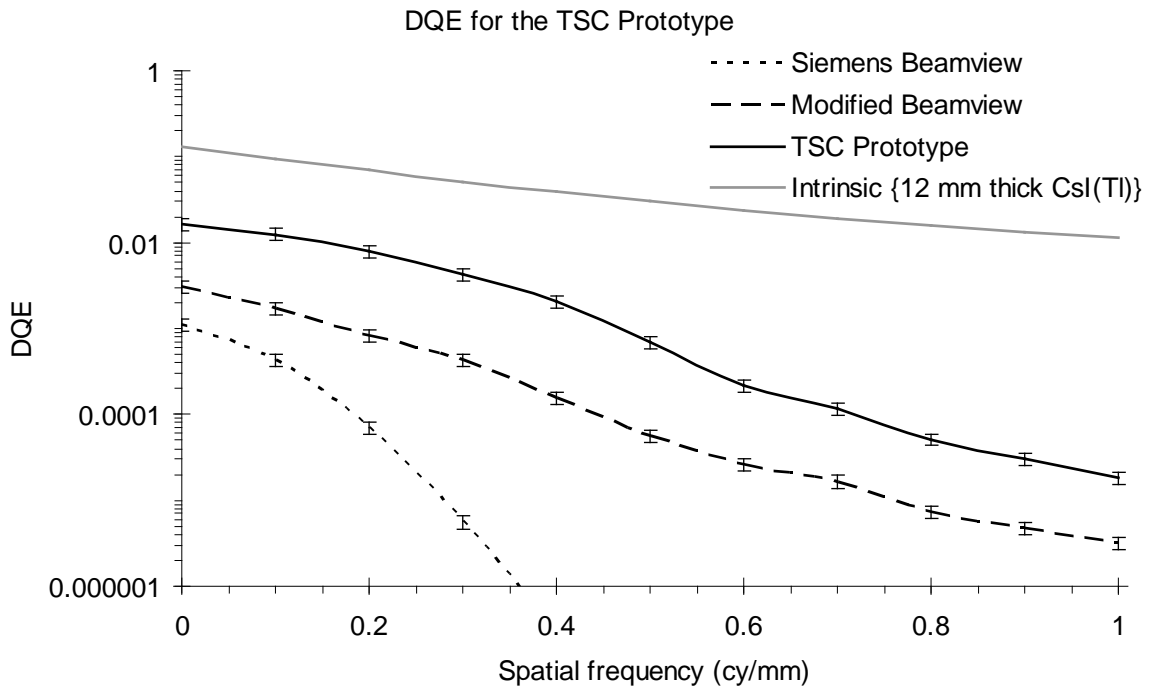


Figure 3-22. Comparison of DQE spectra for the Siemens Beamview and TSC prototype systems.

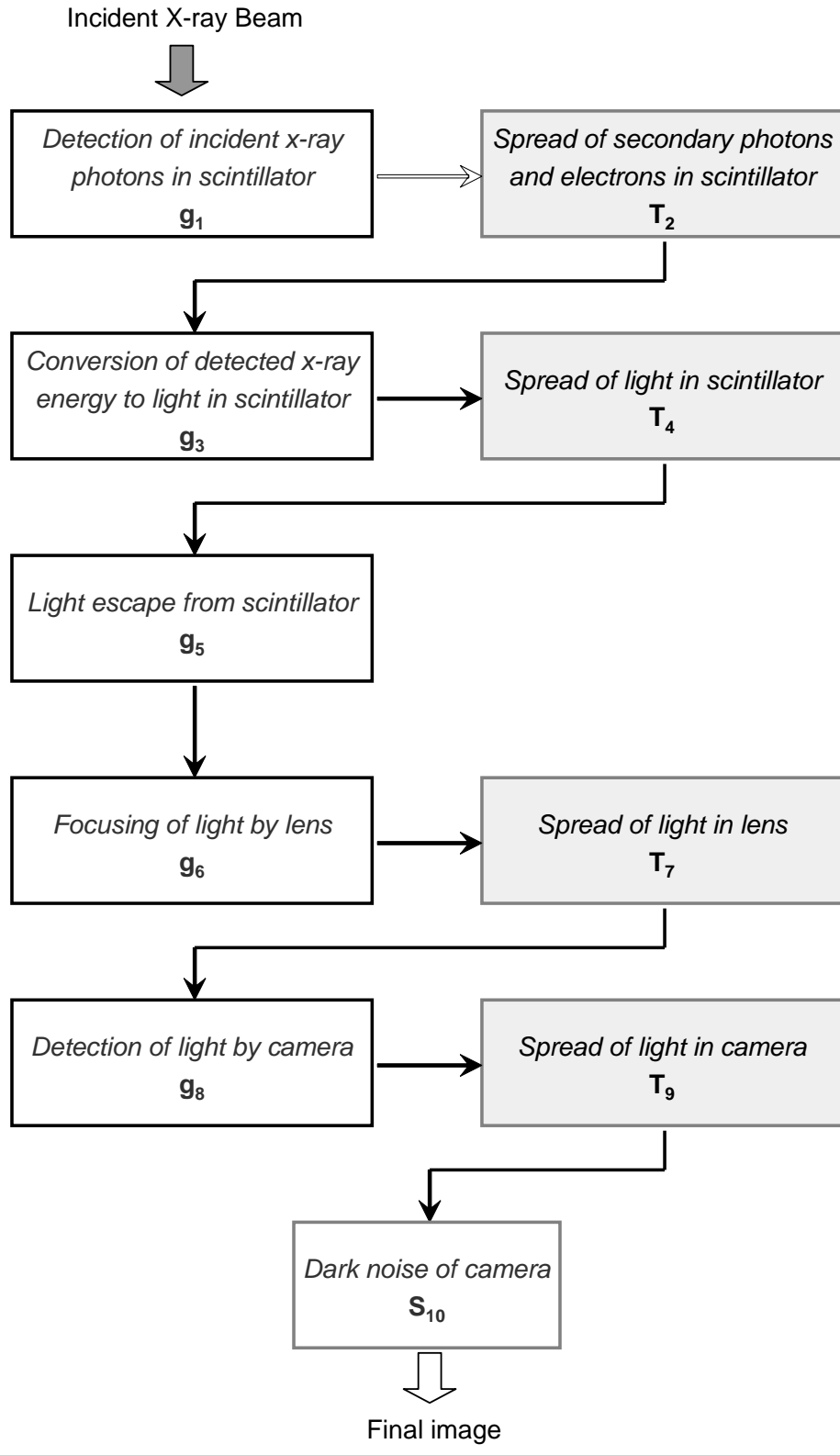


Figure 3-23. Linear cascaded systems model for the TSC system.

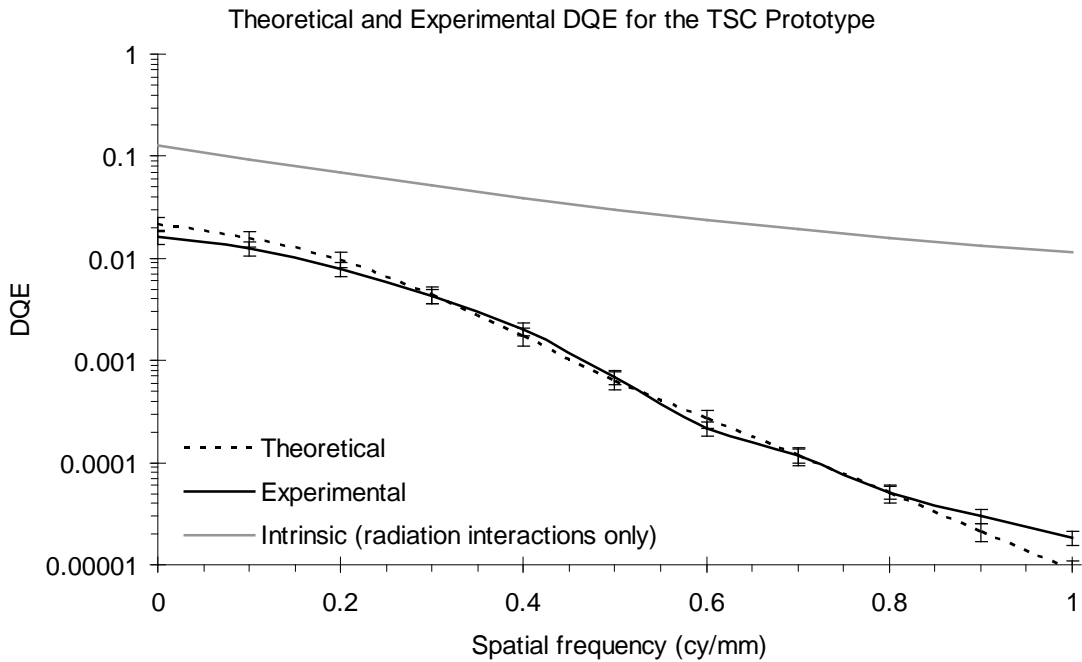


Figure 3-24. Comparison of the theoretical DQE of the TSC prototype from a linear cascaded systems model with its measured DQE.

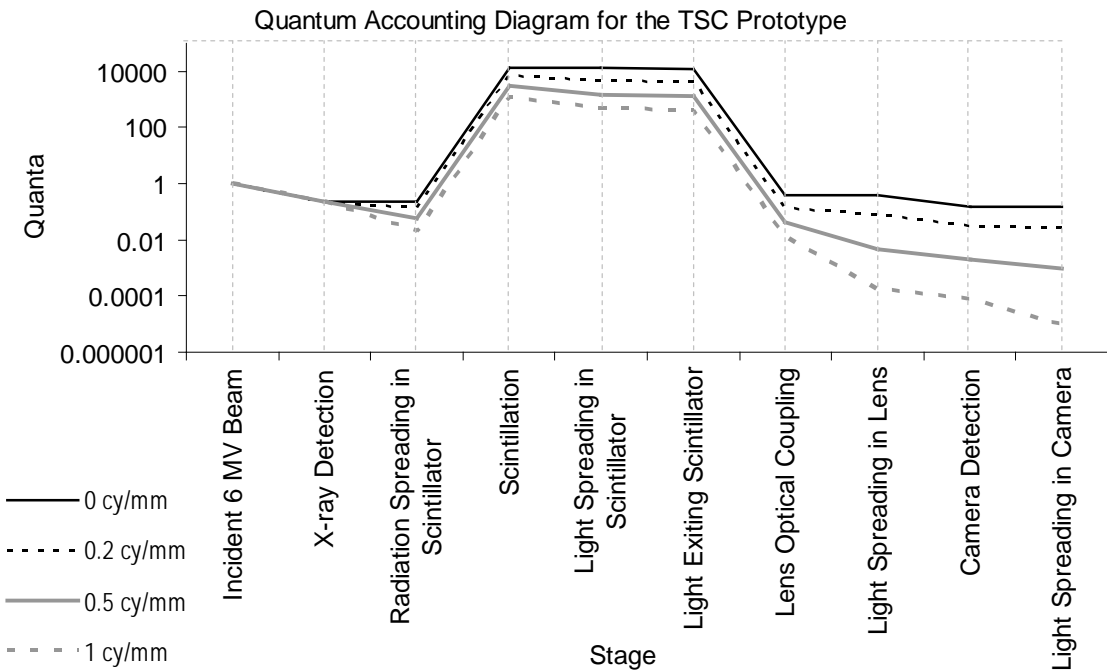


Figure 3-25. Quantum accounting diagram for the TSC prototype indicating quantum levels per stage for selected spatial frequencies.

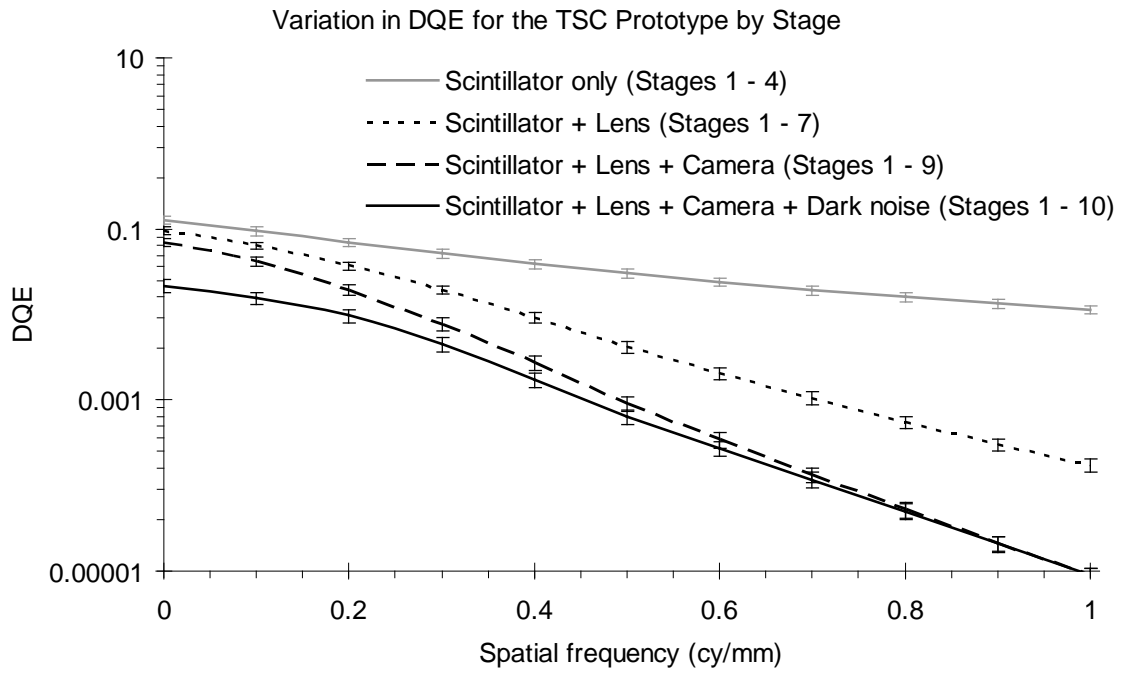


Figure 3-26. Stage – wise theoretical DQE calculations for the TSC prototype indicating its serial variation over stages.

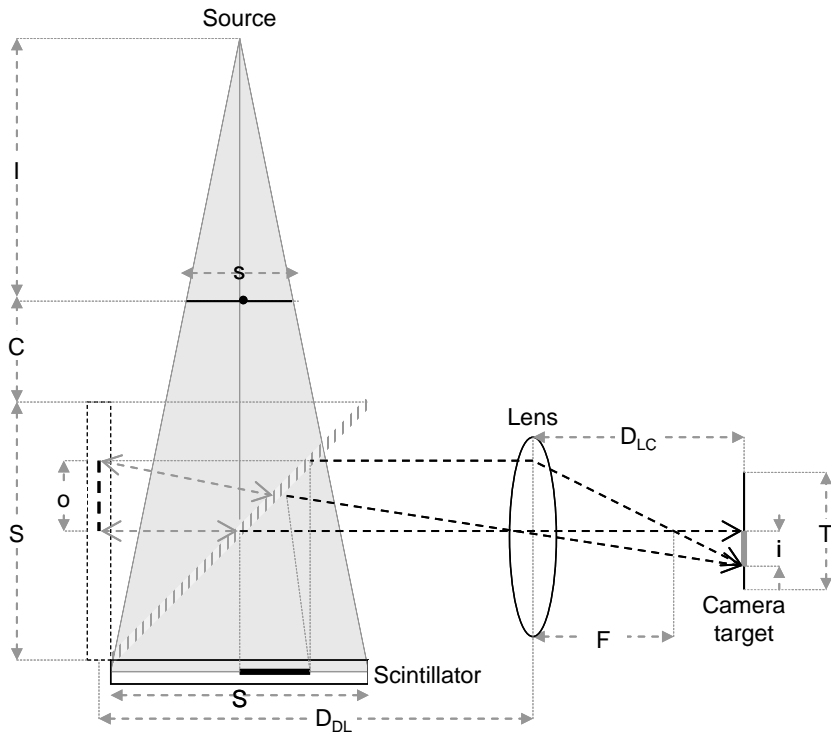


Figure 3-27. Schematic layout of the proposed TSC prototype.

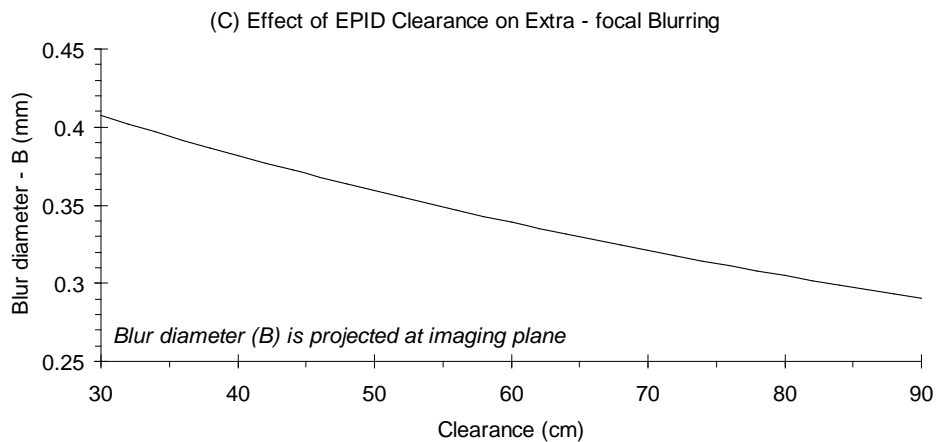
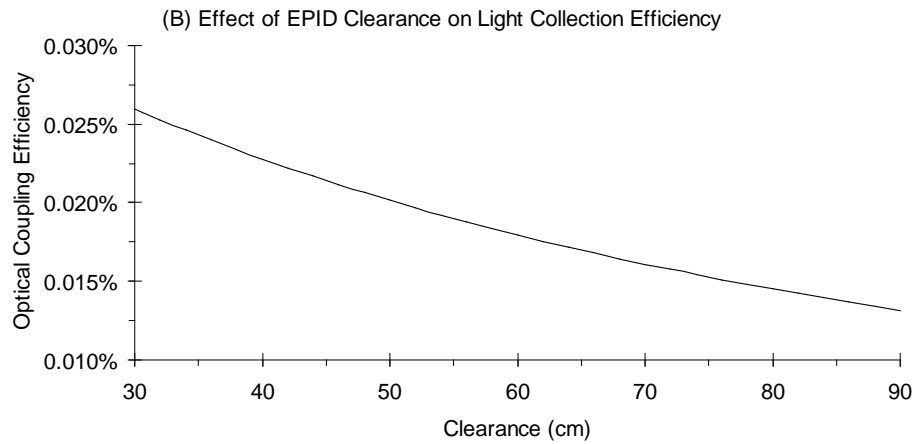
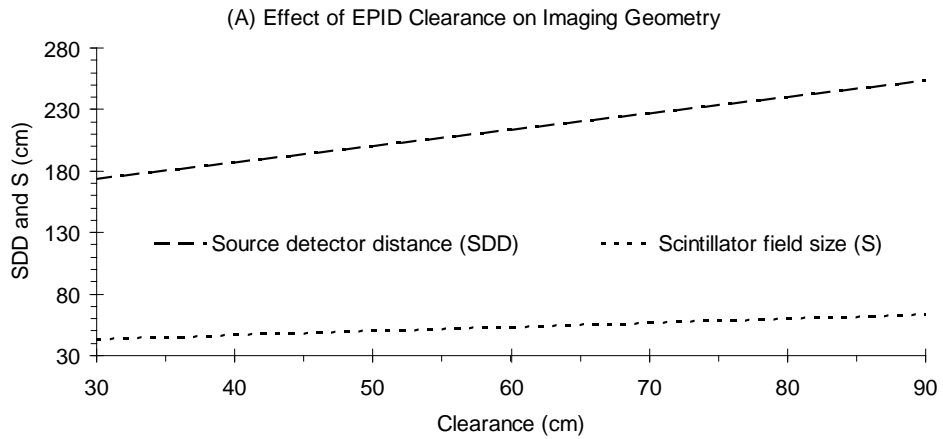


Figure 3-28. Effect of EPID clearance on the imaging and optical design parameters for the TSC. (A) Effect on detector position (*SDD*) and detector size (*S*). (B) Effect light collection efficiency, (C) Effect on extra focal blurring.

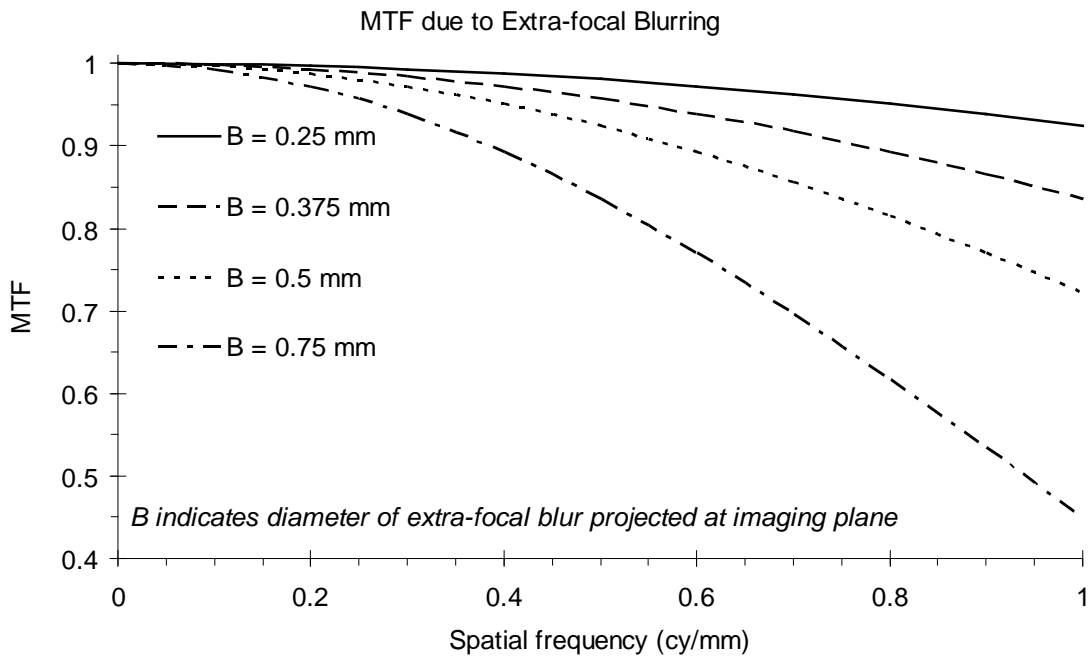


Figure 3-29. The MTF contribution due to extra-focal blurring as a function of blur diameter.

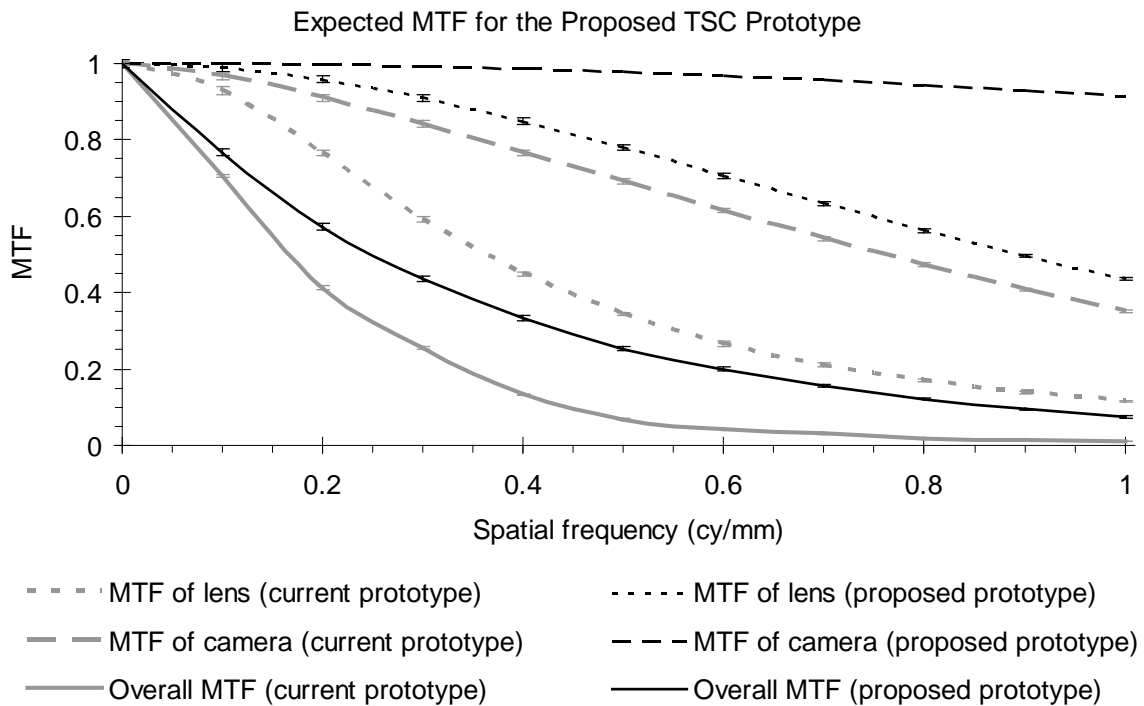


Figure 3-30. The expected MTF of the proposed TSC prototype.

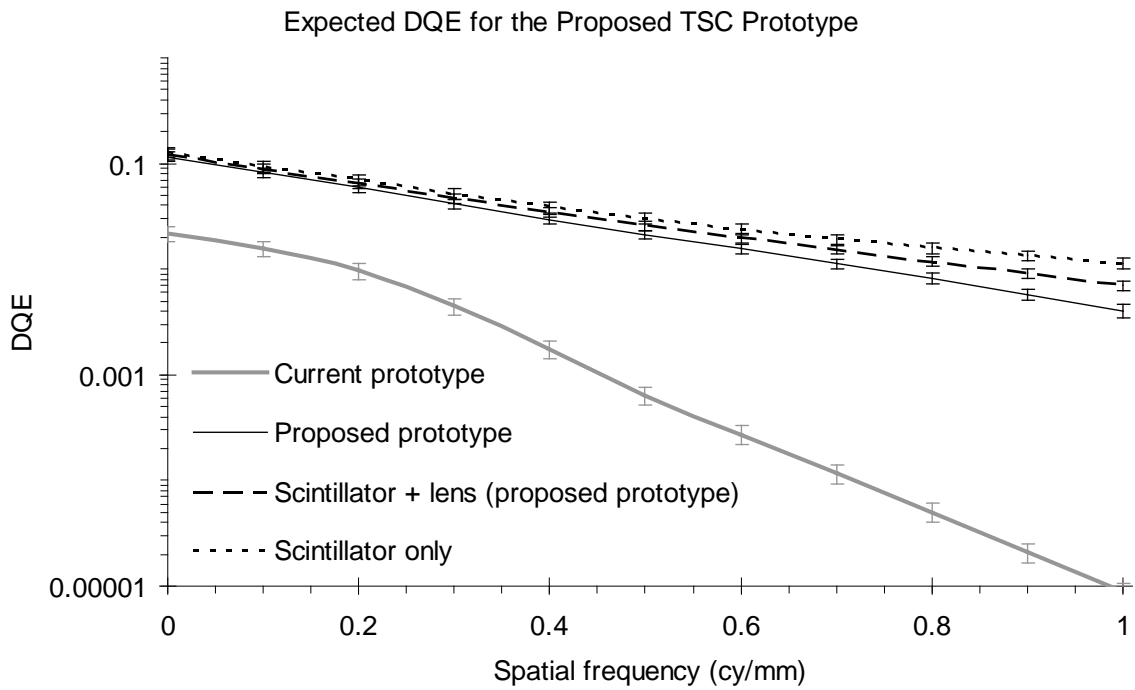


Figure 3-31. The expected DQE of the proposed TSC prototype.

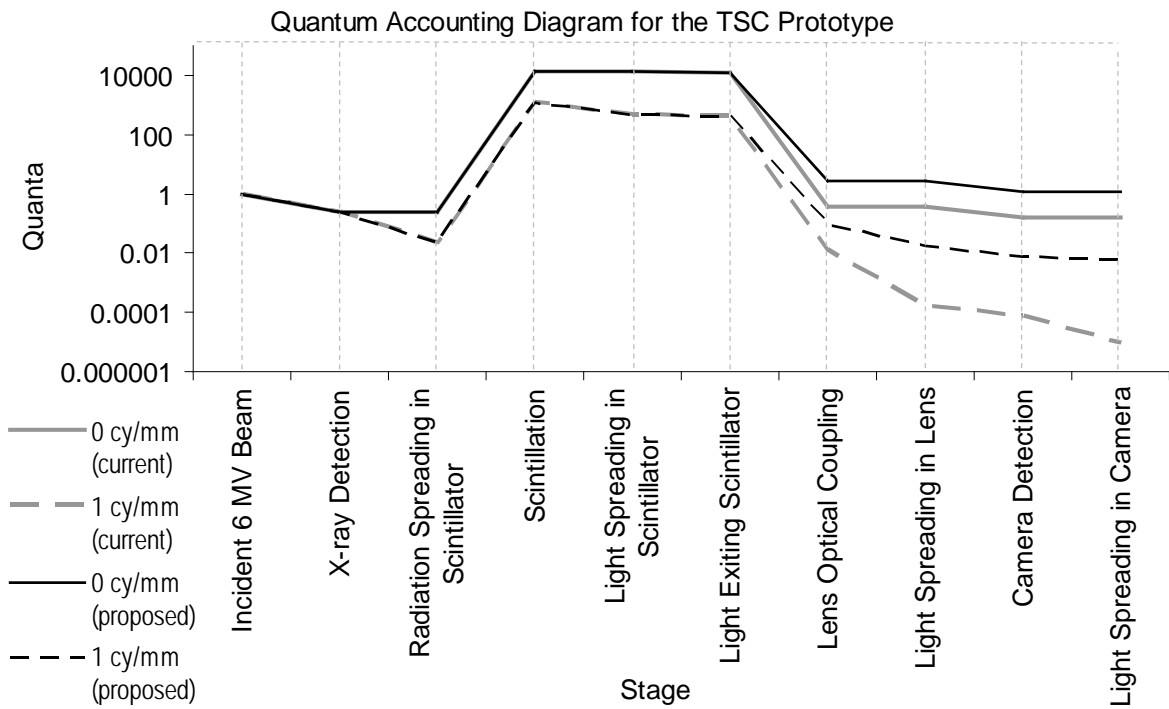


Figure 3-32. Quantum accounting diagram for the proposed TSC prototype.

CHAPTER 4

PROTOTYPE 2 – FIBER-OPTIC SCINTILLATION GLASS ARRAY (FOSGA)

The second prototype EPID system investigated in this research was based on a thick and structured matrix of terbium doped scintillation glass fibers in conjunction with an a-Si flat-panel array. The fibers are housed in a structured grid constructed out of a dense high-Z medium based on a polymer – tungsten composite alloy (or poly-W). The entire detector matrix is collectively referred to as a fiber-optic scintillation glass array (FOSGA). In this chapter, preliminary studies on the radiographic properties of a FOSGA detector and its dependence on two key geometric specifications (detector thickness, and pixel fill factor) are presented. Radiation and optical transport simulations were used in conjunction with a linear cascaded systems analysis to predict the overall imaging performance for a FOSGA based EPID system. In this work, only the study and optimization of the detector geometry was considered. The a-Si flat-panel array to be used for optical read-out was not actively studied since commercial panels of proven quality were readily available, and significant research was not necessary to optimize them separately.

4.1 Background

Unlike the TSC system described in Chapter 3 that utilizes a monolithic CsI(Tl) scintillator, the FOSGA detector is a heterogeneous and highly structured imaging array whose specific design offers several advantages for imaging. The scintillation glass serves as the primary x-ray detection medium that produces light in response to incident x-rays, and it is specifically drawn into fiber-optic conduits to serve as an efficient light coupler for the underlying a-Si photodiodes. Due to its high optical clarity, scintillation glass allows the use of relatively long fiber arrays to obtain thick detector configurations for greater x-ray absorption and subsequently enhanced QE. The high-Z poly-W grid houses the fibers and prevents the passage of light between adjacent fibers. However, its significant advantage is that it limits the

spread of secondary photons and electrons between adjacent fibers, which significantly alleviates the inevitable loss in spatial resolution with detector thickness. In addition, x-rays interact with the high-Z septal material to release high energy secondary electrons into the scintillation glass fibers, which results in an increase in the overall imaging response. This phenomenon will be referred to hereafter in this dissertation as septal build-up, and is similar to the effect of a metal build-up plate that is typically overlaid on film or phosphor screen detectors to promote x-ray sensitivity. However, the unique nature of septal build-up due to the poly-W grid results in more complicated effects that will be discussed later in this chapter.

One of the prominent advantages of the FOSGA detector is the absence of any significant quantum sink as optical read-out is accomplished with an a-Si flat-panel array with significantly greater light collection efficiency compared to lens coupled video EPID systems¹⁷. As a result, any increase in QE with thicker detector arrays directly leads to high DQE, which is an inherent advantage specific to clear and structured scintillators coupled to flat-panel read-out. The use of thick and structured arrays of clear scintillators with flat-panel systems has recently been investigated actively for megavoltage imaging⁸⁹⁻⁹⁴, and initial studies have provided encouraging results [DQE(0) > 20%]^{93,94}. These initial results were used to set specific target goals for the expected imaging performance of a prototype FOSGA EPID system as: DQE(0) > 25%, and MTF(1 cy/mm) > 10%. The overall goal of this research was to propose a prototype imaging configuration for the FOSGA detector that will provide high DQE megavoltage imaging for use in MV-CBCT.

4.2 Detector Concept

The FOSGA imaging concept utilizes scintillation glass fibers that act as luminescent detectors as well as light conduits for enhanced light output. Each scintillation glass element is a fiber-optic channel containing a central “core” glass of high refractive index and an outer “clad”

glass of lower refractive index in a co-axial geometry as shown in Figure 4-1. The core glass forms the bulk of each fiber (~ 80% of fiber cross-section) and provides the active scintillating medium for each discrete pixel. It is composed of high density (3.85 gm/cm^3 , effective $Z \sim 31$) silicate glass predominantly doped with terbium, and has a refractive index of 1.58. The clad glass is composed of borosilicate glass with a density of 2.36 gm/cm^3 and refractive index of 1.48. Following a scintillation event, light rays are emitted in all directions and by virtue of fiber-optic channeling, a significant fraction of rays that would otherwise be lost at the scintillator boundary are retrieved into the scintillator column by total internal reflection. This is facilitated by the difference in refractive indices of the core and clad glass regions. The light exiting the fibers is directly coupled to a-Si photodiodes that are placed in close contact with the fibers to prevent light leakage across pixels and glare. As shown in Figure 4-1, the scintillation glass fibers are inserted into a matched poly-W grid housing with one-to-one hole matching. The apertures of the grid are angulated such that the housed fibers are always focused towards the x-ray source. This prevents any loss of spatial resolution due to geometric beam divergence that would have been significant with thick detector geometries.

4.3 Manufacturing and Assembly

The FOSGA detector consists of three main structural components: the scintillation glass fibers, poly-W tungsten grid housing, and the a-Si photodiode read-out panel.

4.3.1 Scintillation Glass Fibers

The physical geometry, material composition, and radiographic characteristics of scintillation glass for the FOSGA detector were based on commercially available glass fibers provided by an established vendor (Collimated Holes Inc., Campbell, CA). The fibers are drawn using proprietary technology, wherein large arrays of high density terbium doped glass fibers of the desired length and composition are accurately and consistently produced. Glass fibers can be

drawn with diameters in the order of microns either separately or as fused bundles, although only independent fibers of sub-mm diameter have been considered for the FOSGA detector. The glass fibers are reasonably robust and resistant to mechanical damage as they are malleable and can be bent to some degree. Selected pictures of the scintillation glass fibers are presented in Figure 4-2. The extrusion wheels of the fiber drawing apparatus are shown in Figure 4-2 (A). A highly magnified cross sectional view of the fiber is shown in Figure 4-2 (B), which clearly shows the core and clad glass regions in a sample glass fiber of 0.43 mm diameter (0.39 mm core diameter). Samples of the glass fibers of different lengths are shown in Figures 4-2 (B) and (C). The fibers are shone with illumination at one end, and the high intensity of transmitted light at the exit end of the fibers can be clearly visualized.

4.3.2 Grid Housing

The poly-W grid housing will be fabricated using a patented manufacturing process that is referred to as tomolithographic molding (TLM), wherein complex 3-D structures like focused grids can be created using specially engineered cast material. As depicted in Figure 4-3 (A), the desired 3-D target model is initially created via stack-lamination of a series of cross-sectional masks that are micromachined with lithographic techniques to obtain a master mold. Subsequent molds can then be recurrently tooled from the master mold to yield accurate and precise 3-D structures as specified with the master mold. A sample cast mold for a structured grid to be used for scatter rejection in a separate imaging application is shown in Figure 4-3 (B). For the FOSGA detector, TLM is used to construct a thick and focused grid housing out of the poly-W composite alloy, which is a cast material specifically engineered for TLM using a proprietary mixture of powdered tungsten and polymer paste. With TLM, thick and focused grid housing modules of high accuracy and repeatability can be tooled with high precision ($\pm 12 \mu\text{m}$ for cutting and $\pm 27 \mu\text{m}$ for stack-lamination). It must be noted that the TLM methodology (as well

as its included material components and workflow) were developed separately by a commercial vendor (Mikro Systems Inc., Charlottesville, VA), and not as part of this dissertation.

4.3.3 Photodiode Panel

The grid housing containing the scintillation fibers will be coupled to a-Si read-out panels supplied by Hytec Inc (Los Alamos, NM). These commercial panels are currently being used with volumetric CT imagers for radiographic non-destructive testing. The center-to-center spacing of the TFT elements in these read-out panels is 0.385 mm, which is comparable to that used in current commercial MV detectors (0.4 mm). The pitch of the grid housing and the diameter of the glass fiber will be adjusted to match this pixel spacing. Over the last decade, a-Si read-out panels have been used with great success for x-ray imaging¹⁷. Several studies have led to a consensus over the excellent signal read-out properties of these panels^{50-56,58,59}. Conventional a-Si flat-panels have been shown to provide negligible glare with closely coupled scintillators⁵⁷, low dark noise contamination even at low exposures (equivalent to sub-cGy dose in MV imaging)⁵⁸, and remarkable resistance to radiation hardening⁵⁹. With very little electronic cross-talk between adjacent pixels, spatial resolution is affected only by the pixelization of the optical signal that is integrated over the entire sampling area of each photodiode⁵⁸. For this study, it was assumed that the intended a-Si flat-panel will conform to all the above mentioned norms for modern photodiode read-out arrays.

4.3.4 Pixel Loading

With full field detector arrays ($\sim 40 \times 40 \text{ cm}^2$) of sub-mm resolution, one requires up to a million pixels per detector. Therefore, the appropriate insertion of each pixel or grid aperture with scintillation fibers cleanly, completely, and without mechanical damage inside the grid housing in its focused alignment is a significant cost-benefit feature. Possible solutions for automated pixel loading that ensure against mechanical misalignments and damages to the fibers

or housing are currently being investigated. Some preliminary studies were conducted as collaborative work by Mikro Systems Inc. (Charlottesville, VA) and the Los Alamos National Laboratory (LANL, Los Alamos, NM) in testing an automated fiber insertion tool. Herein, glass fibers and the poly-W grid housing were loaded with static charges of opposing polarities and held together in a vacuum gradient. As illustrated in Figure 4-4 (A), the fibers are propelled into the grid housing using the electrostatic and vacuum gradients, while misalignments and incompletely inserted fibers are corrected by mechanical vibration. This prototype loading tool is shown in Figure 4-4 (B) with one quadrant of a sample detector array inserted with fibers. Initial tests with a small field array and 2 cm long fibers yielded close to up to 50% successful pixel loading, and greater success rates (~ 100%) are expected with an optimization of the loading tool in terms of its functional parameters (vacuum and electrostatic gradients, vibration strengths and frequency, etc). Another possible solution to achieve automated pixel loading involves an integration of the detector assembly with the fiber drawing process at Collimated Holes Inc. (Campbell, CA), wherein the drawn glass can be acquired from specifically oriented cooling trays by a motorized robotic arm and inserted into an appropriately cradled poly-W grid.

4.4 Radiation Transport Calculations

The MCNPX 2.5 Monte Carlo simulation codes were used to model the spatial and energy distribution characteristics of radiation interactions within the prototype scintillation glass fibers to study intrinsic x-ray detection characteristics of a FOSGA detector. In this case, AED and LSF profiles were tallied to determine the intrinsic QE, DQE, and MTF of the FOSGA detector along the same lines as the characterization of the CsI(Tl) scintillator described in Chapter 3. The essential workflow for using MCNPX was similar to that described for ITS 3.0 in Figure 3-1. The primary purpose of the radiation transport calculations was to characterize the

effect of detector geometry on intrinsic imaging performance, and to identify theoretical upper limits of MTF and DQE for a given prototype configuration.

4.4.1 MCNPX Simulation Model

The detector geometry was coded into the simulation program using the built-in key word command structure that was similar to that used in ITS 3.0. The specific key words (“LAT” and “FILL”) in MCNPX that are associated with coding spatial repetitions of geometric structures as lattice points were used to specify the entire scintillator array efficiently with only a few lines of code. Following the geometric specification of one complete pixel, a lattice grid corresponding to pixel centers in the imaging plane was defined and populated with pixels, which provided the detector array as shown in Figure 4-5. The imager was specified as a 512 x 512 array of pixels representing discrete sampling voxels. Each pixel consisted of an outer wall of poly-W to represent the grid housing, and the scintillation glass fiber with the core and clad glass regions included. In the actual detector array, each voxel is focused towards the x-ray source. However, in our simulations, geometric focusing was not explicitly specified, but instead approximated by a parallel array of detector voxels in combination with a parallel x-ray source. The poly-W wall material was specified as low density tungsten (12 gm/cm^3), and the core and clad glass regions were defined as indicated by proprietary composition specifications provided to us by the vendors (Collimated Holes Inc., Campbell, CA). The sampling width of the modeled array was selected to be 0.385 mm to match the photodiode spacing of the commercial a-Si read-out panel (Hytec Inc., Los Alamos, NM) to be utilized in our proposed prototype system.

Two key geometric specification parameters that influence detector performance were studied: detector thickness and pixel fill factor. The detector thickness indicated the length of the scintillation glass fibers used for imaging, while the pixel fill factor specified the fraction of the total cross-sectional pixel area that was occupied by the glass fiber based on the fiber diameter

(as indicated in Figure 4-6). Both of these parameters were directly related to the efficiency of detecting incident x-rays as well as the loss in spatial resolution due to the spread of secondary photons and electrons. A range of detector thicknesses (i.e. glass fiber length) of 1 – 10 cm was investigated in these studies. Pixel fill factors of 50, 60, and 70% were tested (the maximum possible fill factor with cylindrical fibers in square pixels is ~ 78.5%), which represented fiber diameters of 0.307, 0.336, and 0.364 mm respectively (including clad glass). In the current study, only cylindrical fibers are being considered. However, scintillation glass can also be drawn into square cross-sections and may be considered in the future.

The megavoltage beam was modeled as a line source of 6 MV x-rays¹⁶⁵ positioned at the detector surface and aligned parallel to the y-axis. The x-ray emission was selected to be monodirectional and perpendicular to the imaging plane. Energy absorption events were recorded for each detector voxel within the core glass region only. The spatial distribution of energy absorption events in the detector was tallied to obtain an LSF profile for the detector array. In addition, the energy distribution of the recorded absorption events (i.e. AED), was tallied in 600 discrete energy bins (0.01 MeV bin width) to quantify the uncertainty in x-ray detection and in the number of subsequently generated light quanta. Energy cut-offs for termination of particle histories were selected to be 10 keV and 521 keV for photons and electrons respectively. Each simulation was performed with 5×10^7 histories, which provided < 1% uncertainty over the useful range of all tallies.

4.4.2 Intrinsic QE and DQE(0)

The AED tallies obtained for the FOSGA detector are shown in Figure 4-7 for selected variations in detector thickness (1, 3, 6, and 10 cm) for all three fill factors (50, 60, and 70%). To account for the fact that a central point source exaggerates the incident x-ray fluence to any detector with < 100% fill factor, the recorded AED tallies were scaled by the fill factor to

represent a practical wide area incident fluence. The pulseheight distributions were used to calculate the intrinsic QE and DQE(0) for all thickness and fill factor combinations using previously described methods (Equations 2-13 and 2-14). The calculated values of QE and DQE(0) are shown in Figures 4-8 (A) and (B) respectively. As expected, both QE and DQE(0) were found to increase with detector thickness due to the increase in interaction pathlengths with longer glass fibers. They were also observed to linearly decrease with fill factor due to smaller active detection areas.

Based on previously specified targets for expected performance standards for FOSGA, it was noted that a detector thickness in the range of 4 – 8 cm was required to achieve $DQE(0) > 20\%$ depending on the fill factor (higher thickness was required with lower fill factors). It can also be seen from Figure 4-8 (B) that at higher thicknesses, the effect of fill factor on DQE(0) was more dominant than that of detector thickness, which can be attributed to the exponential and linear growth characteristics of DQE(0) as a function of thickness. Therefore, greater fill factors are desirable as they could significantly reduce the detector thickness required to achieve $DQE(0) > 20\%$. It was noted that at a fill factor of 70%, a 6 cm thick detector provided an intrinsic $DQE(0) \sim 26\%$. This satisfied the target specifications for the detector, and also allowed some margin for the inevitable decline in DQE due to the effects of system components that were not accounted for in the radiation transport calculations.

4.4.3 Intrinsic MTF

The LSF tallies obtained from the simulations could not be used directly for MTF calculations since they were sampled according to the actual detector sampling grid, and subsequently calculated post-sampled MTF spectra would have been prone to aliasing at higher spatial frequencies. The specification of virtual voxels of sub-pixel dimensions for finer sampling was not considered since the composition of the detector was highly heterogeneous,

and explicit oversampling could potentially affect its radiation transport characteristics.

Therefore, additional simulations were performed and the LSF tallies were repeated with the x-ray source shifted in equal sub-pixel increments along the x – axis between the center and the edge of the pixel underlying the source. The corresponding LSF profiles were superposed to obtain an oversampled LSF response with an effective sampling size equal to the value of the sub-pixel increment shift. With this technique, the LSF was oversampled by a factor of four (i.e. source shift increments of 25% of pixel width).

A study of these LSF profiles revealed unconventional trends in their shape and behavior due to the presence of high-Z heterogeneities in the detector composition, which led to spatially varying contributions of septal build-up in the overall imaging response of the detector. A selected LSF profile that was obtained using shifted source reconstructions is shown in Figure 4-9 for a detector thickness of 6 cm and a fill factor of 70%. For better visualization, separate legends have been used to distinguish between LSF profiles generated using specific shifts in the source position. It can be seen that the values of the black circles (indicating LSF profiles shifted by a half pixel) were noticeably higher than those of the gray and white circles (quarter pixel shifted and unshifted LSF profiles respectively). This can be attributed to the increase in the overall detector response due to greater contributions from septal build-up as the position of the point source was brought closer to the poly-W grid septa. Therefore, when the point source was placed over pixel boundaries (i.e. a half pixel shift), the x-rays were directly incident on the poly-W grid, which corresponded to a maximal increase in the total number of interactions due to septal build-up. Similarly, x-rays incident at the pixel centers led to minimal septal build-up and proportionally lower number of radiation interactions. Thus, the overall imaging response of the detector effectively varies within maximum (black circles) and minimum (white circles) values

dictated by septal build-up contributions from x-ray photon striking the centers of the poly-W grid septa and the scintillation glass fiber respectively.

Oversampled LSF profiles obtained with selected thicknesses (1, 3, 6, and 10 cm) are shown in Figure 4-10 for a fill factor of 70%. It can be seen that the effect of septal build-up on the shape of the LSF profile was more pronounced at smaller thicknesses, and noticeably limited as the detector thickness was increased to 10 cm. This can be attributed to the progressively attenuated x-ray fluence distributions at greater depths within the detector, which proportionally reduced septal build-up. In general, the increased septal build-up in the vicinity of the poly-W grid resulted in a broadening of the LSF in that part of the profile. On the other hand, for points closer to the center of the pixels, septal build-up was minimal and the LSF profiles were significantly narrower. These contrasting spatial variations were more pronounced for smaller thicknesses due to higher septal build-up in the vicinity of the poly-W grid, and also from the traditional decline of the LSF near the pixel centers due to reduced x-ray pathlengths. Figure 4-11 indicates the oversampled LSF profile for a 6 cm thick FOSGA detector with varying fill factors. In this case, the LSF profiles were expectedly broader with lower fill factors since the thicker septa provided increased attenuation of laterally migrating secondary photons and electrons (including those due to septal build-up).

Figures 4-9 – 4-11 represent an atypical yet characteristic shape of an oversampled LSF obtained in a structured detector array due to variations in septal build-up from high-Z heterogeneities. Similar effects were recently reported for a comparable structured scintillator array, wherein the superposition of differently shaped LSF profiles representing spatially varying radiographic characteristics of the detector was analytically validated as an appropriate indication of its overall LSF response⁹³. In other words, the spatial variations in the detector

response require an alternative interpretation of the LSF, wherein its traditional definition (based on a static line source and varying sampling points) is replaced by a spatially varying source and static sampling points. Therefore, the oversampled LSF profiles obtained by shifted source reconstruction were considered appropriate for use in Equation 2-4 to evaluate presampled MTF spectra.

The calculated MTF spectra are shown in Figure 4-12 for selected thicknesses (1 and 6 cm) and all three fill factors that were tested. In general, the variation in MTF with thickness was less pronounced than expected. This was attributed to the increased broadening of the LSF due to septal build-up as detector thickness was reduced. The MTF generally decreased with detector thickness at lower and intermediate spatial frequencies that correspond to the tail or baseline region of the LSF. However, it was notable that this traditional trend was reversed at higher spatial frequencies (corresponding to the peak of the LSF), wherein the MTF was observed to increase with detector thickness. Upon inspection of the LSF peaks in Figure 4-10, these unconventional trends could be clearly related to septal build-up. As expected from the observed trends in Figure 4-11, the MTF was found to consistently decline with increasing fill factors.

Since transfer function metrics are generally defined for shift invariant detectors, the relevance of a single representative MTF spectrum in defining overall spatial resolution may be somewhat compromised. This is illustrated in Figure 4-13, which shows the intrinsic MTF spectra for a 6 cm thick FOSGA detector (50 and 70% fill factors) that were obtained from composite LSF profiles using shifted sources. In comparison, MTF calculations using only the central source LSF (i.e. LSF with the source aligned with the pixel center) are also shown. The plots indicate the significant exaggeration of the MTF when the effects of source position were not considered. They also indicate the potential variability in spatial resolution characteristics of

structured scintillator arrays with high-Z heterogeneities. For example, a distributed set of objects imaged with a wide area x-ray beam may be associated with the overall MTF of the detector obtained with shifted source LSF profiles. However, a single isolated point object in an imaging field can potentially be resolved as indicated by the MTF from the central source LSF alone if the point is overlaid on a pixel center. It must be noted that despite these issues, the use of MTF spectra for the purposes of this research was not compromised. Since they were utilized strictly as relative metrics to optimize detector configurations, the specific results were not affected by the departure of the detector from shift invariance.

4.4.4 Intrinsic DQE(f)

The radiation transport calculations for intrinsic DQE(0) and MTF revealed contrasting influences of fill factor (over all spatial frequencies) and detector thickness (at lower spatial frequencies). Therefore, Equation 3-1 was used to mediate this trade-off by determining the intrinsic DQE(f) spectrum for the FOSGA detector at all thicknesses and fill factors (Figure 4-14). In general, the DQE(f) was observed to improve with detector thickness indicating that the influence of increased x-ray detection was more dominant than that of the declining MTF. The DQE was also found to increase with fill factor at lower spatial frequencies due to the influence of DQE(0), and it decreased with fill factor at higher frequencies indicating the higher MTF of the detector at lower fill factors. However, the improvement in DQE(0) with fill factor was generally more overbearing than the relative loss in MTF at higher spatial frequencies in the overall DQE spectrum.

4.5 Optical Transport Calculations

Following photon and electron interactions in the scintillation glass fibers, the deposited energy is converted into light. The subsequent stages of signal transduction involve a series of stochastic processes, in which light photons emitted in all directions at various points within the

fiber are either scattered, reflected or absorbed as they are channeled towards the a-Si light sensor. A custom written Monte Carlo simulation based light transport algorithm was developed to simulate the fiber-optic coupling characteristics of the FOSGA detector. Optical transport was simulated in three distinct phases: emission, free flight, and location specific optical interactions, as shown in Figure 4-15. Simulations of each phase and all events within a given phase were realized based on random samplings from a series of outcomes that was possible for a light photon at any given instance. The fundamental basis for the light transport algorithm and any Monte Carlo simulation in general is indicated in the formulism for randomly sampling a given stochastic process that is indicated in Equation 4-1.

$$P(x) = \int_a^x p(x') dx' = n \quad \text{where } P(a) = 0, P(b) = 1 \quad \text{and} \quad x = P^{-1}(n) \quad (4-1)$$

In this case, x denotes the random variable to be simulated within some specified limits (where $a \leq x \leq b$), while p and P respectively indicate the probability density function (PDF) and cumulative distribution function (CDF) for x . The term n represents a random number ($0 \leq n \leq 1$) that is appropriately generated and equated to the CDF (also in the range $0 \leq P \leq 1$), so that the variable x can be evaluated from $P(x)$ for each generated n . Therefore, by obtaining a series of values for n via a random number generator and applying Equation 4-1, random samplings of x can be realized in accordance with its intrinsic probability distribution.

This fundamental formulism was implemented to characterize fiber-optic light transport properties for the specific geometry of the glass fibers in a FOSGA detector using a standard computational scripting interface (MATLAB 7.0, MathWorks, Natick, MA). The events described in Figure 4-15 were simulated while a basic “phase space” for the light particles was continuously tallied. The particle phase space consisted of the current spatial position (x, y, z), and direction in terms of polar (θ) and azimuthal (Φ) angles as the particle histories were

followed between its emission and either its absorption or successful transmission. The specific purpose of the light transport algorithm was to evaluate the optical coupling efficiency of the glass fibers including its dependence on fiber length and diameter. The option of placing a mirror at the entrance plane of the fibers (to reflect light quanta that would ordinarily escape undetected back into the fiber-optic column and towards the photodiodes) was tested. In addition, detailed angular and spatial distributions of the emitted light photons were also obtained to characterize any loss in spatial resolution that may be associated with the coupling of the fibers with the underlying photodiodes.

4.5.1 Emission of Light Quanta

A scintillation event marked the origin of each simulated history in the light transport algorithm. An emission event was characterized based on its location (x_0, y_0, z_0) within the fiber, and its direction (θ_0, Φ_0) in 3-D space. During irradiation, scintillation events occur all over the volume of the luminescent core of the fiber in direct proportion to the deposited energy from radiation interactions. Therefore, a detailed spatial distribution of the energy deposition events was necessary to appropriately sample emission locations for optical transport.

4.5.1.1 Spatial distribution of optical emission events

The energy deposited within the luminescent core of each fiber is distributed within the volume of the fiber through several discrete radiation interactions. Assuming azimuthal symmetry, this volumetric distribution can be reduced to a 2-D distribution of energy deposition events as a function of radial distance from central axis and depth. A separate radiation transport model of the scintillation glass fibers was developed using MCNPX to characterize these radial and depth distributions of energy deposition. Interaction events were tallied in discrete spatial voxels that sampled the volume of the luminescent core along its depth and radius (i.e. an array of coaxial “ring” voxels stacked along the depth of the fiber). Each ring voxel was 1 mm deep,

and its radial limits were varied selectively to obtain coaxial samplings between 35 μm to 1 μm radial increments for the central and peripheral regions of the fiber respectively. Finer radial increments were selected at the peripheries to accurately sample the effects of septal build-up. The detector array was specified as a 9 x 9 pixel matrix under irradiation from an equal area parallel source of 6 MV x-rays, and the spatial distribution of energy events was sampled within the central pixel only. In this case, a 9 x 9 pixel array was selected since it was found to sample over 99.9% of a centrally located point x-ray source based on previously obtained LSF profiles. Therefore, a neighborhood of at least 4 pixels was sufficient to represent lateral scatter conditions for the simulation. The scintillation fibers were modeled as described in section 4.4.1 with similar variations in fill factor (50, 60, and 70%), and with a thickness of 10 cm.

The resulting spatial distribution of the recorded events is illustrated as a function of radial distance for selected depths (0.1 – 2 cm) in Figure 4-16. The presented plots represent a pixel fill factor of 70%, for which the fiber radius was $\sim 164 \mu\text{m}$. The increase in energy deposition at peripheral radial locations due to septal build-up was highly pronounced near the surface of the detector, and progressively diminished at deeper regions within the fiber. This was consistent with the trends observed during intrinsic LSF and MTF calculations in section 4.4.3. Radial distributions at depths greater than 2 cm showed no significant variation with radial distance, and were hence not included in Figure 4-16. In Figure 4-17, the variation in energy deposition as a function of depth within the fiber is shown for a pixel fill factor of 70%. The plots indicated that the detector response was generally peaked at a depth of ~ 0.25 cm and declined exponentially with depth thereafter. Only the depth profiles at radial distances of 60 and 164 μm (just within the fiber core boundary) are shown in Figure 4-17 as they were sufficiently indicative of the typical variation with radial distance. Similarly, the presented results for a pixel

fill factor of 70% were indicative of those obtained for 50 and 60% fill factors. The simulated event distributions were finally normalized to a unit integral to represent a 2-D PDF of scintillation events for the light transport simulations.

4.5.1.2 Random sampling of emission variables

The technique used for randomly sampling outcomes from 1-D PDF and CDF profiles was previously summarized with Equation 4-1. However, this technique could not be directly applied with a 2-D CDF. Therefore, a so called random sample “rejection” technique was used to sample the radial distance (r) and depth (d) of emission points. In this case, separate 1-D CDF profiles of the scintillation events [i.e. $P(r)$ and $P(d)$] were obtained by appropriately integrating the 2-D PDF [indicated by $p(r,d)$]. Two random numbers (n_1 and n_2) were generated to sample r and d separately from $P(r)$ and $P(d)$. A third random number (n_3) was then generated, and the sampled values of r and d were accepted only if Equation 4-2 was satisfied.

$$n_3 \leq p(r,d) \text{ where } r = P^{-1}(n_1) \text{ and } d = P^{-1}(n_2) \quad (4-2)$$

If the value of n_3 exceeded that of $p(r,d)$, the sampled values were rejected and the procedure was repeated until Equation 4-2 provided an acceptable emission location to initiate the particle history. For convenience, azimuthal symmetry was assumed for the light transport and all emission points were forced to start on the x – axis (so that $x_0 = r$, $y_0 = 0$, and $z_0 = d$). Finally, the polar (θ_0) and azimuthal (Φ_0) angles of emission were sampled using Equation 4-1 over the ranges $1 \leq \text{Cos}(\theta_0) \leq -1$ and $0 \leq \Phi_0 \leq 2\pi$ respectively to represent an isotropic distribution.

4.5.2 Free Flight

Upon emission, the simulated light particles were allowed to sustain free flight over a sampled pathlength (s) before an interaction event. The sampling of s was carried out based on the effective or total linear *attenuation* coefficient (Σ_{total}) for the scintillation glass material. For

exponential attenuation of particles, the possible values of s could be taken to be exponentially distributed with a mean value of Σ_{total}^{-1} , and the realization of Equation 4-1 for this distribution could be obtained as shown in Equation 4-3.

$$s = \frac{-\ln(n)}{\Sigma_{total}} \quad (4-3)$$

Using this formulism, serially generated random numbers (n) were used to sample s between 0 and ∞ (effectively truncated down to the maximum possible distance to the geometric bounds of the fiber based on the current values of x , y , z , θ , and Φ). At the termination of free flight, the particle position was updated in the phase space tally. For the prototype scintillation glass, Σ_{total} was specified to be 0.008 cm^{-1} ($\sim 2\%$ attenuation over an inch thick scintillation glass) based on optical studies of “green” light (500 – 500 nm) transmission conducted by the vendors (Collimated Holes Inc., Campbell, CA).

4.5.3 Optical Interactions

The nature and type of optical interactions that were simulated at the termination of free flight depended on the updated location of the particle history. The modeled interactions can generally be categorized as absorption, scatter, or reflection, and the possible sites that these could occur may be categorized as within the fiber core, at the clad wall, or at the entrance plane of incident radiation.

4.5.3.1 Interactions in the fiber core

A light photon interacting in the core region was allowed to be either scattered or absorbed. The relative probabilities associated with scatter (p_s) and absorption (p_a) were related to the corresponding linear attenuation cross-sections ($\Sigma_{scatter}$ and Σ_{abs} respectively) as indicated by Equation 4-4. Precise values of the scatter and absorption probabilities were not known for the scintillation glass material. Therefore, an initial series of simulations were conducted with

varying degrees of scatter contribution to observe the sensitivity of the results to the choice of p_s or $\Sigma_{scatter}$ (with p_a and Σ_{abs} adjusted according to Σ_{total} in each case). Due to the high optical clarity of the scintillation glass ($\Sigma_{total} = 0.008 \text{ cm}^{-1}$ corresponds to a mean pathlength of 125 cm), scatter and absorption events in the fiber were not expected to be significant relative to its overall light transmission characteristics.

$$p_s = \frac{\Sigma_{scatter}}{\Sigma_{total}} \quad \text{and} \quad p_a = \frac{\Sigma_{abs}}{\Sigma_{total}} \quad \text{where} \quad \Sigma_{scatter} + \Sigma_{abs} = \Sigma_{total} \quad (4-4)$$

For any specified values of p_s , a core interaction was modeled by generating a random number (n), and the particle history was allowed to scatter only if $n \leq p_s$. Upon scattering, the direction of the particle history was updated based on the scattering angle that was randomly selected over all 4π steradians. A new azimuthal direction was randomly selected from a uniform range ($0 \leq \Phi \leq 2\pi$), and the polar scattering angle was determined using Rayleigh's scattering theory based on the probability distribution in Equation 4-5. Following scatter, the particle history was allowed to proceed in its new direction via free flight until its next interaction. However, if an absorption event was sampled (if $n > p_s$), the particle history was terminated (i.e. failed transmission) and a new history was initiated if required.

$$p(\theta) = 1 + \text{Cos}^2(\theta) \quad (4-5)$$

4.5.3.2 Interactions at the fiber clad wall

If the simulated free flight led to the particle reaching the fiber clad wall, the angle of incidence (α_i) between the particle trajectory and the normal vector to the fiber clad wall at the point of collision was used to select any of two possible outcomes (reflection or absorption). In this case, the normal vector to any point on the clad wall was easily obtained as the radius vector at that point. If a particle with a large enough incident angle ($\alpha_i > \alpha_{crit}$) reached the clad wall, it was automatically redirected into the fiber-optic column via total internal reflection. The critical

incidence angle (α_{crit}) could be computed as a function of the refractive indices (η_{core} and η_{clad}) of the core and clad glass respectively, as $\alpha_{crit} = \text{Sin}^{-1}(\eta_{clad} / \eta_{core})$. For the prototype glass fibers, $\eta_{clad} = 1.48$, $\eta_{core} = 1.58$, for which $\alpha_{crit} \sim 69.5^\circ$.

On the other hand, for the case of $\alpha_i \leq \alpha_{crit}$, a Fresnel reflection event was simulated, for which the probability of the particle being reflected was obtained as the Fresnel reflection coefficient (F) calculated as a function of the incident angle α_i , as shown in Equation 4-6.

$$F = \frac{1}{2} \left\{ \begin{array}{l} \left| \frac{\eta_{core} \text{Cos}(\alpha_i) - \eta_{clad} \sqrt{1 - \left[\frac{\eta_{core}}{\eta_{clad}} \text{Sin}(\alpha_i) \right]^2}}{\eta_{core} \text{Cos}(\alpha_i) + \eta_{clad} \sqrt{1 - \left[\frac{\eta_{core}}{\eta_{clad}} \text{Sin}(\alpha_i) \right]^2}} \right|^2 \\ + \\ \left| \frac{\eta_{core} \sqrt{1 - \left[\frac{\eta_{core}}{\eta_{clad}} \text{Sin}(\alpha_i) \right]^2} - \eta_{clad} \text{Cos}(\alpha_i)}{\eta_{core} \sqrt{1 - \left[\frac{\eta_{core}}{\eta_{clad}} \text{Sin}(\alpha_i) \right]^2} + \eta_{clad} \text{Cos}(\alpha_i)} \right|^2 \end{array} \right\} \quad (4-6)$$

The variation of the calculated Fresnel coefficients with incident angle can be visualized in Figure 4-18. As seen from these plots, the probability of reflection is quite low ($\sim 3\%$) over most incident angles. However, the coefficients were found to increase considerably beyond an incident angle of $\sim 45^\circ$ to a reflection probability of 100% for incident angles beyond the critical angle for total internal reflection. For the light transport simulations, Fresnel reflection was selected for a given particle based on the calculated value of F and a generated random number (n) only if $n \leq F$. Following a reflection event, the particle was allowed to assume free flight along its reflected direction, which could be computed based on simple vector algebra and analytical geometry.

4.5.3.3 Interaction at entrance plane

Since optical emission and scattering was simulated over all directions, some fraction of the light may be transmitted away from the photodiodes towards the entrance plane of the fibers.

With the placement of a high reflectance mirror at the entrance plane (with the reflecting plane facing the fiber core), light particles that could potentially escape the fiber from the entrance plane could be reflected back into the fiber-optic volume towards the photodiodes. For those simulations in which such a mirror was specified, the light particles were allowed to undergo reflection along the same lines as the Fresnel reflection of particles at the clad wall. In this case, the probability of reflection was set equal to the reflection coefficient of the mirror (assumed to be 90% for these calculations). For the case where no mirror was specified, the mirror reflectance was set to zero, which effectively “turned off” the mirror, and particle histories reaching the entrance plane were automatically terminated.

4.5.4 Output Tallies

Based on the processes described in sections 4.5.1 – 4.5.3, particle histories were followed through various scatter and reflection events until its termination either by absorption or transmission. The simulation itself was terminated after the specified number of particle histories were transported completely, and output tallies consisting of the locations and trajectories of the exiting particles were generated. In this case, the radial positions, polar angles, and azimuthal angles of the transmitted histories were binned into fine sampling intervals (12 μm , 3°, and 6° bins respectively) to generate a 3-D tally of the transmitted optical fluence expressed in units of the transmission fraction per unit area per steradian. In this form, the 3-D tally could be easily projected from the exit plane to an underlying a-Si read-out panel situated over any selected gap, and the optical blurring associated with the optical coupling could be characterized.

4.5.5 Simulations

Optical transport simulations were conducted for the same variations in detector geometry that were studied during radiation transport calculations (i.e. 1 – 10 cm thicknesses,

and 50 – 70% fill factors). Each simulation was carried out with 10^7 histories, which was found to provide $< 0.1\%$ relative error in the overall transmitted flux from the fibers. The scatter perturbation studies revealed no significant variations in the transmitted optical flux even as p_s was varied between 0 and 100%. Figure 4-19 shows scatter perturbation results for 1, 6, and 10 cm long fibers of 164 μm core diameter (70% fill factor). As expected, there was very little increase ($\sim 0.5 - 1.5\%$) in the transmitted flux with scatter contribution. Therefore, the value of p_s was nominally set to 50% for all simulations, which was generally consistent with the range recommended by Berdnikov *et al* for dense scintillators¹⁷⁰. The overall fiber-optic coupling efficiency was determined for each fiber configuration as a volume integral of the 3-D tally of radial position, polar and azimuthal angles generated at the end of each simulation.

4.5.5.1 Light transmission efficiency

The calculated transmission efficiencies are shown for various fiber geometries in Figure 4-20. In this case, fiber core diameters of $\sim 138, 151,$ and $164 \mu\text{m}$ were used to represent overall pixel fill factors of 50, 60, and 70% respectively. Light transmission was found to steadily decline with fiber length, and was in the range of 8.5 – 10% with the mirror “on” and in the range of 4.5 – 5.5% with the mirror “off”. Light transmission was also found to reduce slightly with the fiber core diameter. The decline of light transmission with both fiber length and diameter can be attributed to the decreased solid angle fractions subtended by the exit plane to light quanta in longer and narrower fiber-optic columns. The above results were consistent with preliminary findings of the vendors (Collimated Holes Inc., Campbell, CA) that indicated light coupling efficiencies of ~ 5 and 10% with the mirror “off” and “on” respectively.

4.5.5.2 Angular distribution of transmitted light

The angular spread of the transmitted light photons is indicated in Figure 4-21, wherein the polar angle distribution of exiting light quanta is shown for selected fiber lengths (results

were typical of all tested configurations). Much of the transmitted optical fluence ($\sim 97\%$) was concentrated within a cone angle of $25 - 30^\circ$ with respect to the fiber axis. This predominantly forward peaked light distribution is characteristic of fiber-optic tapers and similar results¹⁷¹ were reported by Yu *et al* based on light output measurements for the same brand of scintillation glass. The preferential transmission of smaller polar angles in the fibers can be related to the progressively narrow solid angle cones subtended with longer fiber-optic columns. As a result, the polar angle distribution was slightly narrower for a fiber length of 10 cm compared to that at 1 or 6 cm. The forward peaked light transmission limits the spread of light at the plane of the a-Si photodiodes, and subsequently improves the MTF. Therefore, forward peaked light transmission is highly beneficial to the overall imaging performance of the system.

A slight increase was observed in the angular distributions of the transmitted light at a polar angle of $\sim 21^\circ$ for all fiber geometries. This was attributed to a sharp increase in the contribution of Fresnel reflection events (seen in Figure 4-18) for light quanta incident on the clad wall with incident angles of $\sim 69^\circ$, which was close to the value of the critical angle for total internal reflection. The overall shape of the angular distribution did not vary significantly with radial distance, although the transmitted fluence was higher at the center of the fiber (due to a greater proportion of uncollided light) and at the fiber boundary (due to increased emission events from septal build-up).

4.5.5.3 Optical LSF and MTF at the photodiode panel

The light exiting the fiber can be projected down to the plane of the photodiode sensor to obtain optical components of the LSF and MTF profiles for the FOSGA detector. This part of the optical coupling process was not modeled during in the transport algorithm since the exact geometry of the fiber-photodiode interface is yet to be determined. Specifically, the exact separation between the fiber and the read-out panel (referred to as the coupling contact gap), as

well as the use of external coupling agents (like an appropriately index matched optical gel, polymer resin based optical entrance window of the photodiode, etc.) has not been finalized. The use of a high refractive index coupling agent is desirable between the fibers and the photodiodes to prevent the potential spreading of the exiting light due to the large difference in the refractive indices of the fiber core and air. Commercially available optical gels (eg. Nye Lubricants, Fairhaven, MA) that are specifically designed for scintillator – photodiode contact gaps can provide excellent optical coupling by virtue of high refractive indices (1.46 – 1.62). Therefore, for the subsequent analyses in this study, it was assumed that the exiting light is detected by the photodiodes with no significant change in the magnitude and shape of the polar angle distributions in Figure 4-21.

The spatial and angular distributions of light exiting the fiber were propagated down to the photodiode panel across assumed values of the fiber – photodiode contact gap. In practice, scintillator arrays are typically aligned with underlying flat-panels with as close a contact gap as possible to limit optical spreading and glare¹⁷. Therefore, the exact size of the contact gap may depend on mechanical tolerances associated with the scintillator and flat-panel systems, the clearance afforded by its associated mounts, and the alignment device that holds the scintillator and flat-panel arrays in place. Communications with vendors (Hytec Inc., Los Alamos, NM) indicated that the gap may be as high as 1 mm. Based on these estimates, the exit light distributions were projected across an assumed contact gap of 1 mm. The spatial distribution of the projected light was binned into 1-D spatial intervals of 50 μm to generate optical LSF profiles for all fiber configurations. The optical LSF profiles obtained in this way are shown in Figure 4-22 for 1 and 10 cm long fibers (164 μm core diameter), and the associated optical MTF spectra are shown in Figure 4-23. While no significant variation in the MTF was observed with

fiber diameter, slight improvements in the optical MTF were observed with thickness. This can be explained based on the narrower polar angle distributions associated with longer fibers that limit the lateral spread of light projected on to the photodiode panel. To study the sensitivity of the optical LSF and MTF profiles to the size of the contact gap, the transmission light tallies were projected across a progression of gaps between 0.5 – 1.25 mm. The resulting MTF components are shown in Figure 4-24 (for a 6 cm long fiber with 164 μm core diameter). The calculated MTF spectra decreased significantly with increasing contact gap since the exiting light distributions were projected over wider distances. The MTF at 1 cy/mm was recorded at 64%, 50%, 37%, and 27% for respective contact gaps of 0.5, 0.75, 1, and 1.25 mm.

4.6 Linear Cascaded Systems Analysis

Along the same lines as the linear systems analysis implemented with the TSC system in section 3.3.5, the FOSGA detector was classified into component stages based on the concepts described in section 2.4.2. The cascaded systems model for the FOSGA detector is shown in Figure 4-25. Stages 1 – 3 involved the detection and spread of radiation quanta followed by the emission of light, and were conceptually identical to the corresponding stages in the TSC system. The associated parameters (g_1 , T_2 , g_3 , and C_{g3}) were obtained in the same manner as described for the TSC using the radiation transport tallies described in section 4.4. In this case, the light quantum gain g_3 was evaluated based on vendor specified parameters (Collimated Holes Inc., Campbell, CA) for the intrinsic energy efficiency of scintillation ($\eta_{opt} = 2.25\%$) and the mean energy of emitted light photons ($\bar{E}_{opt} = 2.26 \text{ eV}$).

Stage 4 represented the light transmission efficiency (g_4) of the fiber-optic channel in each pixel, while stage 5 comprised of the MTF (T_5) due to optical blurring at the photodiode panel from the angular distribution of the transmitted light. Both parameters were characterized using the light transport calculations described in section 4.5, and have been displayed in Figures

4-20 and 4-23. Stages 6 and 7 pertained to the optical sensitivity (g_6) of the photodiode sensors, and the inherent MTF (T_7) associated with the sampling aperture of the photodiode pixel (evaluated as a sinc function⁵⁸). The optical sensitivity g_6 was evaluated based on the vendor specified distributions of the sensitivity spectrum for the photodiodes (Hytec Inc., Los Alamos, NM) and the emission spectrum for the scintillation glass (Collimated Holes Inc., Campbell, CA). The value of g_6 was calculated to be 0.62, which included a scaling factor of 0.83 to account for the fill factor of the sensitive surface of the light sensor⁵⁸. Finally, the additive dark noise (S_8) of the read-out electronics for the photodiodes was included as stage 8, even though the contribution of dark noise in modern flat-panel based EPIDs has been reported to be negligible. In this case, the specific reported values of dark noise NPS for a prototype a-Si EPID were used to determine S_8 (~ 0.005) for the cascaded systems model. The MTF components (T_2 , T_5 , and T_7) associated with the spread of radiation quanta in the scintillation glass array, the spread of light at the fiber – photodiode contact gap, and the photodiode sampling aperture respectively were used to evaluate the overall expected MTF for a FOSGA detector with various thickness and fill factor configurations. The theoretical DQE was evaluated by applying Equation 2-19 with the parameters associated with stages (1 – 9), which led to the general expression given in Equation 4-7.

$$DQE(f) = \frac{g_1 T_2^2(f)}{1 + \left(\frac{\epsilon_{g_3}}{g_3} \right) + \left(\frac{1 + S_8(f)}{g_3 g_4 g_6 T_5^2(f) T_7^2(f)} \right)} \quad (4-7)$$

The overall MTF of the FOSGA detector is shown for selected detector configurations (1 and 10 cm thicknesses, 50 and 70% fill factors) in Figure 4-26. The MTF spectra for all other prototype configurations were in the range specified by the displayed plots. In general, the MTF was decreased with higher fill factors, and did not show significant variations with detector

thickness. As previously described in sections 4.4.3, the unique nature of the variation in MTF with thickness can be attributed to the specific effects of septal build-up on MTF spectra. The overall effects of septal build-up were responsible for a preferential attenuation of the MTF at lower thicknesses (especially at higher spatial frequencies). As a result, the traditionally expected differences in MTF with changing thickness were significantly diminished as the MTF improved only slightly with smaller thicknesses. In addition, the optical MTF associated with the angular spread of transmitted light at the photodiode panel also contributed to the unconventional variations in MTF. As described in section 4.4.5.3, longer fiber lengths led to narrower angular distributions for the exiting light, which led to an improvement in MTF with detector thickness. Therefore, since the MTF varied very slightly over all detector configurations, the detector geometry was essentially dependent on its overall DQE characteristics.

Based on intrinsic DQE calculations in section 4.4.4 and Figures 4-8 (B) and 4-14, the detector configuration of 6 cm thickness and 70% fill factor was initially selected to satisfy the target specifications of DQE and MTF. The overall MTF for this configuration was generally comparable to most other detector thicknesses and fill factors, and is shown in Figure 4-27 along with the separate MTF contributions of the spread of radiation quanta (T_2), the optical blur at the fiber – photodiode contact gap (T_5), and photodiode pixelization (T_7). It can be seen that the effects of T_2 and T_5 were generally comparable and significantly more dominant over the contribution of the photodiode aperture. The MTF was found to be ~ 11% at 1 cy/mm, which is better or comparable to the performance of current commercial systems, and satisfied the minimum target specifications for spatial resolution. Moreover, with smaller contact gaps (< 1 mm) at the fiber – photodiode interface, the MTF was shown to improve significantly as shown in Figure 4-24.

The overall system DQE calculated with Equation 4-7 is shown for various detector configurations in Figure 4-28. It can be seen that a DQE(0) of > 25% could be achieved with the selected detector thickness of 6 cm at 70% fill factor. Increasing the detector thickness beyond 6 cm only led to marginal improvements in DQE(0) as x-ray detection was significantly more sensitive to fill factor for those thicknesses. For all detector configurations, the overall DQE(0) did not change significantly from its intrinsic value that was based only in radiation interactions. This indicated that there was no significant quantum sink associated with the imaging system. The DQE(0) also did not reduce significantly (~ 0.1%) when the light transmission efficiency obtained with no mirror was used in the DQE computation. Therefore, a FOSGA detector could be constructed without the inclusion of a high reflectance mirror since the DQE was not limited by the light transmission efficiency. The overall DQE values for the selected detector configuration of 6 cm thickness and 70% fill factors ranged from ~ 26% at 0 cy/mm to ~ 4% at 1 cy/mm, which indicated an order of magnitude improvement in overall imaging performance compared to commercial EPIDs. Therefore, the FOSGA detector in its selected prototype configuration represents a promising solution for low dose, high quality megavoltage imaging that is suitable for volumetric MV-CBCT based treatment verification.

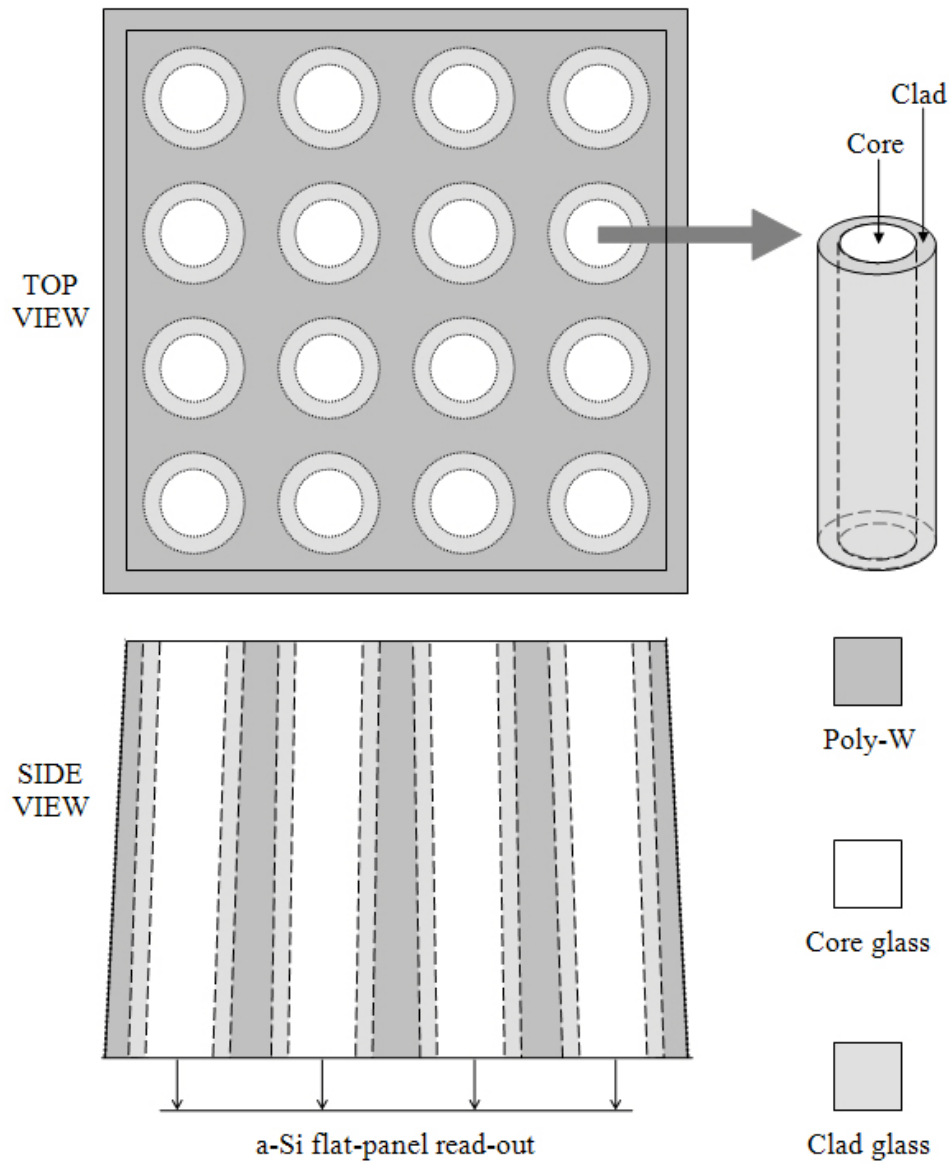


Figure 4-1. The functional and structural layout of the FOSGA detector depicting the constitution of each fiber and its placement in the grid housing.

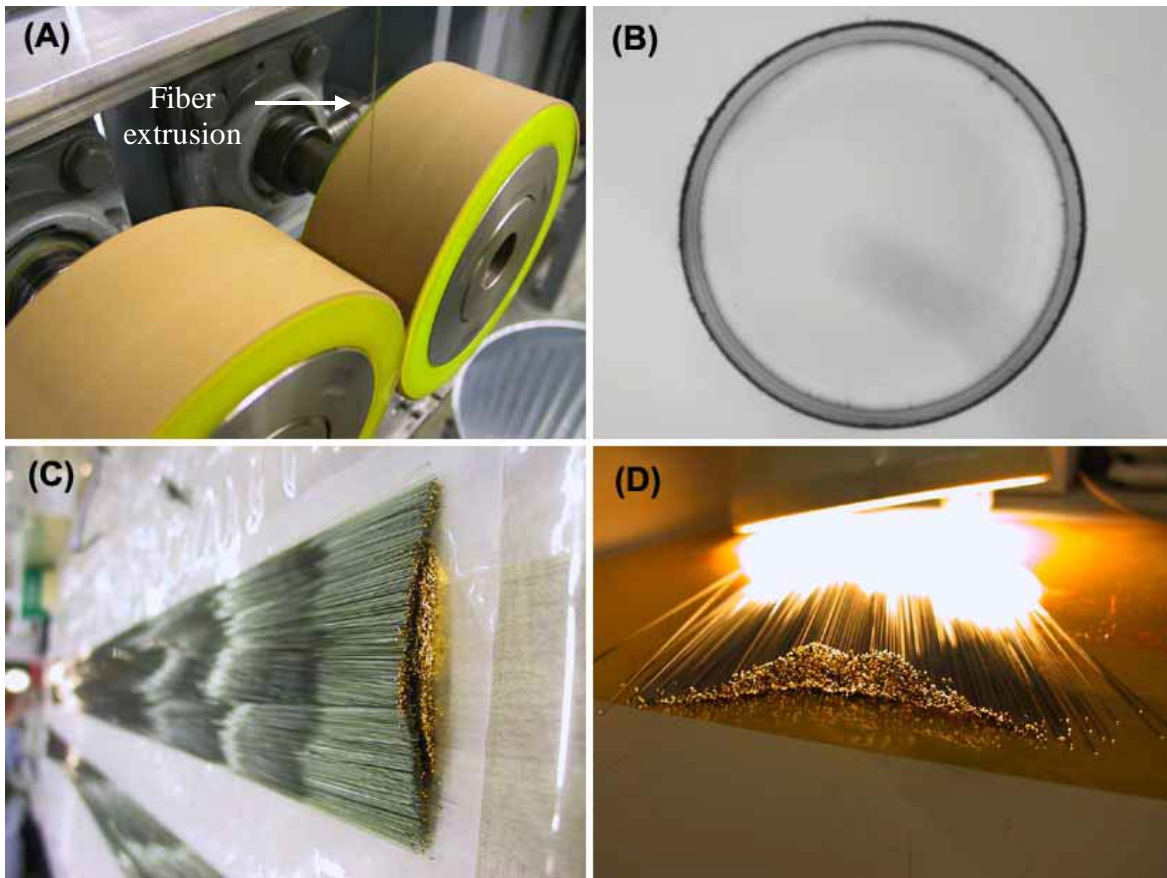


Figure 4-2. Terbium doped scintillation glass fibers used in the FOSGA detector. (A) Extrusion wheels to draw glass fibers, (B) Cross-section of a sample 0.43 mm diameter glass fiber, (C) 1 m long fibers showing transmitted illumination, (D) 6 cm long fibers showing transmitted illumination.

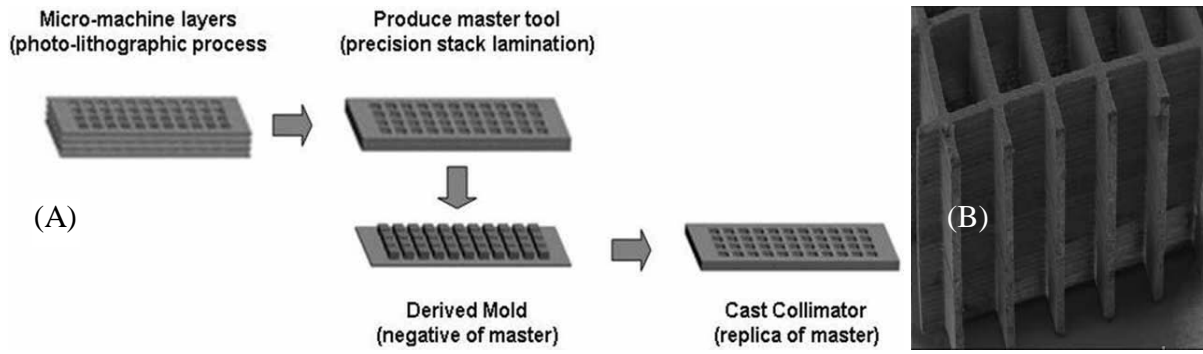


Figure 4-3. The functional outline of tomolithographic molding (TLM) for the cast production of advanced structured grids. (A) Process flow of creating and replicating molds via lithography and stack lamination, (B) Sample cast of a master mold.

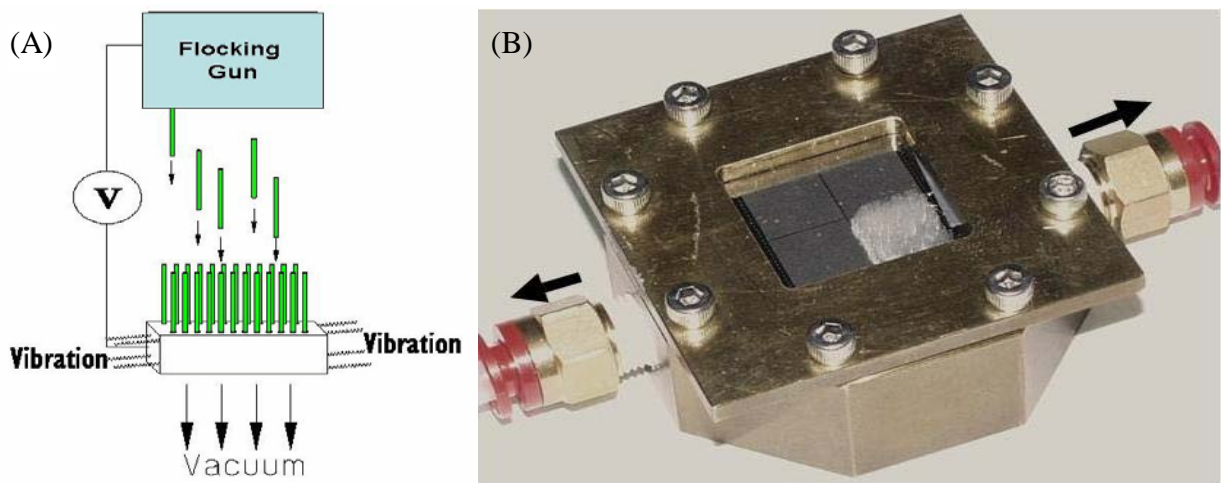


Figure 4-4. Initial tests for automated fiber insertion based on electrostatic and vacuum gradients. (A) Functional form of the loading tool, (B) Prototype loading tool for initial testing.

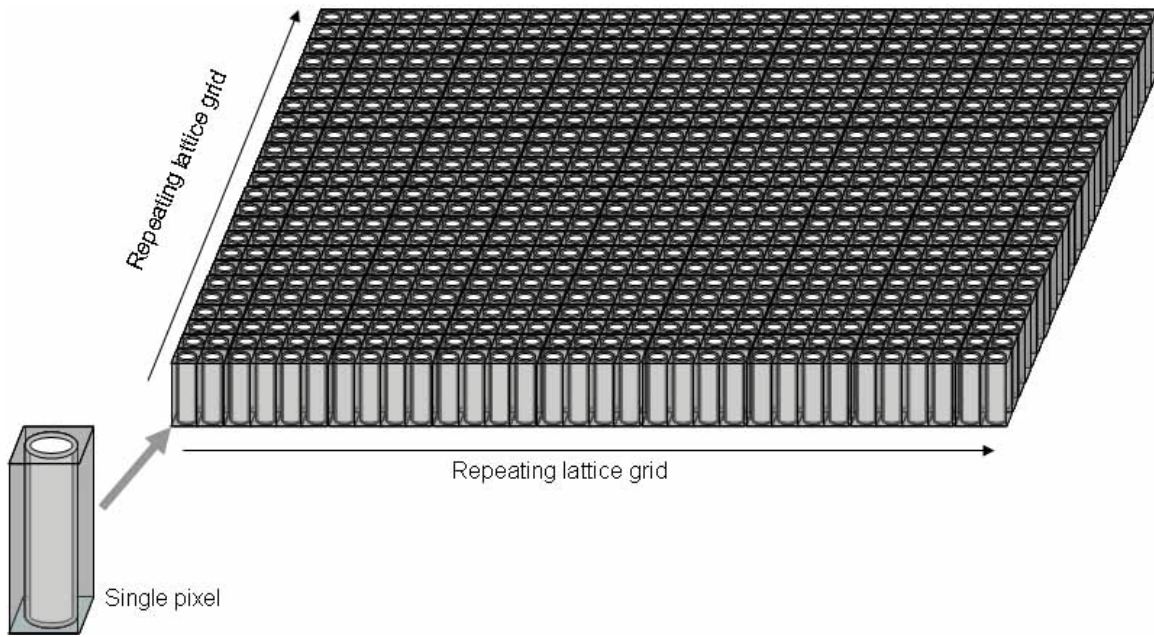


Figure 4-5. Specification of the FOSGA detector array in MCNPX for Monte Carlo simulations.

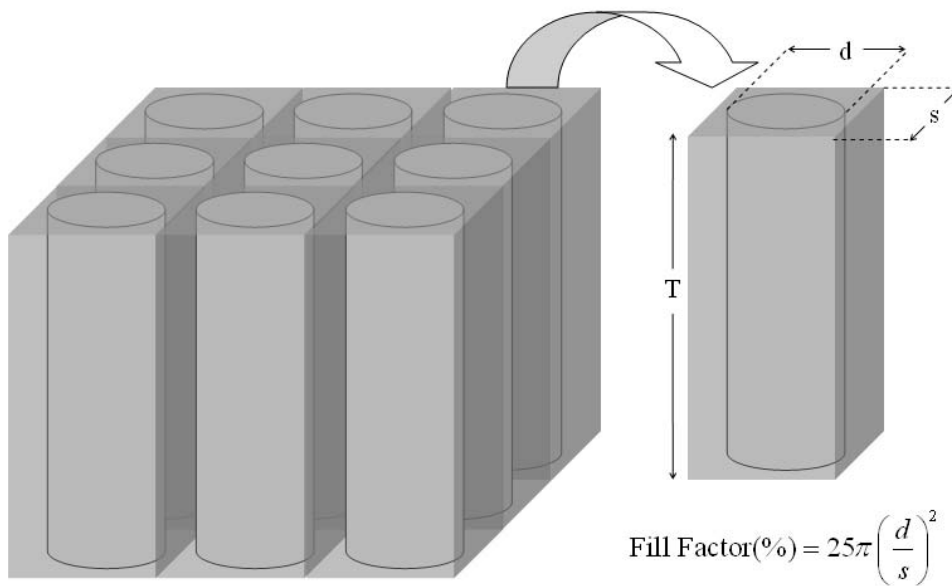


Figure 4-6. Specification of detector geometry based on thickness and pixel fill factor in a FOSGA detector for Monte Carlo simulations.

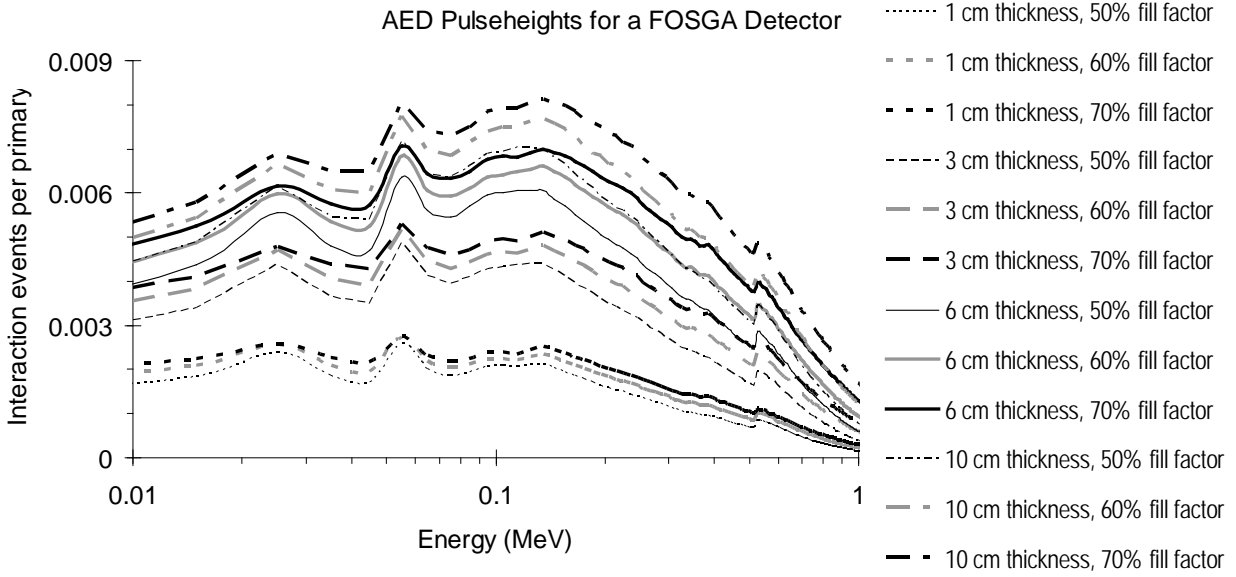


Figure 4-7. Simulation tallies indicating AED pulseheight spectra for the FOSGA detector.

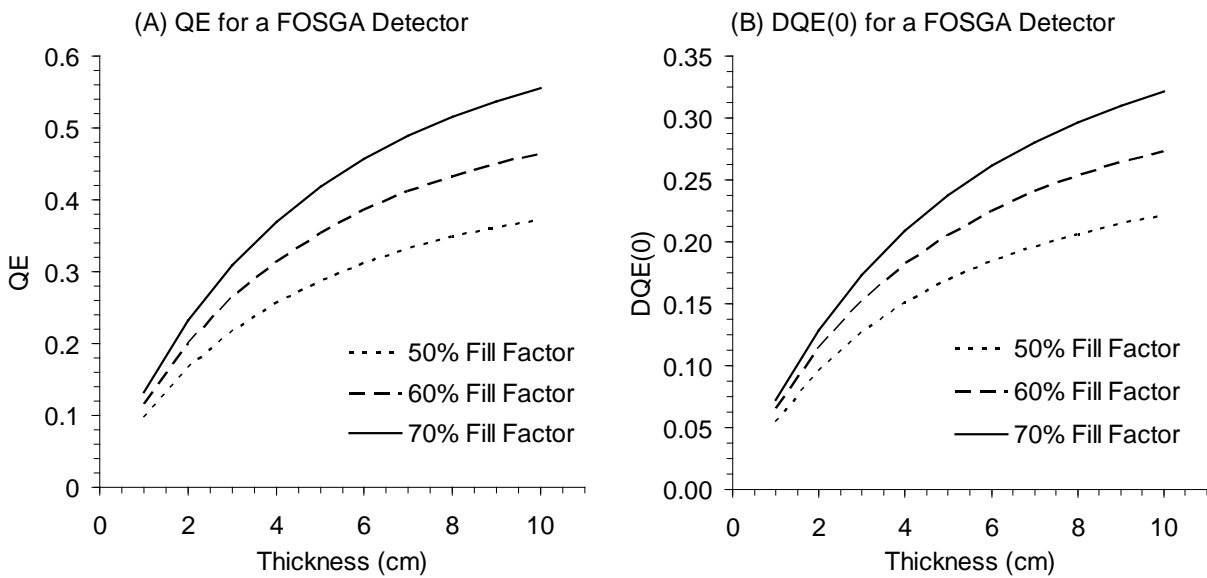


Figure 4-8. Influence of detector thickness and pixel fill factor on intrinsic x-ray sensitivity for a FOSGA detector. (A) Effect on QE, (B) Effect on DQE(0).

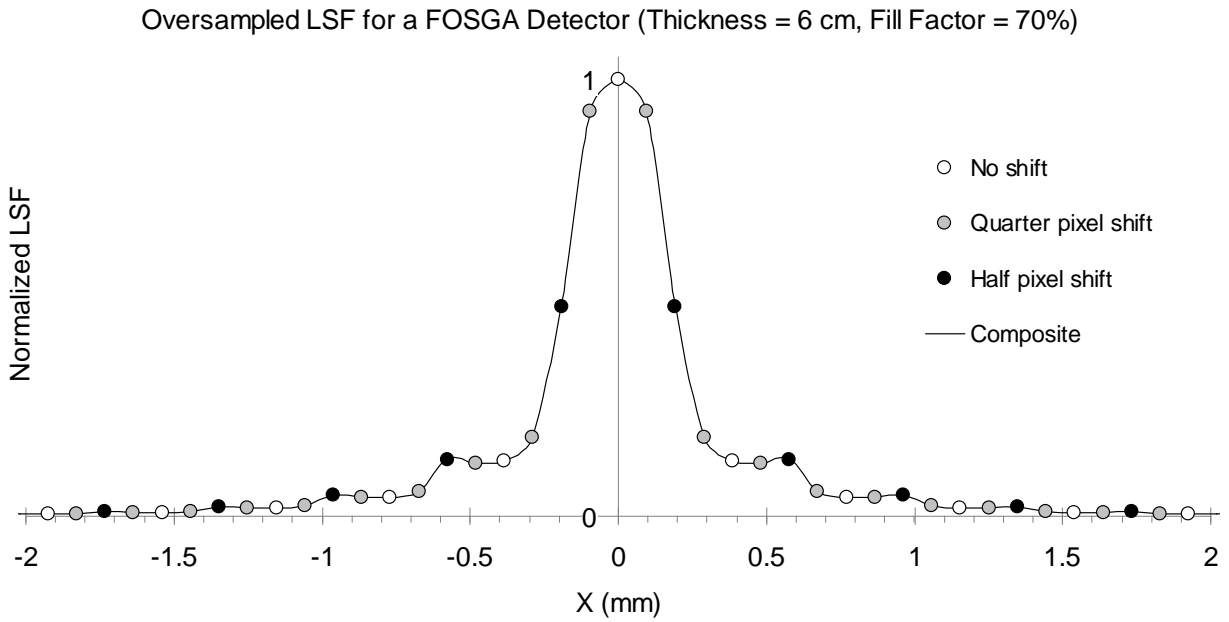


Figure 4-9. Effect of septal build-up on the oversampled LSF of a FOSGA detector.

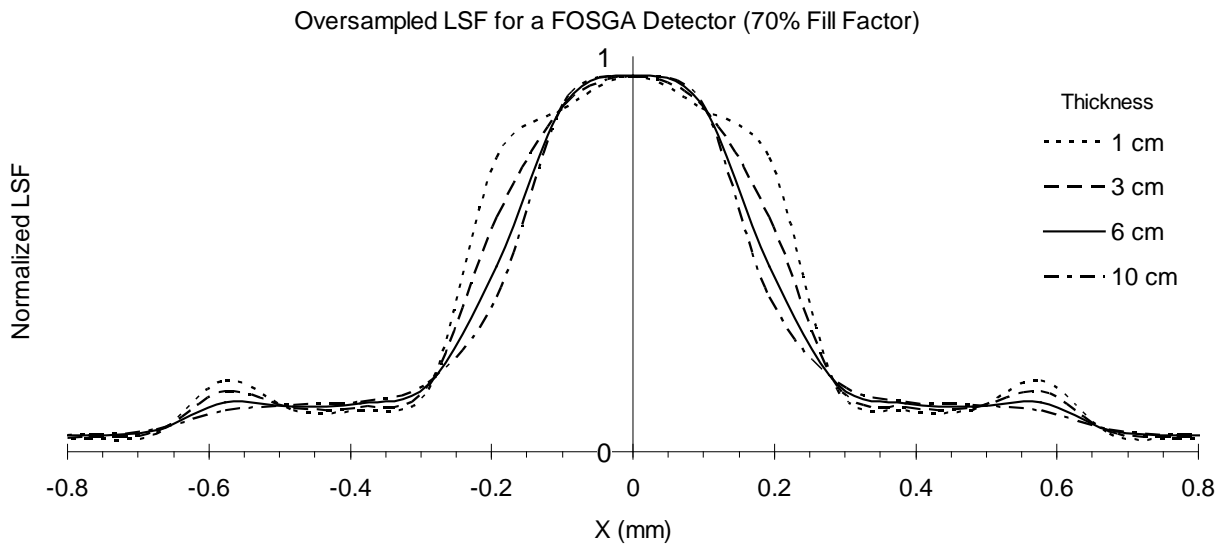


Figure 4-10. Oversampled LSF profiles for a FOSGA detector of varying thicknesses and 70% fill factor.

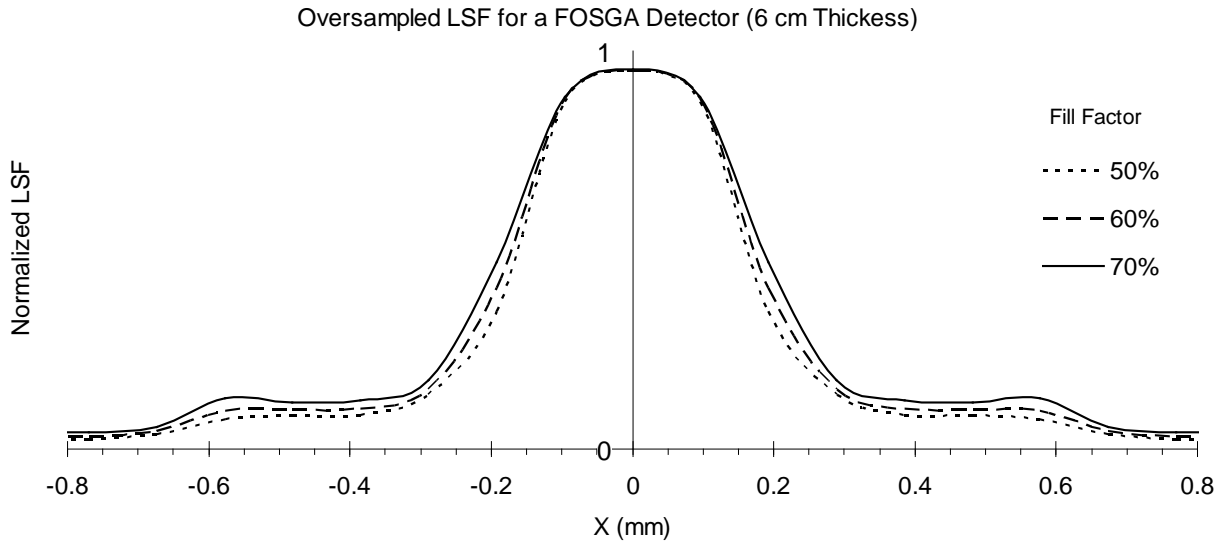


Figure 4-11. Oversampled LSF profiles for a FOSGA detector of varying fill factors and a thickness of 6 cm.

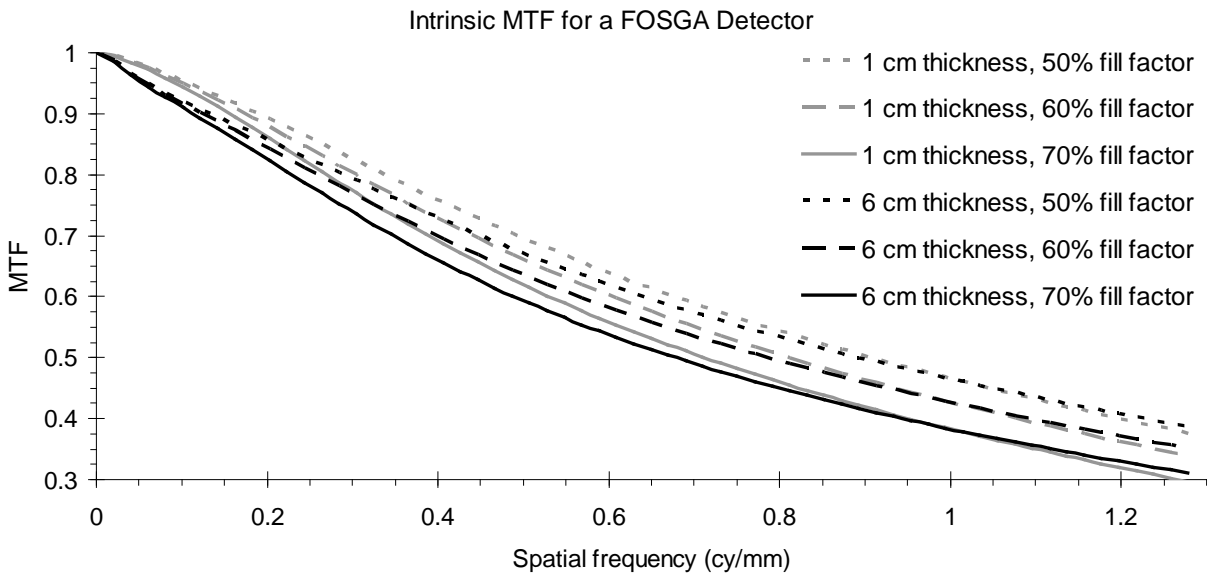


Figure 4-12. Influence of detector thickness and pixel fill factor on intrinsic MTF for a FOSGA detector.

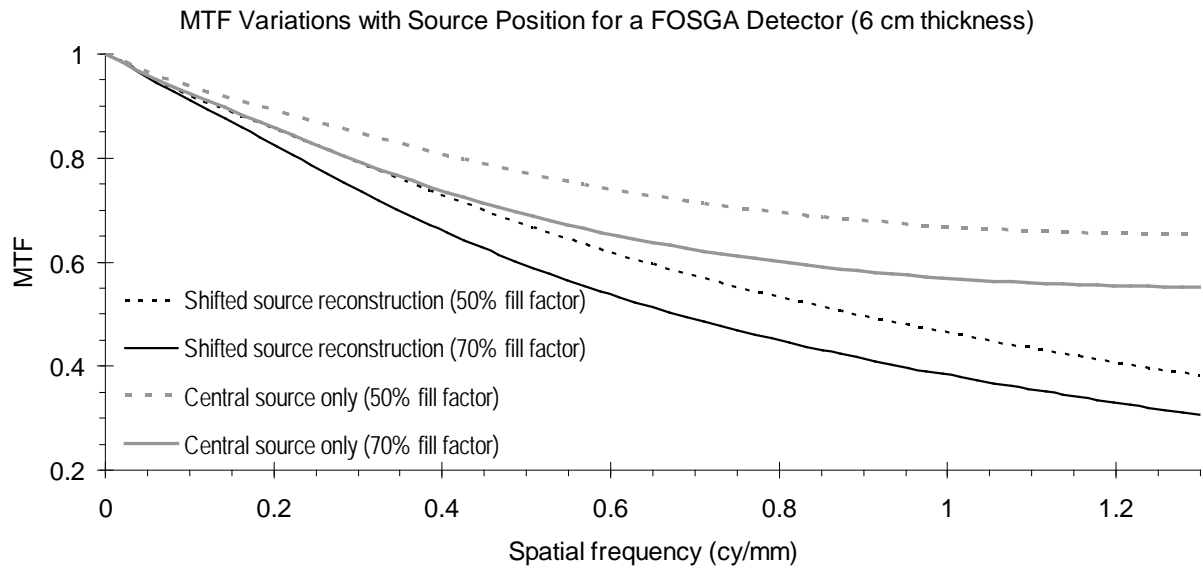


Figure 4-13. Comparison of the overall intrinsic MTF for the FOSGA detector obtained with shifted source reconstruction of LSF profiles with hypothetical MTF spectra from central source LSF profiles only.

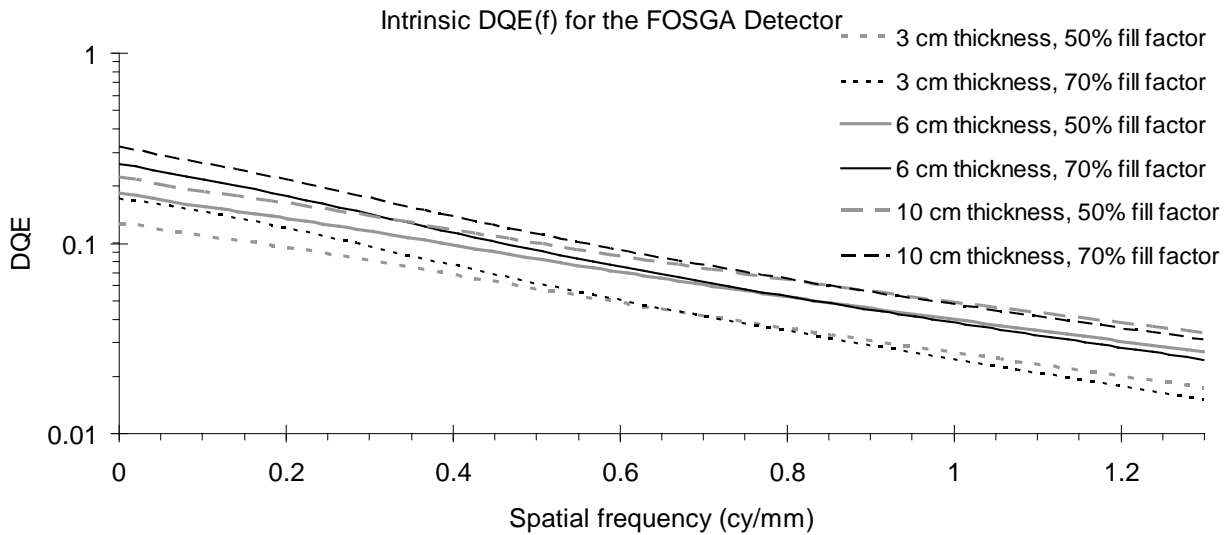


Figure 4-14. Influence of detector thickness and pixel fill factor on intrinsic DQE(f) for a FOSGA detector.

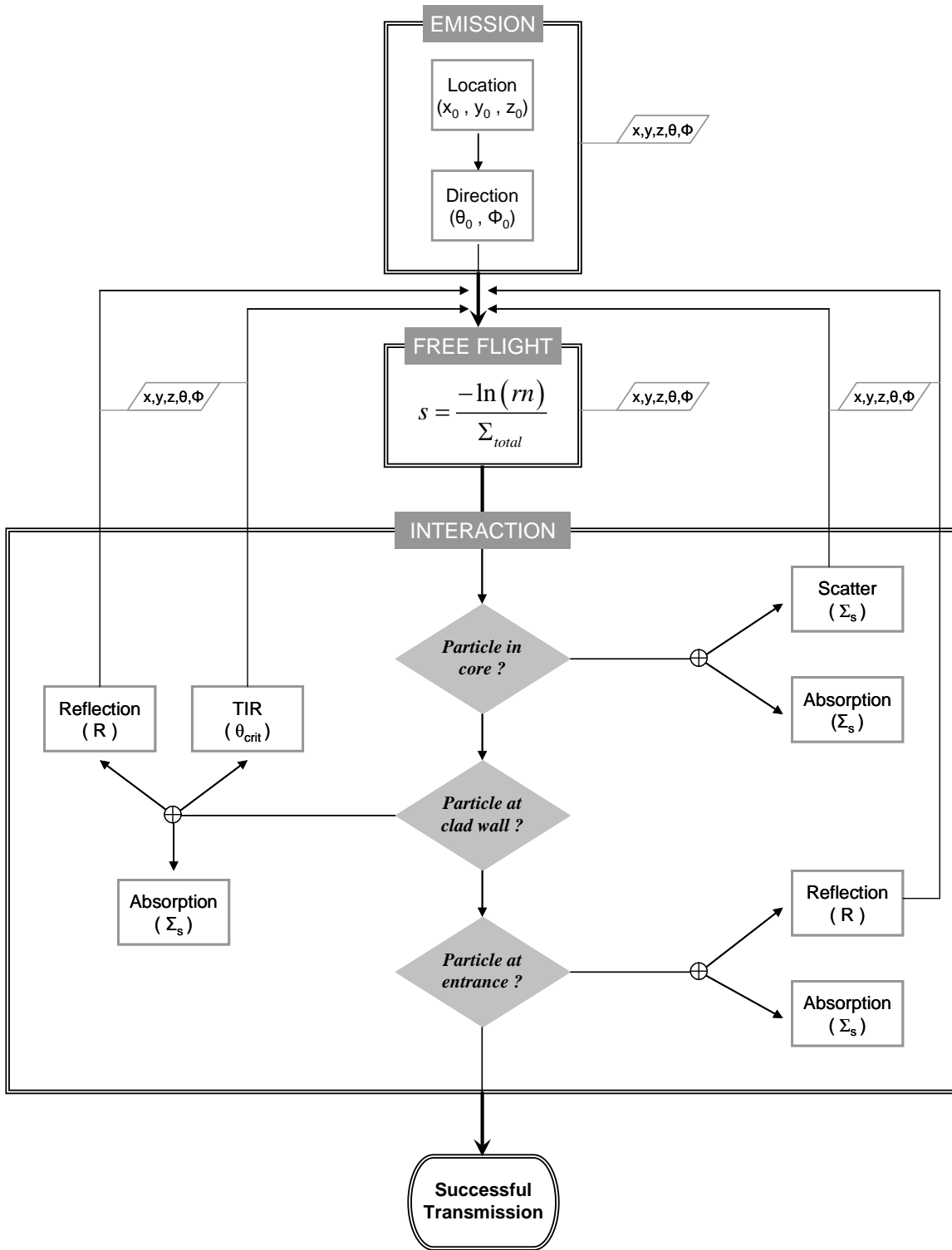


Figure 4-15. A general outline of the process flow for the optical transport algorithm used to model fiber-optic light transmission in the FOSGA detector.

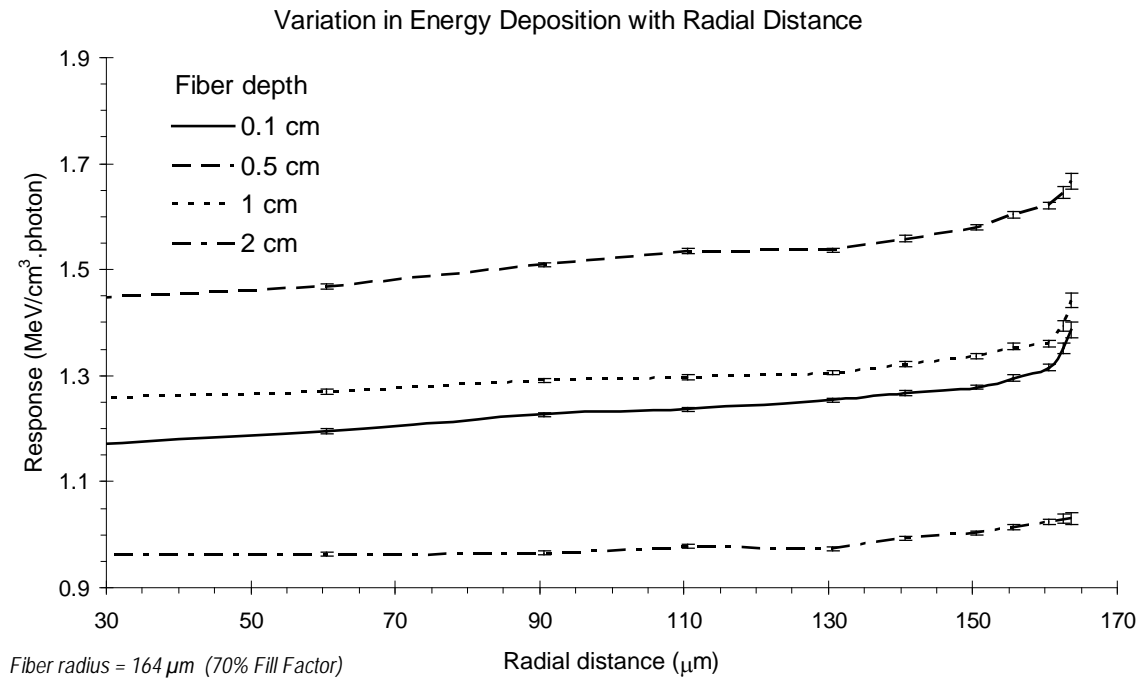


Figure 4-16. Distribution of energy deposition along radial distance from the central axis within the luminescent core of the scintillation glass fiber.

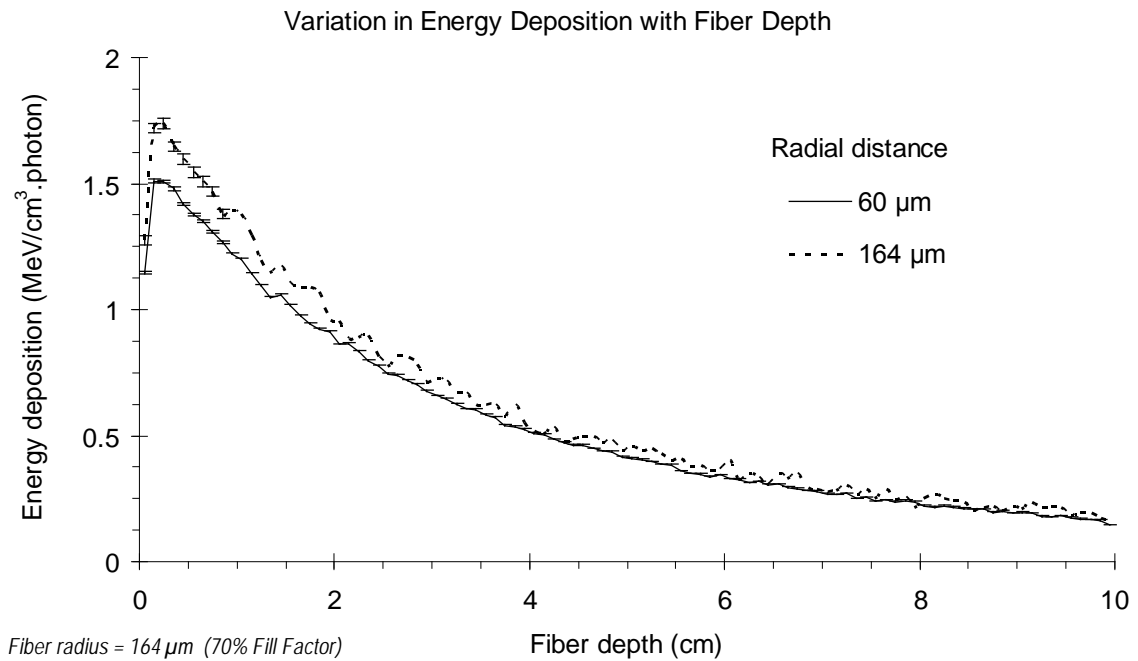


Figure 4-17. Distribution of energy deposition along depth within the luminescent core of the scintillation glass fiber.

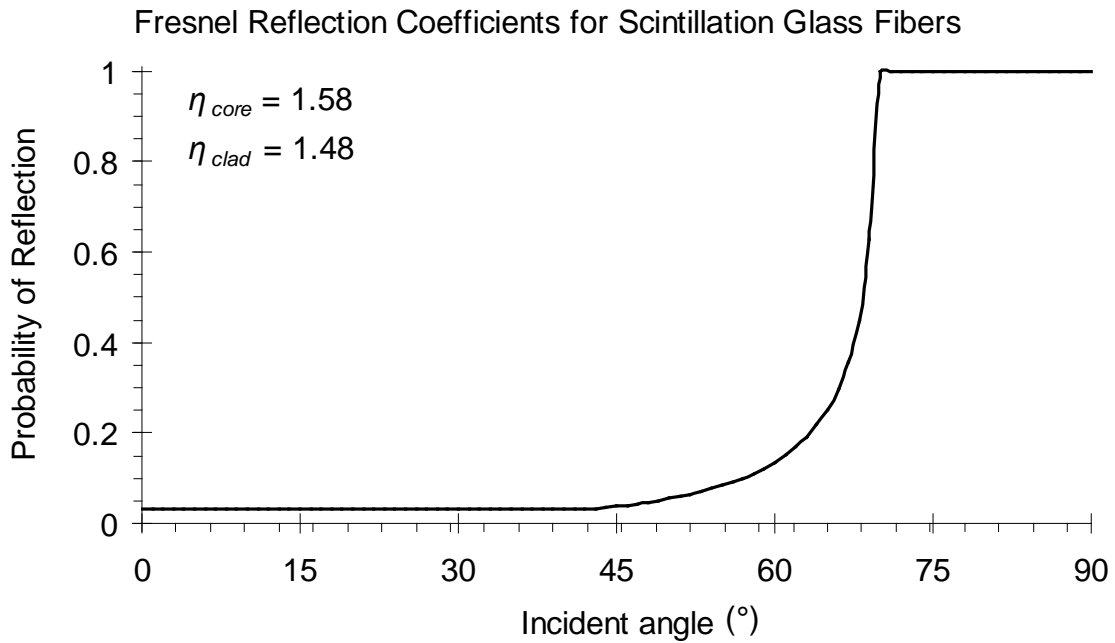
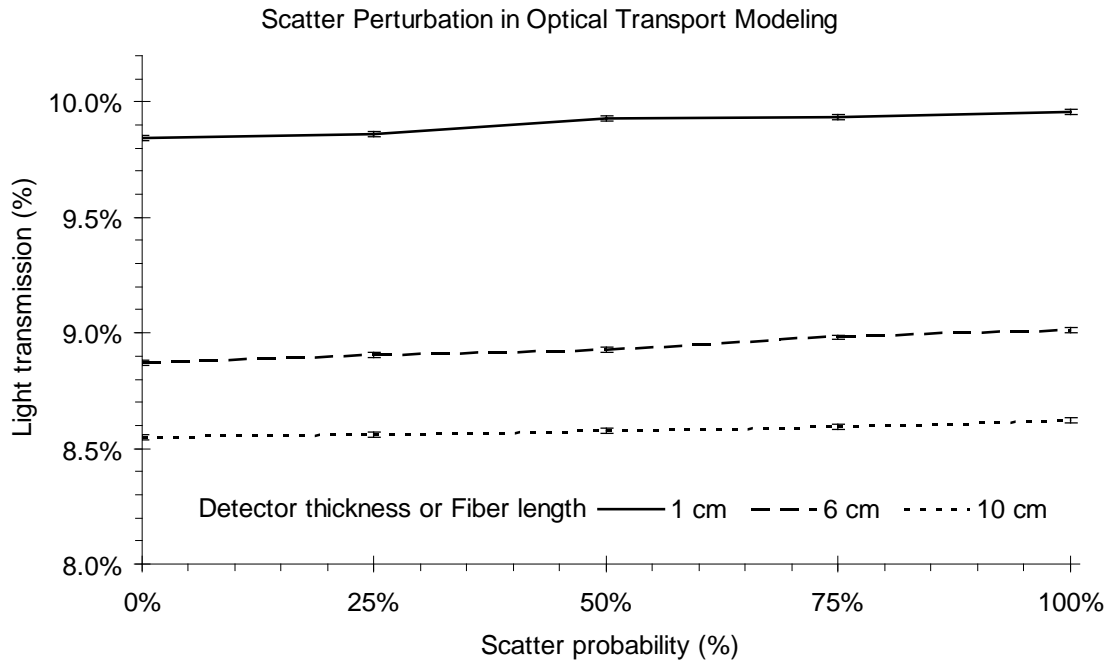


Figure 4-18. Fresnel reflection coefficients for the prototype scintillation glass fibers as a function of the angle of incidence.



Fiber diameter = 164 μm (70% Fill factor)

Figure 4-19. Effect of varying scatter conditions on simulated fiber-optic light transmission.

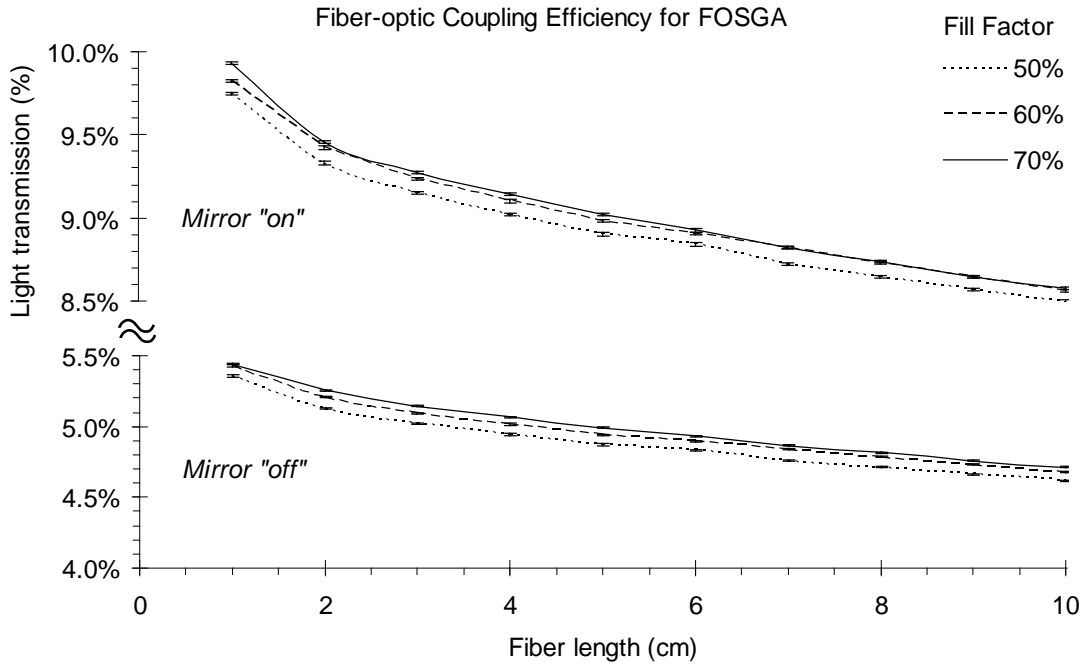


Figure 4-20. Light transmission efficiency for various fiber geometries obtained from light transport calculations.

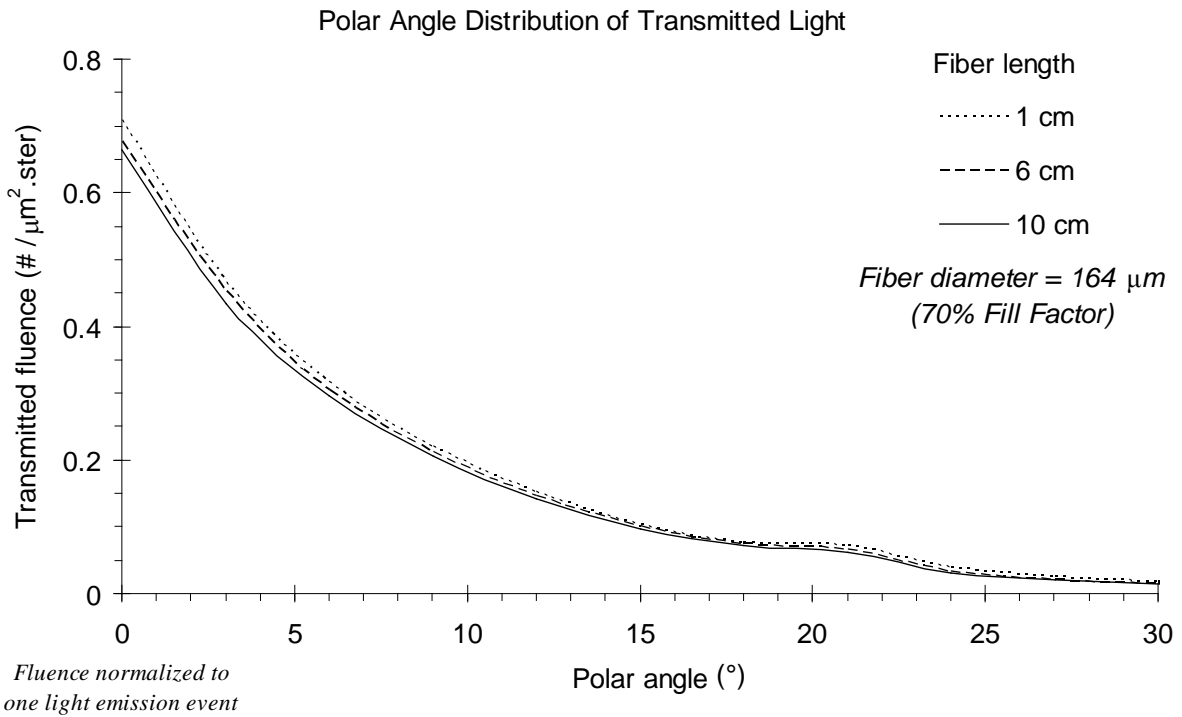


Figure 4-21. Polar angle distribution of light transmission obtained from light transport calculations.

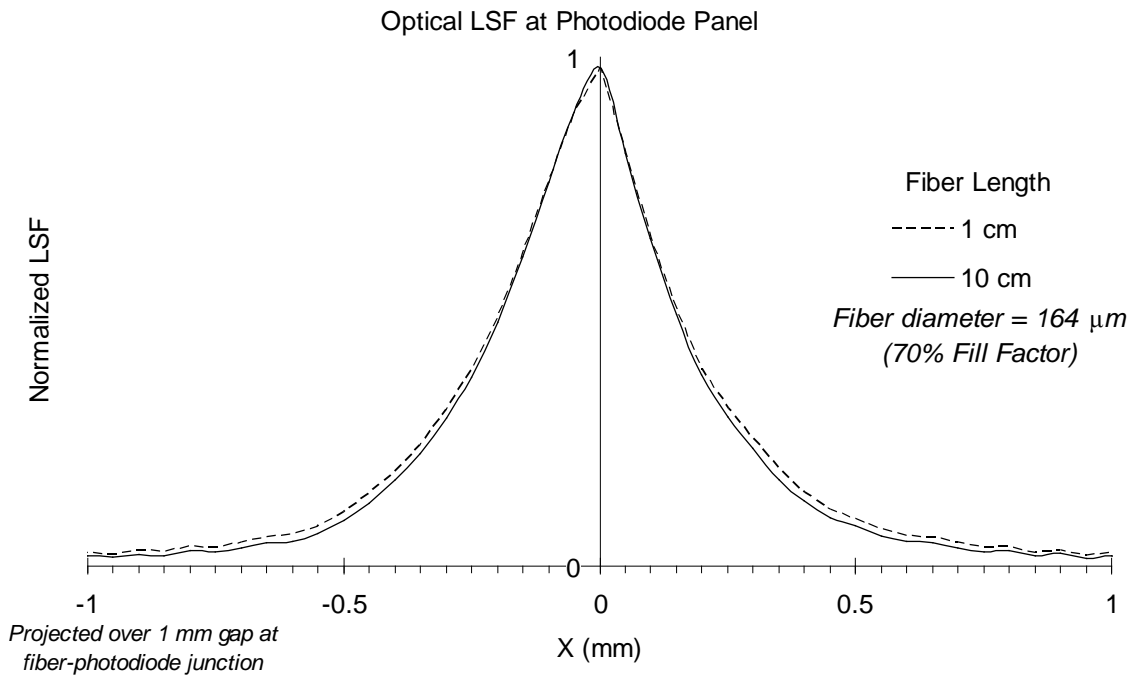


Figure 4-22. Optical LSF profiles for scintillation glass fibers obtained from light transport calculations.

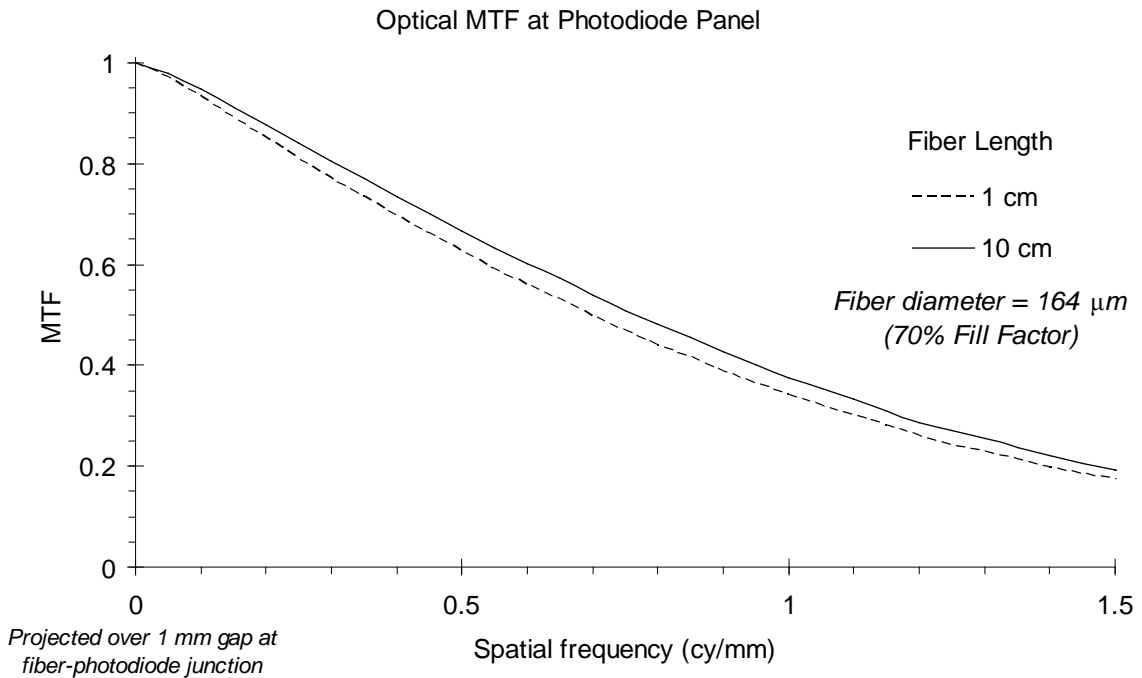


Figure 4-23. Optical MTF profiles for scintillation glass fibers obtained from light transport calculations.

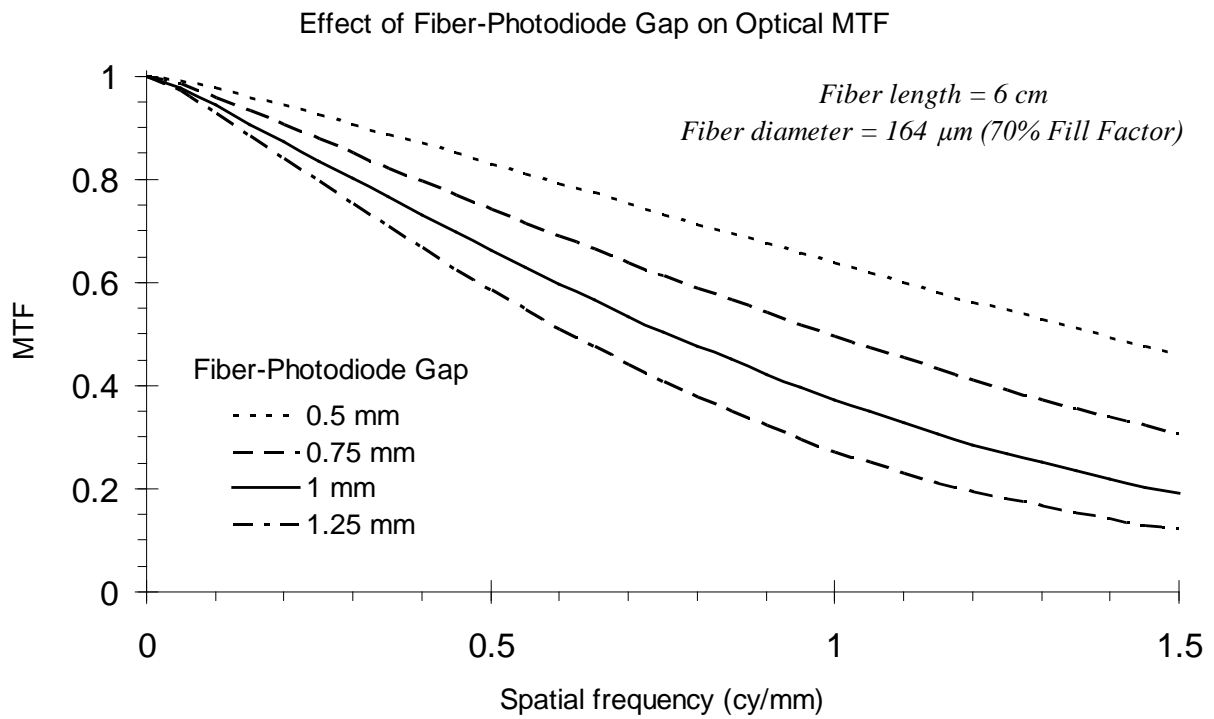


Figure 4-24. Sensitivity of the optical MTF to the fiber – photodiode contact gap.

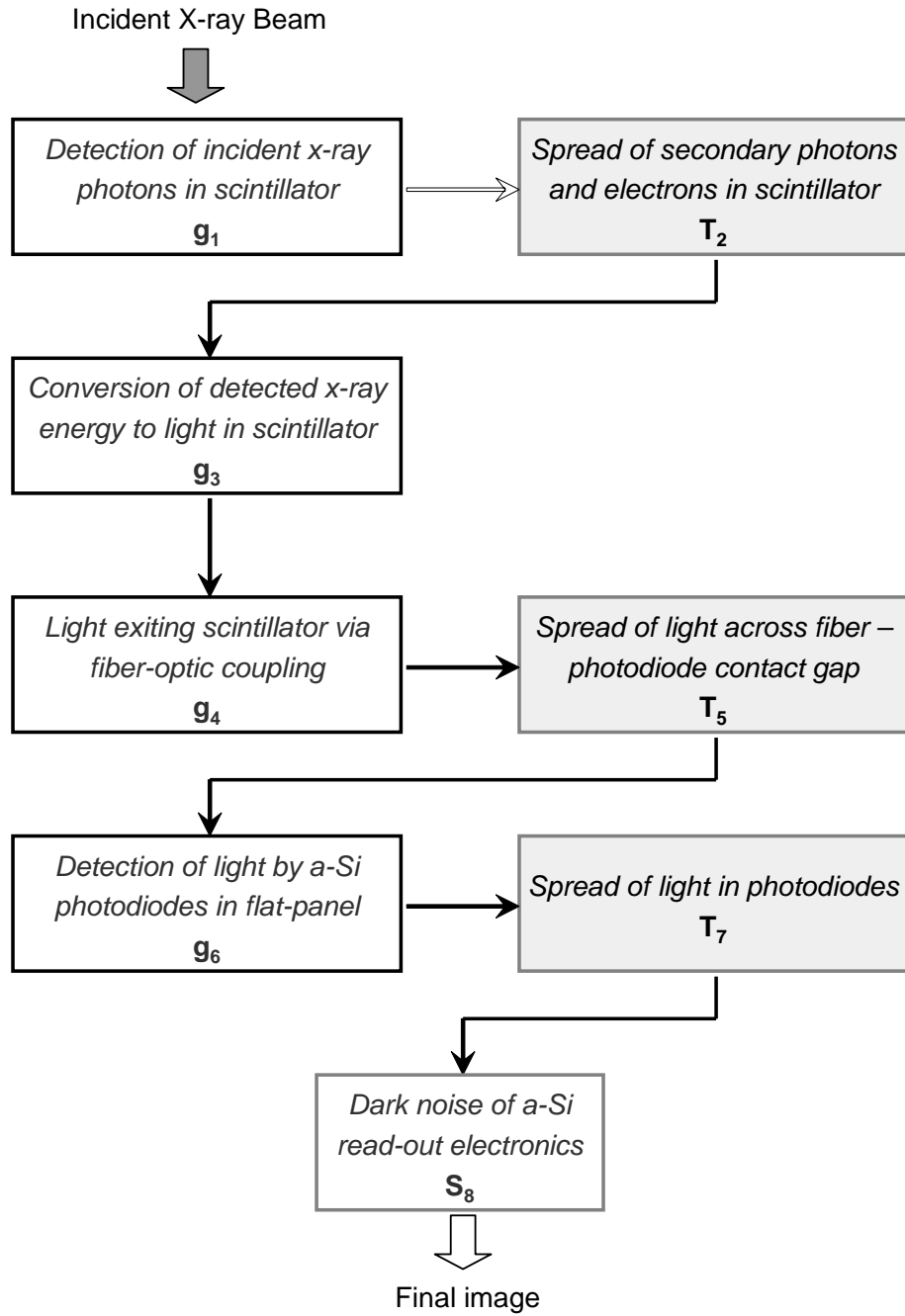


Figure 4-25. Linear cascaded systems model for the FOSGA detector.

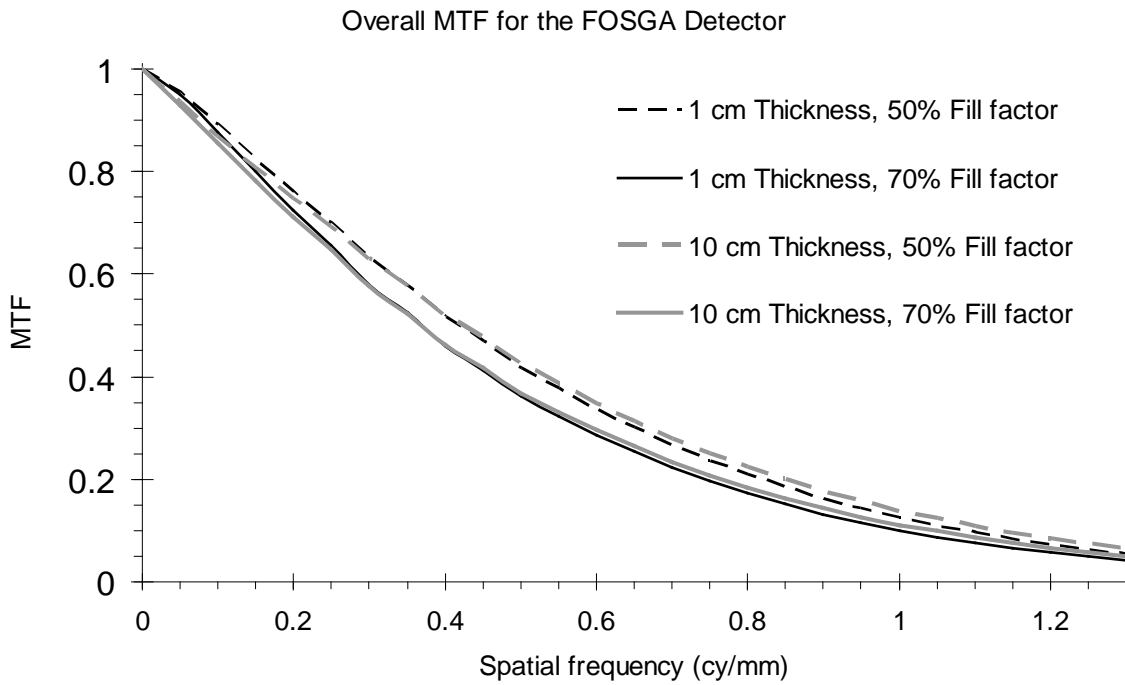


Figure 4-26. The overall MTF for a FOSGA detector at selected prototype configurations.

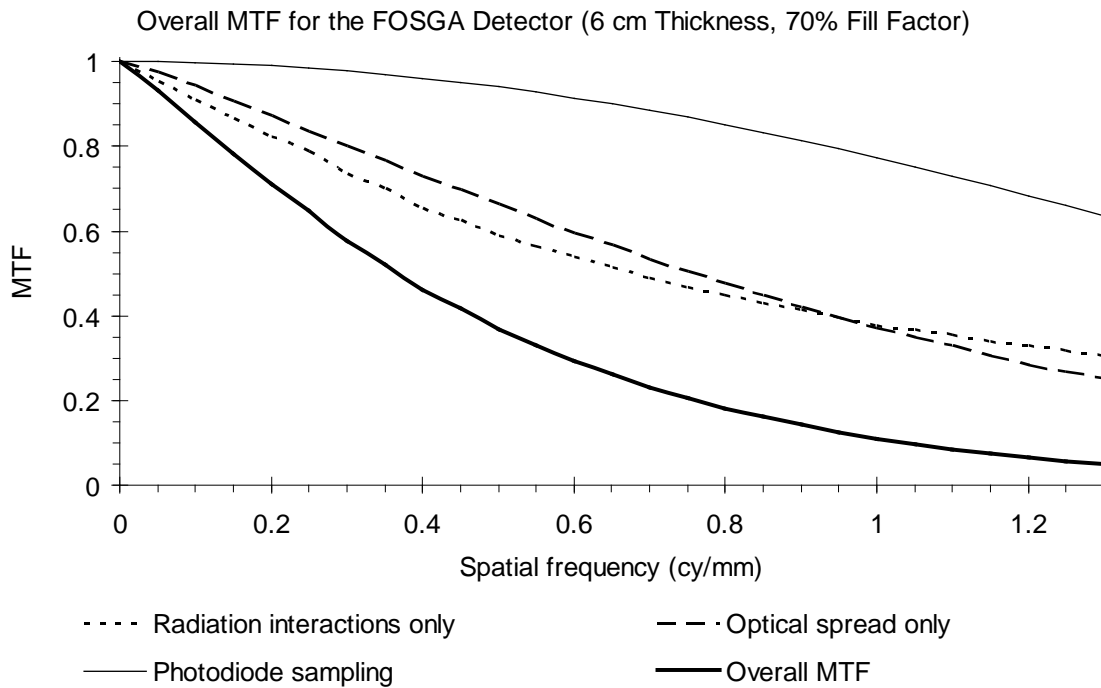


Figure 4-27. The overall MTF for a FOSGA detector in comparison with its component contributions.

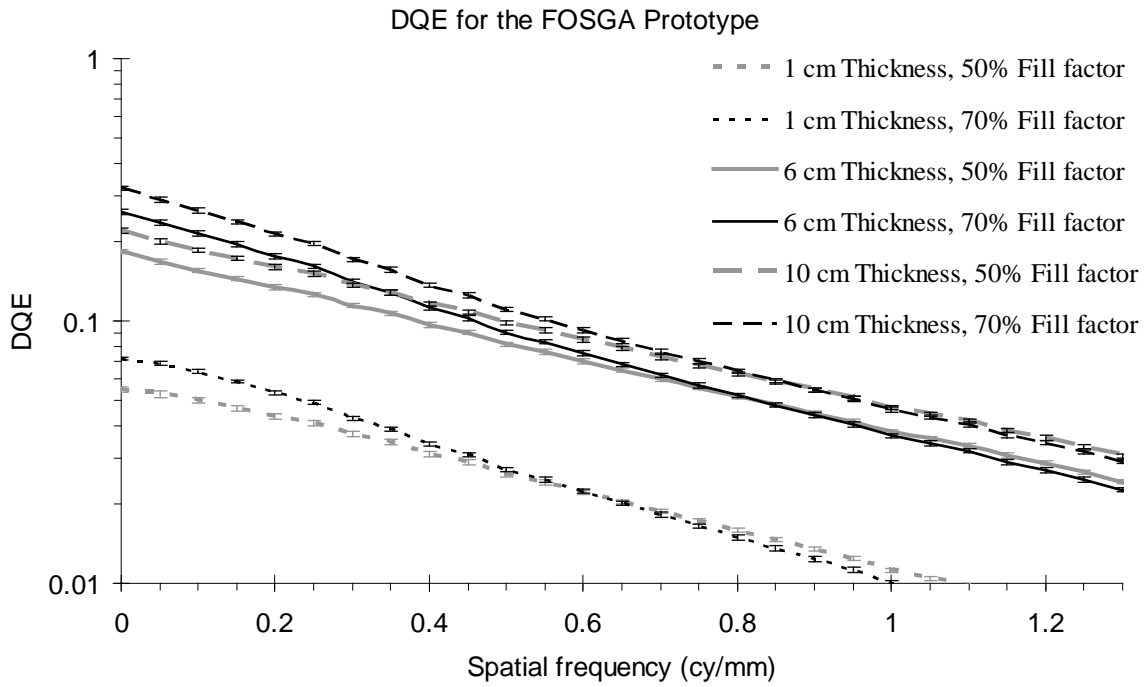


Figure 4-28. The overall DQE for a FOSGA detector for various prototype configurations.

CHAPTER 5 BAR-PATTERN METHODOLOGY FOR EPID QUALITY ASSURANCE

As part of the imaging research conducted to develop the EPID prototypes described in Chapters 3 and 4, an improved methodology to characterize imaging performance of megavoltage imagers was developed that enabled an accurate and reliable measurement of MTF, NPS, and DQE in a clinical setting. The method was developed as an adaptation of the original technique of MTF measurement using line-pair modulations (described in sections 2.1.1 and 2.1.4) to megavoltage imaging. In this chapter, a detailed theoretical treatment of the bar-pattern technique, and its adaptation and implementation with clinical EPIDs are presented along with a statistical comparison and validation with standard techniques. The fundamental aim of these studies was to extend the use of linear systems metrics (i.e. MTF, NPS, and DQE) that are typically only associated with imaging research to clinical EPID systems as part of routine quality assurance (QA).

5.1 Background

With the increasing importance of image quality in an IGRT based approach to radiotherapy, it is essential to rigorously monitor and maintain optimal levels of EPID imaging performance during clinical use through routine and extensive QA³⁰. Traditionally, portal imaging QA has been carried out by imaging calibrated line-pair and contrast resolution phantoms for a qualitative assessment of image quality¹⁷². QA phantoms can also be used in conjunction with image analysis software that provides quantitative indices of imaging performance¹⁷³. However, such methods of QA are limited by the fact that these indices may be arbitrarily defined and often dependent on user sensitivity and imaging conditions. They merely indicate relative trends in imaging performance which severely restricts any comparison to other imaging metrics. In addition, typical QA indices may not be sufficiently sensitive to all aspects

of image quality. On the other hand, linear systems metrics like MTF, NPS, and DQE can completely characterize radiographic detector performance while being normalized to imaging conditions like magnification, intensity gain settings and exposure. However, even as these metrics are considered mandatory in imaging research and detector development, they may not be feasible as QA parameters since traditional methods of obtaining them involve difficult and time consuming measurements of slit and edge response profiles that are not suitable for clinical workflow¹⁴².

The bar-pattern technique for MTF measurement provides a practical solution to implement linear systems metrics for clinical imagers since it is essentially based on phantom imaging that can be done quickly and easily without the need for a complex imaging set-up. The fundamental advantage of this method is its simplicity relative to the slit and edge techniques, as well as the fact that it provides direct visualization of imaging spatial resolution through the images of line-pairs. Bar-pattern based MTF measurements are limited mainly by the accuracy of the normalization at zero-frequency, which has to be approximated from large areas of the bar, and by the need to correct for the presence of higher-order harmonics of the fundamental frequency of the line-pairs that requires interpolation between the discrete spatial frequencies¹⁴². The sensitivity of the measurements to normalization errors is accentuated in megavoltage imaging due to the steeper fall-off of the MTF with spatial frequency compared to diagnostic imaging. Therefore, the bar-pattern method is not widely used for MTF measurements in megavoltage imaging, although line-pair contrast phantoms are often used in routine QA for “pseudo” or “relative” MTF measurements owing to its ease and speed¹⁷⁴.

In this study, a detailed analysis of the bar-pattern methodology for MTF measurements in megavoltage imaging is presented. Theoretical studies were conducted to identify satisfactory

measurement conditions for accurate normalization, and a method to obtain MTF spectra from line-pair modulations was developed. The major focus of this analysis was to compare and characterize the bar-pattern method with respect to the traditional slit and edge techniques to validate its accuracy. To this end, these methods were applied to three conventional portal imaging detectors: a Siemens Beamview video EPID (Siemens Oncology Care Systems, Concord, CA), an Elekta iViewGT a-Si EPID (Elekta Inc., Crawley, West Sussex, UK), and Kodak X-Omat V radiotherapy film (Eastman Kodak, Rochester, NY). Finally, the bar-pattern technique was implemented as a QA algorithm for clinical EPID systems to provide fast and easy MTF, NPS, and DQE measurements using portal images of open-fields and a bar-pattern QA phantom. The QA algorithm was analyzed for accuracy and sensitivity by comparing with a commercial QA technique (PIPSpro™, Standard Imaging, Middleton, WI) on the Beamview video EPID and iViewGT flat-panel systems.

5.2 Practical Aspects of MTF Measurements

The conceptual definitions of the slit, edge, and bar-pattern techniques were described previously (section 2.1), and some insight into the practical implementation of the slit response technique (most of which also translate to the edge method) was provided in the description of MTF measurements for the TSC prototype in Chapter 3 (section 3.3.4.1). However, the undesirable external influences of practical measurement conditions like scatter, beam divergence, and mechanical misalignments can affect each of the three methods differently. In principle, both the slit and edge response measurements can provide an accurate account of the LSF profile of an imaging detector for reliable MTF spectra on a near-analog spatial frequency domain. However, the accuracy of the calculations may be compromised with the presence of noise in the tails of the LSF profiles that can contaminate the Fourier spectrum of the profile¹²⁴. In order to minimize the tail noise relative to the peak, the central axis of the x-ray beam to be

aligned precisely with the center of the slit and edge target to maximize the x-ray transmission through the slit and the geometric gradient rendered by the edge. The alignment of slit and edge targets with the beam is especially difficult in megavoltage imaging due to the higher thickness of the attenuating metal blocks compared to diagnostic imaging. Typically, sophisticated mechanical and optical alignment aids are necessary, and the imaging set-up needs to be optimized through trial and error. This makes the measurements of slit and edge response profiles extremely difficult, laborious, and time consuming. Therefore, these methods cannot be implemented clinically on a routine basis.

Although the slit and edge response methods are both based on a Fourier transformation of the LSF, they may provide different results since the LSF is obtained differently in each case. Specifically, the edge method involves a finite-element differentiation of the ESF, which provides an LSF profile that is highly accurate in the terminal or tail regions but subject to errors in the peak region since the true LSF has to be estimated at each point as the gradient between adjacent pixels¹³¹. On the other hand, the LSF peak from a slit response measurement can be determined quite accurately. However, errors may be introduced when recovering the slit response baseline (either by subtracting the “closed” slit profile or by curve-fitting) due to the presence of scatter, noise and truncation artifacts^{122,175}. Therefore, the edge method is considered more accurate at lower spatial frequencies, while the slit method is preferable at higher frequencies¹⁷⁶.

For the bar-pattern technique, line-pair modulations may be affected by x-ray scatter off the edges of the bars. Scatter leads to a reduction in the detected modulation contrast associated with the line-pair bars. This may not always lead to significant variations in the overall MTF since modulations are finally normalized relative to each other. However, it contributes to

additional uncertainty in the overall measured MTF. Scatter contribution can be significantly minimized by imaging the bars at higher magnification, i.e. with adequate separation between the bar-pattern and the detector surface. In addition, bar-pattern modulations may be affected by geometric artifacts due to beam divergence. This effect is depicted in Figure 5-1. Since the “apparent” thickness of the bar seen along the path of the x-ray beam increases as one goes farther away from the central axis of the beam, the attenuation profile seen by the beam across the line-pair bars is altered in two ways. Firstly, the modulation intensity is enhanced resulting in exaggerated MTF values at points farther away from the center of the field. Secondly, the shape of the profile departs from the original square-wave pattern as shown in Figure 5-1. These geometric artifacts may be expressed at any point away from the center by examining the horizontal projection (Δw) of the thickness seen by the x-ray beam at that point, and also by the difference between the apparent and true thicknesses of the bar (Δt). In this case, Δw indicates variations in the represented spatial frequency due to the departure from a true square-wave. In general, geometric artifacts can be limited if the area and thickness of the bar-pattern are small enough compared to the source-bar distance.

5.3 Development of Bar-pattern Methodology

With the aim of characterizing the fundamental limitations to the accuracy of the bar-pattern method, the effects of imaging and general measurement conditions on the performance of the technique were studied.

5.3.1 Zero Frequency Normalization

Obtaining an accurate estimate of the zero-frequency normalization factor (i.e. M_0 in Equation 2-9) was fundamental to the development of a reliable methodology for absolute MTF measurements from line-pair modulations. Typically, large and uniform regions of the bar and background air are used to calculate M_0 . In this study, the width of the normalization area

(assumed to be equivalent squares for both bar and air regions) will be referred to as w , and its associated spatial frequency will be referred to as the normalization frequency or δ (where $\delta = 0.5/w$). The accuracy of M_0 is directly related to w and δ in that the estimated M_0 approaches the true zero frequency normalization only in the conditional limit of $w \rightarrow \infty$ (or $\delta \rightarrow 0$). Therefore, the normalization width w and the associated frequency (δ) may be interchangeably referred to the normalization condition for acceptable bar-pattern MTF measurements. The choice of an appropriate normalization condition (i.e. a sufficiently large w or a sufficiently low δ) is typically mediated by a trade-off between increasing w to enhance the accuracy of M_0 , and the practical limit to the size of the bar that is imposed by a finite imaging field. An acceptable normalization condition was assumed to be a value of w that was large enough so that any possible errors in M_0 (due to the inequalities of $w < \infty$ or $\delta > 0$) were insignificant relative to the uncertainty of measurement, while sufficiently small to be accommodated within the detector imaging area.

Monte Carlo simulations were used to study the effect of w on M_0 to identify an acceptable normalization condition. A series of square bar – air fields were simulated with w varied between 10 – 200 mm. The bar material was chosen to be tungsten due to its high Z and attenuation properties. The bar had to be made as thin as possible in order to minimize geometric errors from beam divergence, while also providing sufficient attenuation and contrast. Since 2 mm thick bar-patterns had been reported to provide modulations of acceptable contrast^{87,142}, the thickness of the tungsten bars was set at 2 mm. The detector was specified to be a commercial phosphor screen (1 mm thick copper build-up plate over a 134 mg/cm² layer of Gd₂O₂S:Tb) under irradiation from a point isotropic 6 MV x-ray source¹⁶⁵. The bar was positioned at “isocenter” (100 cm below the source), which was 50 cm above the detector plane (i.e. SDD = 150 cm). Since this provided a field magnification factor (M) of 1.5, the actual area of the bar

was made to be $(w \times w)/M^2$. With an equivalent size air region also specified adjacent to the bar, the effective imaging field was $(2w \times w)/M^2$ at the isocenter (with the edge of the bar – air field at the center). Energy deposition events were scored using the ITS 3.0 codes in 0.5 mm voxels, and M_0 was calculated as the difference in energy deposition between voxels underlying the centers of the bar and air regions. Between 10^7 and 10^9 histories were used in these simulations, and the exact number of histories was selected for each field to provide energy deposition tallies with a relative uncertainty in the range of 1 – 3% in voxels underlying the bar region (based on empirical estimates of uncertainty in actual images with comparable detectors). Separate simulations were carried out to obtain the “true” or intrinsic MTF of the phosphor screen by generating the intrinsic LSF profile for the phosphor screen. The calculated values of M_0 were normalized based on the true MTF at a spatial frequency of 0.05 cy/mm, which was also the highest value of δ that was simulated ($w = 10$ mm for $\delta = 0.05$ cy/mm). All values of M_0 were scaled equally by a factor such that $M_0 = \text{MTF}(0.05 \text{ cy/mm})$ at $w = 10$ mm. This reduced all simulated values of M_0 to a convenient form where $M_0 \rightarrow 1$ as $w \rightarrow \infty$, and the relative normalization error associated with any w was obtained as $1 - M_0$.

To represent a realistic imaging system and include the MTF contributions of imaging components that may be coupled to the phosphor screen detector in a conventional video or a-Si EPID, the values of M_0 with each δ was also scaled by an appropriate transfer function $T(\delta)$. In this case, $T(\delta)$ reflects the product of all MTF components that may be coupled to the intrinsic MTF of the phosphor screen in a hypothetical imaging system. For a video EPID representation, $T(\delta)$ included the optical blurring within the screen, and the lens – camera system (obtained during the analysis of MTF for the TSC system). For a-Si EPIDs, $T(\delta)$ included the optical blurring within the screen, and the pixelization by the a-Si photodiode array (obtained as a pixel

sinc function for standard pixel widths ~ 0.4 mm). The MTF due to optical blurring in the phosphor screen was obtained from reported results⁵⁸. The scaling of $M_0(\delta)$ with $T(\delta)$ rendered a steeper reduction in M_0 with δ (or a greater increase in M_0 with w). The effect of the normalization condition on M_0 can be seen in Figure 5-2. As expected from typical shapes of MTF spectra, it was found that the rise of M_0 with respect to w was more pronounced at low values of w . For both the video and a-Si EPID representations, M_0 was significantly lower ($p < 0.1$) than unity for $w < 40$ mm. Previously reported implementations of the bar-pattern technique for megavoltage MTF measurements used normalization areas in the above range^{87,173}. No statistically significant variations were observed in M_0 upon increasing w beyond 100 mm ($p > 0.3$ for $w > 100$ mm). In this case, the specified p-values indicate probability estimates of significant differences based on standard Student's t-tests. From these results, a minimum normalization condition of $w = 100$ mm was found to be necessary for an accurate value of M_0 . It must be noted that, w and δ represented the normalization condition and spatial frequency projected at the plane of the detector.

5.3.2 Bar-pattern Design

A custom designed bar-pattern was manufactured to perform measurements of MTF on commercial portal imagers. Line-pair targets were milled into two 2 mm thick 100 x 50 mm² tungsten bar using precision electrode discharge machining. The following spatial frequencies in line-pairs per mm (lp/mm) were generated: 0.05, 0.1, 0.2, 0.3, 0.5, 0.75, 1, 1.3, 1.6, 2 and 2.5. Selected spatial frequencies were milled into both bars to check for possible differences due to manufacturing variations and other forms of departure from shift invariance. A third tungsten bar of the same area and thickness was used without any spatial frequencies for the normalization measurement (M_0). With these dimensions, the normalization condition rendered by the bar-pattern is given as $w = 100 \times M$ mm, where the magnification factor M depends on the imaging

geometry. The bar-patterns are shown in Figure 5-3. Kilovoltage radiographs (40 kVp, 30 mAs) of the three bars are shown in Figure 5-4. The higher spatial frequencies are positioned closer to the center to minimize effects of beam divergence. Based on edge profiles from these radiographs, the line-pair fabrication was found to be accurate to within 1%. The effective range of spatial frequencies contained in the bar-pattern depends on the magnification M of the imaging field. The above series of frequencies were designed for imaging at the linac isocenter for a maximum spatial frequency of 1.5 – 2 cy/mm depending on the imaging system.

5.3.3 Effect of Scatter

To limit the contribution from scatter, a set-up where $M = 1$ with the bar-pattern placed directly on the surface of the detector is not desirable. If an isocentric set-up is used with the bar-pattern placed 100 cm below the source, M is likely to range between 1.3 and 1.6 based on SDDs for typical clinical EPIDs. In order to observe the effect of scatter on line-pair modulations as a function of magnification, the 2 mm thick tungsten bar-pattern was imaged at varying magnification using a Siemens Beamview video EPID (SDD = 132 cm). Line-pair modulations were recorded with the bar-patterns placed at various distances (0, 2, 5, 10, and 32 cm) from the detector surface, providing a spread in imaging magnification of $1 < M < 1.32$. It was found that for all spatial frequencies within the Nyquist limit, the detected modulation contrast values were statistically equivalent ($0.35 < p < 0.94$, average $p = 0.76$) in all cases when the distance between the bar-pattern and the detector surface was at least 5 cm. With the bar-pattern placed less than 5 cm above the detector surface, the modulation contrast was significantly lower ($0.003 < p < 0.08$, average $p = 0.03$). These results indicated that the effect of scatter could be overcome as long as the bar-pattern was at least a few cm away from the detector surface ($M \geq 1.05$). Since most clinical imaging is performed with the patient at isocenter, the placement of the bar-pattern is

most desirable at the isocenter so that the measurement can appropriately indicate the MTF contribution from the linac focal spot.

5.3.4 Beam Divergence

In order to quantify the effect of beam divergence for the bar-patterns positioned in the imaging field as shown in Figure 5-3, the attenuation profile seen by x-rays emanating from a point source as they traverse the line-pairs in the bar-patterns was determined theoretically by simple geometric ray tracing. Profiles were generated for SDD = 160 cm, with the bar-pattern situated 100 cm from the source, i.e. $M = 1.6$. Similarly, profiles were generated in the absence of beam divergence, i.e. assuming a broad beam parallel source. No visually discernible differences were found upon graphically plotting these two profiles together. To further investigate the effect, the profiles were convolved with the LSF measured for a Siemens Beamview (during the analysis of the TSC system) to simulate the detected line-pair modulation response with and without the effect of beam divergence. The modulation contrast values were determined for all spatial frequencies to check for possible differences due to beam divergence, especially for lower frequencies located away from the center. However, no significant differences were observed in the calculated modulation values ($0.42 < p < 0.99$, average $p = 0.93$), confirming the feasibility of imaging the bar-patterns as shown in Figure 5-3 with a magnification as high as $M = 1.6$.

5.4 MTF Measurements for Clinical Portal Imagers

The custom designed bar-pattern was used to perform MTF measurements for clinical portal imagers in tandem with the separate uncut bar for zero frequency normalization.

5.4.1 Description of Portal Imagers

To validate the accuracy of the bar-pattern methodology with improved zero frequency normalization, MTF measurements were conducted for three commercial megavoltage imaging

systems (Siemens Beamview video EPID, Elekta iViewGT a-Si flat-panel EPID, and a traditional metal plate – film combination. The Beamview system (previously described in section 3.3.2) was installed on a Siemens PRIMUS linac with SDD = 132 cm. It consisted of a standard phosphor screen detector coupled to the lens and prototype Plumbicon camera configuration that was used for the TSC prototype. The iViewGT system consisted of an identical phosphor screen that was coupled to a flat-panel read-out array (1024 x 1024 pixel², 0.4 mm detector pixel width). It was used as originally installed on an Elekta Precise linac with SDD = 160 cm. The metal plate – film combination consisted of Kodak X-Omat V therapy film with a 3 mm thick brass build-up plate. Film imaging was conducted under the Siemens linac with the brass – film combination placed atop the phosphor screen panel of the BEAMVIEW with the same SDD (132 cm). Prior to MTF measurement, a series of open-field exposures at various exposures were acquired with the metal – film combination to obtain H/D curves (that describe the nonlinear calibration of pixel intensities with imaging exposure). Imaging was conducted with 6 MV x-rays for all MTF measurements, and all images were acquired using an exposure of 25 MU.

5.4.2 Slit and Edge Measurements

An angulated slit target was constructed, set-up and aligned with the radiation central axis using the same procedure that was outlined for MTF measurements with the TSC prototype (section 3.3.4.1). Oversampled LSF profiles were generated by using the cyclic variations in the slit response peak intensities over pixel rows to evaluate the slit angle, and populate the LSF grid with the shifted superposition reconstruction technique as described for the TSC. The edge target was rendered by using only one of the 10 x 10 x 16 cm³ steel blocks. As in the case of the slit, the angulated edge was aligned with the radiation beam by adjusting its position for a maximal gradient at the center of the edge response. Several edge images were acquired and an

oversampled ESF profile was obtained based on the method described by Buhr et al¹⁷⁷, which was essentially an adapted variation of the slit response analysis. In this case, the positions of the edge locations were determined along each row of the edge response image based on maximal gradient. The angle of the edge was calculated by determining the average number of rows associated with the transition of the edge location along one full pixel column. Finally, the oversampled ESF was populated via the shifted superposition approach, and a corresponding oversampled LSF was subsequently calculated using finite-element differentiation. The slit and edge angulations in all the imaging measurements were found to be between 2-2.2° resulting in a minimum sampling distance of ~ 10 – 15 μm. However, the oversampled slit and edge response functions were rebinned in sampling grids of 50 μm in an effort to minimize noise. The shifted superposition based oversampling was not required for film measurements since aliasing could be prevented by simply selecting a small sampling aperture for the film digitizer. The films were digitized using an Epson 10000XL film scanner with contrast and spatial resolution respectively set to 16-bits and 2400 dpi, equivalent to a sampling aperture of < 11 μm. The angle of the slit and edge targets was determined from these scanned images similarly based on peak slit response and edge gradients, and the images were rotated to obtain straight slit and edge response profiles. Row profiles were taken and rebinned to obtain LSFs with a sampling width of 50 μm. The presampled MTF was calculated for each image and individual estimates were averaged to obtain an estimate of uncertainty.

5.4.3 Bar-pattern Measurements

The bar-patterns were positioned as shown in Figure 5-3 in an isocentric set-up, i.e. 100 cm below the source. The bars were angulated at approximately 45° with respect to the imaging axis. This was done to avoid sampling phase effects, in which the MTF may be dependent on the coincidence between the centers of the bars and imaging pixels. Placing the bars at some

angulation helped to average these effects out. The placement of the bars was done manually as only approximate positioning was required. A field size of $20 \times 20 \text{ cm}^2$ was sufficient to contain the bars. Several images of the bar-patterns were acquired. To estimate any baseline artifacts including scatter from the two main bars containing the line-pair sets that could possibly affect the normalization factor M_0 , several images were acquired after carefully removing the uncut bar from the field without disturbing the positions of the bars containing line-pairs. Film images were scanned at 16-bits and 100 dpi ($250 \mu\text{m}$ sampling width). During the analysis of the images, an ROI was manually drawn to select the image area corresponding to the line-pairs for each spatial frequency f , and the statistical variance $V(f)$ of the image intensities in each ROI was calculated. This estimate of variance also included image noise associated with the detector that had to be subtracted out. This was accomplished by obtaining variance values from open field exposures at the same ROIs as the line-pairs, and subtracting them from the line-pair variances. Line-pair variances were sampled for all frequencies whose modulation peaks were clearly resolvable.

To estimate the normalization factor M_0 , profiles along the central uncut bar were acquired and baseline corrected by subtracting the corresponding profiles with the uncut bar removed from the imaging field. The value of M_0 was measured by taking the difference between pixel intensities associated with the centers of the image areas underlying the uncut bar and an equivalent size adjacent air region. The MTF was calculated using the sampled values of $V(f)$ and M_0 estimates according to Equation 2-9. The corrections for higher order harmonic components $V(nf)$ required interpolation to evaluate variance values between discrete frequencies. Three methods of interpolation were investigated: cubic spline fits, simple exponential fits, and linear interpolation. However, no significant differences were observed between the results from each

method indicating that the shape of the MTF was adequately sampled by the spatial frequencies presented by the bar-patterns. Therefore, linear interpolation was selected since it was the simplest of all three methods, and the computation of standard error estimates using error propagation was quite convenient.

5.4.4 Comparison of Slit, Edge, and Bar-pattern Techniques

The MTF measurements obtained from the EPID and film systems are presented in Figure 5-4. Although they used the same phosphor screen, the MTF for the Beamview was significantly lower than that for the iViewGT due to the loss in spatial resolution from the lens and camera target. On the other hand, the film measurements provided the highest MTF of all three systems, which was expected on account of their low thickness and analog resolution. To compare the slit, edge and bar-pattern methods, the differences in MTF values between the individual techniques were examined for statistical significance over all spatial frequencies. Comparisons were performed at the discrete spatial frequencies presented by the bar-pattern at the imaging plane. Overall, all three methods were found to be in excellent agreement with each other (mean difference within $\pm 3\%$). Few selected instances of significant differences (identified by $p < 0.1$) were observed.

For the Beamview, the slit measurement was found to be significantly different from the other two methods at 0.04 cycles per mm (cy/mm), while the slit and edge methods were in disagreement at 0.57 cy/mm. None of the methods were in agreement at 0.76 cy/mm, at which point, the MTF was very close to zero. For the iViewGT flat-panel, the edge and bar-pattern methods were found to be different at 0.81 cy/mm, while all three methods were in disagreement at the detector Nyquist limit of 1.25 cy/mm, where the MTF was nearly zero. For the brass-film combination, no significant differences were observed between any of the techniques at any spatial frequency. Finally, when the bar-pattern measurements were compared with a

combination of slit and edge measurements pooled together, no significant differences were obtained. Therefore, despite isolated instances of significant differences in MTF values in pair-wise comparisons of the three methods, there was no clear evidence of the bar-pattern method providing significantly different results from both the slit and edge techniques.

The random pair-wise instances of significant differences in MTF observed in the above MTF spectra may be attributed to fundamental differences in the nature of the three MTF measurement techniques over the spatial frequency range studied, where one technique may be specifically associated with relatively greater error. For example, the slit method may be considered less accurate than the edge method at lower spatial frequencies and vice versa. Based on the statistical analyses, it was shown that overall, the three techniques yielded similar MTF curves, and that the use of line-pair modulations was an effective means to measure MTF for megavoltage imaging devices.

5.5 Implementation for EPID QA

Following the validation of the bar-pattern technique as a simple, fast, and accurate means to obtain MTF measurements in megavoltage imaging, its use for clinical EPID QA was a logical extension to these studies. A modular automated algorithm was developed (Matlab 7.0, MathWorks, Natick, MA) that evaluated user supplied images of bar-pattern and open field images to calculate MTF, NPS, and DQE. A simple corner detection algorithm was included in the modular code that used vertical and horizontal edge detection gradients in conjunction with the orthogonal geometry of the bar-patterns to isolate its corners. Upon identifying the corners, built-in ROI locations are accessed to determine variance selections and normalization regions for applying Equation (2-9). The program was also designed to read in system specific information (pixel width and SDD) as user supplied parameters to automatically determine the imaging magnification and evaluate spatial frequencies at the detector plane. A snap shot of a

sample bar-pattern image acquired during a test QA session for an Elekta iViewGT flat-panel EPID is shown in Figure (5-6) with the phantom corners, line-pair and normalization ROI selections highlighted. The calculated MTF spectra and associated uncertainties are automatically determined (using Equation 2-9) and written to output files.

The NPS calculations were based on reading in two or more open-field images of identical exposure and field size ($\geq 10 \times 10 \text{ cm}^2$ projected at the detector surface). The NPS is calculated as previously described in section 2.2 and Equation (2-11), for a central region of $2N \times 2N$ pixel² selected in each open-field. The value of N was selected to ensure a minimum area of $10 \times 10 \text{ cm}^2$. The use of data array sizes that are powers of two is aimed at minimizing the quantization noise associated with conventional fast Fourier transform (FFT) algorithms that are used in NPS calculations. Finally, the DQE is evaluated based on the calculated MTF and NPS spectra according to Equation (2-15). The fluence factor Φ for the normalization of the DQE is determined in the manner described in section 3.3.4.3 based on the exposure (MU) used to image the open fields in conjunction with tabulated fluence – dose conversion factors and beam spectra that were specified as parameter files.

5.6 Sensitivity Analysis

To evaluate the potential of MTF, NPS and DQE as EPID imaging QA parameters, they were evaluated for their sensitivity to subtle changes in image quality. Images of the bar-patterns and open fields used to evaluate these parameters were subjected to varying levels of degradation of image quality. Loss in spatial resolution was simulated by convolving the bar-pattern images with Gaussian blur kernels. The shape or width of a Gaussian blur kernel is typically specified by the full-width-half-maximum of the kernel profile (commonly referred to by σ). However, in this article, we refer to the full-width-half-maximum of the kernel by FWHM, in order to avoid confusion with imaging noise, a standard deviation measure, that is also denoted by σ . Gaussian

kernels with FWHM ranging from 0 – 2 pixels were convolved with the bar-pattern QA phantom images and the MTF values calculated by our QA algorithm were observed. On the same lines, the open field images were subjected to increased levels of additive noise. Gaussian noise patterns were simulated and added to the open field images. The magnitude of the simulated additive noise was selected based on the subsequent increase in open field noise (obtained by evaluating the standard deviation σ of open-field pixel intensity values). Noise levels were varied to the end of simulating a 0 – 100% increase in σ . In each case, the NPS and DQE values calculated by our QA algorithm were recorded.

For comparison, the sensitivity of a commercial PIPSpro QA algorithm¹⁷³ (Standard Imaging, Middleton, WI) was also studied for the same simulated variation of image quality degradation. The PIPSpro technique also utilized a line-pair resolution phantom that contained a few discrete spatial frequencies along with uniform regions of varying attenuation. In this case, the PIPSpro phantom images were analyzed by its accompanying software, which provided three indices of image quality: F_{50} , Σ , and CNR . The F_{50} is an index of overall spatial resolution and represents the spatial frequency corresponding to a 50% reduction in MTF. In reality, this value is overestimated since it is obtained with a “relative” MTF curve normalized at the lowest spatial frequency contained in the phantom (0.1 lp/mm)¹⁷³, resulting in significantly exaggerated MTF spectra. However, it was presumed that the PIPSpro F_{50} could still be used a spatial resolution index for relative QA. The average of standard deviations of pixel intensities associated with two reference regions on the phantom is used by the PIPSpro software to obtain Σ . The CNR metric is evaluated by the PIPSpro software as the contrast value between the two reference regions normalized to Σ . The sensitivity study was conducted for both the

Siemens Beamview and Elekta iViewGT systems, and relative changes in the values of all tested metrics with image degradation levels were used to characterize their merits.

The MTF measurements obtained from images of the bar-pattern for the Beamview and iViewGT systems with simulated Gaussian blurring are shown in Figure 5-7. Figure 5-8 indicates the effect of additive Gaussian noise on the NPS. It can be seen that increasing the noise by a 100% relative to the open-field σ led to an order of magnitude increase in the NPS. While σ indicated an overall standard deviation metric that includes random as well as structured noise sampled across a raw open-field image, the NPS is strictly a variance measure that specifies only the random noise within the open-field. Therefore, although a 100% increase in σ (i.e. doubling the noise) is expected to increase the NPS only by a factor of four, the measured NPS was significantly greater indicating a considerable contribution of structured noise to the open field σ . The sensitivity of DQE to additive Gaussian noise is depicted in Figure 5-9. The DQE showed a corresponding decrease by an order of magnitude in response to increasing the open-field noise by a 100%. The depletion of DQE showed a strong dependence on spatial frequency by virtue of its proportionality with the square of the MTF. No variation of DQE with Gaussian blurring was expected since the simultaneous effects of blurring on MTF^2 and NPS cancel each other out.

The iViewGT is expected to have higher DQE compared to the Beamview since a-Si EPIDs have significantly better optical coupling characteristics compared to traditional lens-coupled camera EPIDs that are limited by the poor light collection efficiency of the lens focus geometry. However, from our measurements, it was observed that the DQE of the Beamview system was slightly greater than that of the iViewGT system at low spatial frequencies (< 0.3 cy/mm). This can be attributed to the superior performance and reduced dark noise of the

prototype camera system in the modified Beamview EPID. In addition, the performance of the iViewGT system used in this study was markedly reduced relative to its performance at commissioning (2001), which could possibly be due the effects of radiation damage.

In order to demonstrate the sensitivity of the MTF, NPS and DQE in response to simulated blurring and additive noise, they were compared with PIPSpro indices. Since the F_{50} , σ and CNR are singular metrics that correspond to a single spatial frequency, a comparison with fundamental imaging parameters evaluated in spectral form is difficult. Therefore, the areas under the curve taken for the MTF, NPS and DQE, i.e. $\int MTF$, $\int NPS$ and $\int DQE$, were evaluated to present singular forms of these parameters. Even though the integration of MTF, NPS and DQE curves leads to the loss of spatial frequency information, the integrated values include contributions from all spatial frequencies. For ease of comparison, the PIPSpro indices as well as the $\int MTF$, $\int NPS$ and $\int DQE$ metrics are expressed in terms of % change in Figures 5-10, 5-11, and 5-12. It was seen that the sensitivity curves of PIPSpro indices were clearly lower than those observed for $\int MTF$, $\int NPS$ and $\int DQE$.

Compared to a 16% reduction in F_{50} , the value of $\int MTF$ was reduced by 28% in response to a Gaussian blurring kernel with $FWHM$ of 2 pixels for the Beamview. Similarly, for the iViewGT, the $\int MTF$ decreased by 37% while the F_{50} only dropped by 27% for a Gaussian blurring kernel with $FWHM$ of 2.5 pixels. Similarly, the $\int NPS$ and $\int DQE$ curves were far more sensitive to additive noise compared to the PIPSpro σ and CNR indices. For the Beamview, a 100% increase in open-field noise led to an 89% loss in CNR (σ increased by a factor of 8) and a 97% loss in $\int DQE$ ($\int NPS$ increased by a factor of 27). In the case of the iViewGT system, the $\int DQE$ was reduced by 91% ($\int NPS$ increased by a factor of 15) while the CNR dropped by 68% (σ increased by a factor of 3) with a 100% increase in noise. The remarkably greater

sensitivity of linear systems metrics like MTF, NPS, and DQE compared to the PIPSPRO system can be directly related to their conceptual forms. Existing QA techniques like PIPSPRO monitor a narrow window of spatial frequencies and therefore, their ability to detect any degradation in EPID image quality is inherently compromised and limited. On the other hand, the computation of MTF, NPS and DQE spectra can monitor the relevant range of spatial frequencies entirely, which enhances the sensitivity of these metrics. The MTF can be used to comprehensively monitor spatial resolution using either the entire curve or by using summary metrics like \int MTF. Similarly, normalized and relative SNR and CNR based metrics that essentially represent zero or low spatial frequency (i.e. extremely large and uniform objects) cannot match the sensitivity of DQE or \int DQE in characterizing contrast or overall image quality.

Routine QA measurements of MTF, NPS and DQE provide an effective method to quantify any loss in image quality that may be induced during everyday clinical use like mechanical damage, misalignments, inappropriate calibration, mistimed gating sequences, radiation damage to peripheral electronics, etc. The bar-pattern based QA approach provides a basis for characterizing imaging performance for a clinical EPID system relative to critical standards set during commissioning. Moreover, since user specific inconsistencies like exposure, SSD, and field size that may affect qualitative QA methods are for the most part automatically accounted for in measurements of MTF and DQE, these can be more effectively compared to other clinical systems as well as reported measurements of research prototypes. This is demonstrated in Figure 5-13, wherein the degradation in MTF and DQE over time is shown for an Elekta iViewGT flat-panel EPID based on measurements conducted during commissioning in 2001 and more recently in 2008. For comparison, the MTF and DQE spectra reported for a research prototype of an a-Si EPID⁵⁸ using the same phosphor screen as the Elekta system is also

shown. Although widely considered to be a parent prototype to commercial flat-panel EPIDs¹⁷, the significant difference in imaging performance between the prototype and the clinical device even at commissioning can be easily seen in Figure 5-13. Possible reasons for this difference may be variations in the TFT electronics, and superior panel optimization and alignment techniques used during the prototype research phase. In this case, the ability to compare clinical image quality with the theoretical upper limits usually demonstrated with research prototypes could be useful in evaluating possible effects of the choice and/or quality of the luminescent detector, metal build-up plate, a-Si read-out array, and the source characteristics for the linac.

The potential use for practical imaging QA using the bar-pattern methodology for EPID systems in radiation oncology centers would be dependent on the establishment of image quality standards to be used as guidances for decision making along the same lines as conventional QA protocols. For example, clear and direct relationships need to be established between the necessary image quality for clinical applications (eg. image registration and dosimetry) and the measured linear systems metrics based on MTF and DQE. The link between imaging performance and the efficacy of clinical use may be enforced based on physician specified tolerances. Finally, routine QA measurements may be performed and compared to such tolerance standards to recommend appropriate actions (eg. recalibration of electronics, system alignment checks, and replacement of screen or a-Si flat-panel). In the studies discussed in this chapter, the bar-pattern based QA methods were shown to be ideally suited for clinical EPID QA. The robustness and accuracy of linear systems metrics, and the simplicity of bar-pattern QA make this technique an invaluable tool to ensure optimal portal image quality.

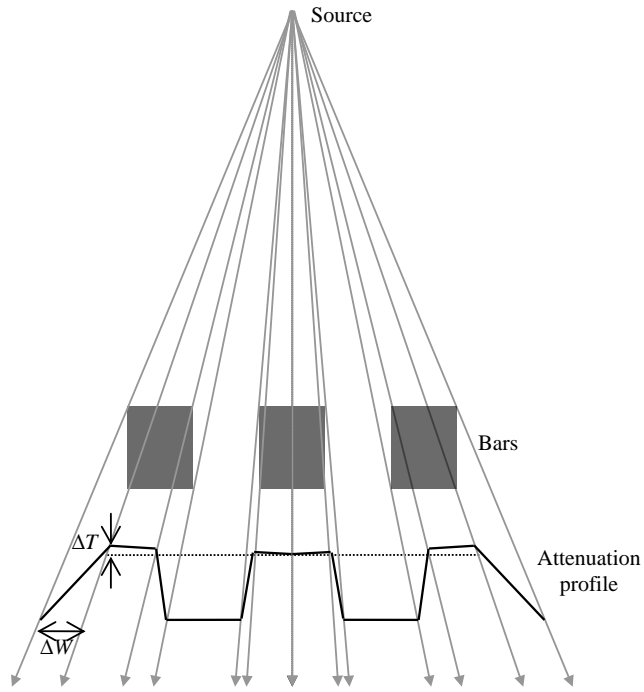


Figure 5-1. Effect of beam divergence on line-pair modulations.

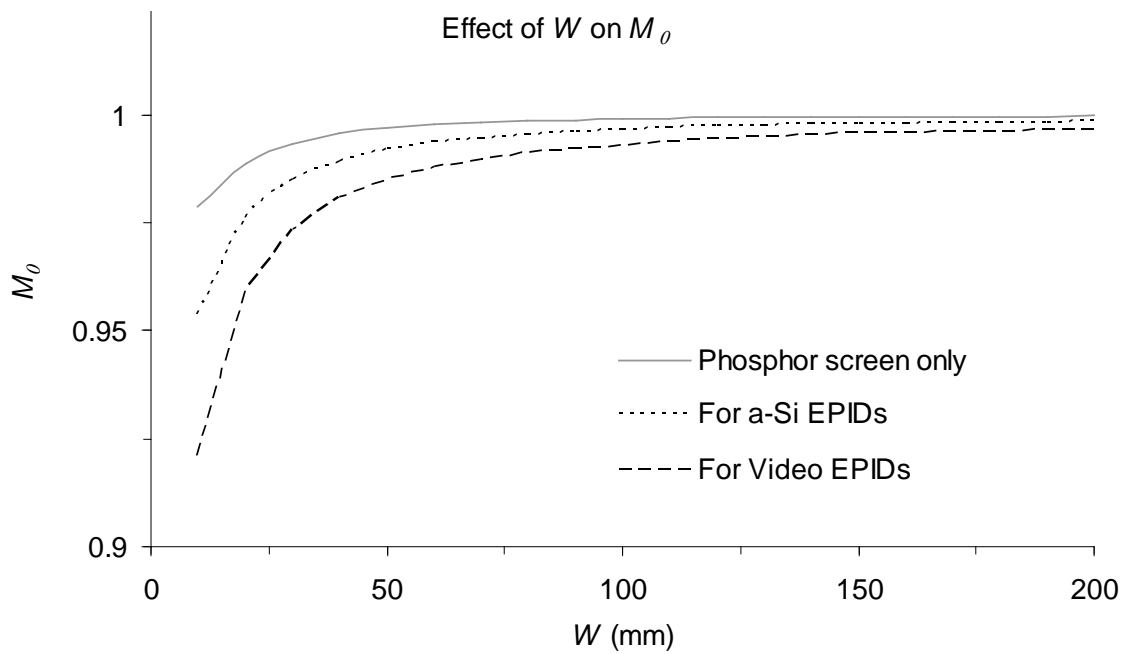


Figure 5-2. Effect of the normalization condition on the accuracy of the zero frequency normalization in bar-pattern MTF measurements.

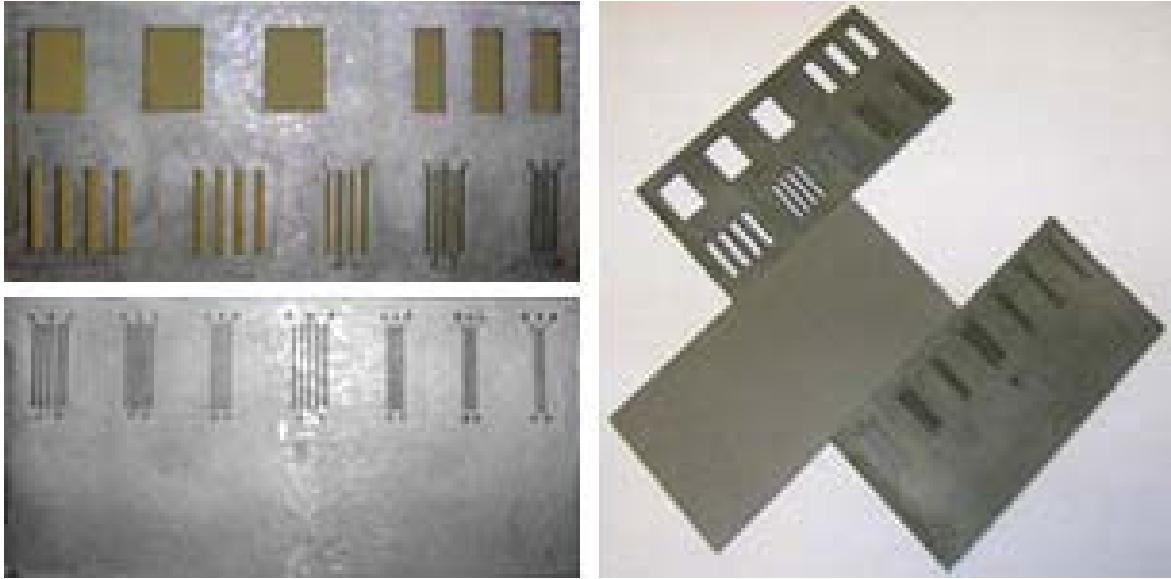


Figure 5-3. The custom designed bar-patterns used for MTF measurements of clinical EPIDs.

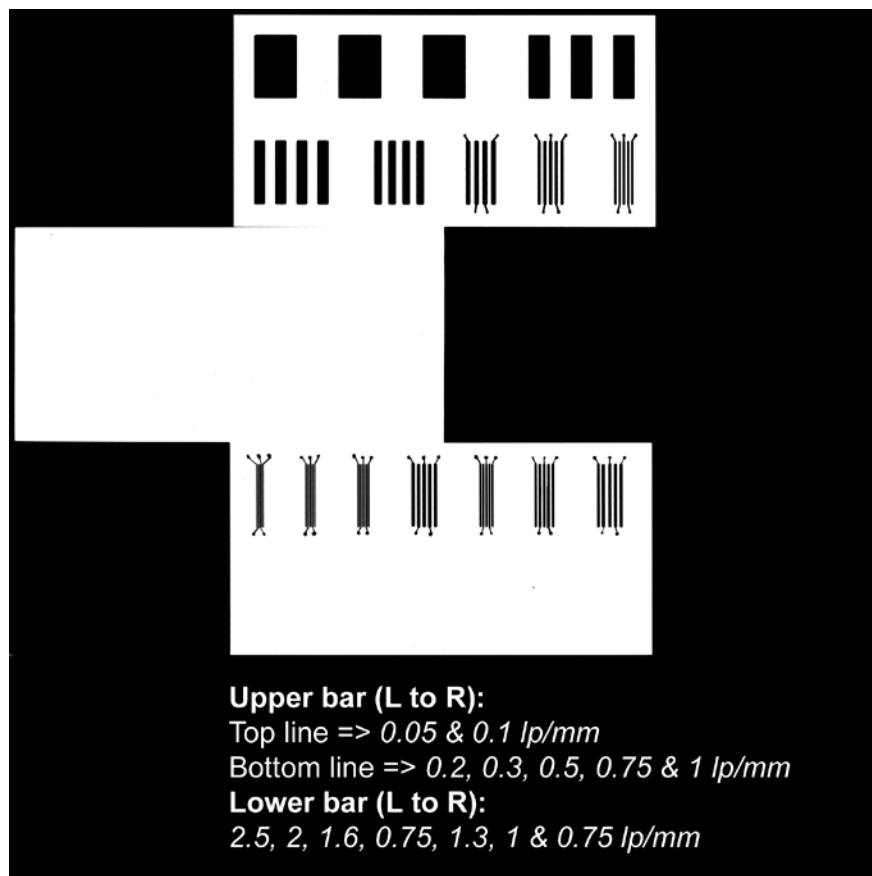


Figure 5-4. Kilovoltage radiographs of the bar-patterns used for MTF measurements of clinical EPIDs with constituent spatial frequencies specified.

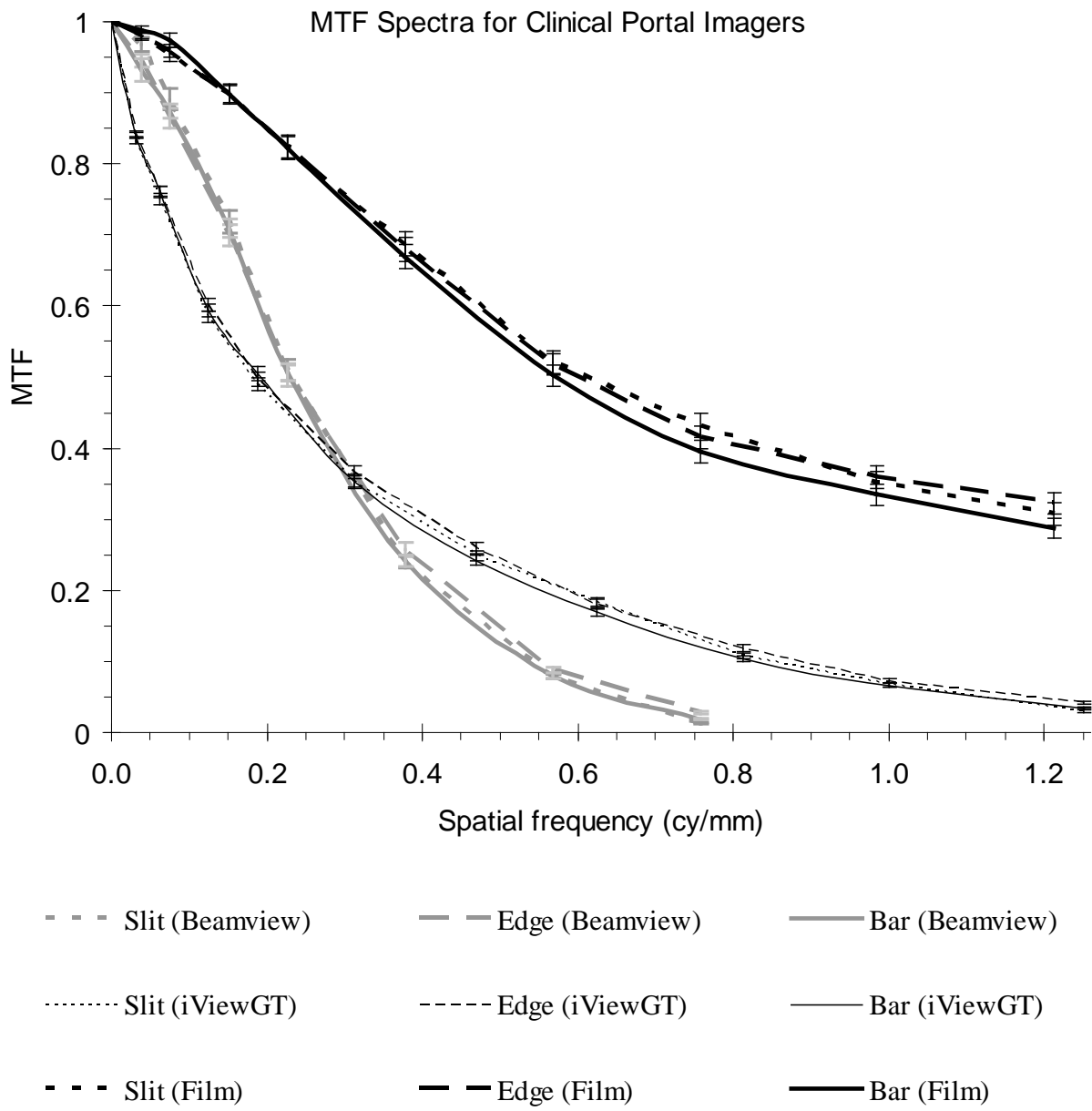


Figure 5-5. Comparison of MTF measurements with the slit, edge, and bar-pattern techniques.

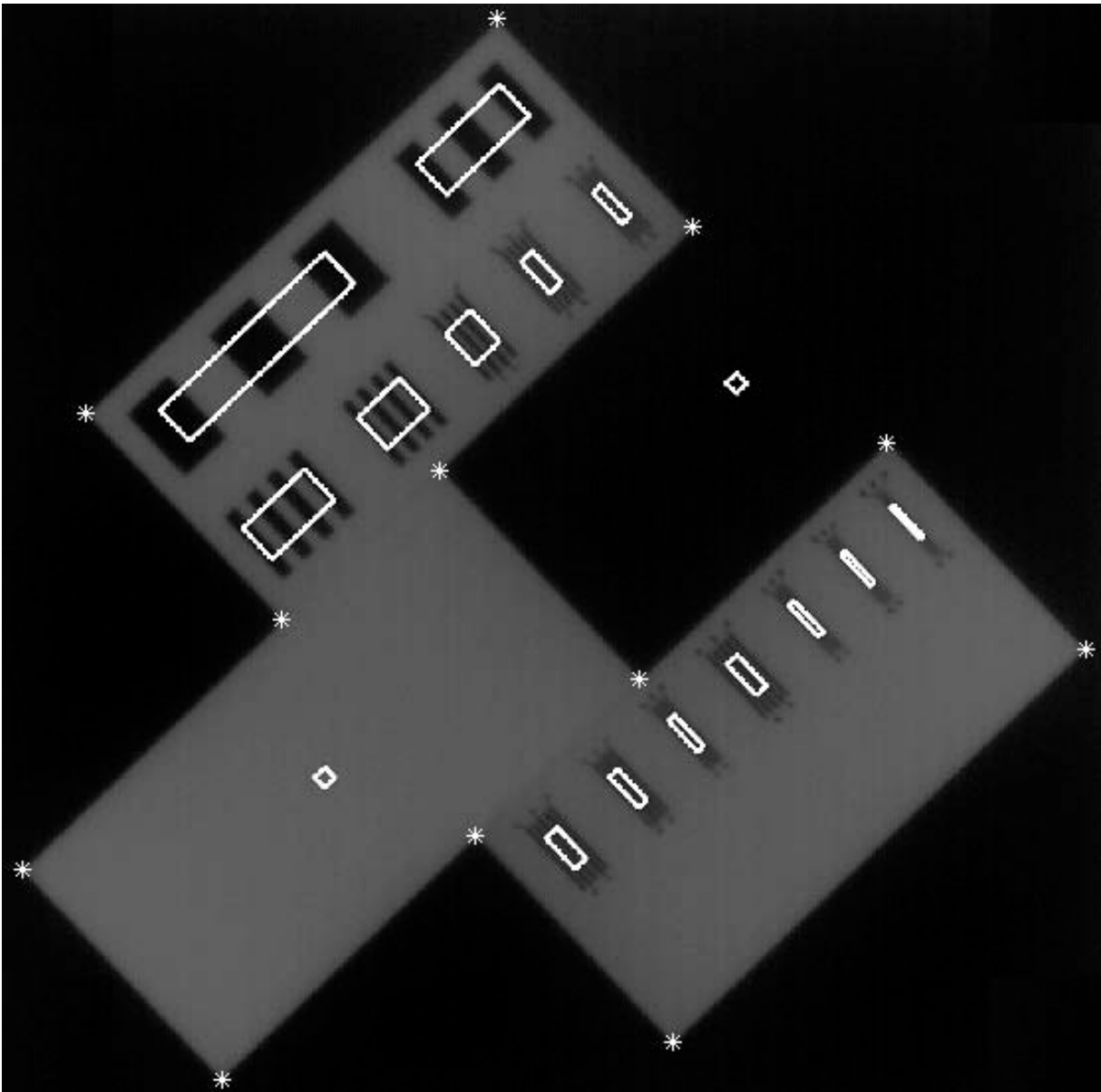


Figure 5-6. Snap shot of a bar-pattern image with relevant ROI selections identified using the computation algorithm developed for clinical EPID QA.

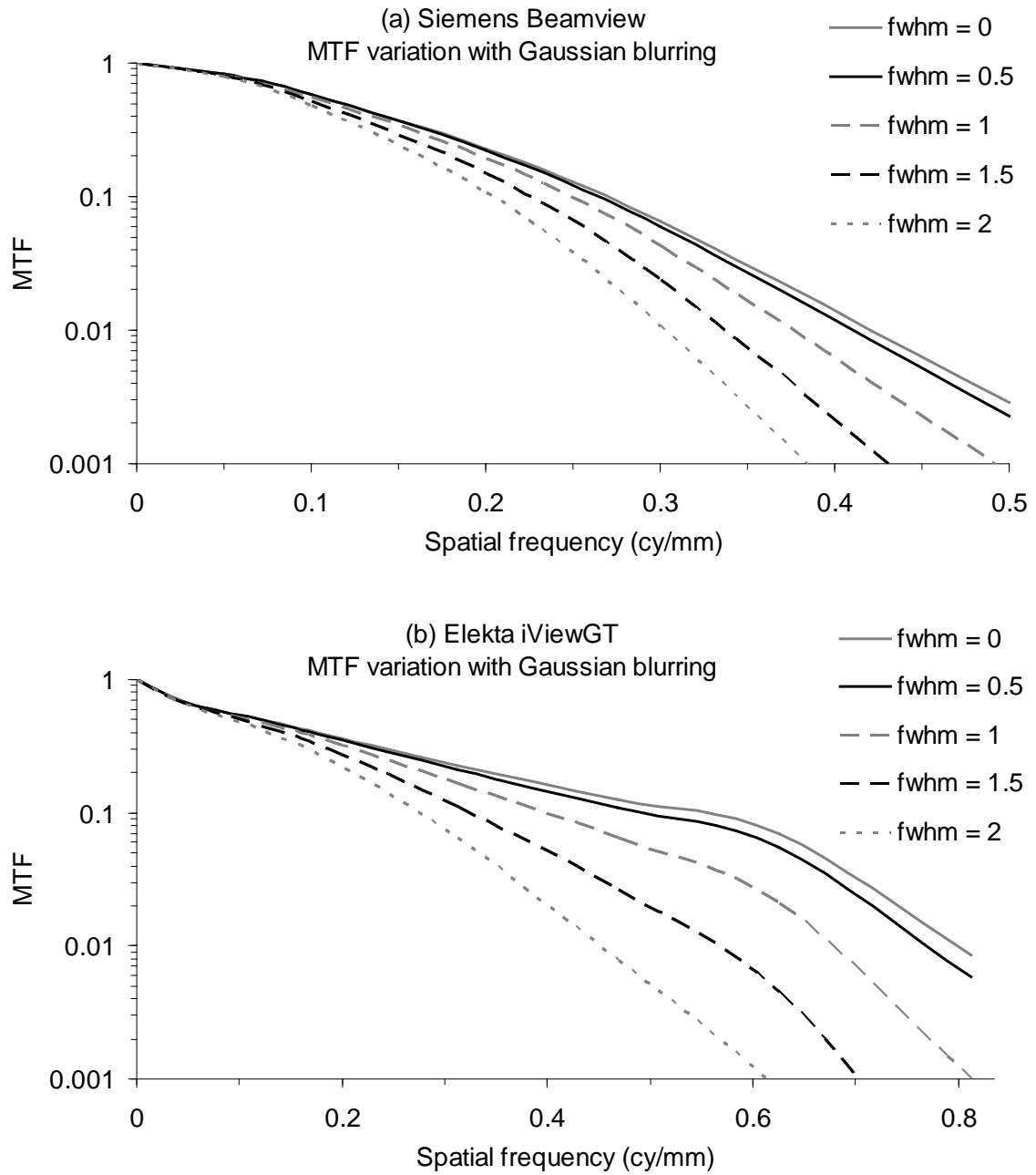


Figure 5-7. Effects of simulated blurring on bar-pattern MTF measurements.

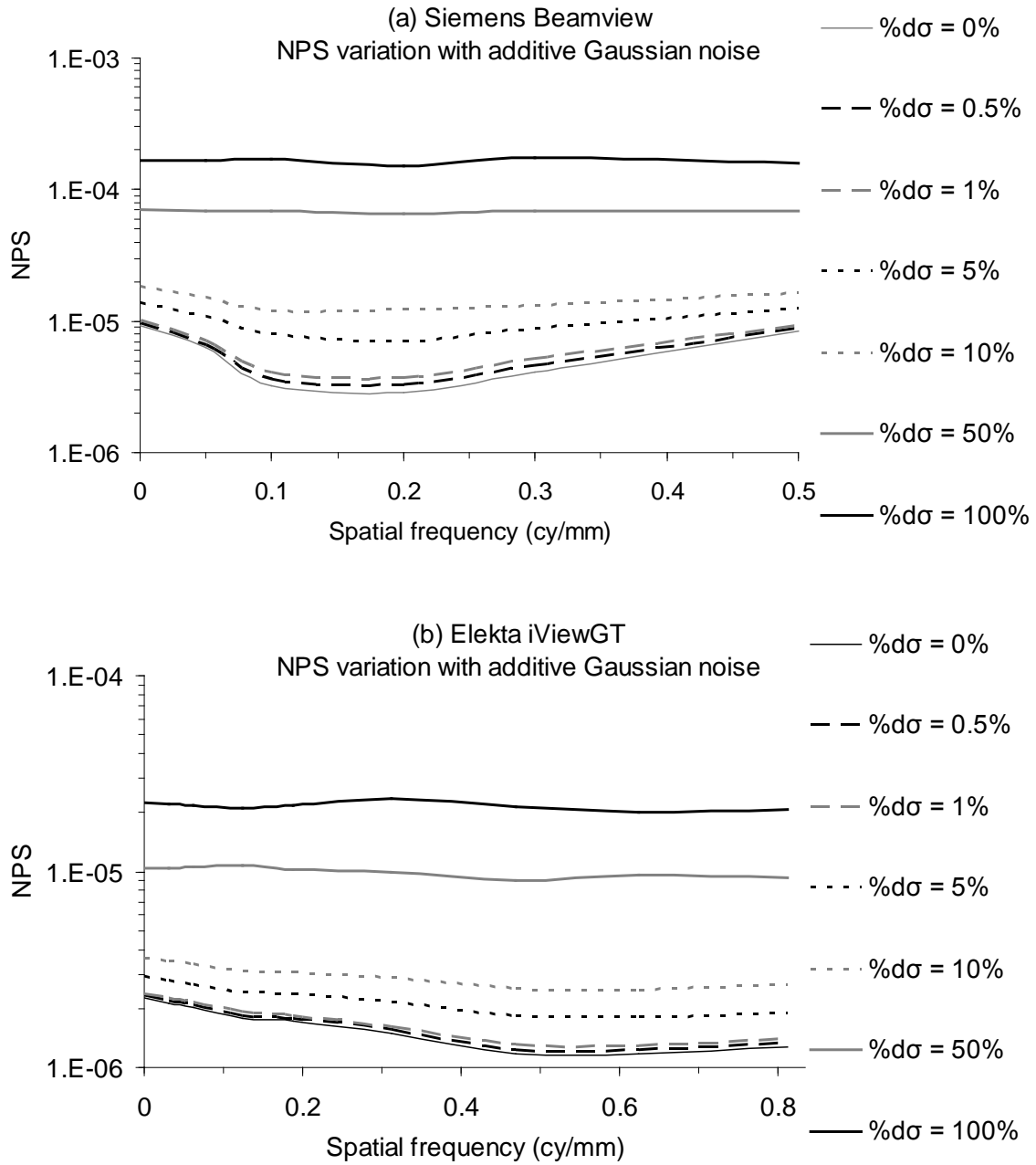


Figure 5-8. Effects of simulated additive noise on NPS measurements.

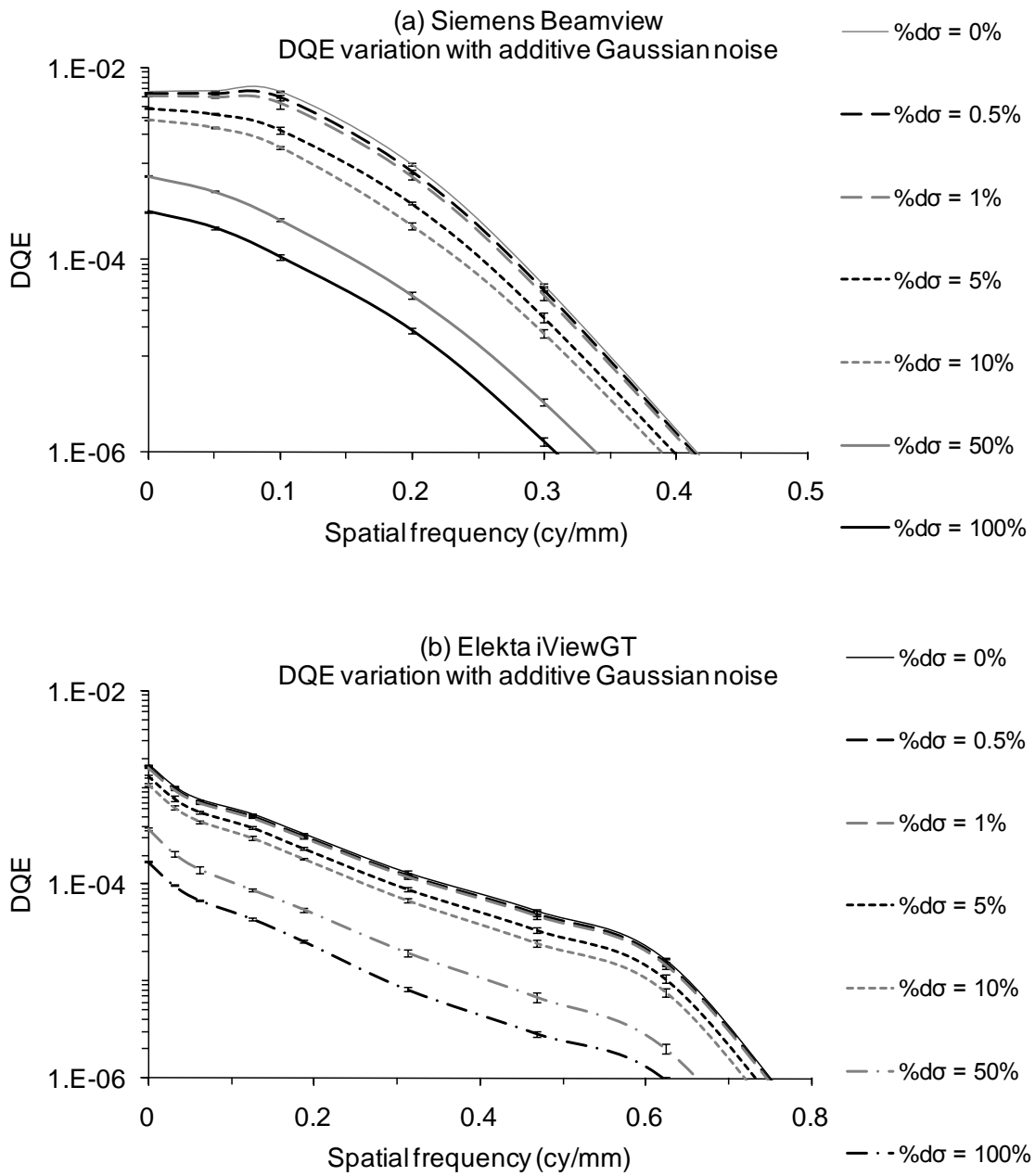


Figure 5-9. Effects of simulated additive noise on DQE measurements.

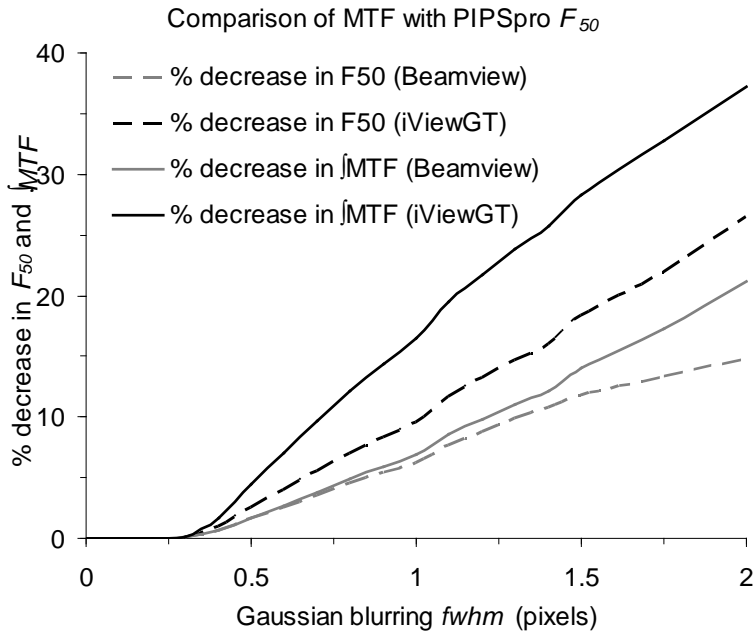


Figure 5-10. Comparison of sensitivities of the bar-pattern MTF and PIPspro F_{50} to simulated blurring.

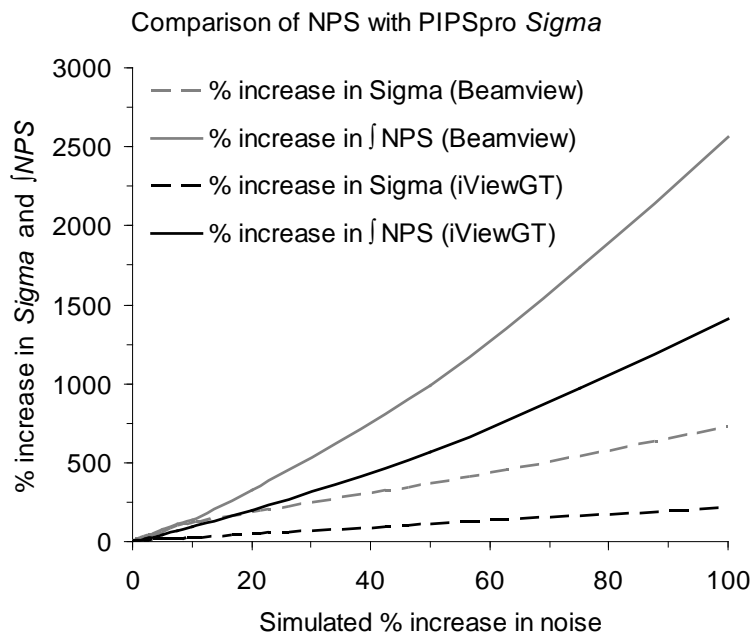


Figure 5-11. Comparison of sensitivities of the NPS and PIPspro Σ to simulated additive noise.

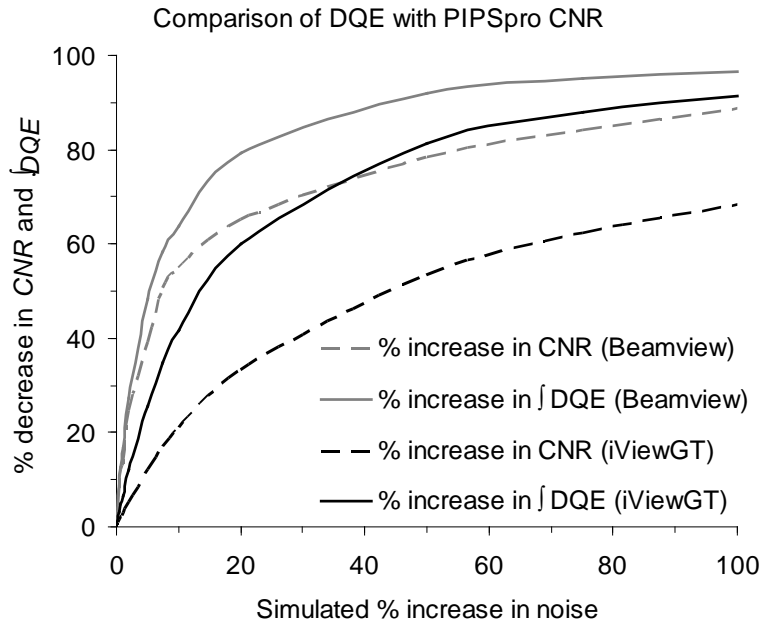


Figure 5-12. Comparison of sensitivities of the DQE and PIPspro *CNR* to simulated additive noise.

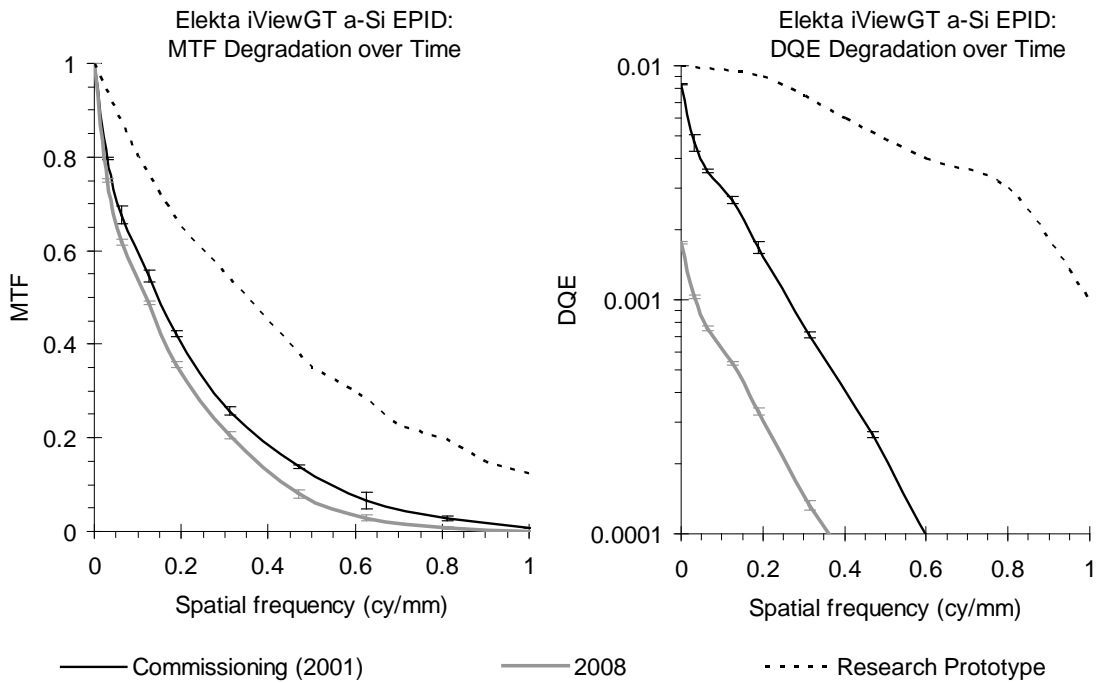


Figure 5-13. Degradation in the imaging performance of an Elekta iViewGT a-Si EPID over time.

CHAPTER 6 BAR-PATTERN METHODOLOGY FOR 3-D IGRT QUALITY ASSURANCE

The growing significance of 3-D IGRT solutions in the wake of IMRT was briefly discussed in section 1.6. To circumvent the limited soft-tissue contrast afforded by megavoltage imaging, KV-CBCT imaging has become increasingly popular as a treatment verification tool^{19,22,23,25,27}. This has also led to increasing efforts towards monitoring and optimizing the imaging performance of KV-CBCT systems. In particular, the excess scatter from the cone beam that results in added patient dose and imaging artifacts has prompted the use of beam filters^{178,179} and varied field size protocols to limit these effects. Image quality may be influenced by a variety of factors associated with the selection of image acquisition parameters like kVp, tube current, field size, beam filter, number of projections, and reconstruction filter. An improper selection of scan protocols may lead to unoptimized image quality and unnecessary dose to the patient. Therefore, a rigorous study of CBCT image quality and its dependence on beam characteristics is vital.

6.1 Imaging Performance QA for CBCT

So far, CBCT image quality has been characterized somewhat qualitatively with the aid of QA phantoms like the CatPhan 500/600 (The Phantom Laboratory, Salem, NY), which includes separate modules with calibrated rods and inserts to judge contrast, spatial resolution, CT number stability and linearity, and geometric accuracy. Recently, a QA strategy for quantitative MTF measurements using line-pairs in a CatPhan phantom was presented¹⁸⁰, although no DQE measurements or equivalent metrics for overall imaging performance were described. Therefore, the use of the bar-pattern technique for MTF, NPS, and DQE characterization of clinical CBCT systems was tested as a QA tool. In this case, the computation algorithm used to obtain these metrics during EPID QA was adapted to a standard CatPhan

phantom. The CatPhan module containing line-pair resolution targets is shown in Figure 6-1. The line-pair bars were utilized to obtain MTF spectra for CBCT axial scans while uniform sections of the phantom between individual modules were used for NPS measurements. The line-pair targets are made out of aluminum bars inserted into a cylindrical water equivalent medium. The line-pair module is 4 cm thick and the entire phantom itself is approximately 20 cm long and with a diameter of 15 cm. Typically, the phantom is placed such that the line-pairs can be visualized in axial slice scans. Line-pair resolutions of up to 2.1 lp/mm are currently included in the module. The largest bars are associated with a spatial frequency of 0.1 lp/mm. Preliminary imaging measurements were conducted for two commercial KV-CBCT systems: an Elekta X-ray Volumetric Imager (XVI) of the Elekta Synergy CBCT system (Elekta Inc., Crawley, West Sussex, UK), and a Varian On Board Imager (OBI) of the Varian Trilogy system (Varian Medical Systems, Palo Alto, CA).

6.2 Description of CBCT Systems

The XVI system consists of an indirect detection flat-panel x-ray detector based on a 1024 x 1024 array of 0.55 mm thick CsI(Tl) elements. The imager is used with an x-ray source that delivers kilovoltage radiation in the energy range of 70 – 150 kVp. The imager and source are integrated with the linac orthogonally to the therapy beam, and rotate about the same isocenter as the linac. The field size is allowed to vary only between preset collimated beam areas that are enforced through collimator cassettes. Three distinct beam widths are available: small (S), medium (M), and large (L), that correspond to 27.7, 42.6, and 52.4 cm respectively in the lateral direction (*x*-axis) at the plane of the isocenter. The length of the beam is set by the craniocaudal length of the collimator cassette. Collimator length indices of 2, 10, and 20 are commonly distributed with XVI systems that approximately correspond to 3.5, 13.8 and 27.7 cm at the isocenter. Thus, an M20 field indicates a beam area of 42.6 x 27.7 cm² at the isocenter.

Typically, S fields are employed to image smaller anatomy (eg. head and neck), while M and L fields are required for larger fields (such as chest and pelvis). The detector panel is large enough to visualize a central field corresponding to an S collimator cassette, but is required to be shifted laterally by 11.5 and 19 cm respectively when imaging M and L fields to accommodate larger imaging volumes. In this case, the effective size of the reconstructed volume is determined by the lateral extents of the projections even as individual projections do not cover the entire physical imaging volume at once. The collimator cassette feeds into a dedicated slot on the tube mount approximately 31.5 cm away from the focal spot. An additional cassette slot is provided under the collimator for the option of inserting a beam filter (referred to as an F1 filter) to modulate the beam suitably and compensate for the lack of peripheral beam hardening in larger (M20 and L20) fields. For other fields, a blank filter cassette (called an F0 filter) is inserted into the filter slot. The detector panel is located 153.6 cm away from the source, and the x-ray tube is oriented at a slight angle (3.5°) from the source – isocenter axis (towards the direction of the lateral shift of the detector for M and L fields).

The OBI system consists of a standard phosphor screen based flat-panel imager integrated along with a kilovoltage x-ray tube orthogonally to the treatment beam in the Varian Trilogy system. The x-ray tube can be used with kVp settings in the range of 40 – 125 kVp. Although field sizes can be controlled via collimator blade positions, preset positions are typically used that render two standard field sizes referred to as a full fan beam and a half fan beam. Full fan beams are used for smaller fields (≤ 24 cm diameter x 14 cm length), while the detector is shifted laterally by 14.8 cm with a half fan beam to accommodate larger anatomy (up to 45 cm diameter x 14 cm volume). Additional beam filters called bow-tie filters are recommended for all fields at higher x-ray energies. Separate bow-tie filters (i.e. full bow-tie and

half bow-tie) are available for each field. Although the detector position can be varied between 150 and 170 cm from the source, an SDD of 150 cm is generally used. The above descriptions of the XVI and OBI systems were obtained based on vendor communications, reported values^{178,179,181,182}, and physical measurements.

6.3 Imaging Measurements

The CatPhan phantom was positioned at the isocenter with the linac light guides intersecting at the center of the module containing line-pairs. Axial CBCT scans were acquired at various field size, beam filter, and gantry rotation settings for the XVI and OBI units. At the time of conducting the imaging experiments, the XVI could only be operated with selected field sizes (S10, S20, M10, M20, and L20) and the F1 filter was utilized only with M20 and L20 fields. All XVI scans were conducted with an x-ray tube setting of 120 kVp and tube current specified as 40 mA and 40 ms (~ 1.6 mAs) per frame or projection. For the OBI, scans were conducted at 125 kVp, 80 mA and 25 ms (2 mAs) per projection, and with field sizes prescribed by full and half fan beams both with and without the bow-tie filter. Typical scan protocols for both systems utilized one complete gantry rotation (~ 360°) for the imager to acquire projections. An additional low dose acquisition mode corresponding to a smaller gantry rotation arc (~ 200°) was also tested with S10 and S20 fields for the XVI and with the full fan beam mode for the OBI.

Built-in reconstruction algorithms were used to obtain 1 mm thick axial slices (providing 3 – 4 slices of line-pairs per scan). The highest resolution setting for both systems that provided voxel dimensions of 0.5 x 0.5 x 1 mm³ were specified for smaller field sizes (S10, S20, and M10 for the XVI, and full fan beam for the OBI). Coarser voxels had to be used for larger volumes due to image size and memory constraints, where the axial pitch was 0.75 mm for the XVI and 0.88 mm for the OBI. The axial slices containing line-pairs were identified for each scan and analyzed using an adapted form of the MTF computation algorithm that was originally coded for

2-D portal imaging QA with the tungsten bar-pattern. Geometric information specific to the CatPhan phantom was supplied for the calculation through parameter files. Line-pair variances were sampled from coaxial spatial profiles extracted at the radial locations of the aluminum bars, and a central $7.5 \times 7.5 \text{ cm}^2$ portion of the slices through uniform CatPhan sections was used to obtain open field samples (Figure 6-2). The MTF and NPS spectra were calculated as described previously according to Equations 2-9 and 2-11 respectively, and the DQE was obtained using Equation (2-15). The fluence factor Φ required to normalize the DQE to the incident beam quanta was estimated from Monte Carlo simulations and dose measurements for all scan geometries.

6.4 Fluence Normalization of DQE

For DQE measurements with the TSC, a reference dose condition for the therapy beam in water was used to estimate the fluence normalization factor Φ based on a fluence – dose conversion ratio obtained from Monte Carlo simulations. In a similar approach, a dose metric associated with each CBCT scan protocol was determined based on ion chamber recordings. The set-up used to perform ion chamber measurements was similar to that used to obtain a CT dose index (CTDI) unit that is typically used to quantify a nominal dose value for a given CT scan¹⁸³. In particular, the measurement set-up for a so called weighted CTDI ($CTDI_w$)^{184,185} was implemented, which was developed as an adaptation of the originally contrived CTDI scheme for single slice CT to account for the added scatter conditions of CBCT imaging. The functional scheme for the dose measurements is shown in Figure 6-3. Herein, the dose readings from central and peripheral ion chambers in a cylindrical water phantom (20 cm diameter and 10 cm length) are essentially pooled as indicated in Figure 6-3 to obtain $CTDI_w$. However, since only a relative dose estimate was required for this study, a single ion chamber reading at the center of the phantom (i.e. the central dose D_c) was sufficient. The methods and equipment described by

Song *et al* for $CTDI_w$ measurements¹⁸¹ for XVI and OBI systems were used to obtain D_c for all the tested scan protocols, since these reported measurements were performed on the exact same systems as the imaging measurements in this study.

The central dose estimates for the specific geometry of the $CTDI_w$ measurements were related to equivalent fluence units by generating a Monte Carlo simulation model of the $CTDI_w$ set-up geometry in MCNPX. In this model, the water cylinder was positioned 100 cm away from the x-ray source, which was modeled as a point divergent beam with spectra as specified by Ding *et al* (for the OBI)¹⁷⁹ and Spezi *et al* (for the XVI)¹⁸². Collimator blades were modeled according to field size locations for each scan geometry (specified as “void” zones wherein histories are terminated upon entry). Radiation scatter was implicitly modeled since it was included in the modeling of the reported beam spectra. The ion chamber was specified as a 0.6 cm³ cylindrical voxel at the center of the water cylinder. Energy deposition tallies in this voxel were used to compute a dose value representing D_c , while fluence tallies were scored in a 10 x 10 cm² area at the center of the detector plane (specified according to the SDD settings of the XVI and OBI systems). The subsequently calculated fluence – dose ratio was used along with the measured value of D_c to determine the fluence factor Φ , with which the DQE was evaluated using Equation (2-15) for all CBCT scans.

6.5 Qualitative Evaluation of Image Quality

Axial slices containing the line-pair targets in the CatPhan phantom acquired with the XVI and OBI systems are shown in Figures 6-4 – 6-6. The difference in image quality due a sparse projection arc is indicated in Figure 6-4 for an S10 field. A standard scan reconstruction using a full 360° projection arc is shown in Figure 6-4 (A). The use of a smaller gantry rotation arc of only 200° in Figure 6-4 (B) revealed two observations. As expected, the sparse projection field added to the graininess of the image, and also led to more imaging artifacts indicated by the

intensity saturation of some pixels in the image of the latter. On the other hand, there was also an apparent improvement in spatial resolution of the line-pair targets. However, this was related to the orientation of the line-pair targets in the phantom relative to the position of the detector during its projection arc. In this case, the colinearity of the x-ray beam with the line-pair targets in its shortened projection arc led to exaggerated spatial resolution compared to Figure 6-4 (A). The overall image quality was found to progressively decline with increased field size due to the effects of scatter. Figures 6-5 (A) – (C) represent slices from S20, M20, and L20 fields respectively when using a neutral (i.e. F0) beam filter. The image quality decreased significantly in Figure 6-5 (D) when the F1 filter was used. This observation was contrary to the expected improvement in image quality with reduced beam hardening artifacts on account of the compensating action of the filter. Figure 6-6 shows line-pair slice reconstructions from the OBI system. Figures 6-6 (A) and (B) represent complete (360°) and sparse (200°) projections respectively, wherein the observations were quite similar to that described for Figure 6-4. The larger field and subsequently greater scatter did not result in significant degradation in image quality for the half fan beam scan in Figure 6-6 (C) compared to the full fan beam reconstruction. Some loss image quality was observed in Figure 6-6 (D) with the use of no bow-tie filter for a full fan beam scan.

6.6 Quantitative Characterization of Imaging Performance

The MTF spectra for the XVI system are shown in Figures 6-7 – 6-9 indicating the effects of gantry rotation arcs, field size settings, and the F1 filter on observed spatial resolution respectively. In Figure 6-7, the localized rise in MTF is clearly evident with the shorter projection arcs for the intermediate range of spatial frequencies where the beam orientation was nearly parallel to those line-pairs. The higher spatial resolution of the S10 scan compared to the S20 scan is also easily seen from these plots. In Figure 6-8, the steady decline of the MTF with

field size indicated the effects of scatter. It was observed that the reduction in MTF was especially significant when progressing from an M10 to an M20 field. The unexpected loss in image quality with the addition of the F1 filter that was observed in Figure 6-5 (D) was confirmed with the MTF measurements in Figure 6-9. The overall imaging performance including the effects of noise and spatial resolution can be seen in the DQE plots for the XVI system in Figures 6-10 and 6-11. From Figure 6-10, the severe effects of scatter can be quantified as nearly two orders of magnitude in the reduction in DQE with M and L fields. The effect of scatter was observed to be compounded further when the F1 filter was used as indicated by Figure 6-11. The reduced imaging performance with the use of the F1 filter was attributed to unoptimized scatter correction kernels in the reconstruction algorithm.

For the OBI, Figure 6-12 shows the MTF spectra associated with various scan acquisition parameters. The plots indicated that the excess scatter in half fan beam scans resulted in a reduction in MTF compared to the full fan beam mode. However, this loss in MTF was significant only at higher spatial frequencies due to which, it was not easily visualized in the images in Figure 6-6. The DQE spectra for the OBI similarly indicated some fall-off in overall imaging performance with field size and lack of the recommended filtration with the bow-tie, although this reduction was not as significant as the decline in DQE with field size for the XVI system. The above results indicated that the OBI provided superior image quality compared to the XVI system based on greater MTF and DQE spectra. The possible reasons for this difference are not clear on account of the variety of differences between the two systems. For example, the x-ray beam for the XVI is significantly harder than that for the OBI despite a lower peak energy¹⁸¹. While they have common mechanisms for providing larger field sizes, they employ very different beam filters. For the OBI, the bow-tie filter was quite symmetrically shaped and

the attenuating thickness varied only at the center of the filter¹⁷⁹. In comparison, the F1 filter had an elliptical thickness function due to which, maximal beam attenuation was limited to the peripheral points only. Characterizing the exact effects of the shape of the beam filter requires further detailed studies. Both the XVI and OBI systems may also have different reconstruction algorithms that may lead to variations in image quality.

The use of the bar-pattern technique for MTF, NPS, and DQE measurements provided useful insight into the overall variations in image quality beyond that which could be observed from qualitative inspection of images. For example, Figures 6-4 (A) and 6-6 (A) represent the optimal scan configurations for the XVI and OBI respectively. From observing images only, the quality of the OBI slice (full fan beam with bow-tie) was significantly superior in visualization compared to that of the XVI (S10, F0 filter). However, the DQE plots indicated that the OBI was only marginally superior to the XVI for the specified acquisition settings since the OBI scans were associated with a far greater exposure or dose value¹⁸¹. The use of greater exposure factors in the OBI was automatically normalized due to the absolute and fundamental nature of the DQE measurement. These preliminary studies indicated that a bar-pattern based QA approach has significant potential as a QA tool in monitoring the imaging performance of CBCT systems, as well as for optimizing scan acquisition parameters and other system components.

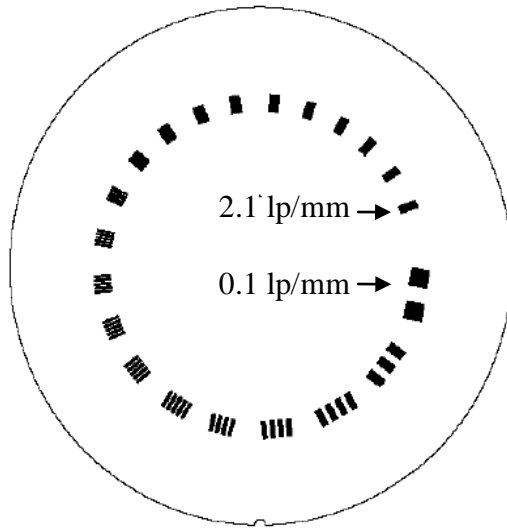


Figure 6-1. The schematic layout of line-pairs in a conventional CatPhan phantom.

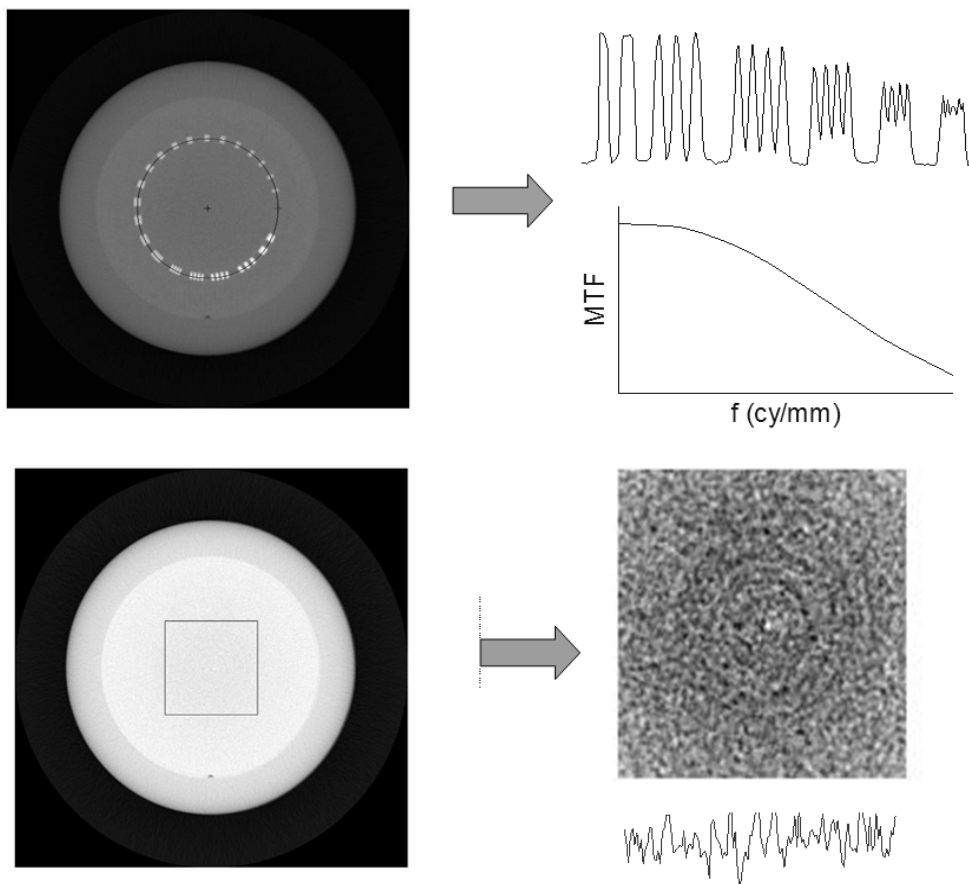


Figure 6-2. Extraction of line-pair variance and open field ROIs for MTF and NPS calculations.

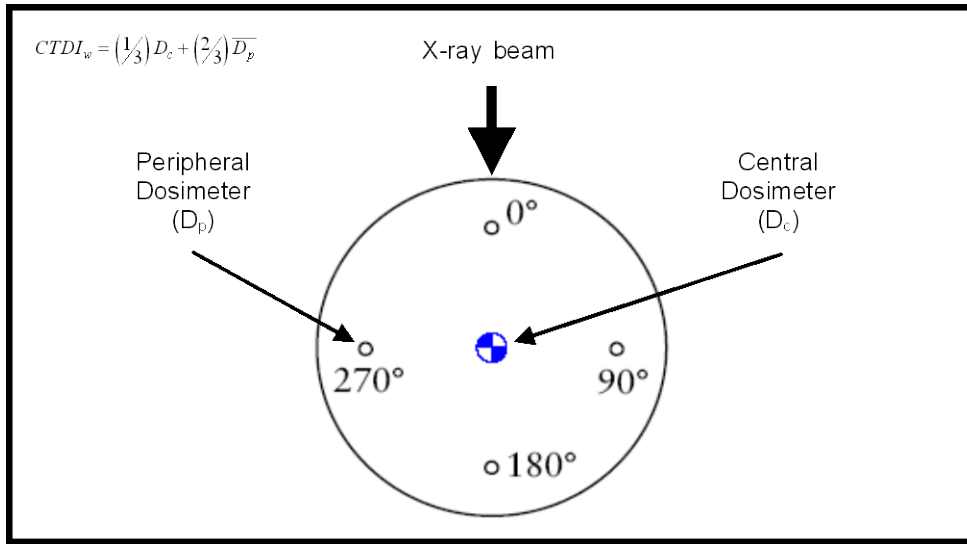


Figure 6-3. The functional schematic of the measurement set-up for $CTDI_w$ values for CBCT imaging.

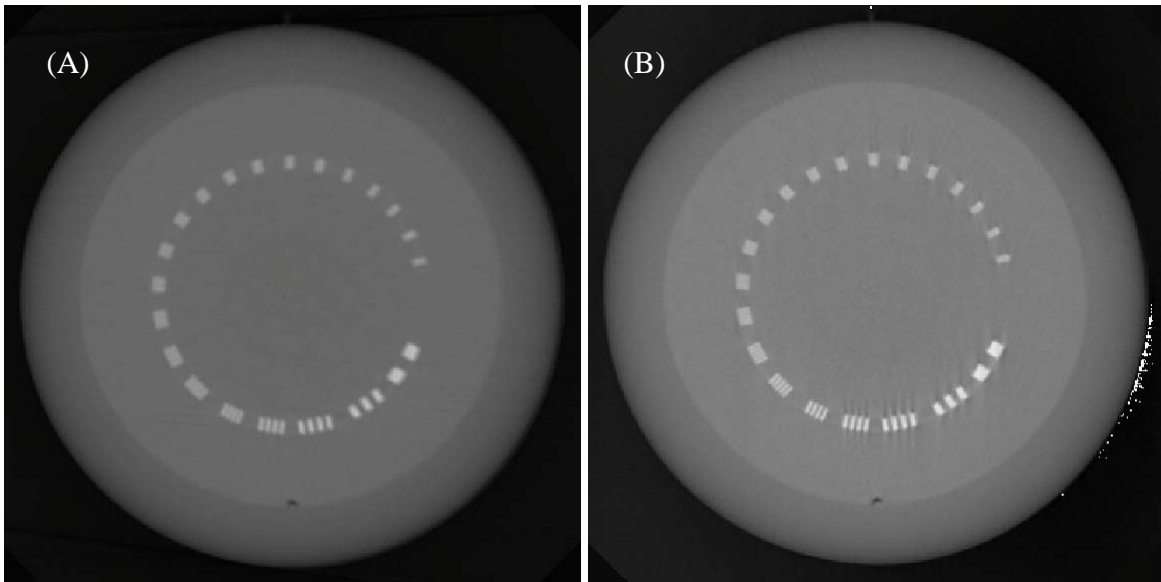


Figure 6-4. Line-pair slices from a CBCT scan of the CatPhan phantom with the XVI indicating the effect of gantry rotation. (A) Full 360° projection arc. (B) 200° projection arc.

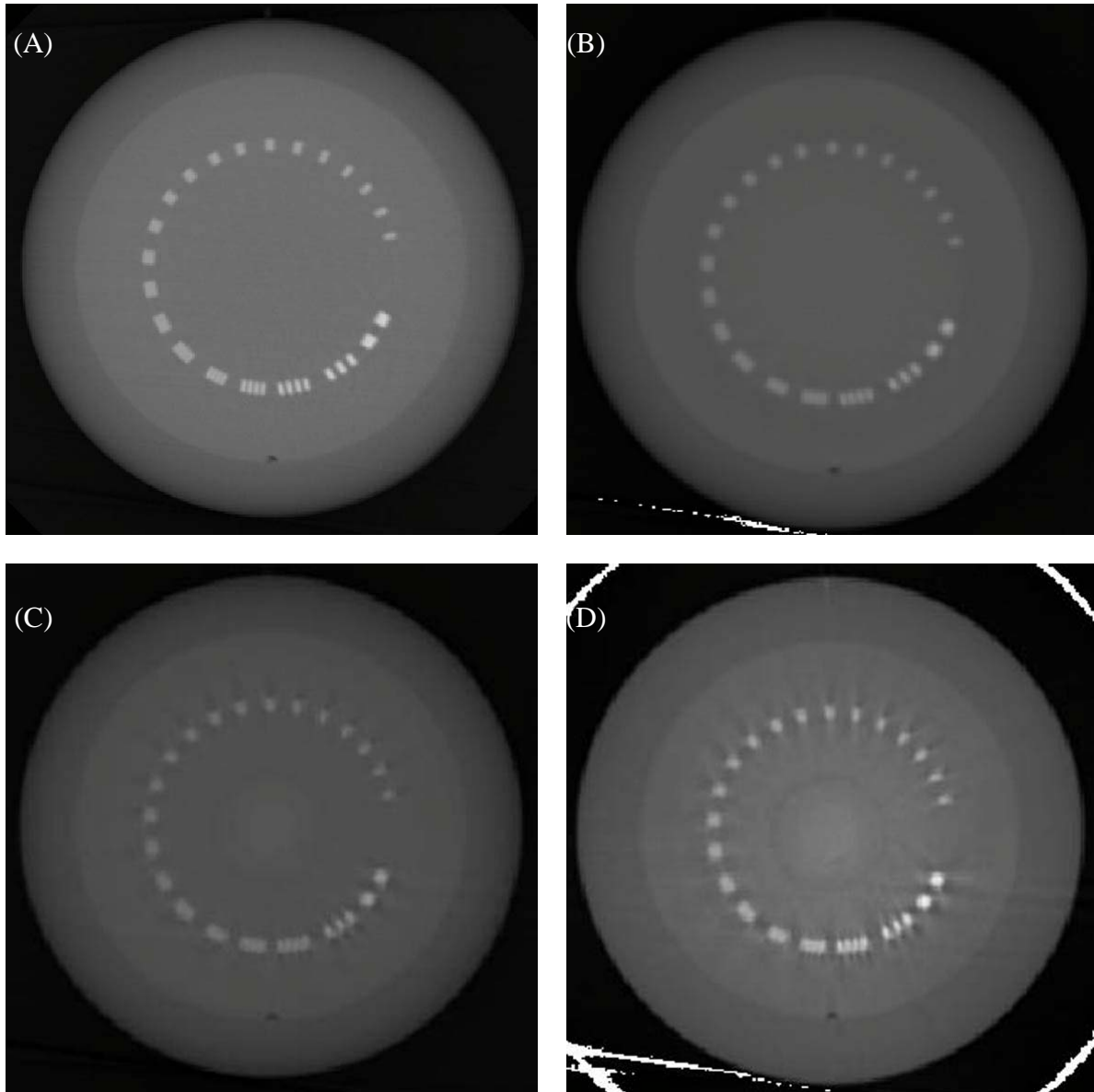


Figure 6-5. Line-pair slices from a CBCT scan of the CatPhan phantom with the XVI indicating the effects of field size and beam filter. (A) S20 field, F0 filter. (B) M20 field, F0 filter. (C) L20 field, F0 filter. (D) L20 field, F1 filter.

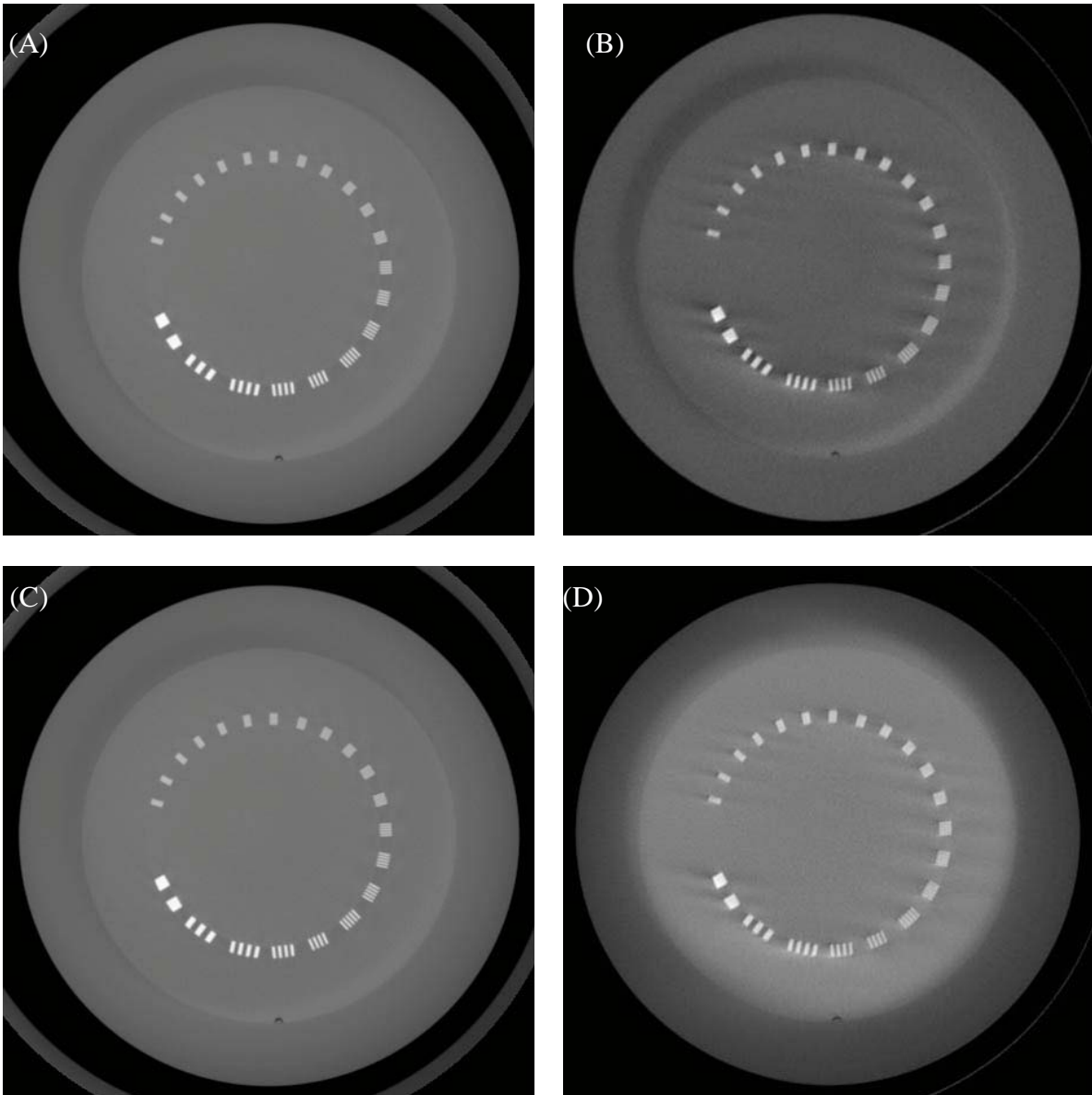


Figure 6-6. Line-pair slices from a CBCT scan of the CatPhan phantom with the OBI. (A) Full fan beam, full bow-tie filter. (B) Full fan beam, full bow-tie filter (200° projection arc). (C) Half fan beam, half bow-tie filter. (D) Full fan beam, no bow-tie filter.

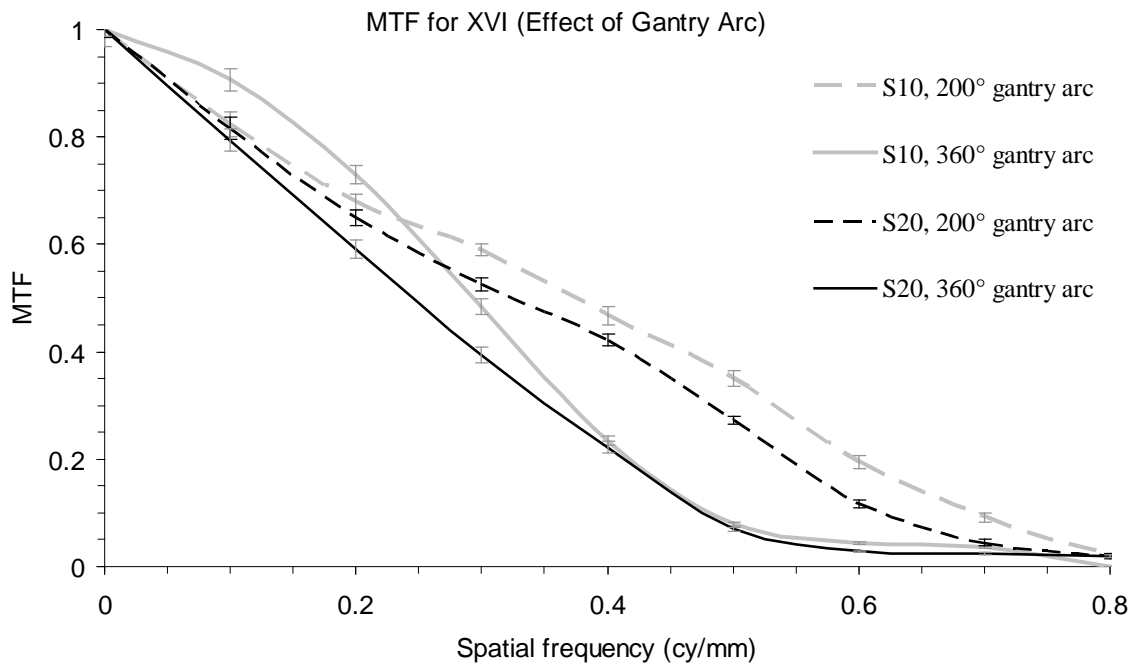


Figure 6-7. Effect of gantry rotation on the MTF for the XVI CBCT system.

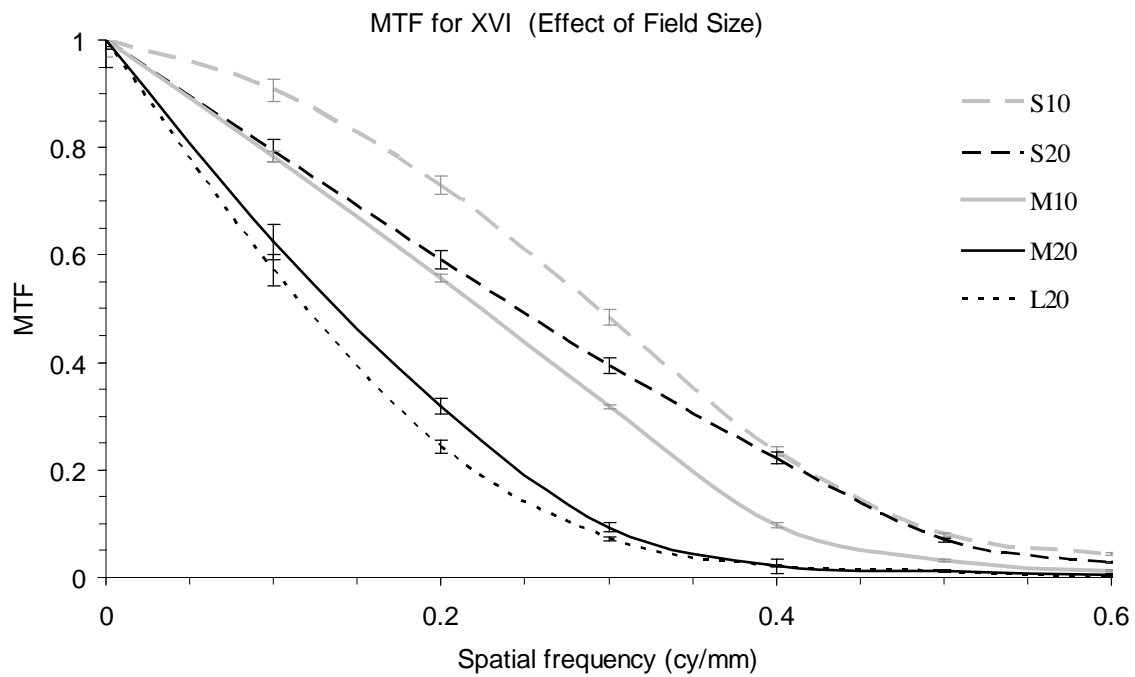


Figure 6-8. Effect of field size on the MTF for the XVI CBCT system.

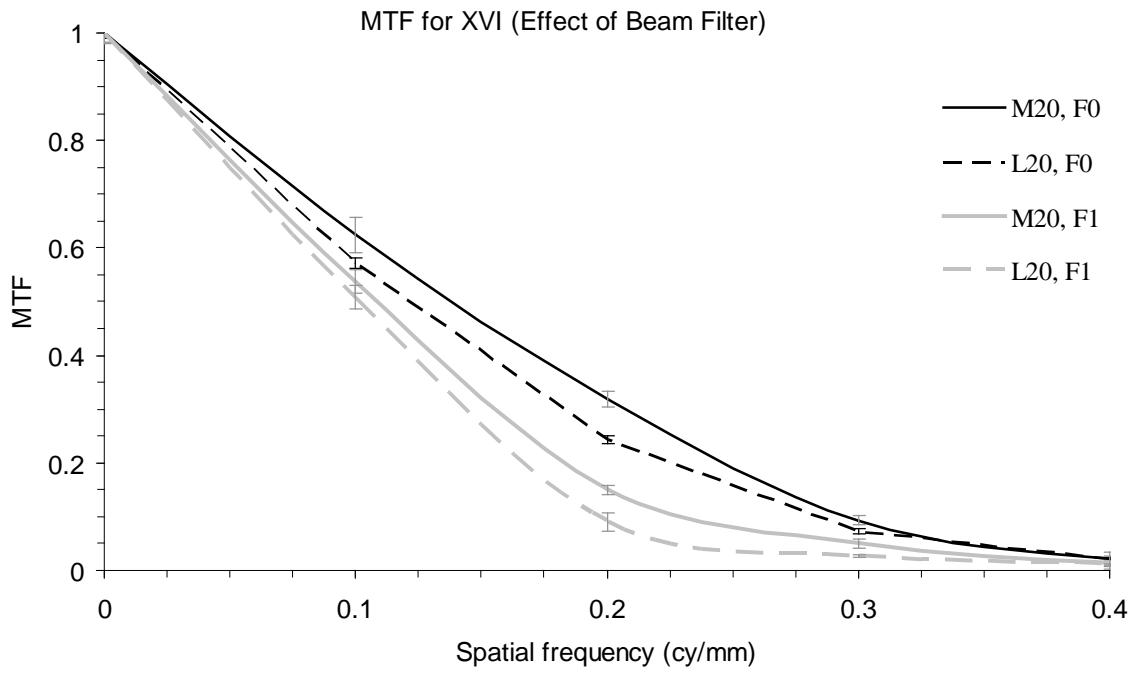


Figure 6-9. Effect of the F1 filter on the MTF for the XVI CBCT system.

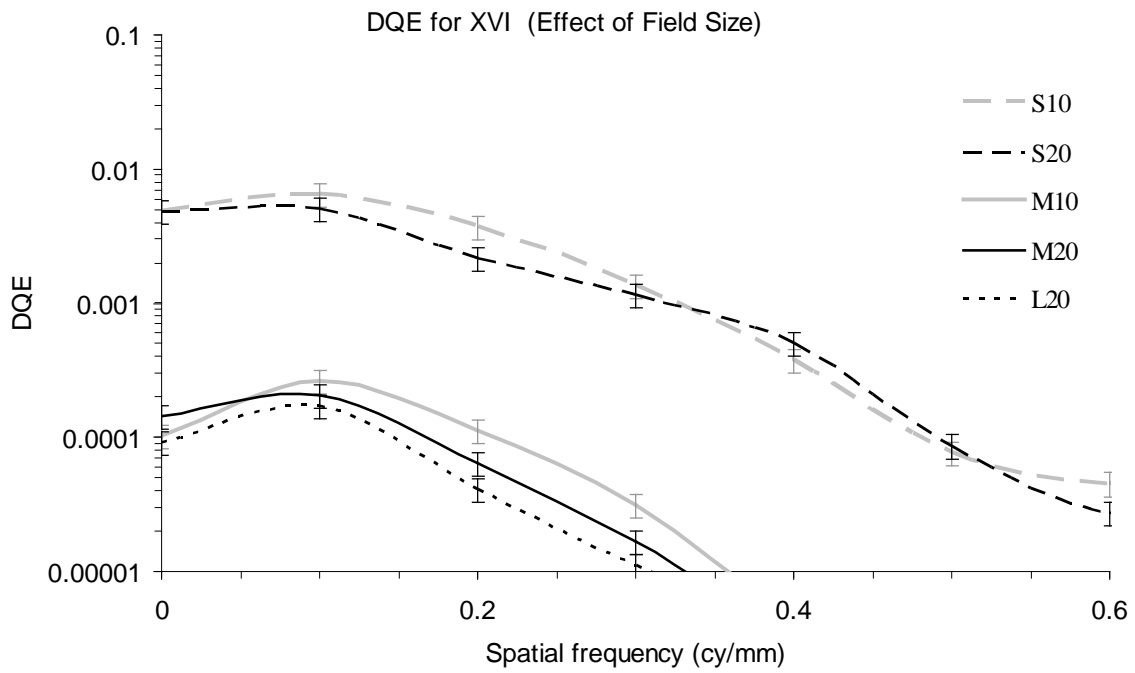


Figure 6-10. Effect of field size on the DQE for the XVI CBCT system.

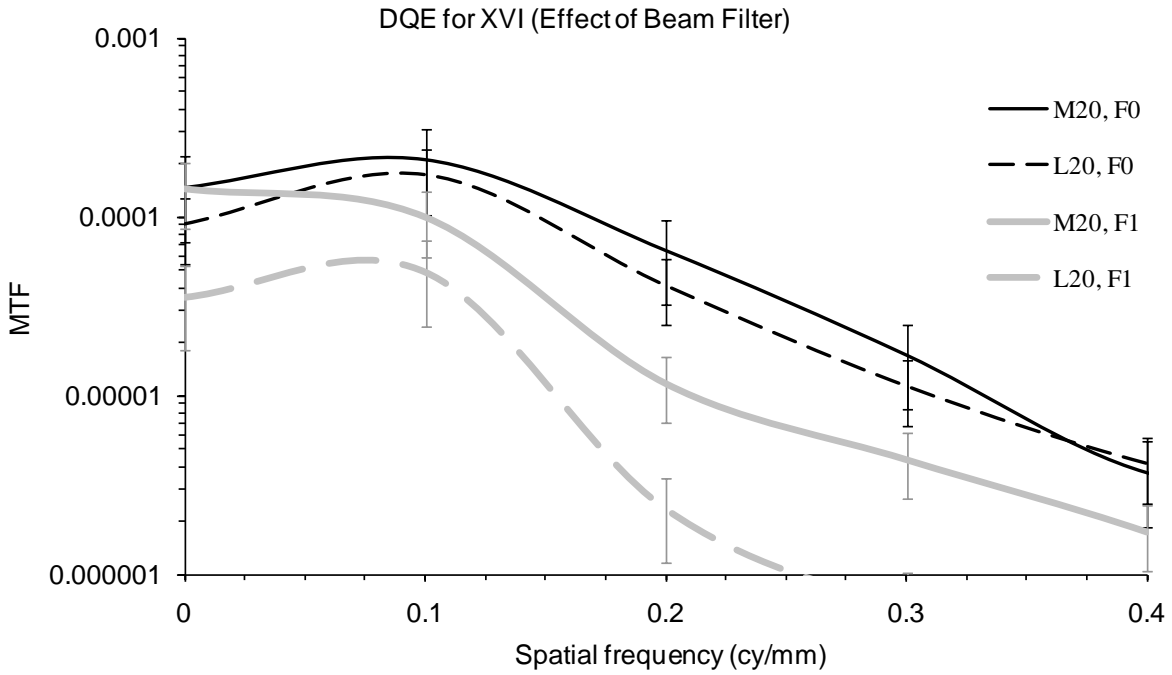


Figure 6-11. Effect of the F1 filter on the DQE for the XVI CBCT system.

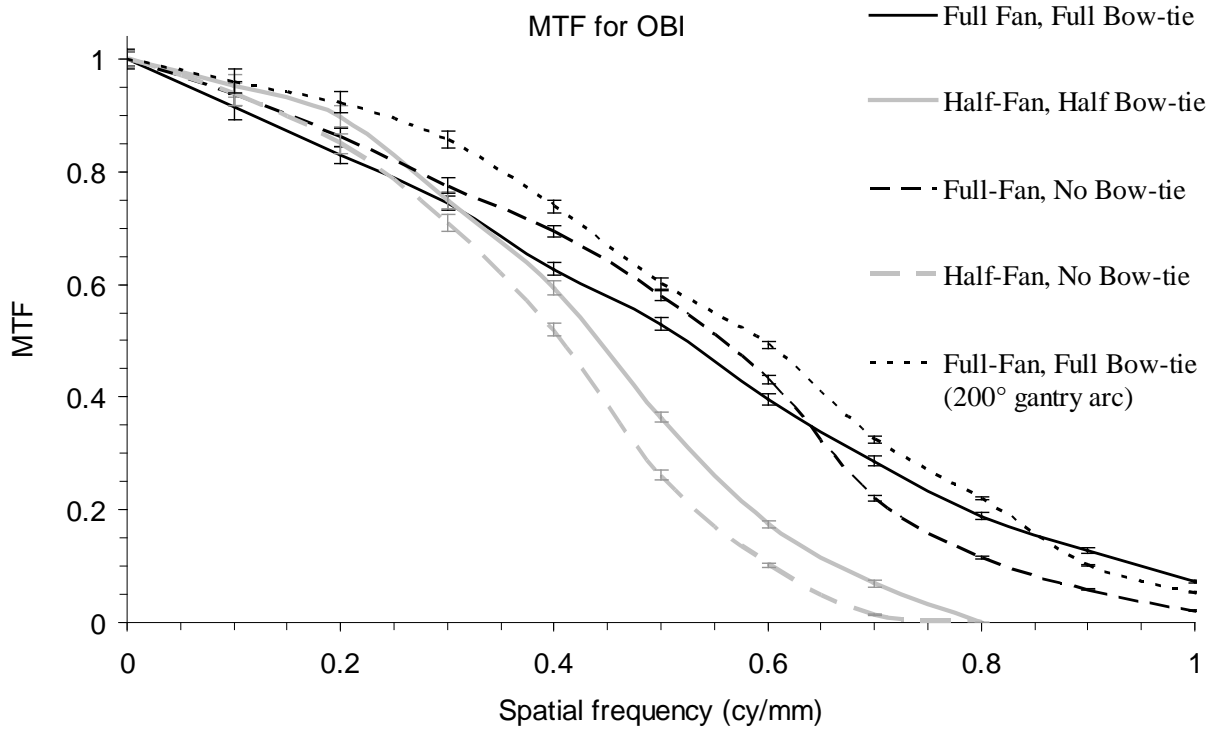


Figure 6-12. The MTF for the OBI CBCT system at various scan acquisition settings.

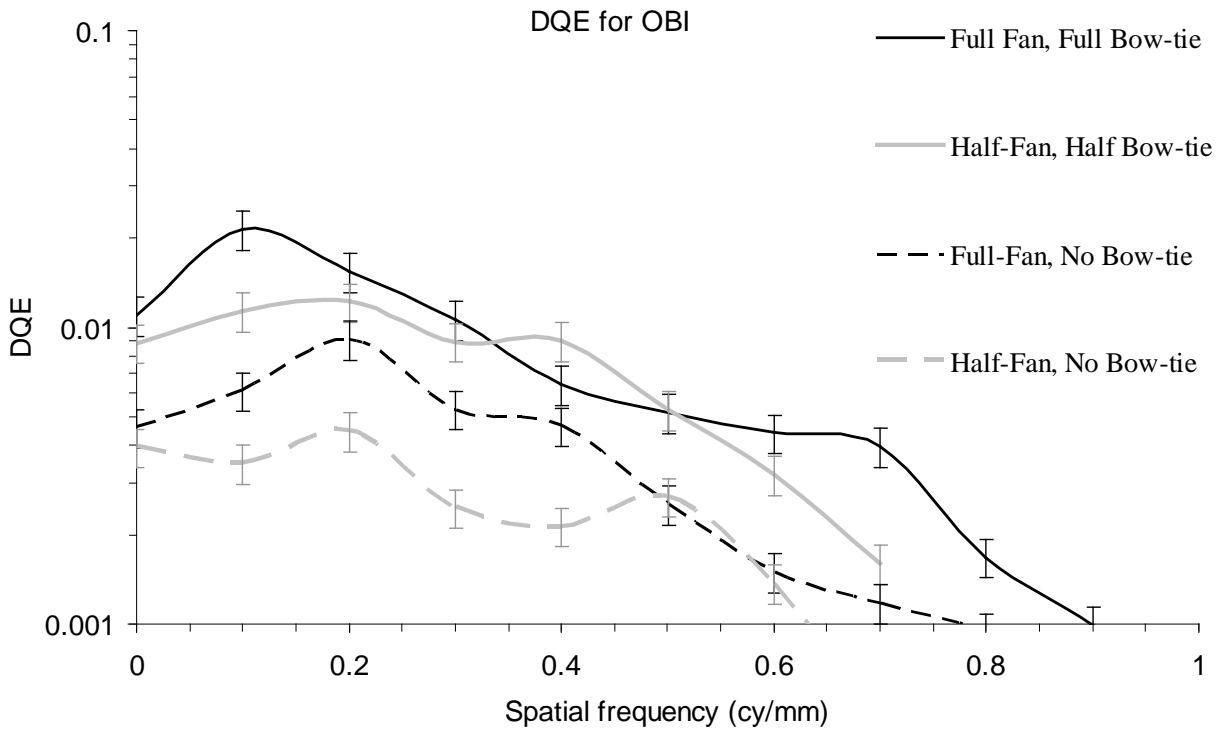


Figure 6-13. The DQE for the OBI CBCT system for various scan acquisitions settings.

CHAPTER 7 SUMMARY AND CONCLUSIONS

The research presented in this dissertation addressed a fundamental problem in radiotherapy – the lack of a sufficient and clear standard of image quality in any form of guidance systems used in IGRT today. Despite tremendous progress in radiation therapy over the years, currently available megavoltage x-ray detectors as well as the clinical techniques used to characterize them are far from ideal. To this end, two prototype imaging configurations: the TSC, and the FOSGA system, were studied in detail. All aspects and components of their imaging performance were evaluated using established linear systems analysis, simulations, and theoretical modeling.

For the CsI(Tl) based TSC system, these analyses were validated with extensive measurements of imaging performance, wherein the current limitations in prototype design were identified, and a platform for further optimization was developed based on linear cascaded systems analysis. A new design model for prototype lens – coupled scintillator – camera systems was outlined that expressed established physical and optical parameters of the system to mechanical and clinical constraints, as an optimized prototype configuration for the TSC system was obtained. The significant finding of this work was that despite the optical quantum sink presented by the poor light collection efficiency of the lens, first generation video EPID systems can still be optimized so that its imaging performance may approach the theoretical limits of the scintillator thickness based radiation interactions. While, the use of cooled CCD targets can drive up the overall system cost and may limit its feasibility as a practical clinical solution, it can provide a valuable tool in high end imaging applications. In this case, the high quality of megavoltage imaging in conjunction with a means to easily adjust the imaging field size and geometry via its lens configuration makes the TSC system a valuable tool in large volume non-

destructive testing. As future work, a large field prototype TSC system based on its optimized configuration must be developed and characterized with imaging measurements to supplement and validate the findings of this research. The use of thicker CsI(Tl) screens and the subsequent trade-off between the improvement in x-ray sensitivity and the loss in spatial resolution due to extra-focal blurring may also be investigated.

The FOSGA system was the second prototype portal imager studied in this research. It featured the use of advanced manufacturing techniques and proven components from material sciences to construct a structured scintillator array using fiber-optic scintillation glass. The major strength of this work was that a high degree of radiographic merit could be achieved in tandem with a cost effective design approach. Detailed theoretical studies of detector performance were carried out that included extensive radiation transport modeling using an established Monte Carlo simulation package, and also a complete modeling of light transport for the coupling of light from the scintillator to the photodiode array using a custom written algorithm tailored to the specific geometry of the FOSGA detector. Unique detector characteristics based on its spatial variance were observed, analyzed, and quantified as a function of detector geometry. Based on a linear systems analysis, an optimal detector configuration was identified, and its expected performance was evaluated. Future directions for this work include the construction and assembly of a test prototype system for the FOSGA detector based on the recommended detector configuration (6 cm thickness, 70% fill factor). The test prototype may be used to validate the results presented in this dissertation and also investigate the feasibility of the FOSGA detector for volumetric imaging via MV-CBCT and in vivo 3-D dosimetry.

Finally, extensive studies were conducted to improve fundamental imaging techniques used to evaluate detector performance with the aim of extending these methods and their

associated advantages to clinical QA of imaging devices in IGRT. An improved adaptation of the bar-pattern method for MTF measurements was developed that was based on a novel normalization measurement using a separate large area bar for robust, accurate, and fast calculations. A QA strategy based on linear systems metrics (MTF, NPS, and DQE) was implemented for clinical EPIDs and also extended to volumetric IGRT solutions like CBCT systems. The bar-pattern technique was used in conjunction with an easily available clinical QA phantom to obtain the first reported measurements of MTF, NPS, and DQE spectra for CBCT systems in the reconstructed domain. Preliminary implementations of a bar-pattern based QA tool for clinical EPIDs and CBCT units provided encouraging results. In particular, the expansion of this technique with customized QA phantoms for more efficient automation can provide an effective platform for QA, device commissioning, optimization of image acquisition parameters, appropriate representation of patient scatter conditions, and detector development for CBCT systems, and in principle, any form of radiographic volumetric imaging device (including MV-CBCT or MVCT).

For the two prototype configurations developed in this research, their projected performances easily exceeded currently available standard for portal image quality. For the proposed TSC prototype, $QE \sim 24\%$, $DQE(0) > 10\%$, and $MTF(1 \text{ cy/mm}) > 7\%$ is expected. This reflects a negligible loss of imaging performance relative to the intrinsic upper limits set by the physics of the detection medium and the x-ray beam. It is also an order of magnitude improvement in overall imaging performance compared to currently available commercial EPIDs as indicated in Figures 7-1 and 7-2. Similarly, for the proposed FOSGA prototype (6 cm thickness, and 70% fill factor), $QE > 45\%$, $DQE(0) > 26\%$, and $MTF(1 \text{ cy/mm}) > 10\%$. As seen in Figures 7-1 and 7-2, the projected performance of a prototype FOSGA detector is greater than

current standards of image quality by more than a factor of 20. This will enable high quality megavoltage imaging and soft tissue contrast visualization at sub-MU exposures, which promotes a logical extension of EPIDs to volumetric imaging via MV-CBCT. In summary, this research provided two significant benefits to radiotherapy – the characterization of a new generation of thick scintillator based megavoltage x-ray imagers for CBCT based IGRT, and the novel adaptation of fundamental imaging metrics from imaging research to routine clinical imaging performance QA.

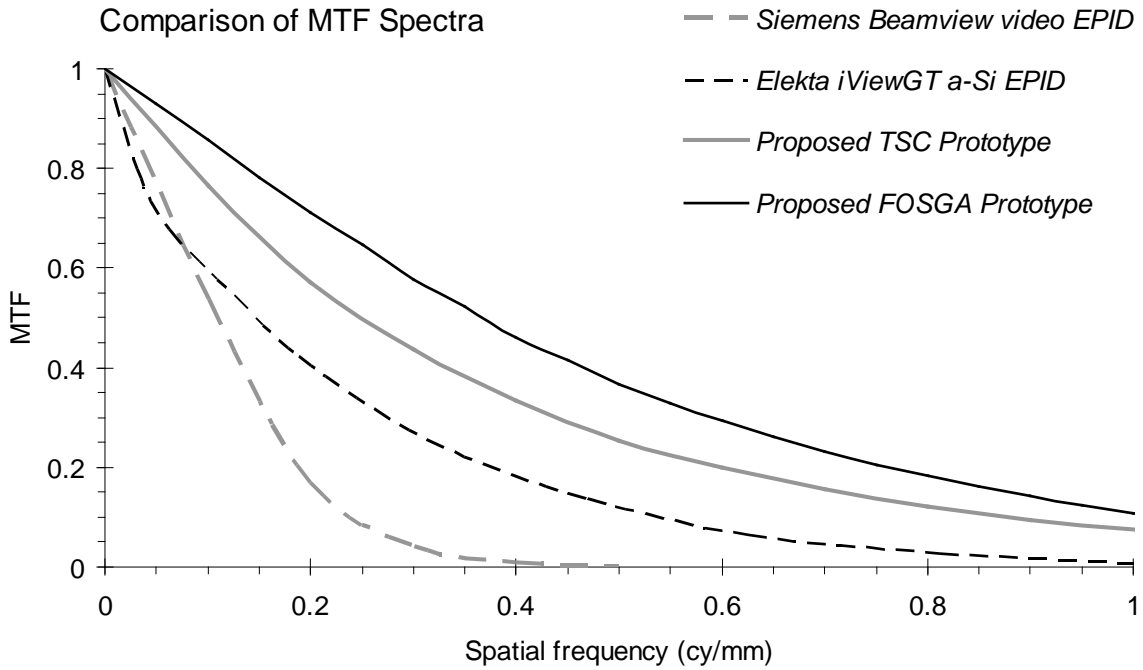


Figure 7-1. Comparison of the projected MTF spectra for the proposed TSC and FOSGA prototypes compared to current conventional EPID systems.

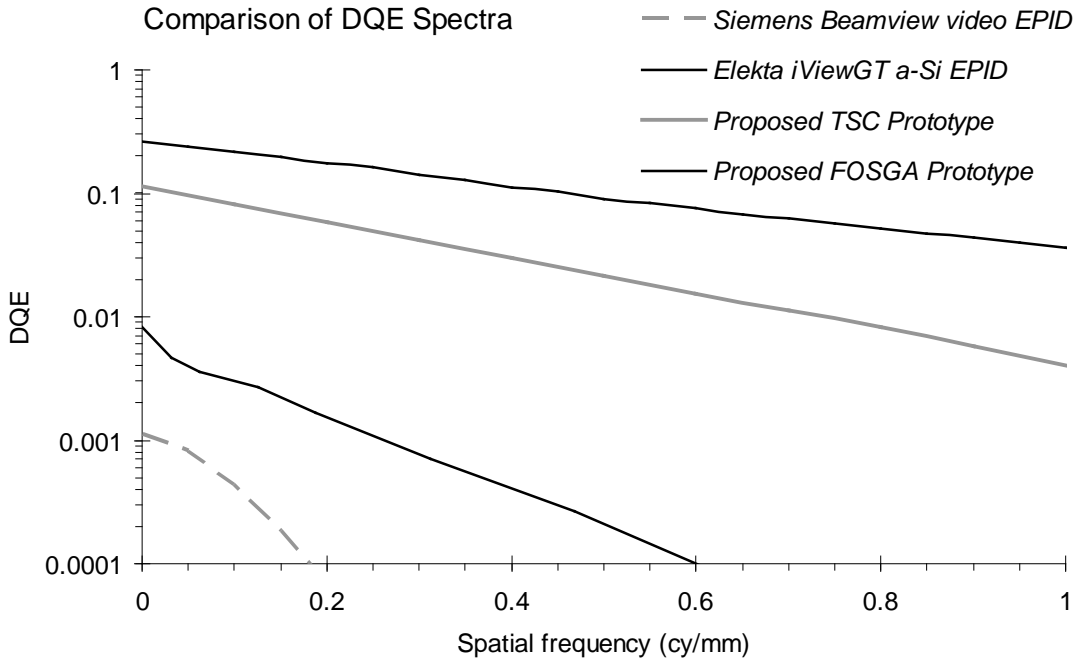


Figure 7-2. Comparison of the projected DQE spectra for the proposed TSC and FOSGA prototypes compared to current conventional EPID systems.

LIST OF REFERENCES

- ¹J. F. Williamson, "Brachytherapy technology and physics practice since 1950: a half-century of progress," *Phys Med Biol* **51** (13), R303-325 (2006).
- ²K. R. Hogstrom and P. R. Almond, "Review of electron beam therapy physics," *Phys Med Biol* **51** (13), R455-489 (2006).
- ³A. R. Smith, "Proton therapy," *Phys Med Biol* **51** (13), R491-504 (2006).
- ⁴S. S. Samant, W. Zheng, N. A. Parra, J. Chandler, A. Gopal, J. Wu, J. Jain, Y. Zhu, and M. Sontag, "Verification of multileaf collimator leaf positions using an electronic portal imaging device," *Med Phys* **29** (12), 2900-2912 (2002).
- ⁵T. Bortfeld, "IMRT: a review and preview," *Phys Med Biol* **51** (13), R363-379 (2006).
- ⁶B. S. Teh, S. Y. Woo, and E. B. Butler, "Intensity modulated radiation therapy (IMRT): a new promising technology in radiation oncology," *Oncologist* **4** (6), 433-442 (1999).
- ⁷P. C. Williams, "IMRT: delivery techniques and quality assurance," *Br J Radiol* **76** (911), 766-776 (2003).
- ⁸A. Djordjevich, D. J. Bonham, E. M. Hussein, J. W. Andrew, and M. E. Hale, "Optimal design of radiation compensators," *Med Phys* **17** (3), 397-404 (1990).
- ⁹S. B. Jiang and K. M. Ayyangar, "On compensator design for photon beam intensity-modulated conformal therapy," *Med Phys* **25** (5), 668-675 (1998).
- ¹⁰R. Topolnjak, U. A. van der Heide, and J. J. Lagendijk, "IMRT sequencing for a six-bank multi-leaf system," *Phys Med Biol* **50** (9), 2015-2031 (2005).
- ¹¹P. Xia and L. J. Verhey, "Multileaf collimator leaf sequencing algorithm for intensity modulated beams with multiple static segments," *Med Phys* **25** (8), 1424-1434 (1998).
- ¹²S. Kamath, S. Sahni, J. Li, J. Palta, and S. Ranka, "Leaf sequencing algorithms for segmented multileaf collimation," *Phys Med Biol* **48** (3), 307-324 (2003).
- ¹³S. Webb, "Configuration options for intensity-modulated radiation therapy using multiple static fields shaped by a multileaf collimator. II: constraints and limitations on 2D modulation," *Phys Med Biol* **43** (6), 1481-1495 (1998).
- ¹⁴D. J. Convery and S. Webb, "Generation of discrete beam-intensity modulation by dynamic multileaf collimation under minimum leaf separation constraints," *Phys Med Biol* **43** (9), 2521-2538 (1998).
- ¹⁵T. R. Mackie, J. Balog, K. Ruchala, D. Shepard, S. Aldridge, E. Fitchard, P. Reckwerdt, G. Olivera, T. McNutt, and M. Mehta, "Tomotherapy," *Semin Radiat Oncol* **9** (1), 108-117 (1999).
- ¹⁶T. R. Mackie, "History of tomotherapy," *Phys Med Biol* **51** (13), R427-453 (2006).

- ¹⁷L. E. Antonuk, "Electronic portal imaging devices: a review and historical perspective of contemporary technologies and research," *Phys Med Biol* **47** (6), R31-65 (2002).
- ¹⁸J. Bernier, E. J. Hall, and A. Giaccia, "Radiation oncology: a century of achievements," *Nat Rev Cancer* **4** (9), 737-747 (2004).
- ¹⁹J. M. Balter and Y. Cao, "Advanced technologies in image-guided radiation therapy," *Semin Radiat Oncol* **17** (4), 293-297 (2007).
- ²⁰J. M. Balter and M. L. Kessler, "Imaging and alignment for image-guided radiation therapy," *J Clin Oncol* **25** (8), 931-937 (2007).
- ²¹L. A. Dawson and D. A. Jaffray, "Advances in image-guided radiation therapy," *J Clin Oncol* **25** (8), 938-946 (2007).
- ²²D. A. Jaffray, "Image-guided radiation therapy: from concept to practice," *Semin Radiat Oncol* **17** (4), 243-244 (2007).
- ²³D. A. Jaffray, J. H. Siewerdsen, J. W. Wong, and A. A. Martinez, "Flat-panel cone-beam computed tomography for image-guided radiation therapy," *Int J Radiat Oncol Biol Phys* **53** (5), 1337-1349 (2002).
- ²⁴C. C. Ling, E. Yorke, and Z. Fuks, "From IMRT to IGRT: frontierland or neverland?," *Radiother Oncol* **78** (2), 119-122 (2006).
- ²⁵M. van Herk, "Different styles of image-guided radiotherapy," *Semin Radiat Oncol* **17** (4), 258-267 (2007).
- ²⁶D. Verellen, M. De Ridder, and G. Storme, "A (short) history of image-guided radiotherapy," *Radiother Oncol* **86** (1), 4-13 (2008).
- ²⁷D. Verellen, M. D. Ridder, N. Linthout, K. Tournel, G. Soete, and G. Storme, "Innovations in image-guided radiotherapy," *Nat Rev Cancer* **7** (12), 949-960 (2007).
- ²⁸L. Xing, B. Thorndyke, E. Schreibmann, Y. Yang, T. F. Li, G. Y. Kim, G. Luxton, and A. Koong, "Overview of image-guided radiation therapy," *Med Dosim* **31** (2), 91-112 (2006).
- ²⁹A. L. Boyer, L. Antonuk, A. Fenster, M. Van Herk, H. Meertens, P. Munro, L. E. Reinstein, and J. Wong, "A review of electronic portal imaging devices (EPIDs)," *Med Phys* **19** (1), 1-16 (1992).
- ³⁰M. G. Herman, J. M. Balter, D. A. Jaffray, K. P. McGee, P. Munro, S. Shalev, M. Van Herk, and J. W. Wong, "Clinical use of electronic portal imaging: report of AAPM Radiation Therapy Committee Task Group 58," *Med Phys* **28** (5), 712-737 (2001).
- ³¹H. E. Johns and I. A. Cunningham, "The Physics of Radiology," Charles C. Thomas, Springfield, IL (1983).

- ³²J. Nielsen and S. H. Jensen, "Some experimental and clinical light on rotation therapy, its basis and possibilities," *Acta Radiologica* **23**, 16 (1942).
- ³³J. G. Trump, E. W. Webster, K. A. Wright, W. W. Evans, R. C. Granke, H. F. Hare, S. W. Lippincott, Jr., and D. Sawyer, "Physical and clinical aspects of supervoltage rotational therapy," *Radiology* **57** (2), 157-168 (1951).
- ³⁴C. R. Perryman, Allister Jd Mc, and J. A. Burwell, "Cobalt 60 radiography," *Am J Roentgenol Radium Ther Nucl Med* **83**, 525-532 (1960).
- ³⁵W. J. Tuddenham, J. F. Gibbons, J. Hale, and E. P. Pendergrass, "Supervoltage and multiple simultaneous roentgenography; new technics for roentgen examination of the chest," *Radiology* **63** (2), 184-191 (1954).
- ³⁶W. J. Tuddenham, J. Hale, and E. P. Pendergrass, "Supervoltage diagnostic roentgenography; a preliminary report," *Am J Roentgenol Radium Ther Nucl Med* **70** (5), 759-765 (1953).
- ³⁷J. R. Andrews, R. W. Swain, and P. Rubin, "Continuous visual monitoring of 2 mev. roentgen therapy," *Am J Roentgenol Radium Ther Nucl Med* **79** (1), 74-78 (1958).
- ³⁸M. Strandqvist and B. Rosengren, "Television-controlled pendulum therapy," *Br J Radiol* **31** (369), 513-514 (1958).
- ³⁹S. Benner, B. Rosengren, H. Wallman, and O. Netteland, "Television monitoring of a 30 MV x-ray beam," *Phys Med Biol* **7**, 29-34 (1962).
- ⁴⁰N. A. Baily, R. A. Horn, and T. D. Kampp, "Fluoroscopic visualization of megavoltage therapeutic x ray beams," *Int J Radiat Oncol Biol Phys* **6** (7), 935-939 (1980).
- ⁴¹J. P. Bissonnette, I. A. Cunningham, and P. Munro, "Optimal phosphor thickness for portal imaging," *Med Phys* **24** (6), 803-814 (1997).
- ⁴²S. S. Samant and A. Gopal, "Study of a prototype high quantum efficiency thick scintillation crystal video-electronic portal imaging device," *Med Phys* **33** (8), 2783-2791 (2006).
- ⁴³W. Swindell, "The lens coupling efficiency in megavoltage imaging," *Med Phys* **18** (6), 1152-1153 (1991).
- ⁴⁴B. J. Heijmen, K. L. Pasma, M. Kroonwijk, V. G. Althof, J. C. de Boer, A. G. Visser, and H. Huizenga, "Portal dose measurement in radiotherapy using an electronic portal imaging device (EPID)," *Phys Med Biol* **40** (11), 1943-1955 (1995).
- ⁴⁵H. Meertens, M. van Herk, J. Bijhold, and H. Bartelink, "First clinical experience with a newly developed electronic portal imaging device," *Int J Radiat Oncol Biol Phys* **18** (5), 1173-1181 (1990).
- ⁴⁶H. Meertens, M. van Herk, and J. Weeda, "A liquid ionisation detector for digital radiography of therapeutic megavoltage photon beams," *Phys Med Biol* **30** (4), 313-321 (1985).

- ⁴⁷M. van Herk, "Physical aspects of a liquid-filled ionization chamber with pulsed polarizing voltage," *Med Phys* **18** (4), 692-702 (1991).
- ⁴⁸M. van Herk, J. Bijhold, B. Hoogervorst, and H. Meertens, "Sampling methods for a matrix ionization chamber system," *Med Phys* **19** (2), 409-418 (1992).
- ⁴⁹M. van Herk and H. Meertens, "A matrix ionisation chamber imaging device for on-line patient setup verification during radiotherapy," *Radiother Oncol* **11** (4), 369-378 (1988).
- ⁵⁰L. E. Antonuk, J. Yorkston, J. Boudry, M. J. Longo, J. Jimenez, and R. A. Street, "Development of hydrogenated amorphous silicon sensors for high energy photon radiotherapy imaging," *IEEE Trans. Nucl. Sci.* **37**, 6 (1990).
- ⁵¹L. E. Antonuk, J. Boudry, W. Huang, D. L. McShan, E. J. Morton, J. Yorkston, M. J. Longo, and R. A. Street, "Demonstration of megavoltage and diagnostic x-ray imaging with hydrogenated amorphous silicon arrays," *Med Phys* **19** (6), 1455-1466 (1992).
- ⁵²L. E. Antonuk, J. Boudry, W. Huang, K. L. Lam, E. J. Morton, R. T. Haken, J. Yorkston, and N. H. Clinthorne, "Thin-film, flat-panel, composite imagers for projection and tomographic imaging," *IEEE Trans Med Imaging* **13** (3), 482-490 (1994).
- ⁵³L. E. Antonuk, J. Yorkston, W. Huang, J. H. Siewerdsen, J. M. Boudry, Y. el-Mohri, and M. V. Marx, "A real-time, flat-panel, amorphous silicon, digital x-ray imager," *Radiographics* **15** (4), 993-1000 (1995).
- ⁵⁴L. E. Antonuk, J. Yorkston, W. Huang, H. Sandler, J. H. Siewerdsen, and Y. el-Mohri, "Megavoltage imaging with a large-area, flat-panel, amorphous silicon imager," *Int J Radiat Oncol Biol Phys* **36** (3), 661-672 (1996).
- ⁵⁵L. E. Antonuk, Y. El-Mohri, J. H. Siewerdsen, J. Yorkston, W. Huang, V. E. Scarpine, and R. A. Street, "Empirical investigation of the signal performance of a high-resolution, indirect detection, active matrix flat-panel imager (AMFPI) for fluoroscopic and radiographic operation," *Med Phys* **24** (1), 51-70 (1997).
- ⁵⁶L. E. Antonuk, Y. El-Mohri, W. Huang, K. W. Jee, J. H. Siewerdsen, M. Maolinbay, V. E. Scarpine, H. Sandler, and J. Yorkston, "Initial performance evaluation of an indirect-detection, active matrix flat-panel imager (AMFPI) prototype for megavoltage imaging," *Int J Radiat Oncol Biol Phys* **42** (2), 437-454 (1998).
- ⁵⁷P. Munro and D. C. Bouius, "X-ray quantum limited portal imaging using amorphous silicon flat-panel arrays," *Med Phys* **25** (5), 689-702 (1998).
- ⁵⁸Y. El-Mohri, K. W. Jee, L. E. Antonuk, M. Maolinbay, and Q. Zhao, "Determination of the detective quantum efficiency of a prototype, megavoltage indirect detection, active matrix flat-panel imager," *Med Phys* **28** (12), 2538-2550 (2001).
- ⁵⁹J. M. Boudry and L. E. Antonuk, "Radiation damage of amorphous silicon, thin-film, field-effect transistors," *Med Phys* **23** (5), 743-754 (1996).

- ⁶⁰J. W. Wong, W. R. Binns, A. Y. Cheng, L. Y. Geer, J. W. Epstein, J. Klarmann, and J. A. Purdy, "On-line radiotherapy imaging with an array of fiber-optic image reducers," *Int J Radiat Oncol Biol Phys* **18** (6), 1477-1484 (1990).
- ⁶¹P. Munro, J. A. Rawlinson, and A. Fenster, "A digital fluoroscopic imaging device for radiotherapy localization," *Int J Radiat Oncol Biol Phys* **18** (3), 641-649 (1990).
- ⁶²D. G. Drake, D. A. Jaffray, and J. W. Wong, "Characterization of a fluoroscopic imaging system for kV and MV radiography," *Med Phys* **27** (5), 898-905 (2000).
- ⁶³G. Pang and J. A. Rowlands, "Electronic portal imaging with an avalanche-multiplication-based video camera," *Med Phys* **27** (4), 676-684 (2000).
- ⁶⁴K. S. Lam, M. Partowmah, and W. C. Lam, "An on-line electronic portal imaging system for external beam radiotherapy," *Br J Radiol* **59** (706), 1007-1013 (1986).
- ⁶⁵G. Entine, M. R. Squillante, R. Hahn, L. J. Cirignano, W. McGann, and P. J. Biggs, "High contrast, CdTe portal scanner for radiation therapy," *IEEE Trans Nucl Sci* **39**, 5 (1992).
- ⁶⁶S. C. Taborsky, W. C. Lam, R. E. Sterner, and G. M. Skarda, "Digital imaging for radiation therapy verification," *Opt Eng* **21**, 6 (1982).
- ⁶⁷T. Falco, H. Wang, and B. G. Fallone, "Preliminary study of a metal/a-Se-based portal detector," *Med Phys* **25** (6), 814-823 (1998).
- ⁶⁸M. Lachaine, E. Fourkal, and B. G. Fallone, "Detective quantum efficiency of a direct-detection active matrix flat panel imager at megavoltage energies," *Med Phys* **28** (7), 1364-1372 (2001).
- ⁶⁹D. Mah, J. A. Rawlinson, and J. A. Rowlands, "Detective quantum efficiency of an amorphous selenium detector to megavoltage radiation," *Phys Med Biol* **44** (5), 1369-1384 (1999).
- ⁷⁰G. Pang, D. L. Lee, and J. A. Rowlands, "Investigation of a direct conversion flat panel imager for portal imaging," *Med Phys* **28** (10), 2121-2128 (2001).
- ⁷¹A. Brahme, M. Danielsson, C. Iacobaeus, J. Ostling, V. Peskov, and M. Wallmark, "Evaluation of a GEM and CAT-based detector for radiation therapy beam monitoring," *Nucl Instrum Methods A* **454**, 6 (2000).
- ⁷²F. Sauli, "GEM: a new concept for electron amplification in gas detectors," *Nucl Instrum Methods A* **386**, 4 (1997).
- ⁷³X. Mei and G. Pang, "Development of high quantum efficiency, flat panel, thick detectors for megavoltage x-ray imaging: an experimental study of a single-pixel prototype," *Med Phys* **32** (11), 3379-3388 (2005).
- ⁷⁴X. Mei, J. A. Rowlands, and G. Pang, "Electronic portal imaging based on cerenkov radiation: a new approach and its feasibility," *Med Phys* **33** (11), 4258-4270 (2006).

- ⁷⁵G. Pang and J. A. Rowlands, "Development of high quantum efficiency flat panel detectors for portal imaging: intrinsic spatial resolution," *Med Phys* **29** (10), 2274-2285 (2002).
- ⁷⁶G. Pang and J. A. Rowlands, "Development of high quantum efficiency, flat panel, thick detectors for megavoltage x-ray imaging: a novel direct-conversion design and its feasibility," *Med Phys* **31** (11), 3004-3016 (2004).
- ⁷⁷S. S. Samant and A. Gopal, "Analysis of the kinestatic charge detection system as a high detective quantum efficiency electronic portal imaging device," *Med Phys* **33** (9), 3557-3567 (2006).
- ⁷⁸F. A. DiBianca and M. D. Barker, "Kinestatic charge detection," *Med Phys* **12** (3), 339-343 (1985).
- ⁷⁹A. Gopal and S. S. Samant, "Effect of recombination in a high quantum efficiency prototype ionization-chamber-based electronic portal imaging device," *Med Phys* **34** (8), 3224-3232 (2007).
- ⁸⁰T. Radcliffe, G. Barnea, B. Wowk, R. Rajapakshe, and S. Shalev, "Monte Carlo optimization of metal/phosphor screens at megavoltage energies," *Med Phys* **20** (4), 1161-1169 (1993).
- ⁸¹B. Wowk, T. Radcliffe, K. W. Leszczynski, S. Shalev, and R. Rajapakshe, "Optimization of metal/phosphor screens for on-line portal imaging," *Med Phys* **21** (2), 227-235 (1994).
- ⁸²B. Wowk and S. Shalev, "Thick phosphor screens for on-line portal imaging," *Med Phys* **21** (8), 1269-1276 (1994).
- ⁸³M. A. Mosleh-Shirazi, P. M. Evans, W. Swindell, J. R. Symonds-Taylor, S. Webb, and M. Partridge, "Rapid portal imaging with a high-efficiency, large field-of-view detector," *Med Phys* **25** (12), 2333-2346 (1998).
- ⁸⁴M. A. Mosleh-Shirazi, P. M. Evans, W. Swindell, S. Webb, and M. Partridge, "A cone-beam megavoltage CT scanner for treatment verification in conformal radiotherapy," *Radiother Oncol* **48** (3), 319-328 (1998).
- ⁸⁵M. A. Mosleh-Shirazi, W. Swindell, and P. M. Evans, "Monte Carlo Simulations of CsI(Tl) Scintillation Crystals for Use in a Three-Dimensional Megavoltage CT Scanner," *Nucl. Instrum. Methods A* **348**, 4 (1994).
- ⁸⁶M. A. Mosleh-Shirazi, W. Swindell, and P. M. Evans, "Optimization of the scintillation detector in a combined 3D megavoltage CT scanner and portal imager," *Med Phys* **25** (10), 1880-1890 (1998).
- ⁸⁷A. Sawant, H. Zeman, S. Samant, G. Lovhoiden, B. Weinberg, and F. DiBianca, "Theoretical analysis and experimental evaluation of a CsI(Tl) based electronic portal imaging system," *Med Phys* **29** (6), 1042-1053 (2002).

- ⁸⁸H. Zeman, S. S. Samant, G. Lovhoiden, B. Weinberg, and A. Sawant, "Portal Imaging with a CsI(Tl) Transparent Scintillator X-Ray Detector," *Proc. SPIE* **3336**, 12 (1998).
- ⁸⁹T. T. Monajemi, B. G. Fallone, and S. Rathee, "Thick, segmented CdWO₄-photodiode detector for cone beam megavoltage CT: a Monte Carlo study of system design parameters," *Med Phys* **33** (12), 4567-4577 (2006).
- ⁹⁰T. T. Monajemi, D. Tu, B. G. Fallone, and S. Rathee, "A bench-top megavoltage fan-beam CT using CdWO₄-photodiode detectors. II. Image performance evaluation," *Med Phys* **33** (4), 1090-1100 (2006).
- ⁹¹S. Rathee, D. Tu, T. T. Monajemi, D. W. Rickey, and B. G. Fallone, "A bench-top megavoltage fan-beam CT using CdWO₄-photodiode detectors. I. System description and detector characterization," *Med Phys* **33** (4), 1078-1089 (2006).
- ⁹²T. T. Monajemi, S. Steciw, B. G. Fallone, and S. Rathee, "Modeling scintillator-photodiodes as detectors for megavoltage CT," *Med Phys* **31** (5), 1225-1234 (2004).
- ⁹³A. Sawant, L. E. Antonuk, Y. El-Mohri, Q. Zhao, Y. Li, Z. Su, Y. Wang, J. Yamamoto, H. Du, I. Cunningham, M. Klugerman, and K. Shah, "Segmented crystalline scintillators: an initial investigation of high quantum efficiency detectors for megavoltage x-ray imaging," *Med Phys* **32** (10), 3067-3083 (2005).
- ⁹⁴A. Sawant, L. E. Antonuk, Y. El-Mohri, Q. Zhao, Y. Wang, Y. Li, H. Du, and L. Perna, "Segmented crystalline scintillators: empirical and theoretical investigation of a high quantum efficiency EPID based on an initial engineering prototype CsI(Tl) detector," *Med Phys* **33** (4), 1053-1066 (2006).
- ⁹⁵A. F. Holloway, "A localising device for a rotating cobalt therapy unit," *Br J Radiol* **31** (364), 227 (1958).
- ⁹⁶L. J. Verhey, M. Goitein, P. McNulty, J. E. Munzenrider, and H. D. Suit, "Precise positioning of patients for radiation therapy," *Int J Radiat Oncol Biol Phys* **8** (2), 289-294 (1982).
- ⁹⁷Y. Aoki, A. Akanuma, K. Karasawa, K. Sakata, K. Nakagawa, N. Muta, Y. Onogi, and M. Iio, "An integrated radiotherapy treatment system and its clinical application," *Radiat Med* **5** (4), 131-141 (1987).
- ⁹⁸C. W. Cheng, J. Wong, L. Grimm, M. Chow, M. Uematsu, and A. Fung, "Commissioning and clinical implementation of a sliding gantry CT scanner installed in an existing treatment room and early clinical experience for precise tumor localization," *Am J Clin Oncol* **26** (3), e28-36 (2003).
- ⁹⁹L. Court, I. Rosen, R. Mohan, and L. Dong, "Evaluation of mechanical precision and alignment uncertainties for an integrated CT/LINAC system," *Med Phys* **30** (6), 1198-1210 (2003).

- ¹⁰⁰K. Kuriyama, H. Onishi, N. Sano, T. Komiyama, Y. Aikawa, Y. Tateda, T. Araki, and M. Uematsu, "A new irradiation unit constructed of self-moving gantry-CT and linac," *Int J Radiat Oncol Biol Phys* **55** (2), 428-435 (2003).
- ¹⁰¹M. Uematsu, A. Shioda, A. Suda, K. Tahara, T. Kojima, Y. Hama, M. Kono, J. R. Wong, T. Fukui, and S. Kusano, "Intrafractional tumor position stability during computed tomography (CT)-guided frameless stereotactic radiation therapy for lung or liver cancers with a fusion of CT and linear accelerator (FOCAL) unit," *Int J Radiat Oncol Biol Phys* **48** (2), 443-448 (2000).
- ¹⁰²W. Swindell, R. G. Simpson, J. R. Oleson, C. T. Chen, and E. A. Grubbs, "Computed tomography with a linear accelerator with radiotherapy applications," *Med Phys* **10** (4), 416-420 (1983).
- ¹⁰³P. S. Cho, R. H. Johnson, and T. W. Griffin, "Cone-beam CT for radiotherapy applications," *Phys Med Biol* **40** (11), 1863-1883 (1995).
- ¹⁰⁴D. A. Jaffray, D. G. Drake, M. Moreau, A. A. Martinez, and J. W. Wong, "A radiographic and tomographic imaging system integrated into a medical linear accelerator for localization of bone and soft-tissue targets," *Int J Radiat Oncol Biol Phys* **45** (3), 773-789 (1999).
- ¹⁰⁵D. A. Jaffray and J. H. Siewerdsen, "Cone-beam computed tomography with a flat-panel imager: initial performance characterization," *Med Phys* **27** (6), 1311-1323 (2000).
- ¹⁰⁶J. H. Siewerdsen and D. A. Jaffray, "Cone-beam computed tomography with a flat-panel imager: effects of image lag," *Med Phys* **26** (12), 2635-2647 (1999).
- ¹⁰⁷J. H. Siewerdsen and D. A. Jaffray, "Cone-beam computed tomography with a flat-panel imager: magnitude and effects of x-ray scatter," *Med Phys* **28** (2), 220-231 (2001).
- ¹⁰⁸J. Chen, O. Morin, M. Aubin, M. K. Bucci, C. F. Chuang, and J. Pouliot, "Dose-guided radiation therapy with megavoltage cone-beam CT," *Br J Radiol* **79 Spec No 1**, S87-98 (2006).
- ¹⁰⁹H. Guan and Y. Zhu, "Feasibility of megavoltage portal CT using an electronic portal imaging device (EPID) and a multi-level scheme algebraic reconstruction technique (MLS-ART)," *Phys Med Biol* **43** (10), 2925-2937 (1998).
- ¹¹⁰E. K. Hansen, D. A. Larson, M. Aubin, J. Chen, M. Descovich, A. M. Gillis, O. Morin, P. Xia, and J. Pouliot, "Image-guided radiotherapy using megavoltage cone-beam computed tomography for treatment of paraspinal tumors in the presence of orthopedic hardware," *Int J Radiat Oncol Biol Phys* **66** (2), 323-326 (2006).
- ¹¹¹S. Midgley, R. M. Millar, and J. Dudson, "A feasibility study for megavoltage cone beam CT using a commercial EPID," *Phys Med Biol* **43** (1), 155-169 (1998).
- ¹¹²O. Morin, J. Chen, M. Aubin, A. Gillis, J. F. Aubry, S. Bose, H. Chen, M. Descovich, P. Xia, and J. Pouliot, "Dose calculation using megavoltage cone-beam CT," *Int J Radiat Oncol Biol Phys* **67** (4), 1201-1210 (2007).

- ¹¹³O. Morin, A. Gillis, J. Chen, M. Aubin, M. K. Bucci, M. Roach, 3rd, and J. Pouliot, "Megavoltage cone-beam CT: system description and clinical applications," *Med Dosim* **31** (1), 51-61 (2006).
- ¹¹⁴J. Pouliot, A. Bani-Hashemi, J. Chen, M. Svatos, F. Ghelmansarai, M. Mitschke, M. Aubin, P. Xia, O. Morin, K. Bucci, M. Roach, 3rd, P. Hernandez, Z. Zheng, D. Hristov, and L. Verhey, "Low-dose megavoltage cone-beam CT for radiation therapy," *Int J Radiat Oncol Biol Phys* **61** (2), 552-560 (2005).
- ¹¹⁵K. J. Ruchala, G. H. Olivera, J. M. Kapatoes, E. A. Schloesser, P. J. Reckwerdt, and T. R. Mackie, "Megavoltage CT image reconstruction during tomotherapy treatments," *Phys Med Biol* **45** (12), 3545-3562 (2000).
- ¹¹⁶K. J. Ruchala, G. H. Olivera, E. A. Schloesser, and T. R. Mackie, "Megavoltage CT on a tomotherapy system," *Phys Med Biol* **44** (10), 2597-2621 (1999).
- ¹¹⁷K. M. Langen, S. L. Meeks, D. O. Poole, T. H. Wagner, T. R. Willoughby, P. A. Kupelian, K. J. Ruchala, J. Haimerl, and G. H. Olivera, "The use of megavoltage CT (MVCT) images for dose recomputations," *Phys Med Biol* **50** (18), 4259-4276 (2005).
- ¹¹⁸S. L. Meeks, J. F. Harmon, Jr., K. M. Langen, T. R. Willoughby, T. H. Wagner, and P. A. Kupelian, "Performance characterization of megavoltage computed tomography imaging on a helical tomotherapy unit," *Med Phys* **32** (8), 2673-2681 (2005).
- ¹¹⁹J. C. Dainty and R. Shaw, "Image Science: Principles, Analysis and Evaluation of Photographic-Type Imaging Processes," Academic Press, San Diego, CA (1974).
- ¹²⁰C. E. Metz and K. Doi, "Transfer function analysis of radiographic imaging systems," *Phys Med Biol* **24** (6), 1079-1106 (1979).
- ¹²¹C. D. Bradford, W. W. Pepler, and J. M. Waidelich, "Use of a slit camera for MTF measurements," *Med Phys* **26** (11), 2286-2294 (1999).
- ¹²²R. T. Droege, "A megavoltage MTF measurement technique for metal screen-film detectors," *Med Phys* **6** (4), 272-279 (1979).
- ¹²³R. T. Droege and B. E. Bjarngard, "Metal screen-film detector MTF at megavoltage x-ray energies," *Med Phys* **6** (6), 515-518 (1979).
- ¹²⁴T. Falco and B. G. Fallone, "Characteristics of metal-plate/film detectors at therapy energies. I. Modulation transfer function," *Med Phys* **25** (12), 2455-2462 (1998).
- ¹²⁵H. Fujita, D. Y. Tsai, T. Itoh, K. Doi, J. Morishita, K. Ueda, and A. Ohtsuka, "A simple method for determining the modulation transfer function in digital radiography," *IEEE Trans Med Imaging* **11** (1), 34-39 (1992).

- ¹²⁶C. E. Metz, K. A. Strubler, and K. Rossmann, "Choice of line spread function sampling distance for computing the MTF of radiographic screen-film systems," *Phys Med Biol* **17** (5), 638-647 (1972).
- ¹²⁷K. Rossmann, "Point spread-function, line spread-function, and modulation transfer function. Tools for the study of imaging systems," *Radiology* **93** (2), 257-272 (1969).
- ¹²⁸K. Rossmann, A. G. Haus, and K. Doi, "Validity of the MTF of magnification radiography," *Phys Med Biol* **17** (5), 648-655 (1972).
- ¹²⁹K. Rossmann and G. Lubberts, "Some characteristics of the line spread-function and modulation transfer function of medical radiographic films and screen-film systems," *Radiology* **86** (2), 235-241 (1966).
- ¹³⁰A. Sawant, L. Antonuk, and Y. El-Mohri, "Slit design for efficient and accurate MTF measurement at megavoltage x-ray energies," *Med Phys* **34** (5), 1535-1545 (2007).
- ¹³¹I. A. Cunningham and A. Fenster, "A method for modulation transfer function determination from edge profiles with correction for finite-element differentiation," *Med Phys* **14** (4), 533-537 (1987).
- ¹³²H. Illers, E. Buhr, S. Gunther-Kohfahl, and U. Neitzel, "Measurement of the modulation transfer function of digital X-ray detectors with an opaque edge-test device," *Radiat Prot Dosimetry* **114** (1-3), 214-219 (2005).
- ¹³³J. W. Israel and N. J. Schneiders, "Calculation of the MTF from the ERF," *Med Phys* **6** (1), 72-73 (1979).
- ¹³⁴U. Neitzel, E. Buhr, G. Hilgers, and P. R. Granfors, "Determination of the modulation transfer function using the edge method: influence of scattered radiation," *Med Phys* **31** (12), 3485-3491 (2004).
- ¹³⁵E. Samei, M. J. Flynn, and D. A. Reimann, "A method for measuring the presampled MTF of digital radiographic systems using an edge test device," *Med Phys* **25** (1), 102-113 (1998).
- ¹³⁶N. J. Schneiders and S. C. Bushong, "Single-step calculation of the MTF from the ERF," *Med Phys* **5** (1), 31-33 (1978).
- ¹³⁷J. W. Coltman, "The Specification of Imaging Properties by Response to a Sine Wave Input," *J Opt Soc Am* **44**, 4 (1954).
- ¹³⁸G. Lubberts, "Some aspects of the square wave response function of radiographic screen film systems," *Am J Roentgenol* **106**, 5 (1969).
- ¹³⁹H. Nyquist, "Certain topics in telegraph transmission theory," *Trans AIEE* **47**, 28 (1928).
- ¹⁴⁰C. E. Shannon, "Communication in the presence of noise," *Proc Institute of Radio Engineers* **37**, 12 (1949).

- ¹⁴¹A. K. Jain, "Fundamentals of Digital Image Processing," Prentice Hall, Englewood Cliffs, NJ (1989).
- ¹⁴²A. Gopal and S. S. Samant, "Validity of the line-pair bar-pattern method in the measurement of the modulation transfer function (MTF) in megavoltage imaging," *Med Phys* **35** (1), 270-279 (2008).
- ¹⁴³J. T. Dobbins, 3rd, D. L. Ergun, L. Rutz, D. A. Hinshaw, H. Blume, and D. C. Clark, "DQE(f) of four generations of computed radiography acquisition devices," *Med Phys* **22** (10), 1581-1593 (1995).
- ¹⁴⁴R. T. Droege and R. L. Morin, "A practical method to measure the MTF of CT scanners," *Med Phys* **9** (5), 758-760 (1982).
- ¹⁴⁵R. T. Droege and M. S. Rzeszotarski, "An MTF method immune to aliasing," *Med Phys* **12** (6), 721-725 (1985).
- ¹⁴⁶J. T. Dobbins, 3rd, E. Samei, N. T. Ranger, and Y. Chen, "Intercomparison of methods for image quality characterization. II. Noise power spectrum," *Med Phys* **33** (5), 1466-1475 (2006).
- ¹⁴⁷M. L. Giger, K. Doi, and H. Fujita, "Investigation of basic imaging properties in digital radiography. 7. Noise Wiener spectra of II-TV digital imaging systems," *Med Phys* **13** (2), 131-138 (1986).
- ¹⁴⁸M. L. Giger, K. Doi, and C. E. Metz, "Investigation of basic imaging properties in digital radiography. 2. Noise Wiener spectrum," *Med Phys* **11** (6), 797-805 (1984).
- ¹⁴⁹R. F. Wagner, "Fast Fourier digital quantum mottle analysis with application to rare earth intensifying screen systems," *Med Phys* **4** (2), 157-162 (1977).
- ¹⁵⁰M. B. Williams, P. A. Mangiafico, and P. U. Simoni, "Noise power spectra of images from digital mammography detectors," *Med Phys* **26** (7), 1279-1293 (1999).
- ¹⁵¹R. K. Swank, "Absorption and noise in x-ray phosphors," *J Appl Phys* **44**, 5 (1973).
- ¹⁵²J. H. Siewerdsen, L. E. Antonuk, Y. el-Mohri, J. Yorkston, W. Huang, and I. A. Cunningham, "Signal, noise power spectrum, and detective quantum efficiency of indirect-detection flat-panel imagers for diagnostic radiology," *Med Phys* **25** (5), 614-628 (1998).
- ¹⁵³J. M. Hammersly and D. C. Handscomb, "Monte Carlo Methods," Methuen, London, UK (1964).
- ¹⁵⁴T. M. Jenkins, W. R. Nelson, and A. Rindi, "Monte Carlo Transport of Photons and Electrons," Plenum Press, New York, NY (1988).
- ¹⁵⁵H. A. Meyer, "Symposium on Monte Carlo Methods," John Willey and Sons, New York, NY (1954).

- ¹⁵⁶R. L. Morin, "Monte Carlo Simulation in the Radiological Sciences," CRC Press, Boca Raton, FL (1988).
- ¹⁵⁷J. A. Halbleib, R. P. Kensek, T. A. Mehlhorn, G. D. Valdez, S. M. Seltzer, and M. J. Berger, "ITS Version 3.0: Integrated Tiger Series for Coupled Photon/Electron," SANDIA91-1634, Sandia National Laboratories, Albuquerque, NM (1992).
- ¹⁵⁸D. B. Pelowitz, "MCNPX User's Manual," LA-CP-05-0369, Los Alamos National Laboratories, Los Alamos, NM (2005).
- ¹⁵⁹J. P. Bissonnette, I. A. Cunningham, D. A. Jaffray, A. Fenster, and P. Munro, "A quantum accounting and detective quantum efficiency analysis for video-based portal imaging," *Med Phys* **24** (6), 815-826 (1997).
- ¹⁶⁰I. A. Cunningham, M. S. Westmore, and A. Fenster, "A spatial-frequency dependent quantum accounting diagram and detective quantum efficiency model of signal and noise propagation in cascaded imaging systems," *Med Phys* **21** (3), 417-427 (1994).
- ¹⁶¹C. W. van Eijk, "Inorganic scintillators in medical imaging," *Phys Med Biol* **47** (8), R85-106 (2002).
- ¹⁶²M. J. Weber, "Scintillations: mechanisms and new crystals," *Nucl. Instrum. Methods A* **527**, 6 (2004).
- ¹⁶³C.L. Woody, J.A. Kierstead, P. W. Levy, and S. Stoll, "Radiation Damage in Undoped CsI and CsI(Tl)," *IEEE Transon Nucl Sc* **39**, 8 (1992).
- ¹⁶⁴G. F. Knoll, "Radiation Detection and Measurement," John Wiley & Sons, New York, NY (1989).
- ¹⁶⁵R. Mohan, C. Chui, and L. Lidofsky, "Energy and angular distributions of photons from medical linear accelerators," *Med Phys* **12** (5), 592-597 (1985).
- ¹⁶⁶D. A. Jaffray, J. J. Battista, A. Fenster, and P. Munro, "X-ray sources of medical linear accelerators: focal and extra-focal radiation," *Med Phys* **20** (5), 1417-1427 (1993).
- ¹⁶⁷J. P. Bissonnette, D. A. Jaffray, A. Fenster, and P. Munro, "Optimal radiographic magnification for portal imaging," *Med Phys* **21** (9), 1435-1445 (1994).
- ¹⁶⁸D. W. O. Rogers, "Fluence to Dose Equivalent Conversion Factors Calculated with EGS for Electrons from 100 Kev to 20 Gev and Photons from 11 Kev to 20 Gev," *Health Phys* **46**, 14 (1984).
- ¹⁶⁹H. Liu, A. Karellas, L. J. Harris, and C. J. D'Orsi, "Methods to calculate the lens efficiency in optically coupled CCD x-ray imaging systems," *Med Phys* **21** (7), 1193-1195 (1994).

- ¹⁷⁰Y. A. Berdnikov, V. V. Grebenshchikov, V. F. Kosmach, I. E. Leonov, V. M. Samsonov, O. Y. Khrushcheva, and A. P. Shishlo, "Special Features of Light Collection Processes in Heavy-Crystal-Based Scintillation Detectors," *Instr Exper Tech* **44**, 16 (2001).
- ¹⁷¹T. Yu, J. M. Sabol, J. A. Seibert, and J. M. Boone, "Scintillating fiber optic screens: a comparison of MTF, light conversion efficiency, and emission angle with Gd₂O₂S:Tb screens," *Med Phys* **24** (2), 279-285 (1997).
- ¹⁷²A. Gopal and S. Samant, "Use of a line-pair resolution phantom for comprehensive quality assurance of electronic portal imaging devices based on fundamental imaging metrics," *Med Phys* **36**, 10 (2009).
- ¹⁷³R. Rajapakshe, K. Luchka, and S. Shalev, "A quality control test for electronic portal imaging devices," *Med Phys* **23** (7), 1237-1244 (1996).
- ¹⁷⁴M. G. Herman, R. A. Abrams, and R. R. Mayer, "Clinical use of on-line portal imaging for daily patient treatment verification," *Int J Radiat Oncol Biol Phys* **28** (4), 1017-1023 (1994).
- ¹⁷⁵K. Doi, K. Strubler, and K. Rossmann, "Truncation errors in calculating the MTF of radiographic screen-film systems from the line spread function," *Phys Med Biol* **17** (2), 241-250 (1972).
- ¹⁷⁶I. A. Cunningham and B. K. Reid, "Signal and noise in modulation transfer function determinations using the slit, wire, and edge techniques," *Med Phys* **19** (4), 1037-1044 (1992).
- ¹⁷⁷E. Buhr, S. Gunther-Kohfahl, and U. Neitzel, "Accuracy of a simple method for deriving the presampled modulation transfer function of a digital radiographic system from an edge image," *Med Phys* **30** (9), 2323-2331 (2003).
- ¹⁷⁸N. Mail, D. J. Moseley, J. H. Siewerdsen, and D. A. Jaffray, "The influence of bowtie filtration on cone-beam CT image quality," *Med Phys* **36** (1), 22-32 (2009).
- ¹⁷⁹G. X. Ding, D. M. Duggan, and C. W. Coffey, "Characteristics of kilovoltage x-ray beams used for cone-beam computed tomography in radiation therapy," *Phys Med Biol* **52** (6), 1595-1615 (2007).
- ¹⁸⁰J. P. Bissonnette, D. J. Moseley, and D. A. Jaffray, "A quality assurance program for image quality of cone-beam CT guidance in radiation therapy," *Med Phys* **35** (5), 1807-1815 (2008).
- ¹⁸¹W. Y. Song, S. Kamath, S. Ozawa, S. A. Ani, A. Chvetsov, N. Bhandare, J. R. Palta, C. Liu, and J. G. Li, "A dose comparison study between XVI and OBI CBCT systems," *Med Phys* **35** (2), 480-486 (2008).
- ¹⁸²E. Spezi, P. Downes, E. Radu, and R. Jarvis, "Monte Carlo simulation of an x-ray volume imaging cone beam CT unit," *Med Phys* **36** (1), 127-136 (2009).
- ¹⁸³T. B. Shope, R. M. Gagne, and G. C. Johnson, "A method for describing the doses delivered by transmission x-ray computed tomography," *Med Phys* **8** (4), 488-495 (1981).

¹⁸⁴R. Fahrig, R. Dixon, T. Payne, R. L. Morin, A. Ganguly, and N. Strobel, "Dose and image quality for a cone-beam C-arm CT system," *Med Phys* **33** (12), 4541-4550 (2006).

¹⁸⁵K. Perisinakis, J. Damilakis, A. Tzedakis, A. Papadakis, N. Theodoropoulos, and N. Gourtsoyiannis, "Determination of the weighted CT dose index in modern multi-detector CT scanners," *Phys Med Biol* **52** (21), 6485-6495 (2007).

BIOGRAPHICAL SKETCH

Arun Gopal was born in 1977 in Mumbai, India. He graduated from the University of Mumbai with a Bachelor of Engineering degree in biomedical engineering in 1999, a master's degree in biomedical engineering at the University of Tennessee, Health Science Center, Memphis in 2004. He enrolled into the PhD program in medical physics at the Department of Nuclear and Radiological Engineering in 2005. His major research area is in the development of improved radiographic imaging applications for radiotherapy, as well as in the formulation of fundamental metrics of imaging performance characterization for imaging systems.